Statistical Impact Prediction of Space Debris

The Uncertainty Propagation Approach

R. Hoogendoorn

Delft University of Technology

TU Delft Delft University of Technology

Challenge the future

Cover picture: artist impression of the Automated Transfer Vehicle during atmospheric entry. Image courtesy: European Space Agency (ESA)

STATISTICAL IMPACT PREDICTION OF SPACE DEBRIS

THE UNCERTAINTY PROPAGATION APPROACH

by

R. Hoogendoorn

in partial fulfillment of the requirements for the degree of

Master of Science
in Aerospace Engineering

at the Delft University of Technology,
to be defended publicly on Tuesday August 30, 2016 at 09:30.

Supervisors:	Dr. Ir. E. Mooij
	Ir. J. Geul
Thesis committee:	Prof. Dr. L. L. A. Vermeersen
	Prof. Dr. F. H. J. Redig

TU Delft Delft University of Technology

Preface

This MSc. thesis is the final deliverable for my studies at the Delft University of Technology. This report describes the research that I have performed at the Astrodynamics & Space Missions group of the Aerospace Engineering faculty. This topic has combined my interest in mathematics and spaceflight dynamics in a challenging way. Because I have had no course in statistics before, I always wanted to learn about statistics, so I find it very valuable to perform my thesis research on this topic. Furthermore, I consider the C++ programming skills that I have developed during my thesis very valuable for my further carreer. I enjoyed the time at the faculty and I hope that I can persue a carreer that includes some form of research.

The work that I have carried out during this project is highly influenced by other people. Therefore, I would like to thank these people for the support and technical advice. I would like to thank my supervisor dr. Erwin Mooij for the technical advice, the ideas and the good laughs that we had during our conversations and meetings. My second supervisor Jacco Geul also deserves a sincere thank you for the advice, the collaboration on the uncertainty model, programming help and the good laughs. The profesors from the mathematics department of the Delft University of Technology were also of great help and a special thanks goes to Prof. Dr. F.H.J. Redig for the support on the statistical methods. Furthermore, I would like to thank the students of the 9^{th} floor, which helped me in good times and in worse, and who supported me during the long days. To my friends and family I also owe a word of thanks, because of their support and encouragement. A special word of thanks goes to my girlfriend Eleni, who supported me throughout the research project and my studies and helped me such that I could work at my best.

Delft, August 2016
René Hoogendoorn

Abstract

The in-orbit explosion of the US Transit-4A satellite in 1961 marks the start of Space Debris as the largest group of observable objects in Earth orbit. These objects are a notable hazard to satellites and humans in space and on Earth. An example of these hazards is that the International Space Station executes on average one debris avoidance maneuver per year to reduce the risk of impact.

Impact predictions of space debris are performed using numerical simulations with models of the debris object and the environment. These predictions are subject to many uncertainties present in the models and the state of the body, which makes the prediction inherently statistical. Currently, Monte Carlo (MC) methods are used to obtain statistical information of the impact location and time. These methods require a large number of trajectory simulations to obtain impact footprints, which makes the method computationally expensive.

Recent research has shown that direct methods are available to propagate uncertainty in time, which have the potential to provide more accurate results with the same or even less computational effort. These methods directly propagate probability density functions in time, which can be used to obtain statistical impact footprints. This thesis work aims to improve statistical impact predictions by improving the statistical methods to obtain these predictions.

Two methods were selected that can propagate a probability density function: an approximate method referred to as the Least-Squares Kernel Density (LSQKD) method and an exact method called the Direct Probability Density Function Propagation (DPP) method. However, a preliminary analysis on the Least-Squares Kernel Density (LSQKD) method showed that the accuracy is not sufficient for atmospheric entry problems. Nevertheless, highly accurate results were obtained with the DPP method for several test cases.

The results of the DPP method is a scattered dataset of a multi-dimensional probability density function. Because strong relations were observed in the data and the high-dimensionality of the function, defining a generic method to process the data is difficult. Therefore, the data could not be processed such that accurate results are obtained. In addition, simulations performed using the DPP method showed that numerical issues occur, because of the choice of the state variables that was made. The simulations of uncontrolled atmospheric entry trajectories ended with almost vertical flight, which resulted in singularities in the DPP

method, which did not result in problems using the Monte Carlo (MC) method. Because of the problems of processing the data and the numerical issues, no accurate results could be obtained for statistical impact prediction using this method.

An analysis on the uncertainty model showed that the uncertainty in the atmospheric density has a lognormal distribution in contrast to a uniform distribution, which was used in previous research. Statistical impact predictions were performed using the MC method with the improved uncertainty model to obtain statistical information about the time of impact. The results showed that the impact time window is underestimated if a uniform distribution is used instead of a lognormal distribution. A statistical validation showed that all obtained impact time windows were overestimated, which is preferred over underestimated windows.

Table of Contents

Nomenclature

Abbreviations

AIAA	American Institute of Aeronautics and Astronautics
CDF	Cumulative Distribution Function
DoF	Degrees of Freedom
DPP	Direct Probability Density Function Propagation
DQMOM	Direct Quadrature Method of Moments
ESA	European Space Agency
GSL	GNU Scientific Library
GPS	Global Positioning System
GMST	Greenwich Mean Sidereal Time
ISS	International Space Station
JPL	Jet Propulsion Laboratory
JSPOC	Joint Space Operation Center
KDE	Kernel Density Estimate
LEO	Low-Earth Orbit
LSQKD	Least-Squares Kernel Density
MC	Monte Carlo
MISE	Mean Integrated Square Error
MSE	Mean Square Error
NASA	National Aeronautics and Space Administration

NORAD	North American Aerospace Defense Command
NRLMSISE-00	NRL Mass Spectrometer and Incoherent Scatter Radar
ODE	Ordinary Differential Equation
PDF	Probability Density Function
PF	Perron-Frobenius
PDE	Partial Differential Equation
QMOM	Quadrature Method of Moments
RBF	Radial Basis Function
RK5(6)	Runge-Kutta 5(6)
SSN	Space Surveillance Network
SGP4	Simplified General Perturbations 4
TLE	Two Line Element
Tudat	TU Delft Astrodynamics Toolbox
TIP	Tracking and Impact Prediction
USSTRATCOM	United States Strategic Command
UT1	Universal Time

Latin symbols

Symbol	Description	Unit
$\boldsymbol{a}$	Acceleration	m/s^2
a	Speed of sound	m/s
$\boldsymbol{C}$	Aerodynamic coefficient vector	-
$\boldsymbol{C}_{A,B}$	Transformation matrix from the B to the A frame.	-
$\boldsymbol{C}$	Cholesky factor	-
C_L	Aerodynamic lift coefficient	-
C_D	Aerodynamic drag coefficient	-
C_S	Aerodynamic sideforce coefficient	-
c_i	Coefficient	-
d	Dimension	-
e	Ellipticity of the Earth	-
$\boldsymbol{F}$	State derivative model	-
$\boldsymbol{F}$	Force vector	N
f	Probability density function	-
$\hat{f}$	Approximation of the function f	-
F	Cummulative density function	-
F_X	Cummulative marginal density function of X	-
g	Gravitational acceleration	m/s^2
h	Smoothing parameter of kernel density estimation	var.
$\boldsymbol{H}$	LSQKD Matrix	-
$\mathbf{I}$	Inertia tensor	kgm^2
J	Cost function	-
J_2	Gravity coefficient	-
K	Kernel function	-
K_n	Knudsen number	-
L	Aerodynamic lift force	N
L_{ref}	Aerodynamic reference length	m
m	Mass	kg
$\boldsymbol{M}$	Moment	Nm
M	Molar mass	kg
N	Number of samples	-
n	Number density	-
$\boldsymbol{p}$	Vector with model parameters	var.
$\boldsymbol{q}$	Quaternion vector	-
q_i	Quaternion	-
R	Radial distance	m
$\boldsymbol{r}$	Position vector	var.
r	Radial distance	var.
$\boldsymbol{R}$	Correlation matrix	-
R	Gas constant	J/kgK
R_{abs}	Absolute gas constant	J/molK
R_S	Surface radius of the Earth	m
R_E	Equatorial radius of the Earth	m

S	Surface area	m^2
S_{ref}	Aerodynamic reference surface	m^2
t	Time	s
T	Temperature	K
w	weight factor	-
$\boldsymbol{w}$	weight factor vector	-
$\boldsymbol{V}$	Velocity vector	m/s
$\boldsymbol{V}_G$	Ground velocity vector	m/s
V_R	Radial velocity	m/s
V_E	East velocity	m/s
V_N	North velocity	m/s
U	Uniformly distributed random variable	var.
u_i	Random sample generated from a uniform distribution	var.
$\boldsymbol{X}$	State variable vector	var.
$\boldsymbol{X}_0$	State variable vector at the initial time	var.
$\boldsymbol{x}_f$	State variable vector at the final time	var.
$\boldsymbol{X}_L$	Local state variables (LSQKD method)	var.
$\boldsymbol{X}_G$	Global state variables (LSQKD method)	var.
$\bar{x}$	Sample mean of x	var.
X_ρ	Atmospheric density factor	-

Greek symbols

Symbol	Description	Unit
α	Angle of attack	rad
β	Angle of sideslip	rad
β	Inverse scale height	rad
$\boldsymbol{\beta}$	Kernel parameters vector	var.
γ	Flight-path angle	rad
γ	Specific heat ratio	-
δ	Latitude	rad
δ	Dirac delta function	rad
θ_g	Vernal offset angle	rad
λ	Mean free path	m
λ	Lagrange multiplier	-
μ	Mean	
μ	Gravitational parameter	m^3/s^2
ρ	Correlation	
ρ_r	Rank correlation	
ρ	Atmospheric density	kg/m^3
ρ_M	Modelled Atmospheric density	kg/m^3
ρ_O	Observed Atmospheric density	kg/m^3
σ	Bank angle	rad

σ	Standard deviation	var.
σ	Collision diameter	m
$\mathbf{\Sigma}$	Covariance matrix	var.
σ_{XY}	Covariance between random variable X and Y	var.
τ	Longitude	rad
φ	Probability density function	-
χ	Heading angle	rad
Ψ	State derivative of PDF correction factor Ω	rad
$\boldsymbol{\omega}$	Rotational velocity	rad/s
ω_E	Rotational velocity of the Earth	rad/s
Ω	PDF correction factor	-

"No knowledge can be certain, if it is not based upon mathematics or upon some other knowledge which is itself based upon the mathematical sciences. Instrumental, or mechanical, science is the nobles and, above all others, the most useful."

Leonardo da Vinci

"In order to determine whether we can know anything with certainty, we first have to doubt everything we know."

René Descartes

Chapter 1

Introduction

Spaceflight has brought a tremendous number of possibilities and opportunities that changed the world. About 1,000 currently active satellites provide communication, navigation, weather information and data for science. A total of 3,600 satellites are in orbit around Earth, which means that only 28% of the satellites are currently operational. The remaining satellites are non-operational and part of the space-debris group. The space debris group contains a large number of man-made objects that are non functional, which originate from explosions of satellites, spent upper stages of launchers, decommissioned satellites and mission-related items.

These space-debris objects that are in orbit around Earth will eventually enter Earth's atmosphere through a process called atmospheric decay. Although the atmosphere is thin at higher altitudes, aerodynamic drag will decellerate the satellite. The centripetal acceleration that counteracts the gravitational acceleration will decrease and the debris gradually decreases in altitude untill the debris enters the atmosphere and impacts Earth. With velocities in the order of 7 km/s, the debris will fall through the atmosphere while converting a large amount of energy into heat. As a result, the object will either burn up in the atmosphere or breakup and impact Earth with a velocity in the order of 100 m/s.

For larger objects, it is estimated that 10% to 40% of the mass survives until ground impact. Because of the large population of space debris, these objects thus pose a hazard to humans or human possessions. An example of hazards involved with space debris entering the Earth's atmosphere is the entry of the Cosmos-954 satellite. The uncontrolled entry of this satellite spreaded 30 kg of radioactive material over Canada in the year 1978. This illustrates the need to provide accurate predictions of the impact location and impact time of these objects.

Impact predictions of space debris were mostly performed by propagating the position and velocity of the space-debris object. The rotational state of the body is neglected and the aerodynamic forces were derived by averaging methods. The impact footprint is derived by introducing an entry window, which is used to account for uncertainty, or by performing a break-up analysis and propagate each fragment until the Earth's surface. The result of such methods is an impact footprint, which does not account for uncertainty in the initial state of

the rocket body or uncertainty in the models. In the research of Ronse (2013), it was shown that these uncertainties have a large influence on the impact time. Because a large number of uncertainties are present in impact predictions, they are inherently statistical. This research is focussed on improving those statistical preditions, which leads to the following research question:

Can we improve the accuracy of statistical predictions of the impact location or impact time of objects that enter the atmosphere?

Statistical impact predictions can be improved by using better statistical methods or using a better uncertainty model, which are both assessed in this research. Current methods to perform statistical impact predictions use Monte Carlo simulations to obtain an impact footprint. This method is based on performing a large number of simulations using random samples. This results in a large number of samples, which can be used to obtain probability distributions of the impact time or location.

Recent research has shown that methods are available that directly propagate uncertainty, expressed by probability distributions, in time. These methods have the potential to provide more accurate results with the same or even less computational effort. Research has been performed on two of these methods during this thesis work. An approximate method called the Least-Squares Kernel Density (LSQKD) method and an exact method referred to as the Direct Probability Density Function Propagation (DPP) method are evaluated here. Statistical impact predictions are performed with an improved uncertainty model for the Delta-K rocket body and compared to previous work by Ronse (2013) and impact predictions provided by United States Strategic Command (USSTRATCOM)[1].

This thesis starts with the mission heritage in Chapter 2, which explains some basic concepts and the insights that were obtained from a literature study performed on the subject. In Chapter 3, uncertainty-analysis methods are discussed, which are used to perform statistical impact predictions using information about the uncertainty in the initial state and in the models. Chapter 4 presents a preliminary analysis that is performed on the uncertainty propagation methods in which the performance of the methods is evaluated and limitations are discussed. Subsequently, Chapter 5 discusses the dynamics and models that are used to simulate the decay and entry trajectories of the Delta-K rocket body. Chapter 6 describes the uncertainty model of the initial state and atmospheric density that is used in the statistical methods to produce impact time distributions. This is an important chapter, because it provides the main input for the statistical methods, determining the shape and width of the impact time distributions that are obtained later in the research. Chapter 7 describes the statistical methods that are used to perform the statistical impact prediction. This chapter discusses how the methods described in Chapter 3 are applied to statistical impact prediction. Chapter 8 describes the development of the simulators that are used to perform the simulations and the process that is used to verify and validate the simulators. The results of the simulations are described in Chapter 9 and this thesis is concluded with the conclusions and recommendations in Chapter 10.

[1] `https://www.space-track.org/`; date accessed: 15-08-2016

Chapter 2

Mission Heritage

Impact predictions of space debris are subjected to a large number of uncertainties. The impact prediction is thus generally a statistical impact prediction, because these uncertainties have an influence on the predictions. The uncertainties are described by an uncertainty model and statistical methods are used to determine the uncertainty in the impact location or time. The space debris problem is introduced in Section 2-1 and previous studies are described in Section 2-2, from which knowledge can be used to improve the predictions. The reference vehicle that is used for the predictions in this research is described in Section 2-4. Subsequently, a survey on uncertainty propagation methods is described in Section 2-3 that can be used to perform these predictions. The chapter is ended with conclusions that are drawn from the literature review (Section 2-5).

2-1 The Space Debris Problem

Since the in-orbit explosion of the US Transit-4A satellite in 1961, space debris is the largest group of observable objects in Earth orbit making it a notable hazard to satellites and humans both in space and on Earth.

Currently, it is known that more than 21,000 objects larger than 10 cm orbit the Earth. The number of objects with a size between 1 and 10 cm is estimated to be 500,000, and it is believed that more than 100 million particles smaller than 1 cm orbit the Earth. These objects originate mostly from explosions of satellites, collisions, an increasing number of spent upper stages of launchers, decommissioned satellites and other mission-related items.

Space debris objects can impact satellites, the International Space Station or enter the Earth's atmosphere and impact the Earth's surface. The first recorded accidental collision occurred in 1996 when a fragment of an exploded Ariane stage hit the Cerise satellite. Another accident happened in February 2009 when a U.S. Iridium 33 communications satellite collided with a fragment from Cosmos 2251 resulting in more than 2000 large pieces of debris added to the

population[1]. An anti-satellite missile test performed by China is noted as the largest debris creation event, which took place in 2007. This test resulted in more than 2800 pieces with a size of at least 5 cm added to the space debris population (Klinkrad, 2006).

Considering the large amount of space debris orbiting the Earth, re-entering debris poses a serious hazard for impacts or a release of substances in the atmosphere. An example of such a hazard is the entry of the Cosmos-954 satellite in 1978. This satellite re-entered uncontrolled, spreading 30 kg of radioactive material over Canada. Another source of impacts is the second stage of the Delta-II launcher. For this second stage, it is expected that in 2002, all second stages have survived atmospheric entry and impacted the Earth. Debris of two impact events of this rocket body is shown in Figure 2-1. The figure shows a tank of 250 kg that impacted the Earth in Texas at a distance of 50 meter from a farmhouse. Of all trackable objects, 18,000 (66.7%) have re-entered the Earth's atmosphere in between 1957 and 2002. It was estimated that 10% to 40% of the mass of the larger objects may survive until ground impact. Considering the size and mass of these objects, they pose risks to humans and human posessions on Earth (Klinkrad, 2006).

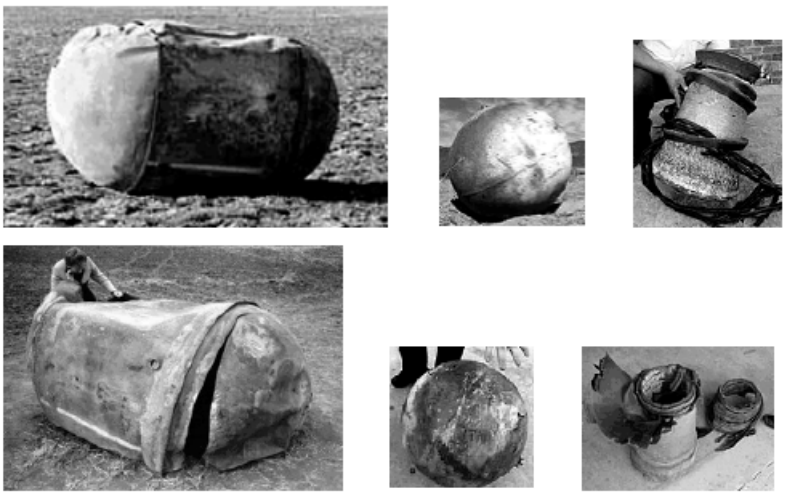

Figure 2-1: Typical survivor objects of the Delta-II second stage that survived re-entry and was retrieved in South Africa on 27-04-2000 and on 22-01-1997 in the USA (Klinkrad, 2006).

Since 1990 it is postulated that the collision of intact space-debris objects and collision fragments will cause a self-sustained growth of the population. This is called Collisional Cascading or the *Kessler Syndrome*. Therefore, it is expected that the hazards involved with space debris will increase with time and thus the risks for impact on Earth will increase (Klinkrad, 2006).

2-2 Previous Impact and Atmospheric Entry Studies

Impact predictions of space debris are generally performed using tools that can be divided in two categories: lifetime and impact prediction tools, and atmospheric-entry analysis tools

[1]Orbital Debris Quaterly News, July 2011: `http://orbitaldebris.jsc.nasa.gov/Quarterly-News/newsletter.html/`; date accessed: 15-08-2016

(Ronse, 2013). The studies presented here are not a complete set, but provide insight in the current methods that are used to perform these predictions.

Lifetime and impact prediction tools use numerical or (semi-) analytical methods to propagate the state of the debris object in time for the decay phase of the trajectory. A numerical simulation is performed in the atmospheric entry phase, because of the rapidly changing aerodynamic conditions. These tools only consider the translational state of the body, so the aerodynamic forces are obtained by averaging methods. No uncertainty or breakup is account for, but an impact window is introduced to account for uncertainties. However, in the research of Ronse (2013), it was found that the evolution of the rotational state is important for impact predictions.

Examples of atmospheric-entry analysis tools are ORSAT of the European Space Agency (ESA) and SCARAB of the National Aeronautics and Space Administration (NASA). In the research of Portelli et al. (2004), an impact analysis was performed for the BeppoSAX satellite, which impacted the Earth in 2003. The translational state and rotational state of the satellite were propagated until Mach 6, whereafter only the translational state is propagated until impact. A fragmentation or break-up analysis is performed and each fragment is seperately propagated to determine an impact footprint of the fragments. The resulting footprint and fragmentation history are shown in Figure 2-2 and Figure 2-3.

A similar analysis was performed using the ORSAT tool by Rochelle and Johnson (2004). This tool only propagates the translational state in time, so the rotational motion is neglected. The assumed breakup altitude was defined to be 78 km and each fragment is seperately propagated after breakup to obtain an impact footprint.

All of these tools only derive an impact footprint based on a breakup analysis or by introducing an entry window, without providing any additional statistical information or including uncertainties in the analysis. In the research of Ronse (2013) it was found that these uncertainties have an important influence on the impact footprint.

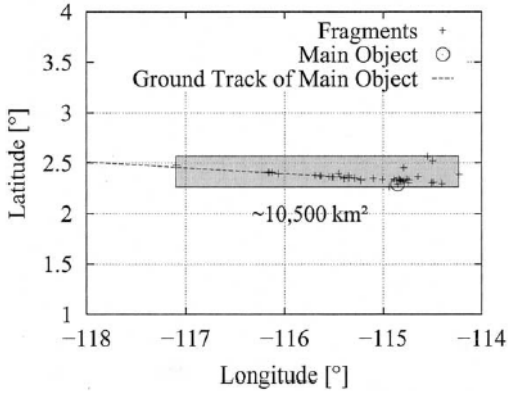

Figure 2-2: Footprint resulting from re-entry analysis of BeppoSAX (Portelli et al., 2004).

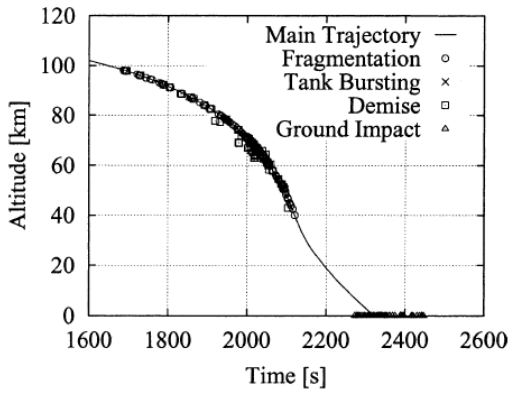

Figure 2-3: Fragmentation history resulting from re-entry analysis of BeppoSAX (Portelli et al., 2004).

A series of studies have been performed to determine the dispersion in the impact location due to uncertainties in the parameters that are used to estimate the trajectory (Cheatwood and Desai, 2001; Desai et al., 1997, 1999, 2006; Queen et al., 1999). These studies used the

Monte Carlo method (Section 2-3) with a 6 Degrees-of-Freedom (DoF) trajectory simulator to obtain statistical information about the impact location. The studies included uncertainty in approximately 40 parameters to derive a dispersion meausre of the impact location. These uncertainties were mostly based on expert judgement instead of a rigorous analysis. Gaussian and uniform distributions were used to model the uncertainty in the parameters. Dispersions in the impact location were obtained that are in the order of $20 - 60$ km as a result of the uncertainties present in the models. A sensitivity analysis was performed to determine which uncertainties have the largest influence on the impact footprint. These studies concluded that the atmospheric density, wind model and the initial state have the largest influence on the impact dispersion.

2-2-1 Impact Prediction

Impact predictions of space debris are provided by the United States Strategic Command (USSTRATCOM) for bodies that have a risk of reaching the surface without breaking up that is higher than 5%. These Tracking and Impact Prediction (TIP) are published on space-track.org[2] and provide an impact epoch and window in which the body is expected to impact. TIPs are generated using observations of the Space Surveillance Network (SSN), which are published as a Two-Line Element (TLE). In addition, the USSTRATCOM also provides historical information about the impact time and location of a large number of bodies, so this data can be used to verify the predictions.

An advanced impact prediction analysis was performed by Ronse (2013), who performed several statistical impact predictions of historical impacts of the Delta-K rocket body. A trajectory simulator was developed that propagates the translational and rotational state of the rocket body and a panel method was used to obtain an aerodynamic database as a function of the angle of attack, angle of sideslip and Mach number. A Monte Carlo analysis was performed and the results were used to form 99.73% probability impact footprints. The results were validated using the true impact points and it was concluded that the obtained impact time distribution matches with the derived footprints. A comparison with TIP windows showed that the obtained impact windows were smaller than the TIP windows in 79% of the cases. An example of the impact time distributions that were obtained is shown in Figure 2-4. The figure shows that the obtained distribution is in good agreement with the true impact point.

A sensitivity analysis showed that the uncertainty in the atmospheric density has the largest influence on the impact time. Furthermore, the uncertainty in the initial rotational state also has a large influence on the impact time dispersion and it was found that the uncertainty in the initial translational state has the smallest influence.

2-2-2 Conclusion

These studies show that uncertainty in parameters and the state of the body can cause a large dispersion in the impact location and impact time. Furthermore, the research of Ronse (2013) has shown that the rotational state needs to be included to determine a statistical impact footprint.

[2] `https://www.space-track.org/`; date accessed: 15-08-2016

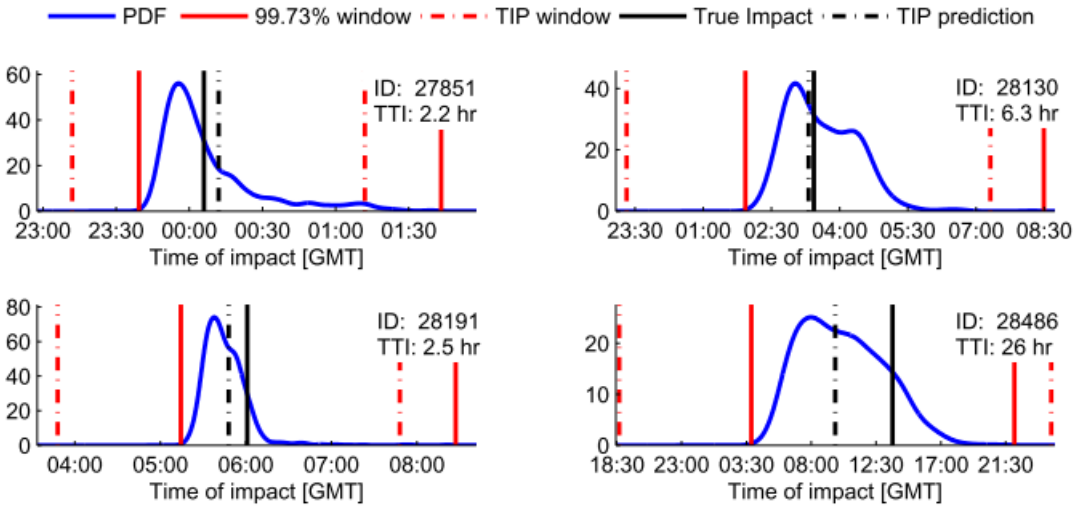

Figure 2-4: Impact time distributions obtained in the research of Ronse (2013).

All studies that were found in literature use the MC method to obtain statistical information about the impact time and location. It was found that there are more statistical methods that can be used for this kind of analysis, which could possibly have a better performance. Therefore, a literature survey has been performed on these method and a discussion is presented in Section 2-3.

2-3 Uncertainty Propagation Methods

Obtaining statistical information about the impact location and impact time requires a method that can derive this information from an uncertainty model. Atmospheric entry problems generally have uncertainty in the initial state and in a large number of parameters that are included in the equations of motion, for example: the atmospheric density and the aerodynamic coefficients. To obtain statistical information about the state of a body at a later time, the initial uncertainty needs to be propagated in time. Several methods have been found that can propagate uncertainty, which are discussed in this section. Before discussing the methods a short introduction on uncertainty modelling is provided.

2-3-1 Uncertainty Modelling

If there is uncertainty in the impact time of the object, it means that the impact time is a random variable. Therefore, the impact time lies within a certain interval with a certain probability, so the impact time is not equal to one value. Information about these probabilities is stored in the probability distribution of the random variable. The Probability Density Function (PDF) is one of the functions that can be used to describe the probability distribution of a random variable.

An example of a Probability Density Function (PDF) is shown in Figure 2-5 for a random variable X. The area under the PDF curve corresponds to probabilities. Because the area

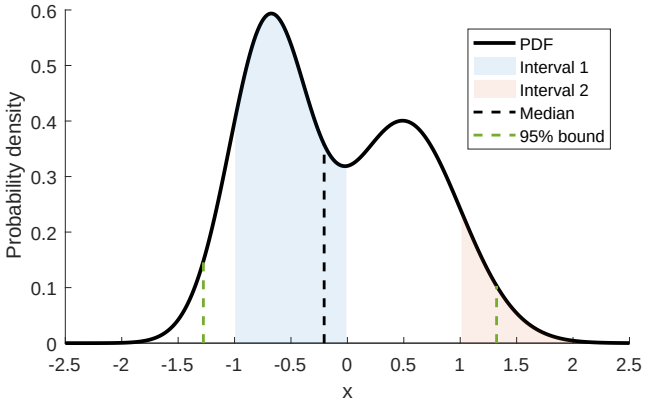

Figure 2-5: Example of a probability density function.

under the PDF in interval one is larger than interval two, the probability of X to have a value in $[-1, 0]$ is larger than the probability of X to have a value in $[1, 2]$. The median corresponds to the center of the distribution, because it marks the 50% probability border. This means that there is a probability of 50% that the value of X is higher or lower. In addition the 95% probability bound is shown in the figure, which mark the enclosed area that corresponds to 95% probability. The random variable X thus has a value between $[-1.28, 1.32]$ with 95% probability. More information on probability theory is provided in Appendix A.

2-3-2 Monte Carlo

A way to obtain statistical information of a variable is to randomly sample the variables and to perform a large number of simulations using these samples. Statistical information is obtained by analyzing the distribution of the samples after the simulations. Methods that use this technique are called Monte Carlo (MC) methods. In general, MC methods can be described as a method based on random sampling. These methods are widely used for the propagation of uncertainty for atmospheric entry problems.

The benefit of the method is that it avoids the curse of dimensionallity, which refers to an exponential increase with increasing dimension that is observed in, for example, numerical quadrature. The probabilistic error bound that is obtained for MC is $O(\sigma/\sqrt{N})$ for determining the mean value of a dataset, where N is the number of samples. This error bound shows that generally a large number of samples is required to obtain accurate results. The convergence rate can be increased using Quasi-MC methods, which employ a different sampling technique that is explained in Section 3-1-1. These methods can have a convergence rate that approaches $O(\sigma/N)$ (Niedereiter, 1992).

To illustrate the convergence rate of the MC method, an example is shown in Figure 2-6. The figure shows an exact PDF and several estimates of this PDF that are obtained using MC samples drawn from the exact distribution. The exact PDF is generated using a summation of two Gaussian distributions and the MC samples are used to estimate the PDF using kernel density estimation, which is discussed in Section 3-2. The figure shows that the distribution

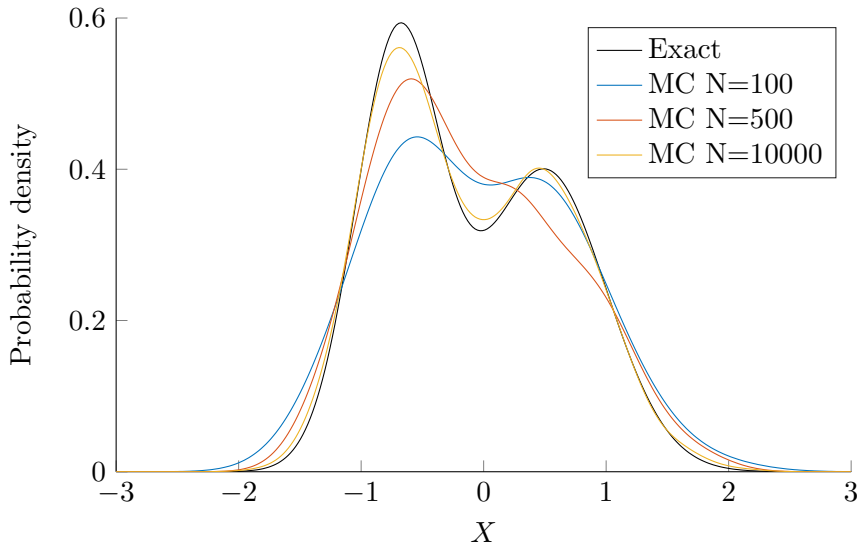

Figure 2-6: Example of the distribution estimation of a random variable X using MC.

converges towards the exact distribution for an increasing number of samples, but a large number of samples is required to obtain an accurate estimate. If computationally extensive simulations are required to obtain these samples, a full MC simulation will thus require a large computational effort to obtain an accurate probability distribution of a variable of interest.

As an example, the numerical error is plotted versus computation time in Figure 2-7. This figure is obtained using MC integration, but it is used to illustrate convergence rate of general MC methods. The figure shows that the error of the MC method is random and decreases with computation time, which corresponds to the number of samples. The figure shows that Quasi-MC indeed results in a faster convergence than standard MC methods. Even though the MC method is able to produce accurate results, a method that could obtain accurate results within less computation time would be preferred. Therefore, a method that has the highest accuracy over computation time ratio is preferred. Several methods have been found that have the potential for such performance characteristics, which will be discussed in the next sections.

2-3-3 Direct PDF Propagation

The Direct Probability Density Function Propagation (DPP) method is introduced by Halder and Bhattacharya (2011) for atmospheric entry problems. If uncertainty exist in the initial state of an entry vehicle, the initial state cannot be modeled as a single value, but the whole probability distribution must be considered. Therefore, this method models the initial state as a PDF of the state at the initial time. Instead of propagating a single initial state in time, the whole PDF of the state is propagated in time. A graphical illustration of this process is shown in Figure 2-9, which shows that the distribution of x evolves in time.

Similar to propagating a single initial state, the state derivative governs the evolution of the state and the uncertainty (PDF) in time. The PDF propagation process is performed in an exact way if numerical error is not considered, because it is derived from probability theory.

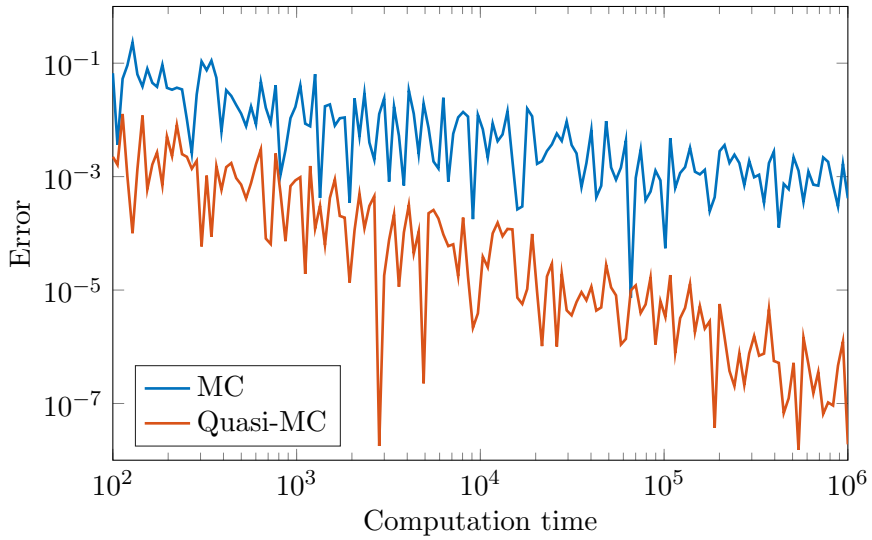

Figure 2-7: Example of computation time vs error plots. The MC results are obtained for a MC integration example.

The method results in several datapoints of the PDF, which are solved by propagating the state in time and simultaniously solving the probability density that corresponds to the value of that state. The result is graphically shown in Figure 2-8, which is generated with the assumption that no numerical error is present. The figure shows that with 100 datapoints a more accurate representation of the PDF can be obtained than with 100 MC samples. Therefore, the method is able to obtain more accurate solutions with less simulations. More details on the method are provided in Section 3-4.

In the research of Halder and Bhattacharya (2011), the method is applied to several problems related to atmospheric entry. The method was succesfully applied to obtaining the uncertainty in landing footprints, to obtain heating rate uncertainty and to parachute-deployment uncertainty. It was concluded that the method has a higher accuracy than the MC method for the same number of samples (or computation time).

2-3-4 The Least Squares Kernel Density Method

The LSQKD method is a method that is used to propagate a PDF in time, similar to the Direct PDF propagation method. Instead of propagating the PDF in an exact way, the method models the PDF $\varphi(x)$ of X as a weighted summation of kernels K_m:

$$\varphi(x) = \sum_{m=1}^{N_K} w_m K_m(x, \beta_m) \tag{2-1}$$

where w_m are the weight factors, N_K is the number of kernels and β_m is a shape parameter of the kernel K_m. These kernels are functions that have a total integral of one and are possitive for every value of x. An example of a PDF that is modeled using three Gaussian kernels (Gaussian PDFs) is shown in Figure 2-10. The figure shows the three kernels multiplied with their weight factor and the PDF that is obtained by taking the sum.

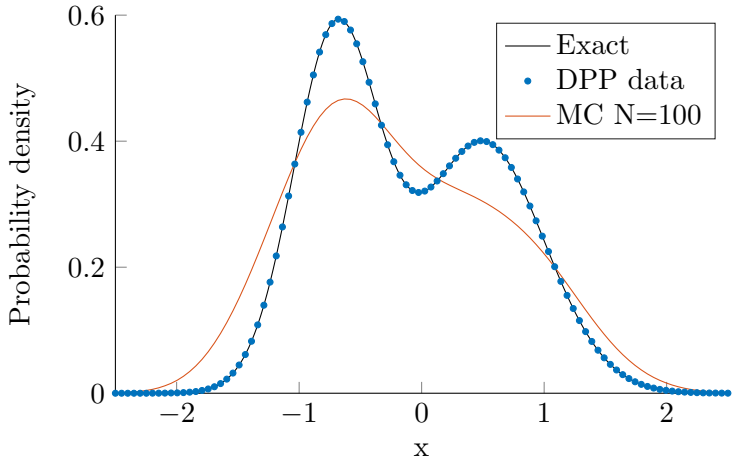

Figure 2-8: Illustration of data obtained from the DPP method.

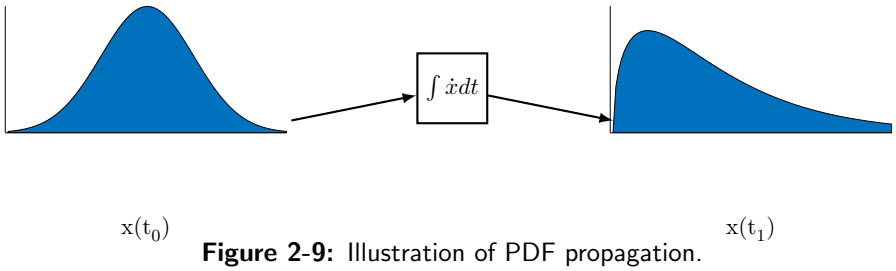

Figure 2-9: Illustration of PDF propagation.

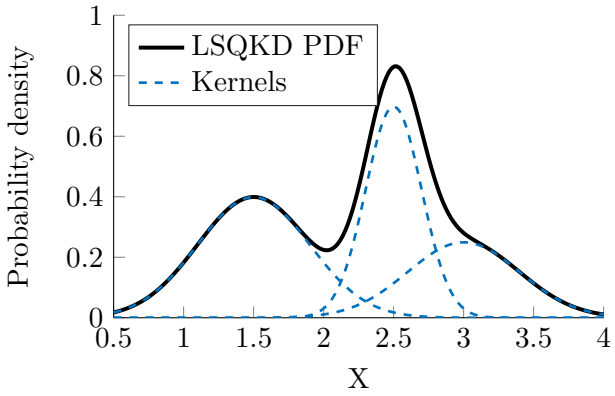

Figure 2-10: Example of a one-dimensional PDF modeled using three Gaussian kernels with $\mu = [1.5, 2.5, 3]$, $\sigma = [0.4, 0.2, 0.4]$ and $w = [0.4, 0.35, 0.25]$.

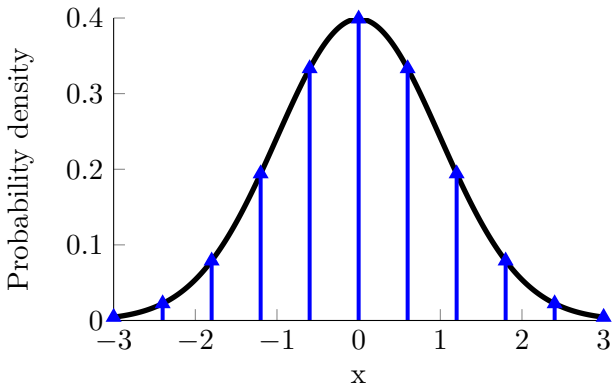

Figure 2-11: Illustration of representing a Gaussian PDF by Dirac delta functions.

A system of Ordinary Differential Equation (ODE)s is solved that governs the evolution of the weights w_m and the parameters β_m of the kernels in time. Hereby, the method can propagate a PDF in time by solving a significantly smaller amount of ODEs than the direct PDF propagation method. Therefore, it was concluded that the LSQKD method has the potential to obtain reasonably accurate results with a significant reduction in computational efforts compared to Monte Carlo and the Direct PDF propagation method.

2-3-5 Direct Quadrature Method Of Moments

The Direct Quadrature Method of Moments (DQMOM) is a method developed by Marchisio and Fox (2004) for tracking the PDFs of the size of particles in a flow. The method is an improvement on the Quadrature Method of Moments (QMOM). The method uses a weighted summation of Dirac delta functions to model the PDF. A visualization of such an approximation is shown in Figure 2-11. The location and the weights of these Dirac delta functions are propagated in time to determine the evolution of the PDF in time. The benefit of using Dirac delta functions is that every integration of the function can be expressed as a summation. This method is similar to the LSQKD method and the difference with the LSQKD method is that DQMOM uses Dirac delta functions as kernels and employs a different solution procedure to propagate these Dirac delta functions.

In the research of Attar and Vedula (2008), the DQMOM is proposed to propagate a PDF in time for stochastic nonlinear dynamical systems. A computation time of 10 seconds was observed for a method similar to the DPP method, 4 seconds for the DQMOM and 1500 seconds for the Monte Carlo method. This shows that the method is highly efficient.

A disadvantage of the method is that the method suffers from the Hausdorff moment problem, which affects the accuracy of the solution (Pantano and Shotorban, 2007). This is the problem that for certain PDFs, the reconstruction of a PDF using the statistical moments (discussed in Section A-1) of the PDF does not have a unique solution. These problems occur with PDFs of which the probability density at the tails do not decrease fast enough, which is similar to the problem of a divergent integral[3].

[3]Private communication with Prof. Dr. F.H.J. Redig, TU Delft (2015)

Two known examples were found in which the method was applied to aerospace problems. In the research of Xu (2009), the method was used for a stochastic controller of an unmanned aerial vehicle and in the research of Xu (2011), the method was applied to a control system of space launch vehicles. For both studies, excellent results were obtained, which shows that the Hausdorff moment problem does not have to occur.

2-3-6 Covariance Propagation

Covariance propagation is a parametric method which can be used to propagate a Gaussian uncertainty in the state $\boldsymbol{x}$ subjected to linear dynamics. The mean $\overline{\boldsymbol{x}}$ is propagated using the linear system of differential equations. The Gaussian distribution is defined by the covariance matrix, which contains the variance of each state and the covariance between each variable. The covariance matrix $\boldsymbol{\Sigma}$ is propagated using the following equations (Gelb, 1974):

$$\dot{\overline{\boldsymbol{x}}} = \boldsymbol{A}\overline{\boldsymbol{x}} \tag{2-2a}$$

$$\dot{\boldsymbol{\Sigma}} = \boldsymbol{A}^T\boldsymbol{\Sigma} + \boldsymbol{\Sigma}\boldsymbol{A} \tag{2-2b}$$

This method is extended using Gaussian Mixture Models as proposed by Terejanu et al. (2008). A linear combination of Gaussian distributions is used to represent an arbitrary PDF. This method is similar to the LSQKD method and the DQMOM, because a weighted summation of functions is used to approximate the PDF, but the solution procedure is different.

The results obtained with this method showed that it is able to propagate uncertainty in non-linear dynamics to some extent. Several test cases were used to test the performance of the method. The integrated error between the approximate solution and the exact solution was used to determine the accuracy and values were observed in the order of 0.3 to 0.5. Considering that the integral of a PDF equals one, the integrated error is large, so it is expected that the accuracy for atmospheric entry problems is not sufficient.

2-3-7 Polynomial Chaos

A polynomial chaos-based uncertainty propagation method was applied to atmospheric entry by Prabhakar et al. (2010). The uncertainty in the initial state is modelled using a PDF, which is approximated by a weighted summation of orthogonal polynomials. The approximate model of the PDF is defined using several time-varying coefficients, which are solved using a deterministic set of ODEs.

The method is tested by propagating uncertainty in the state of an entry vehicle and the results are compared with Monte Carlo results. The results initially showed a good agreement, but degraded with time to an unacceptable level.

2-3-8 Interval Analysis

Interval Analysis is a method introduced by Moore (1962) that can be used to perform calculations with an interval of values instead of a single value. A calculation with an interval

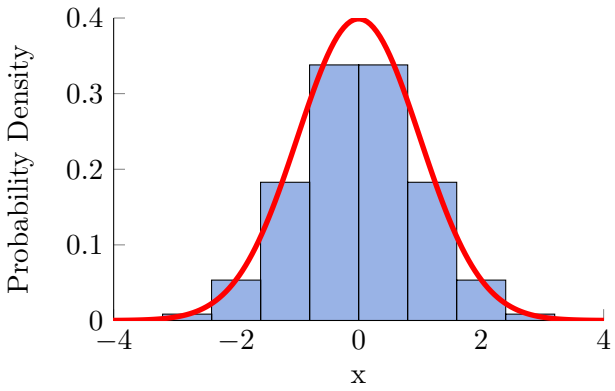

Figure 2-12: Example of representing a PDF using intervals.

than results in output interval in contrast to a single output value. After introducing Interval Analysis, Moore (1984) introduced a risk-analysis method based on Interval Analysis. This method propagates a PDF by subdividing it in intervals, which is shown in Figure 2-12. The bounds of these intervals are propagated in time and the resulting intervals can be used to reconstruct a PDF. This essentially means that the bars in Figure 2-12 that approximate the PDF are propagated in time.

A problem with Interval Analysis is that the growth of the intervals are overestimated, which means that the intervals are wider than they should be. Because overestimation can be large (Römgens et al., 2013), it is expected that this has a significant impact on the accuracy. In addition, using interval analysis would mean that it is assumed that the distribution within each interval stays uniform, which is generally not the case. Because Interval Analysis requires more computational effort than conventional computations and specialized software is required, it is expected that this method is not feasible for propagating a PDF in time.

2-3-9 Conclusion

Based on the review on these uncertainty propagation methods, the following conclusions were derived:

- The DPP can accurately propagate uncertainty with a higher accuracy than MC within less computational effort.
- The LSQKD method has the potential to obtain a sufficient accuracy with a considerable reduction in computational effort compared to the DPP method and the MC method. This is verified by a highly nonlinear three-dimensional problem in the research of Pantano and Shotorban (2007).
- The DQMOM also has the potential to obtain accurate results for statistical impact prediction, but it is not known to what degree the Hausdorff moment problem limits the performance of the method for statistical impact prediction.
- It is expected that the DPP method, LSQKD method and the DQMOM method will provide significantly more accurate results than covariance propagation, polynomial chaos-based uncertainty propagation and interval analysis-based PDF propagation.

It is chosen to investigate the LSQKD method further and compare this method to the DPP method and the MC method. This method is preferred over the DQMOM method, because it is not known if the Hausdorff moment problem will affect the accuracy of the DQMOM. Furthermore, it was indicated that the LSQKD method can be adjusted such that a solution is obtained that is similar to the DQMOM method.

2-4 Reference Vehicle and Trajectory

The Delta-K rocket body is used for the analysis, because it has been shown that sufficient test cases are available for validation and the trajectories could be reconstructed (Ronse, 2013). An inertia model and an aerodynamic database are constructed and available for the simulations for this research. The shape model that is used to generate the aerodynamic database and the inertial properties is shown in Figure 2-13.

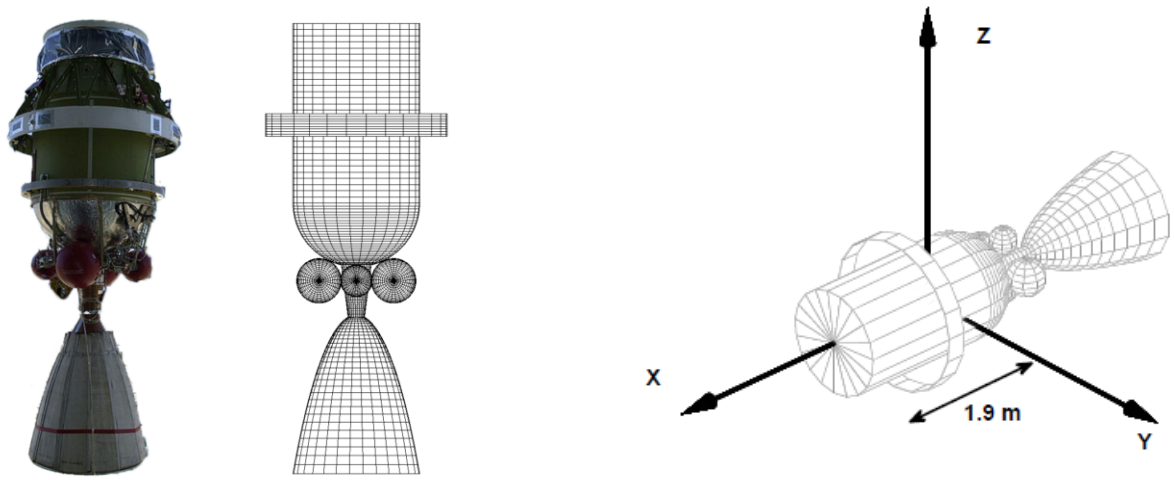

Figure 2-13: Delta-K rocket body compared to the model obtained by Ronse (2013).

The mass of the body is equal to:

$$m_{Delta-K} = 924 \text{ kg}$$

Data of the geometry and materials was obtained from documentation and used to model the shape of the Delta-K body. The center of mass was estimated at 1.9 m behind the vehicle's frontal surface as shown in Figure 2-13. The inertial properties of the Delta-K rocket body were obtained using the shape model, resulting in:

$$\boldsymbol{I_{Delta-K}} = \begin{bmatrix} 544.0 & 0.0 & 0.0 \\ 0.0 & 2139.2 & 0.0 \\ 0.0 & 0.0 & 2146.6 \end{bmatrix}$$

The aerodynamic model and the aerodynamic database of the body are described in Section 5-5.

The trajectories that will be simulated consist of two phases: the decay phase and the entry phase. The decay phase is the part in which the rocket body gradually loses energy and decreases its semi-major axis. When the lowest altitude in its orbit reaches about 100 km, the body will enter the atmospheric entry phase. The decay phase typically lasts hours to days and the entry phase lasts about 20 minutes until impact. An example of such a trajectory is shown in Figure 2-14. The figure shows that the altitude gradually decreases until an altitude of about 100 km, whereafter the impact occurs within minutes. The oscillations in the altitude are a result of the eccentricity of the orbit.

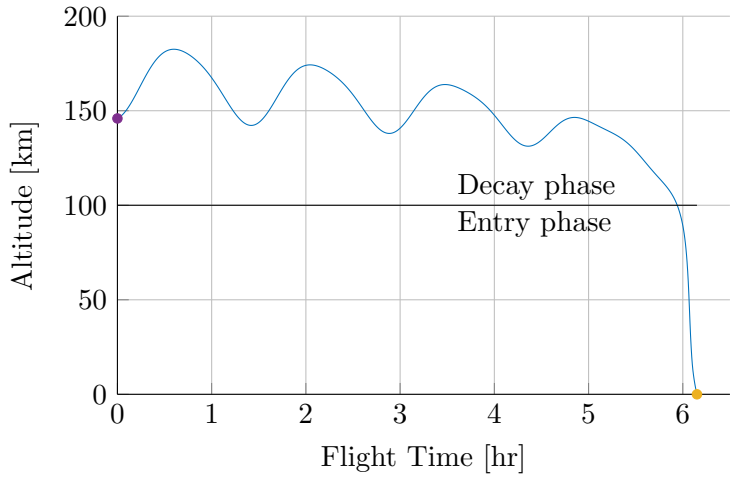

Figure 2-14: Example trajectory of a Delta-K rocket body generated using the trajectory simulator described in Chapter 8.

In the research of Ronse (2013), it was shown that the dispersion in impact location is large. The impact locations are all located around the ground track of the original orbit, so impact time distributions were derived to perform the impact predictions. A similar analysis will be performed in this research, so the same simulation cases are used. The 33 simulation cases that can be compared with TIP data are shown in Table 2-1. The time of decay is published on space-track.org[4] and corresponds to the true time of impact.

2-5 Conclusions

The literature study has shown that statistical impact predictions are mostly performed using the MC method. However, several methods exist that directly propagate a PDF of which some were already applied to problems related to atmospheric entry. These methods could potentially provide more accurate results with a similar computational effort as the MC method. Therefore, the following mission requirements are defined for this research:

MR-1 The DPP method shall be applied to statistical impact prediction.

MR-2 The applicability of the LSQKD method to statistical impact prediction shall be investigated.

[4] `https://www.space-track.org/`; date accessed: 15-08-2016

MR-3 The impact time predictions shall be compared with TIPs corresponding to the cases in Table 2-1 and the impact prediction model developed in Ronse (2013).

The following system requirements are defined for the simulators that will be developed in this research:

SR-1 The impact footprint shall be expressed as a PDF of the impact time.

SR-2 The dynamical model of the object shall include translational and rotational dynamics.

SR-3 The uncertainty model shall, at least, contain uncertainty in the translational state, the rotational state and the atmospheric density.

SR-4 The Delta-K rocket body shall be used as a test subject for the simulations.

Table 2-1: Simulation cases.

ID	Norad ID	TLE Line 1 (19-32)	Time of Decay	Time to impact [Hr]
1	27851	04206.91433301	25-7-2004 00:06	2.2
3	28130	04258.88060554	15-9-2004 03:26	6.3
4	28191	04266.14715545	22-9-2004 06:01	2.5
5-1	28486	04356.47442410	22-12-2004 13:39	26
5-2		04357.20711024		8.7
7	28519	05171.14438062	20-6-2005 06:21	2.9
8	28655	05185.81556696	5-7-2005 08:29	13
10-1	29109	06186.46619959	6-7-2006 13:48	27
10-2		06186.95598165		15
10-3		06187.32199935		6.1
11	29488	06357.05947935	23-12-2006 12:14	11
12	29603	07125.38021505	6-5-2007 12:56	28
13	30585	07197.05842497	16-7-2007 15:38	14
14	31599	07227.42677306	16-8-2007 09:23	23
15-1	32061	07300.30198803	28-10-2007 07:29	24
15-2		07300.80911948		12
15-3		07301.21803581		2.3
17-1	32377	08044.38345118	13-2-2008 21:47	13
17-2		08044.80990222		2.3
18	32386	08098.67563328	8-4-2008 12:24	20
19-1	32262	08120.55257127	30-4-2008 12:14	23
19-2		08121.40727165		2.5
21-1	32713	08250.72565516	7-9-2008 20:52	27
21-2		08251.39836102		11
22	33332	08294.79752669	21-10-2008 20:21	25
23-1	33592	09110.72505575	21-4-2009 20:00	27
23-2		09111.70274798		3.1
24-1	35947	10068.05287140	10-3-2010 21:33	44
24-2		10068.85110937		25
26-1	37217	10349.63301335	16-12-2010 16:47	26
26-2		10350.18421186		12
26-3		10350.61056312		2.1
27	37674	11211.19195177	30-7-2011 11:31	6.9

Chapter 3

Uncertainty Analysis

In statistical impact prediction, one is interested in the probability distribution of the impact time and location of the body given the uncertainty in the initial state and other parameters. In uncertainty analysis methods, knowledge about uncertainty in input variables is used to obtain statistical information of output variables. This chapter describes several methods that use an uncertainty model to obtain information about the uncertainty in output variables. An overview of the content of this chapter is provided below. Before reading this chapter it is advised to read Appendix A, which provides background on probability theory that is used in this chapter.

- Monte Carlo Methods (Section 3-1) - The Monte Carlo method is discussed in general in this section and several random sampling techniques are discussed that are used in the Monte Carlo method.

- Density Estimation (Section 3-2) - This section discusses a technique that is used to construct a PDF from the results of Monte Carlo simulations. This technique is used to construct impact time distributions samples of the impact time obtained from Monte Carlo simulations.

- Static Probability Density Transformations (Section 3-3) - This section discusses static transformations of PDFs that are used to derive the PDFs for the uncertainty model in Chapter 6.

- Probability Density Propagation (Section 3-4) - This section discusses the DPP method, which is used to propagate uncertainty in the state of the Delta-K rocket body.

- The Least Squares Kernel Density Method (Section 3-5) - This section discusses the LSQKD method, which is an approximate method to propagate uncertainty in the state variables. This method is further investigated and tested in Chapter 4.

3-1 Monte Carlo Methods

Monte Carlo (MC) methods are methods that use random sampling to perform computations. These methods use the principle that if a large number of samples are drawn from a distribution, the sample distribution will approximate the distribution that is used to generate the samples. These methods can be used for a large number of applications, such as integration, optimization and uncertainty propagation.

Because the samples are randomly generated, the statistical properties that can be derived from these samples are also random. This means that two sets of samples will, most probably, not have the exact same statistical properties (Montgomery and Runger, 2014). One of the most useful theorems in statistics, is the central limit theorem, which describes the distribution of the sample mean of a large number of random samples. This theorem states that as the number of samples N goes to infinity, the mean of the samples X_i will have a normal distribution with the following properties (Dekking et al., 2005):

$$\bar{X} = \frac{X_1 + X_2 + \cdots + X_N}{N} \tag{3-1a}$$

$$\mu_{\bar{X}} = \mu \tag{3-1b}$$

$$\sigma^2_{\bar{X}} = \frac{\sigma^2}{N} \tag{3-1c}$$

This shows that the mean that can be obtained from the samples approaches the exact mean of the underlying distribution. Therefore, the mean of an output variable can be calculated using a large number of samples of an input variable. In addition, the estimate of the standard deviation of the sample mean can be used to estimate the error in the estimation of the mean.

In this research, the MC method is used for statistical impact prediction. The idea is that the initial state is sampled using the known distribution of the initial state and each sample is propagated in time. The distribution of the samples approximates the distribution of the state as the number of simulations increases. Statistical information can be obtained from the samples and its distribution can be reconstructed using methods like kernel density estimation (Section 3-2).

Since the MC method largely relies on the generation of random samples, it is important that these samples are correctly generated. These sampling methods are discussed in the following section.

3-1-1 Sampling Methods

A large number of methods and techniques exist to obtain random samples from a given distribution. These methods can only generate one-dimensional random variables, so additional techniques are required to include correlation in the samples. The following sections discusses these methods.

Uniformly Distributed Random Samples

Uni-variate random samples can be generated using several different algorithms that are referred to as a Random Number Generator (RNG). The RNGs first generates uniformly distributed random variables and converts these variables such that they have the correct distribution. In general, the RNGs that are in use are not truly random, because it is difficult to model an algorithm that produces truly random results. Therefore, RNGs generate pseudo random numbers, which are not truly random. This affects the accuracy of the methods that use these random samples, but currently available RNGs produce random numbers that are close to random samples.

In contrast to pseudo-random number generators, other sampling techniques can be used to increase the convergence speed of a MC simulation. Quasi-Monte Carlo methods are methods that use a deterministic set of samples, which distribution closely match with a uniform distribution. These methods aim for a deterministic error bound that is smaller than the probabilistic error bound obtained using standard MC. Three methods have been proposed by Faure, Halton and Sobol that generate uniformly spaced multi-dimensional samples (Ridolfi, 2013). In Figure 3-1, three examples are shown of random numbers that are generated using pseudo-random sampling, Sobol sampling and Halton sampling. The figure shows that pseudo-random sampling results in clustering of the samples and a spacing that is non-uniform. The Sobol and Halton samples are better spaced, but patterns emerge making the samples less random. For high-dimensional samples, these methods produce stronger patterns that might cause accuracy issues. These quasi-MC methods can have an error near $O(1/N)$ in contrast to a standard MC with an error of $O(1/\sqrt{N})$ (Glasserman, 2004).

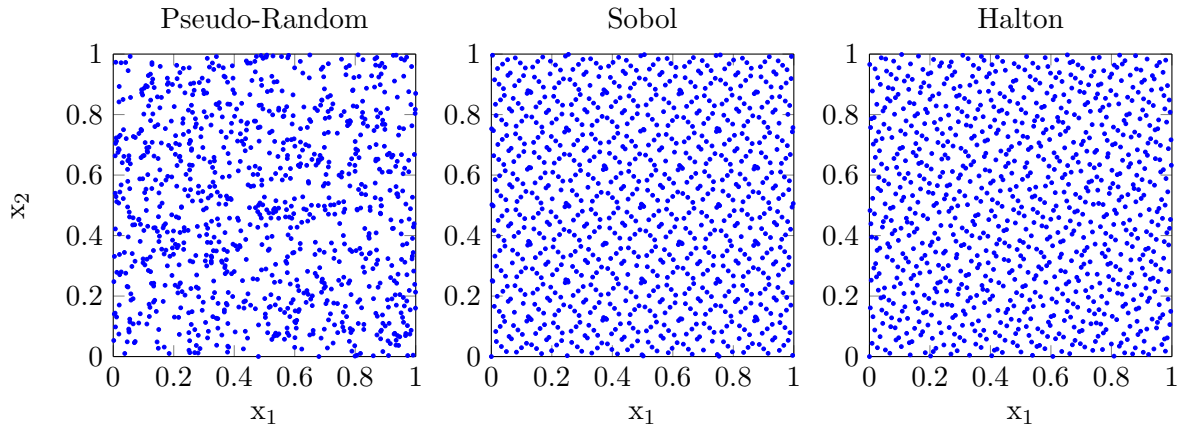

Figure 3-1: Two-dimensional random samples generated using a pseudo-random number generator, a Sobol sample generator and Halton sample generator.

3-1-2 Arbitrarily Distribution Random Samples

Uniformly distributed random samples can be used to generate random samples with an arbitrary distribution. One of the methods that can be used is called *the inverse transform method*, which is based on the following property (Thomopoulos, 2013):

$$U = F_X(X) \tag{3-2}$$

where U is a uniformly distributed variable on $[0, 1]$ and F_X is the Cumulative Distribution Function (CDF) of the random variable X. This property states that the output of inserting a random variable in its own CDF is uniformly distributed. From this property it can be derived that:

$$X = F_X^{-1}(U) \tag{3-3}$$

which states that random variables with a certain distribution can be generated by transforming uniformly distributed random variables using the inverse of the CDF of the desired distribution.

Correlation

Generating multi-variate random variables with correlation between the variables could be performed using several different methods. The goal of these sampling methods is to generate multi-variate random samples that correspond to the joint distribution of the multi-variate random variables. The samples could be generated by subsequently sampling one of the random variables using conditional and marginal distributions of the joint distribution. However, a more efficient method could be used to generate multi-variate samples with a Gaussian distribution or uniform distribution (Thomopoulos, 2013):

1. Generate a vector $\boldsymbol{Z}$ with samples from a standard normal or uniform distribution.
2. Use the Cholesky decomposition[1] to obtain the Cholesky factor $\boldsymbol{C}$ of the covariance matrix $\boldsymbol{\Sigma}$ of $\boldsymbol{X}$.
$$\boldsymbol{\Sigma} = \boldsymbol{C}\boldsymbol{C}^T \tag{3-4}$$
3. Calculate a vector $\boldsymbol{X}$ with correlated normally distributed samples using the Cholesky factor $\boldsymbol{C}$ and the mean vector $\boldsymbol{\mu}$:
$$\boldsymbol{X} = \boldsymbol{C}\boldsymbol{Z} + \boldsymbol{\mu} \tag{3-5}$$

3-2 Density Estimation

Monte Carlo simulations result in a large number of samples from which statistical properties need to be calculated and distributions need to be reconstructed. The process of reconstructing a distribution from a given number of samples is called density estimation. The technique discussed in this section is used to generate the impact time distributions discussed in Chapter 9.

Parametric and non-parametric methods exist to reconstruct these distributions. A parametric method could be used that assumes that the distribution is Gaussian and the mean μ and standard deviation σ are determined such that the distribution is completely defined. Such methods require that information about the distribution shape is known, which is not always

[1] Cholesky decomposition is a technique that transforms a matrix into a product of a triangular matrix and its transpose. The technique is based on a theorem that states that if a matrix $\boldsymbol{A}$ is positive definite, the matrix can be decomposed using a triangular matrix called the Cholesky factor $\boldsymbol{C}$ in a unique way that results in $\boldsymbol{A} = \boldsymbol{C}\boldsymbol{C}^T$ (Watkins, 2002).

the case. The benefit of non-parametric methods is that they can be used without assumptions about the distribution of the data. A *histogram* is widely used non-parametric method, which results in a PDF similar to a barplot. The range of the data is divided into bins and the number of samples in each bin is counted to obtain information about the distribution of the samples.

A widely used non-parametric method is Kernel Density Estimation, which results in a more smooth PDF than the histogram method. Essentially, the method estimates the probability density by placing a Kernel Density Function (KDF) $K(x)$ at each datapoint X_i. The PDF obtained using Kernel Density Estimate (KDE) is described using the following equation:

$$\hat{f}(x) = \frac{1}{Nh} \sum_{i=1}^{N} K\left(\frac{x - X_i}{h}\right) \tag{3-6}$$

where h is called the smoothing parameter or window width. An example of a KDE is shown in Figure 3-2. The figure shows several samples marked on the x-axis and Gaussian KDFs that are placed at each datapoint. A summation of these KDFs result in the smooth PDF that is shown in the figure.

Several different KDFs are provided in Table 3-1. These KDFs are functions that have the following property:

$$\int_{-\infty}^{\infty} K(x)dx = 1 \tag{3-7}$$

These kernels can be multi-dimensional such that a multi-dimensional KDE is obtained. It can be derived that using the Epanechnikov KDF provides the most accurate results for a one-dimensional KDE, so this kernel has an efficiency of 1. This can be derived by minimizing the error of the KDE with the exact PDF if it is assumed that the exact PDF is a Gaussian PDF (Silverman, 1998).

Table 3-1: Kernel density functions (Silverman, 1998)

KDF	**K(x)**	**Range (otherwise 0)**	**Efficiency**
Epanechnikov	$\frac{3}{4\sqrt{5}}\left(1 - \frac{x^2}{5}\right)$	$\lvert x\rvert \leq \sqrt{5}$	1
Biweight	$\frac{15}{16}(1 - x^2)^2$	$\lvert x\rvert \leq 1$	≈ 0.9939
Triangular	$1 - \lvert x\rvert$	$\lvert x\rvert < 1$	≈ 0.9859
Gaussian	$\frac{\exp(-x^2/2)}{\sqrt{2\pi}}$		≈ 0.9512
Rectangular	$1/2$	$\lvert x\rvert < 1$	≈ 0.9295

The window width h has an influence on the smoothness of the resulting PDF. A value that is too small results in a PDF with a large number of spikes and a value that is too large results in a PDF where the features are smoothed out. An optimal window width can be derived if the distribution that is estimated is known. If one assumes that the distribution is Gaussian, the following optimal bandwidth can be derived for a multi-dimensional PDF with dimension d (Bowman and Azzalini, 1997):

$$h_i = \left(\frac{4}{(d+2)N}\right)^{1/(d+4)} \sigma_i \tag{3-8}$$

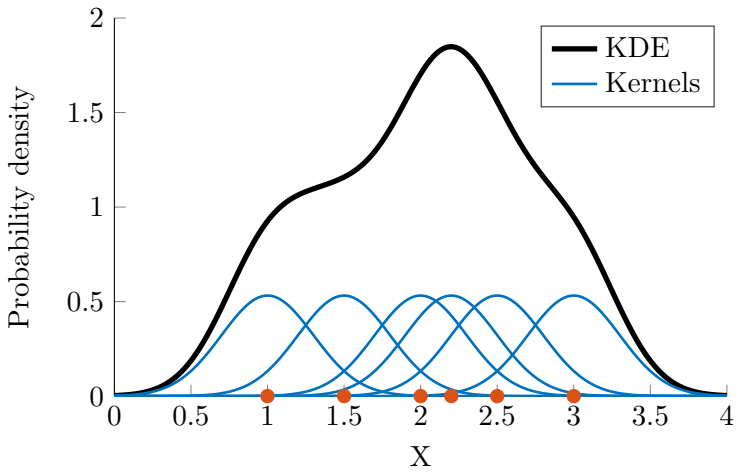

Figure 3-2: An example of a kernel density estimate with Gaussian kernels ($h = 0.3$) not drawn to scale.

where σ_i is the standard deviation of the data samples for dimension i. The optimal bandwidth h_i is calculated for each dimension and used in a multi-dimensional kernel to obtain a joint PDF that represents the distribution of the data.

3-3 Static Probability Density Transformations

Static transformations that are performed with random variables changes the distribution of the random variable. This section describes how the PDF of an output variable can be determined given the PDFs of the input variables of static transformations. These static transformations are time-invarient transformations that do not involve differential equations. These PDF transformations are for defining the uncertainty model in Chapter 6. Dynamic transformations, which are time varying, of random variables are discussed in Section 3-4.

3-3-1 The Perron-Frobenius Operator

Transformations of PDFs are performed by Markov operators. These operators are linear operators that transform a PDF. A special case of a Markov operator is the Perron-Frobenius (PF) operator. The PF operator can be used to determine the PDF $f_Y(y)$ of a random variable Y using the PDF $f_X(x)$ of X that is defined using the transformation $Y = S(X)$. The PF operator is defined as (Lasoata and Mackey, 1994):

$$\int_A f_Y(y)\mu dy = \int_{S^{-1}(A)} f_X(x)\mu dx \tag{3-9}$$

Consider A as an array containing all possible values of Y, $S^{-1}((A)$ will contain all possible values of X. Therefore, the integral can be interpreted as an equation that states the conservation of probability. An explicit solution for $f_Y(y)$ can be obtained if S is differentiable and invertible, resulting in:

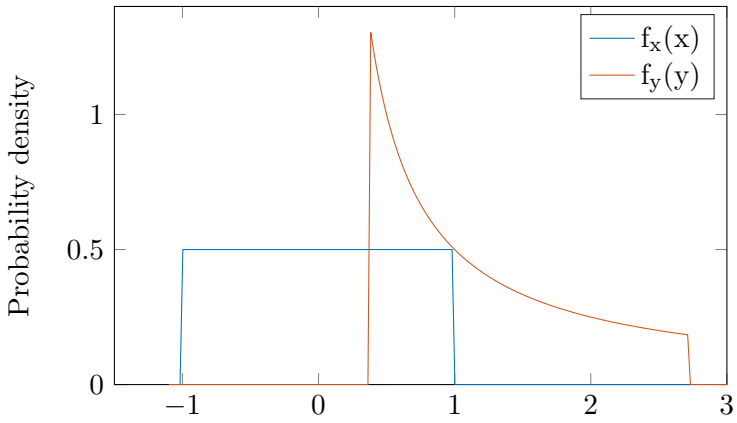

Figure 3-3: Example of a transformation of a uniform PDF that is subjected to $y = S(x) = e^x$.

$$f_Y(y) = f_X\left(S^{-1}(y)\right)\left|\frac{d}{dy}\left(S^{-1}(y)\right)\right| \tag{3-10}$$

As an example, the PDF $f_Y(y)$ of the random variable Y is derived with the transformation $S(X)$ and the PDF of X are defined as:

$$y = S(x) = e^x \tag{3-11a}$$

$$f_X(x) = \begin{cases} \frac{1}{2} & -1 < x < 1 \\ 0 & \text{otherwise} \end{cases} \tag{3-11b}$$

The inverse of the transformation $S(X)$ and its derivative are defined as:

$$S^{-1}(x) = \ln x \tag{3-12a}$$

$$\frac{d}{dx}\left(S^{-1}(x)\right) = \frac{1}{x} \tag{3-12b}$$

Inserting these results in Equation (3-10), results in the PDF $f_Y(y)$ of the random variable Y:

$$f_Y(y) = \begin{cases} \frac{1}{2} \cdot \left|\frac{1}{y}\right| & -1 < \ln y < 1 \\ 0 & \text{otherwise} \end{cases} \tag{3-13a}$$

$$f_Y(y) = \begin{cases} \frac{1}{2y} & e^{-1} < y < e \\ 0 & \text{otherwise} \end{cases} \tag{3-13b}$$

The PDF of X and Y are plotted in Figure 3-3. The figure shows that the distribution of Y varies between $[e^{-1}, e^1]$. This example shows how the distribution of Y can be derived from the distribution of X.

3-3-2 Combining random variables

When it is desired to determine the distribution of a random variable that is a function of two other random variables. For example, one may be interested in the distribution of Z when it is known that $Z = XY$.

The distribution of a random variable that is the multiplication of two random variables can be derived using (Rohatgi and Saleh, 2001):

$$Z = XY \tag{3-14a}$$

$$f_Z(z) = \int_{-\infty}^{\infty} f\left(x, \frac{z}{x}\right) \frac{1}{|x|} dx \tag{3-14b}$$

This integral can be simplified if the random variables X and Y are independent, yielding:

$$f_Z(z) = \int_{-\infty}^{\infty} f_X(x) f_Y\left(\frac{z}{x}\right) \frac{1}{|x|} dx \tag{3-15}$$

These equations are the result of rewriting the joint PDF, which is a function of X and Y, to a joint PDF that is a function of X and Z using the known relation. The marginal PDF of Z is then the distribution of Z, which is obtained using integration.

3-4 Probability Density Propagation

In contrast to static transformations, variables can also be transformed dynamically. These problems are generally stated as an initial value problem with a dynamical model $\boldsymbol{F}(\boldsymbol{X}(t), t)$ of the state $\boldsymbol{X}(t)$:

$$\dot{\boldsymbol{X}} = \boldsymbol{F}(\boldsymbol{X}(t), \boldsymbol{p}, t) \quad \text{with} \quad \boldsymbol{X}(0) = \boldsymbol{X_0} \tag{3-16}$$

where $\boldsymbol{p}$ represents a vector of parameters. The equations of motion, which are described in Section 5-4, are dynamic equations of this form. These equations have a unique solution for each initial state $\boldsymbol{X}_0$, which results in a unique trajectory of the Delta-K body.

If the initial state is uncertain, the trajectory of the body will also be uncertain. To obtain information about the uncertainty in the state, the uncertainty in the initial state needs to be propagated in time. This can be performed by modeling the uncertainty in the initial state as a PDF of the initial state. The PDF of the state can be propagated in time, which will be referred to as probability density propagation.

The propagation of a PDF is mathematically related to one of the fundamental principles that is used in engineering. The conservation of mass, which states that *mass cannot be created nor destroyed* (if we do not consider conversion into energy). If one considers a closed volume V, the principle can be translated into an equation for a one-dimensional flow (Anderson, 2001):

$$\frac{\partial \rho(x,t)}{\partial t} + \frac{\partial \rho(x,t)}{\partial x} \frac{dx}{dt} = 0 \tag{3-17}$$

The first part of the equation is the local change in density ρ, which is described by the partial derivative of the density to time. The second part of the equation is the outflow of density.

This equation thus states that the local increase in density is equal to the inflow of density. In other words, the density(mass) has to come from somewhere and cannot be arbitrarily created.

Similar to the conservation of mass, the principle of conservation of probability can be defined. The total probability of all events is always equal to 1 and if all possible outcomes are considered, the total probability of all the outcomes must also be 1. Therefore, the total probability must be and remain 1, so the total probability (mass) must be conserved. This principle can be used to formulate an equation similar to the conservation of mass (Halder and Bhattacharya, 2011):

$$\frac{\partial \varphi(\boldsymbol{X}(t),t)}{\partial t} + \sum_{i=1}^{N} \frac{\partial}{\partial X_i} \left[\varphi(\boldsymbol{X}(t),t) F_i(\boldsymbol{X}(t),t)\right] = 0 \tag{3-18a}$$

$$\dot{\boldsymbol{X}} = \boldsymbol{F}(\boldsymbol{X}(t),t) \tag{3-18b}$$

where the function φ is the PDF and N is the number of state variables. This quasi-linear Partial Differential Equation (PDE) is called the *Liouville equation* and can be used to propagate the PDF of $\boldsymbol{X}$ in time. The equation states that the PDF is a function of time and its transformation is governed by the dynamical model $\boldsymbol{F}(\boldsymbol{X},t)$. Similar to the equation for the conservation of mass (Equation (3-17)), this equation states that the local increase (first term) in probability density is equal to the inflow (second term) of probability density. Thus, *probability cannot be created nor destroyed* and will remain equal to 1. This means that probability flows with a similar mathematical behavior as mass.

The Liouville equation is actually a special case of the more general *Fokker-Planck equation*. The difference between the Fokker-Planck equation and the Liouville equation is a diffusion term that can be seen as the addition of noise $\boldsymbol{\xi}$ (Gardiner, 2004):

$$\frac{\partial \varphi(\boldsymbol{X}(t),t)}{\partial t} = \frac{1}{2} \sum_{i,j=1}^{N} \frac{\partial^2}{\partial x_i \partial x_j} \left[a_{ij} \varphi(\boldsymbol{X}(t),t)\right] - \sum_{i=1}^{N} \frac{\partial}{\partial X_i} \left[\varphi(\boldsymbol{X}(t),t) F_i(\boldsymbol{X}(t))\right] \tag{3-19a}$$

$$\dot{\boldsymbol{X}} = \boldsymbol{F}(\boldsymbol{X}(t)) + \boldsymbol{\sigma}(\boldsymbol{X}(t))\boldsymbol{\xi} \tag{3-19b}$$

The uncertainty in the state of the Delta-K rocket body is propagated by propagating the PDF of the state in time using the Liouville equation, because there is no additional noise term added to the model. In addition, any addition of noise can also be included in the Liouville equation using a method discussed in the next section.

3-4-1 Solving the Liouville Equation

The Liouville equation can be solved directly using PDE solving methods, for example finite difference or finite elements techniques. However, a more direct solution of the Liouville equation can be obtained using the method of characteristics. This method uses characteristic curves to convert a PDE to a series of ODEs, which can be solved using standard numerical integrators.

The method of characteristics can be used to rewrite a semi-linear PDE to a system of ODEs. Equation (3-20) is an example of such a PDE in two dimensions. However, the method can be generalized to any dimension.

$$a(x_1, x_2)\frac{\partial u}{\partial x_1} + b(x_1, x_2)\frac{\partial u}{\partial x_2} = f(x_1, x_2, u) \tag{3-20}$$

It can be shown that this PDE contains characteristic curves on which the following relations hold (Haberman, 2003):

$$\frac{dx_1}{a(x_1, x_2)} = \frac{dx_2}{b(x_1, x_2)} = \frac{du}{f(x_1, x_2, u)} \tag{3-21}$$

This system of equations can be used to transform the PDE to a system of ODEs and solve the PDE. The Liouville equation is solved by first expanding it using the product rule of differentiation:

$$\frac{\partial \varphi(\boldsymbol{X}(t), t)}{\partial t} + \sum_{i=1}^{N}\left(F_i(\boldsymbol{X}(t), t)\frac{\partial \varphi(\boldsymbol{X}(t), t)}{\partial X_i}\right) = -\varphi(\boldsymbol{X}(t), t)\sum_{i=1}^{N}\frac{\partial F_i(\boldsymbol{X}(t), t)}{\partial X_i} \tag{3-22}$$

Similar to Equation (3-21), the characteristic curves are defined by:

$$\frac{dt}{1} = \frac{dX_1}{F_1} = \frac{dX_2}{F_2} = \frac{dX_3}{F_3} = \cdots = \frac{dX_N}{F_N} = \frac{d\varphi(\boldsymbol{X}(t), t)}{-\varphi(\boldsymbol{X}(t), t)\Psi(\boldsymbol{X}(t))} \tag{3-23a}$$

$$\Psi(\boldsymbol{X}(t)) = \sum_{i=1}^{N}\frac{\partial F_i}{\partial X_i} \tag{3-23b}$$

where $\Psi(\boldsymbol{X}(t))$ is a parameter introduced to simplify the notation. These equations represent the relations that hold on the characteristic curves. From the first equality it can be obtained that:

$$F_1 = \frac{dX_1}{dt} \tag{3-24}$$

which corresponds to the definition of F_1 that is the state derivative model of X_1. This result was not obtained using the definition of F_1, but using the Liouville equation. Therefore, this result shows that the characteristic curves are the trajectories itself.

An ODE of the PDF can be obtained using Equation (3-23a):

$$\frac{d\varphi(\boldsymbol{X}(t), t)}{dt} = -\varphi(\boldsymbol{X}(t), t)\Psi(\boldsymbol{X}(t)) \tag{3-25}$$

This ODE can be solved by integration:

$$\int \frac{d\varphi(\boldsymbol{X}(t), t)}{\varphi(\boldsymbol{X}(t), t)} = -\int \Psi(\boldsymbol{X}(t))dt \tag{3-26}$$

This results in the following equation of the PDF of the state:

$$\varphi(\boldsymbol{X}(t),t) = \varphi(\boldsymbol{X_0}) \exp\left(-\int_0^t \Psi(\boldsymbol{X}(\tau))d\tau\right) \tag{3-27}$$

This result is also derived in the research of (Halder and Bhattacharya, 2011). This equation allows to determine the PDF of the current state $\varphi(\boldsymbol{X}(t),t)$ using the PDF of the initial state $\varphi(\boldsymbol{X_0})$ and the dynamical model of the state $\boldsymbol{F(X)}$. The fact that the characteristic curves are the trajectories of the body implies that this equation can be solved for a trajectory and $\Psi(\boldsymbol{X}(t))$ can be calculated using the state history. The PDF of the state variables can thus be obtained by simulating multiple trajectories with a different initial state $\boldsymbol{X_0}$.

A method to determine the integral of $\Psi(\boldsymbol{X}(t))$ is to use numerical quadrature with the state history $\boldsymbol{X}(t)$. However, the numerical integrator that solves the trajectory of $\boldsymbol{X}(t)$ integrates the trajectory without considering $\Psi(\boldsymbol{X}(t))$, so timesteps that are used may be too large to get an accurate solution. In a preliminary analysis it was found that this results in inaccurate solutions.

The numerical integrator that solves the trajectory of $\boldsymbol{X}(t)$ integrates the state derivative over time. Considering that $\Psi(\boldsymbol{X}(t))$ (Equation (3-27)) is defined using an integral over time, the integral can also be computed using an ODE solver if it is defined as a differential equation. Therefore, the integral of $\Psi(\boldsymbol{X}(t))$ is defined by adding the PDF correction factor Ω to the state variables, defined as:

$$\Omega(t) = \int_0^t \Psi(\boldsymbol{X}(t))dt \tag{3-28}$$

The definition of Ω is substituted in Equation (3-27), which results in the following set of ODEs that can be used to solve the evolution of the PDF $\varphi(\boldsymbol{X}(t),t)$ in time:

$$\varphi(\boldsymbol{X}(t),t) = \varphi(\boldsymbol{X_0}) \exp\left(-\Omega(t)\right) \tag{3-29a}$$

$$\begin{pmatrix} \dot{\boldsymbol{X}} \\ \dot{\Omega} \end{pmatrix} = \begin{pmatrix} \boldsymbol{F}(\boldsymbol{X}(t),t) \\ \Psi(\boldsymbol{X}(t)) \end{pmatrix} \tag{3-29b}$$

$$\Omega(0) = 0 \tag{3-29c}$$

Using the variable stepsize numerical integrator to solve Ω improves the accuracy, because the accuracy can be controlled by the integrator.

3-4-2 Numerical Solution Method

The previous subsection described the solution method to propagate the PDF of the state of the Delta-K rocket body. The final result, Equation (3-29), can be used to propagate the PDF of the state. The only known in this equation is the uncertainty in the initial state, so the definition of the PDF of the initial state $\varphi(\boldsymbol{X}_0)$. The PDF can be propagated in time using two different methods:

- The initial state $\boldsymbol{X}_0$ can be sampled and forward propagated in time to $\boldsymbol{X}(t)$ and $\Omega(t)$ can be solved simultaniously. This results in samples of $\boldsymbol{X}$ and the corresponding value

of the PDF $\varphi(\boldsymbol{X}(t), t)$. This is a shootinglike method that results in scattered datapoints of $\boldsymbol{X}(t)$ and the corresponding value of the PDF.

- The state $\boldsymbol{X}(t)$ can be sampled and backward propagated in time to $\boldsymbol{X}_0$ and simultaniously $\Omega(t)$ can be solved. This results in samples of the value of the PDF $\varphi(\boldsymbol{X}(t), t)$ at the chosen values of $\boldsymbol{X}(t)$. Backward time propagation is further discussed in Section 8-1.

If the state is forward propagated in time, the outcome may be such that the datapoints are concentrated near areas of higher probability density. This means that less information is obtained about the areas of lower probability density. This problem can be avoided if the state is propagated backward in time, because the location of the datapoints can be chosen. Depending on the application it is chosen to use backward or forward time propagation. Both methods are referred to as the Direct Probability Density Function Propagation (DPP) method.

3-4-3 Uncertainty in Model Parameters

The state derivative model of the state $\boldsymbol{F}(\boldsymbol{X}, \boldsymbol{p}, t)$ can contain model parameters $\boldsymbol{p}$, which are variables that are not states. For example, the atmospheric density is used in the equations of motion to calculate the drag. This atmospheric density is determined using a model that is not exact, so uncertainty in this parameter can be present. Similarly, uncertainty can be present in the mass or inertia parameters of the Delta-K rocket body, aerodynamic coefficients, etc.

Uncertainty in the model parameters can only be added if the parameters are converted to a state variable, because the method can only include uncertainty in the states. This means that the model of the parameters $\boldsymbol{p}$ need to be converted to an ODE:

$$\begin{pmatrix} \dot{\boldsymbol{X}} \\ \dot{\boldsymbol{p}} \end{pmatrix} = \begin{pmatrix} \boldsymbol{F}(\boldsymbol{X}(t), t) \\ \boldsymbol{F}_p \end{pmatrix} \tag{3-30a}$$

$$\boldsymbol{X}_{new} = \begin{pmatrix} \boldsymbol{X} \\ \boldsymbol{p} \end{pmatrix} \tag{3-30b}$$

Important to consider is that if the following property holds for a parameter p_1:

$$\frac{\partial F_{p_1}}{\partial p_1} = 0$$

the derivative of Ω does not include terms from the ODE of the parameter p_1. This means that the PDF of the parameter can be included, but the method of solving p_1 is not important. Therefore, p_1 can be solved using the original model without converting it to an ODE. This is advantageous for, for example, including uncertainty in the atmospheric density, because the atmospheric density is generally not computed using an ODE. This property thus shows that the atmospheric density does not have to be solved by converting it to an ODE.

3-4-4 Example

To illustrate the propagation of a PDF in an exact way, an example will be discussed where the following dynamical model is used:

$$\dot{x} = F_x = -ax \tag{3-31a}$$

This ODE has the following analytical solution:

$$x(x_0, t) = x_0 \exp(-at) \tag{3-32}$$

The evolution of the initial PDF $\varphi(x_0)$ to $\varphi(x, t)$ is given by:

$$\dot{\Omega} = \Psi(\boldsymbol{X}) = \frac{\partial F_x}{\partial x} = -a \tag{3-33a}$$

$$\varphi(x, t) = \varphi(x_0) \exp\left(-\int_0^t -a d\tau\right) = \varphi(x_0) e^{at} \tag{3-33b}$$

Solving for the initial condition $x_0(x, t)$ using Equation (3-32) and substituting it into Equation (3-33b), results in the PDF as a function of time:

$$\varphi(x, t) = \varphi(x e^{at}) e^{at} \tag{3-34}$$

Equation (3-34) is used to plot the probability density of the state at several time instances, which is shown in Figure 3-4. The figure shows that the initial distribution is a Gaussian distribution, which changes shape and moves in time. In the second plot one can see several trajectories originating from different initial conditions. These trajectories show that all states will converge towards $x = 0$ with increasing time. This is also observed in the plot of the PDFs, because the figure shows that each PDF later in time is more close to $x = 0$ with a decreasing width.

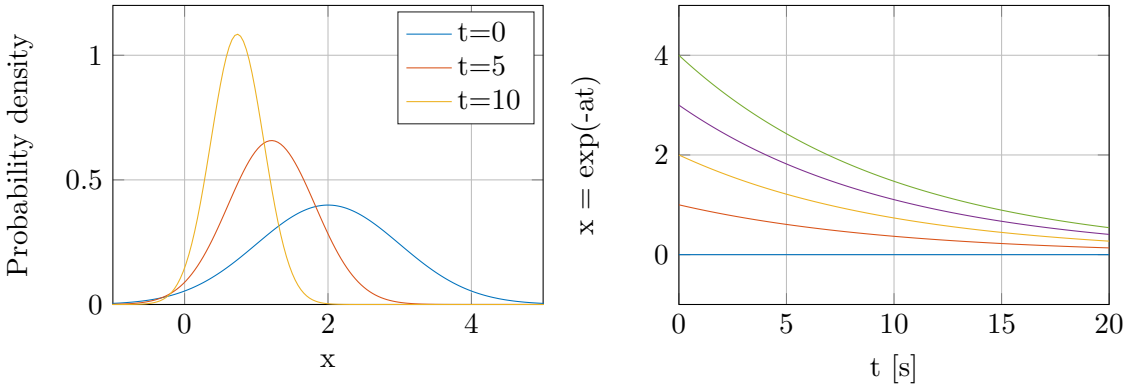

Figure 3-4: Example of the evolution of the PDF of x (Initially Gaussian $\mu = 2, \sigma = 1$) subject to $\dot{x} = -ax$ with $a = 0.1$.

The flowlike behavior of probability density is more clearly observed in Figure 3-5, which is a color plot of the probability density as a function of time and state. The plot shows that the probability density indeed flows towards $x = 0$ for increasing time.

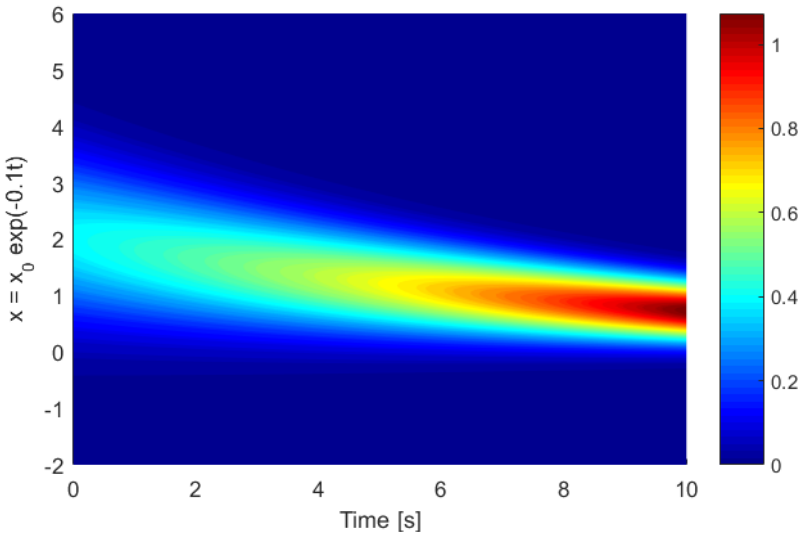

Figure 3-5: The probability density(colors) as a function of the state x and time.

An important observation to make in this example is that the state of x converges towards a constant value, which means that the solution is stable. In contrast the PDF also converges towards this value, however, the height of the PDF will continue to increase, because it becomes increasingly certain that the state is close to zero for increasing time. This means that, because x converges towards a constant value, the height of the PDF grows unbounded and will eventually approach a Dirac delta in $x = 0$. The value of Ω thus grows unbounded to a larger negative value.

If $a < 0$, the ODE would be unstable and the trajectories would diverge. This means that the states spread out and the probability density gets more spread out, so it flattens. For this case the value of Ω will grow towards a larger positive value, such that the value of the PDF will converge towards zero. The value of Ω thus evolves in a stable way, so no problems are expected specifically for the DPP method. However, the unstable trajectory of the state can cause problems for the numerical integrator, but these are not induced by the DPP method.

Time Distributions

The DPP method propagates a PDF of the state in time, by keeping the integral of the PDF constant for every timestep. The PDF is not a function of the time, so to obtain impact time distributions, the time needs to be included. It was found that the time can be included in the PDF without any conversion process. This means that the values of the PDF that are obtained from the DPP method do not represent the PDF of the state only, but also of the time. However, including the time in the PDF means that the PDF is not normalized anymore, so the integral is not equal to one and additional normalization is required.

To illustrate how a time distribution can be obtained, a test is performed using the example presented in Figure 3-5. The PDF, which is a function of the state is converted to a PDF of the state and time:

$$\varphi(\boldsymbol{X}(t), t) \rightarrow \varphi(\boldsymbol{X}, t)$$

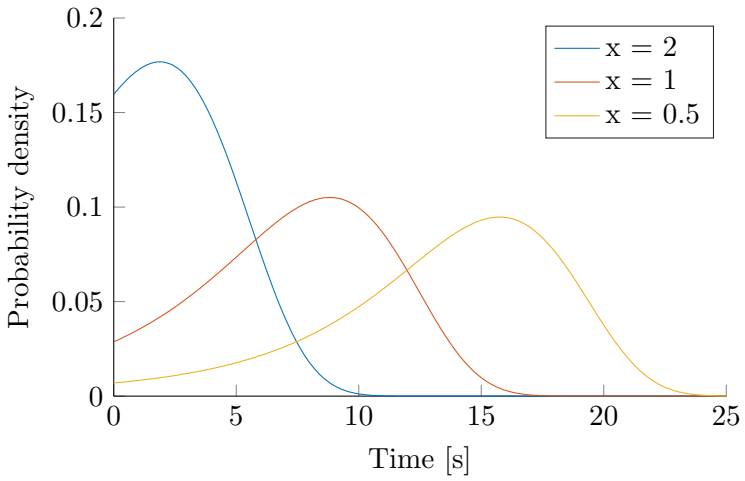

Figure 3-6: Example of conditional distributions of the time at $x = 0.5$, $x = 1$ and $x = 2$.

This does not change anything about the plot shown in Figure 3-5, but it only changes the way we interpret the plot. The plot now represents a bi-variate PDF of the state and time, with the consequence that the PDF is not normalized anymore:

$$\int_{-\infty}^{\infty}\int_{-\infty}^{\infty} \varphi(\boldsymbol{X}, t)dxdt \neq 1 \tag{3-35}$$

Three conditional distributions of the time are calculated and shown in Figure 3-6. These distributions are calculated by taking the cross-section of the PDF in Figure 3-5 at three different values of x and subsequently normalizing the PDFs:

$$\varphi_t(t) = \frac{\varphi(x = x_i, t)}{A} \tag{3-36}$$

where A is a normalization factor. Observing the figures, one can see that the PDF moves towards the right for a decreasing value of x. This means that it is more probable that the time is higher when it is known that the value of x is lower. This is also observed in Figure 3-5, which shows that the probability density moves towards $x = 0$ for increasing time. Comparing Figure 3-6 with Figure 3-5, it can be concluded that these conditional distributions of the time are cross-sections of the total PDF. These conditional distributions have been verified using MC, so the method can be used to derive impact time distributions.

3-4-5 Limitations

The Liouville equation seems to be general and the solution method seems to solve the evolution of the PDF in time without assumptions. However, it was found that there are limitations to the method. One of the limitations was found by experimenting with several test cases. Consider the following state derivative model:

$$\begin{pmatrix}\dot{x}\\ \dot{y}\end{pmatrix} = \begin{pmatrix}F_x\\ F_y\end{pmatrix} = \begin{pmatrix}ax\\ by^2\sin(x)\end{pmatrix} \tag{3-37}$$

The value of Ω is then governed by the following model:

$$\dot{\Omega} = \frac{\partial F_x}{\partial x} + \frac{\partial F_y}{\partial y} = a + 2by\sin(x) \tag{3-38}$$

The initial state of x and y are uncertain and defined using a PDF. The evolution of the PDF of the states x and y can then be determined using Equation (3-29). A test was performed to check if the solution still holds when only one of the two initial states has uncertainty and the results were compared to a Monte Carlo simulation. It was found that the PDF could indeed be correctly propagated, however, the model of Ω is not the same as when both initial states are uncertain. When only uncertainty was present in x_0, the model of Ω was found to be:

$$\dot{\Omega} = \frac{\partial F_x}{\partial x} = a \tag{3-39}$$

When only uncertainty is present in y_0, the model of Ω was found to be:

$$\dot{\Omega} = \frac{\partial F_y}{\partial y} = 2by\sin(x) \tag{3-40}$$

The reason that only the derivative of the uncertain variable should be taken into account is because the ODEs can be decoupled:

$$x(t) = x_0 \exp(at) \tag{3-41a}$$

$$\dot{y} = by^2 \sin(x_0 \exp(at)) \tag{3-41b}$$

These equations show that the evolution of x and y can be solved independently using these equations. The only coupling that is present is the value of x_0 in the model of y. The uncertainty in $y(0)$ does not have to originate from x, because the uncertainty does not have to come from the x_0 term in the equation. In addition, uncertainty in x_0 will cause uncertainty in y, but it does not have an effect on x itself or its distribution. Therefore, if uncertainty exists in one of the two initial states, the PDF can be propagated seperately using the Liouville Equation.

A second test was performed with a slightly different state derivative model that contains an extra coupling term:

$$\begin{pmatrix} \dot{x} \\ \dot{y} \end{pmatrix} = \begin{pmatrix} F_x \\ F_y \end{pmatrix} = \begin{pmatrix} ax - 0.1\cos(y) \\ b\sin(x)y^2 \end{pmatrix} \tag{3-42}$$

where the model of Ω is the same as the model of the first test case (Equation (3-38)). Simulations were performed using only uncertainty in one of the initial states and it was found that they do not agree with the Monte Carlo simulations, so the result is incorrect. Other tests were also performed with different state derivative models and it was found that the solution becomes incorrect when the extra coupling term is added.

A reason why the solution is incorrect is that the extra coupling term causes a sort of circular dependence of uncertainty. For example, uncertainty in y will cause uncertainty in x, which will cause uncertainty in y again. Therefore, only solving for the evolution of the uncertainty in y is incorrect, because uncertainty in x has an influence on the evolution of uncertainty

in y. This means that the assumption, which is used to derive $\dot{\Omega}$, that only uncertainty is present in one of the states does not hold anymore when the propagation starts.

A way to obtain a solution is to model the joint PDF of x and y where x_0 has a marginal PDF $f_{X_0}(x_0)$ and y_0 has one fixed value. The marginal distribution of y can be modeled as the Dirac delta at y_0, because the integral of the distribution should be 1 and the value of y_0 can only have one value. Therefore, the joint PDF of the initial state is actually the PDF of x_0 multiplied with a Dirac delta at y_0, because the initial states are statistically independent:

$$f_{X_0Y_0}(x_0, y_0, 0) = f_{X_0}(x_0)\delta(z - y_0) \tag{3-43}$$

The Liouville equation is used to solve the evolution of the PDF $f_{XY}(x, y, t)$, which now contains a Dirac delta function. Therefore, the solution method using the Method of Characteristics presented in Section 3-4-1, needs to be valid for this approach. Unfortunately, in Equation (3-26) the PDF is solved by integrating 1 divided by the PDF $\varphi(x, t)$ value over the PDF value. Performing such an operation with a Dirac delta in the PDF cannot be performed in this way. In addition, it is possible that earlier in the derivation or in the Method of Characteristics, implicit assumptions have been made such that these cases cannot be simulated.

Another way of looking at it is that uncertainty in the initial state of x will cause uncertainty in y, so the distribution of y will probably get a finite width and a certain shape. However, the initial distribution of y is a Dirac delta, thus changing the width and height cannot be performed using this solution method. Therefore, a more fundamental analysis on the solution method and the Liouville equation is required to obtain solutions that involve only uncertainty in a subset of the initial states.

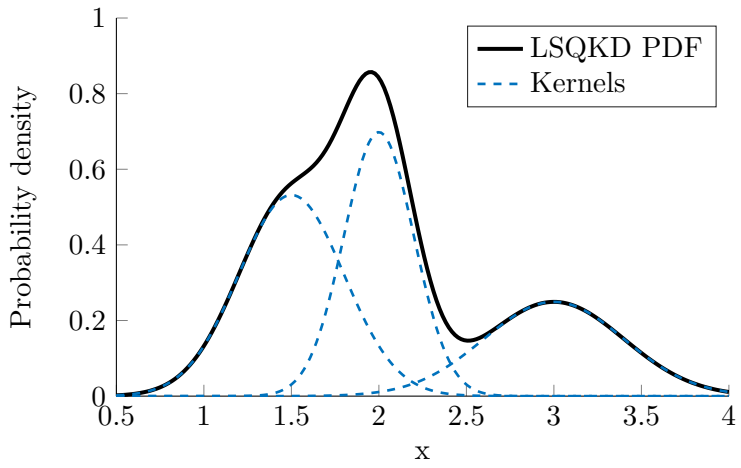

Figure 3-7: Example of a one-dimensional PDF modeled using three Gaussian kernels with $\mu = [1.5, 2, 3]$, $\sigma = [0.3, 0.2, 0.4]$ and $w = [0.4, 0.35, 0.25]$.

3-5 The Least Squares Kernel Density method

The LSQKD method developed by Pantano and Shotorban (2007) is an approximate method that can be used to propagate uncertainty in time. This method could potentially be used to propagate uncertainty in the state of the Delta-K rocket body in time, which can be used to perform statistical impact predictions. Similar to the DPP method, the LSQKD method propagates the uncertainty by propagating the PDF of the state in time. Instead of solving the evolution of the PDF in an exact way, the method assumes a parametric model of the PDF to approximate the true PDF. The parametric model consists of a summation of kernels K_m with weights w and function parameters β. A one-dimensional example of such an approximation is:

$$\varphi(x) = \sum_{m=1}^{N_K} w_m K_m(x, \beta_m) \tag{3-44}$$

Instead of propagating the entire PDF in time, the parameters β_m and the weights w_m are propagated in time. The method approximately solves the Liouville equation (Equation (3-18a)) using the parametric representation of the PDF. A set of differential equations is derived that governs the evolution of the parameters in time. Because the number of differential equations that is solved is equal to the number of parameters, the method has the potential to produce results within significant less computation time than other methods like MC or DPP.

The multi-dimensional PDF is modeled using a weighted summation of kernels K_m that are dependent on the parameters $\boldsymbol{\beta}_m$:

$$\varphi(\boldsymbol{X}, t) = \sum_{m=1}^{N_K} w_m(t) K_m\left(\boldsymbol{X}, \boldsymbol{\beta}_m(t)\right) \tag{3-45}$$

where N_K is the number of kernels that is used to model the PDF. An example of a model of the PDF is shown in Figure 3-7. The figure shows three Gaussian kernels (Gaussian PDFs)

multiplied with their weights and the PDF that is obtained with the weighted summation. The parameters vector $\boldsymbol{\beta}_m$ of each kernel consists of a mean values μ and a standard deviation σ. The figure illustrates how the three kernels are combined to form a PDF.

In principle, any function can be used as a kernel. However, the kernels must be positive on its domain and the following property must hold:

$$\int_{-\infty}^{\infty} K(x)dx = 1 \tag{3-46}$$

which means that kernels must have the same properties as PDFs.

The LSQKD method assumes that the PDF has the shape of Equation (3-45). Therefore, the shape of the PDF is constraint by this model and the Liouville equation cannot be solved in an exact way. A constraint minimization problem is solved instead that minimizes the error in the Liouville equation. This process results in Equation (3-47), which is a system of equations that is used to propagate the weights $\boldsymbol{w}$ and parameters $\boldsymbol{\beta}$.

$$\boldsymbol{H}\begin{pmatrix}\dot{\boldsymbol{w}}\\ \dot{\boldsymbol{\beta}}\\ \lambda\end{pmatrix} = \begin{bmatrix}2\boldsymbol{A} & \boldsymbol{C}^T & \mathbf{1}\\ \boldsymbol{C} & 2\boldsymbol{B} & \mathbf{0}\\ \mathbf{1}^T & \mathbf{0}^T & 0\end{bmatrix}\begin{pmatrix}\dot{\boldsymbol{w}}\\ \dot{\boldsymbol{\beta}}\\ \lambda\end{pmatrix} = \begin{pmatrix}-\boldsymbol{D}\\ -\boldsymbol{E}\\ 0\end{pmatrix} \tag{3-47}$$

This system of equations can be used to solve for $\dot{\boldsymbol{w}}$ and $\dot{\boldsymbol{\beta}}$, which can be used to propagate $\boldsymbol{w}$ and $\boldsymbol{\beta}$ using a numerical integrator. The terms in Equation (3-47) will be explained in the following subsections. The LSQKD method is used to approximately solve the Liouville equation in this research. However, the method can also be used to obtain an approximate solution of the Fokker-Planck equation (Section 3-4), which is explained in the research of Shotorban (2010).

3-5-1 Local State Variables

The assumed form of the PDF (Equation (3-45)) constraints the shape of the PDF. If large non-linearities are present in the state derivative model, the actual shape of the PDF can differ significantly from the assumed form. For a multi-dimensional state vector, these non-linearities can be present in a subset of the states, while the propagation of other state variables is almost linear. The LSQKD method allows to make a distinction between these variables, by seperating the state variables in local $\boldsymbol{X}_L$ and global $\boldsymbol{X}_G$ state variables:

$$\boldsymbol{X} = \begin{pmatrix}\boldsymbol{X}_L\\ \boldsymbol{X}_G\end{pmatrix} \tag{3-48}$$

The shape of the PDF for the global state variables is constaint by the form of Equation (3-45). However, the parameters and weights become functions of the local state variable, so that the shape of the PDF can change more freely in the direction of the local state variables. The multi-dimensional PDF is then modelled using the following equation:

$$\varphi(\boldsymbol{X}, t) = \sum_{m=1}^{N_K} w_m(\boldsymbol{X_L}, t) K_m\left(\boldsymbol{X_G}, \boldsymbol{\beta}_m(\boldsymbol{X_L}, t)\right) \tag{3-49}$$

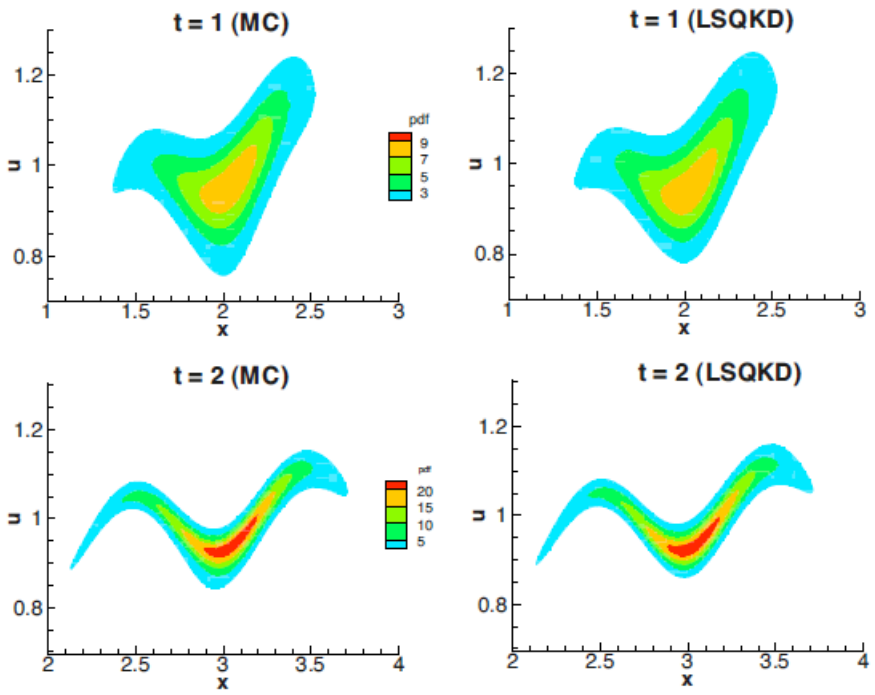

Figure 3-8: Bivariate PDFs of the state variables at two moments in time. Comparison of MC and LSQKD results for a two-dimensional test case performed by Pantano and Shotorban (2007).

Seperating the variables in local and global states can increase the accuracy when the shape of the PDF is difficult to approximate in the direction of the local variables. An example is shown in Figure 3-8, which shows the result of a two-dimensional test case performed in Pantano and Shotorban (2007). The following dynamical model was used for this test case:

$$\begin{pmatrix} \dot{x} \\ \dot{u} \end{pmatrix} = \begin{pmatrix} u \\ \frac{1+a\sin(2\pi x)-u}{b} \end{pmatrix} \tag{3-50}$$

The figure shows bivariate PDFs at two moments in time generated using the MC method and the LSQKD method. For the LSQKD method, the state variables are seperated in global and local state variables:

$$\boldsymbol{X} = \begin{pmatrix} \boldsymbol{X}_L \\ \boldsymbol{X}_G \end{pmatrix} = \begin{pmatrix} x \\ u \end{pmatrix} \tag{3-51}$$

Because the state x is chosen as a local state variable, the shape of the PDF can change freely in this direction. The shape of the PDF in the u direction is approximated using a Gaussian kernel (Gaussian PDF). If one looks at several instances of x, one can observe that the variation in probability density in the u direction is symmetric, which is caused by the Gaussian kernel. Furthermore, the comparison with MC results show that the LSQKD method is able to obtain accurate results for a highly non-linear problem.

A hypothetical example for entry trajectories is the evolution of the uncertainty in the altitude and velocity. For example, the uncertainty in the altitude can vary in a linear way, while uncertainty in the velocity can vary in a non-linear way due to aerodynamic forces. As a result, the shape of the probability distribution of the altitude does not change significantly,

while the probability distribution of the velocity can change largely. The altitude can then be chosen as a global variable, which is approximated and the velocity can be chosen as a local variable. This example is not based on exact knowledge about these distributions, but it shows the use local and global variables applied to atmospheric entry problems.

3-5-2 Derivation of the LSQKD Equations

The LSQKD method propagates a parametric model of the PDF that approximates the true PDF. Because this constraints the shape of the PDF, the Liouville equation cannot be solved in an exact way. Therefore, minimization is performed that minimizes the error in the Liouville equation with the constraint that the PDF has a total integral (total probability) that equals to one. Several auxilary variables are introduced in the derivation, which are used to reduce the size of the equations.

The Liouville Equation (Equation (3-18a)) can be rewritten by separating the state in local $\boldsymbol{X}_L$ and global $\boldsymbol{X}_G$ states:

$$\frac{\partial \varphi(\boldsymbol{X},t)}{\partial t} + \sum_{i=1}^{N_L} \frac{\partial}{\partial X_{L,i}} \left[\varphi(\boldsymbol{X},t) F_{L,i}(\boldsymbol{X},t)\right] + \sum_{i=1}^{N_G} \frac{\partial}{\partial X_{G,i}} \left[\varphi(\boldsymbol{X},t) F_{G,i}(\boldsymbol{X},t)\right] = 0 \tag{3-52a}$$

$$\begin{bmatrix} \dot{\boldsymbol{X}}_{\boldsymbol{L}} \\ \dot{\boldsymbol{X}}_{\boldsymbol{G}} \end{bmatrix} = \begin{bmatrix} \boldsymbol{F}_{\boldsymbol{L}}(\boldsymbol{X},t) \\ \boldsymbol{F}_{\boldsymbol{G}}(\boldsymbol{X},t) \end{bmatrix} \tag{3-52b}$$

where N_L is the number of local states and N_G is the number of global states.

The model of the PDF (Equation (3-49)) is substituted into the left-hand side of the Liouville equation. The result will not be equal to zero, which means that the Liouville equation is violated. This results from the fact that the PDF is forced to a shape defined by the model. Therefore, a residual r remains:

$$r(\boldsymbol{X},t) = \sum_{m=1}^{N_K} \left(K_m \frac{\partial w_m}{\partial t} + w_m \left[M(m) + Q(\boldsymbol{X},t,m)\right] + V(\boldsymbol{X},t,m) \right) \tag{3-53}$$

where the variables M , Q and V are used to reduce the size of the equation:

$$M(m) = \sum_{j=1}^{N_\beta} \frac{\partial K_m}{\partial \beta_{m,j}} \frac{\partial \beta_{m,j}}{\partial t} \tag{3-54a}$$

$$Q(\boldsymbol{X},t,m) = \sum_{i=1}^{N_G} \frac{\partial}{\partial X_{G,i}} \left[(K_m) F_{G,i}(\boldsymbol{X},t)\right] \tag{3-54b}$$

$$V(\boldsymbol{X},t,m) = \sum_{i=1}^{N_L} \frac{\partial}{\partial X_{L,i}} \left[w_m K_m F_{L,i}(\boldsymbol{X},t)\right] \tag{3-54c}$$

where m corresponds to the m^{th} kernel and $\beta_{m,j}$ to the j^{th} parameter of the m^{th} kernel. The residual can be written in a more compact form using matrices and vectors:

$$r(\boldsymbol{X}, \boldsymbol{w}, \boldsymbol{\beta}, \dot{\boldsymbol{w}}, \dot{\boldsymbol{\beta}}) = \boldsymbol{P}^T \dot{\boldsymbol{w}} + \boldsymbol{w}^T \boldsymbol{M} \dot{\boldsymbol{\beta}} + \boldsymbol{w}^T \boldsymbol{Q} + V \tag{3-55}$$

where $\boldsymbol{w}$ is a vector containing the weights of the kernels, $\boldsymbol{\beta}$ is a vector containing all parameters of all kernels and the kernel vector $\boldsymbol{P}$ contains the kernels:

$$\boldsymbol{w} = \begin{bmatrix} w_1 & w_2 & \dots & w_{N_k} \end{bmatrix}^T \tag{3-56a}$$

$$\boldsymbol{\beta} = \begin{bmatrix} \beta_{1,1} & \dots & \beta_{1,N_\beta} & \beta_{2,1} & \dots & \beta_{2,N_\beta} & \dots & \beta_{N_K,N_\beta} \end{bmatrix}^T \tag{3-56b}$$

$$\boldsymbol{P} = \begin{bmatrix} K_1 & K_2 & \dots & K_{N_k} \end{bmatrix}^T \tag{3-56c}$$

The parameters stored in the vector $\boldsymbol{\beta}$ can be stored in any order. For this derivation, the parameters are sorted by kernel. The vector $\boldsymbol{Q}$, the vector $\boldsymbol{V}$ and the matrix $\boldsymbol{M}$ are introduced to describe the residual:

$$\boldsymbol{Q} = \sum_{i=1}^{N_G} \frac{\partial}{\partial X_{G,i}} \left(F_{G,i} \boldsymbol{P} \right) \tag{3-57a}$$

$$V = \sum_{i=1}^{N_L} \frac{\partial}{\partial X_{L,i}} \left(F_{L,i} \boldsymbol{w}^T \boldsymbol{P} \right) \tag{3-57b}$$

$$\boldsymbol{M} = \frac{\partial \boldsymbol{P}}{\partial \boldsymbol{\beta}} \tag{3-57c}$$

The matrix $\boldsymbol{M}$ is defined by the jacobian of the kernel vector $\boldsymbol{P}$ to the parameters of the kernels $\boldsymbol{\beta}$. The evolution of the parameters $\boldsymbol{\beta}$ and weights $\boldsymbol{w}$ in time is solved by minimizing the square of the residual r. The cost function δJ, which will be used for the minimization procedure, is defined as:

$$\delta J(\boldsymbol{X}, \boldsymbol{w}, \boldsymbol{\beta}, \dot{\boldsymbol{w}}, \dot{\boldsymbol{\beta}}, \lambda) = \int_{-\infty}^{\infty} r^2 d\boldsymbol{X_G} + \lambda(t) \mathbf{1}^T \dot{\boldsymbol{w}} \tag{3-58a}$$

$$\mathbf{1}^T \dot{\boldsymbol{w}} = \sum \dot{w}_i = 0 \tag{3-58b}$$

$$\mathbf{1} = \begin{bmatrix} 1 & 1 & \dots & 1 \end{bmatrix}^T \tag{3-58c}$$

A constraint is added that uses the derivatives of the weights to enforce that the total probability will be conserved and equal to 1. A lagrange multiplier λ is multiplied with the summation of the derivatives of all the weights w_m to enforce the constraint. The total cost function is obtained by integrating over the local variables:

$$J = \int_{-\infty}^{\infty} \delta J d\boldsymbol{X_G} \tag{3-59}$$

The cost function J is equal to δJ if there are no local variables. Considering the situation that there are no local variables, the cost function can be rewritten by performing the integration in Equation (3-58a) yielding:

$$\delta J = \dot{\boldsymbol{w}}^T \boldsymbol{A} \dot{\boldsymbol{w}} + \dot{\boldsymbol{\beta}} \boldsymbol{B} \dot{\boldsymbol{\beta}}^T + \dot{\boldsymbol{\beta}}^T \boldsymbol{C} \dot{\boldsymbol{w}} + \boldsymbol{D}^T \dot{\boldsymbol{w}} + \boldsymbol{E}^T \dot{\boldsymbol{\beta}} + f + \lambda \mathbf{1}^T \dot{\boldsymbol{w}} \tag{3-60}$$

using the following definitions:

$$\boldsymbol{A} = \int_{-\infty}^{\infty} \boldsymbol{P} \boldsymbol{P}^T d\boldsymbol{X_G} \tag{3-61a}$$

$$\boldsymbol{B} = \int_{-\infty}^{\infty} \boldsymbol{M}^T \boldsymbol{w}\boldsymbol{w}^T \boldsymbol{M} d\boldsymbol{X_G} \tag{3-61b}$$

$$\boldsymbol{C} = 2\int_{-\infty}^{\infty} \boldsymbol{M}^T \boldsymbol{w}\boldsymbol{P}^T d\boldsymbol{X_G} \tag{3-61c}$$

$$\boldsymbol{D} = 2\int_{-\infty}^{\infty} \left(\boldsymbol{w}^T\boldsymbol{Q} + \boldsymbol{V}\right)\boldsymbol{P} d\boldsymbol{X_G} \tag{3-61d}$$

$$\boldsymbol{E} = 2\int_{-\infty}^{\infty} \left(\boldsymbol{w}^T\boldsymbol{Q} + \boldsymbol{V}\right)\boldsymbol{M}^T \boldsymbol{w} d\boldsymbol{X_G} \tag{3-61e}$$

$$f = \int_{-\infty}^{\infty} \left(\boldsymbol{w}^T\boldsymbol{Q} + (\boldsymbol{F_L}\boldsymbol{w}^T\boldsymbol{P})_{\boldsymbol{X_L}}\right)^2 d\boldsymbol{X_G} \tag{3-61f}$$

The cost function only contains the variables $\dot{\boldsymbol{w}}$ and $\dot{\boldsymbol{\beta}}$, which can be solved by minimizing the cost function. The cost function is minimized by setting the derivatives of the cost function to $\dot{\boldsymbol{w}}$ and $\dot{\boldsymbol{\beta}}$ to zero:

$$\frac{\partial \delta J}{\partial \dot{\boldsymbol{w}}} = 2\boldsymbol{A}\dot{\boldsymbol{w}} + \boldsymbol{C}^T\dot{\boldsymbol{\beta}} + \boldsymbol{D} + \lambda\boldsymbol{1} = 0 \tag{3-62a}$$

$$\frac{\partial \delta J}{\partial \dot{\boldsymbol{\beta}}} = 2\boldsymbol{B}\dot{\boldsymbol{\beta}} + \boldsymbol{C}\dot{\boldsymbol{w}} + \boldsymbol{E} = 0 \tag{3-62b}$$

The solution of these equations can be obtained by rewriting these equations and adding the constraint.

$$\boldsymbol{H}\begin{pmatrix}\dot{\boldsymbol{w}}\\ \dot{\boldsymbol{\beta}}\\ \lambda\end{pmatrix} = \begin{bmatrix}2\boldsymbol{A} & \boldsymbol{C}^T & \boldsymbol{1}\\ \boldsymbol{C} & 2\boldsymbol{B} & \boldsymbol{0}\\ \boldsymbol{1}^T & \boldsymbol{0}^T & 0\end{bmatrix}\begin{pmatrix}\dot{\boldsymbol{w}}\\ \dot{\boldsymbol{\beta}}\\ \lambda\end{pmatrix} = \begin{pmatrix}-\boldsymbol{D}\\ -\boldsymbol{E}\\ 0\end{pmatrix} \tag{(3-47)}$$

Solving Equation (3-47) for the derivatives of the parameters and the weights results in a set of ODEs that can be used to propagate these variables in time. Obviously, it is prefered that the integrals in Equation (3-61) result in analytical solutions. In this way the system of equations is only solved once to obtain the ODEs and the weights and parameters can directly be propagated in time.

3-5-3 Solution Validity

The solution (Equation (3-47)) described in the previous section is derived by finding the stationary points of the cost function. This does not guarantee that the stationary point is a minimum, so additional information is required to determine if the stationary point is a minimum. This information is found by using a multi-dimensional Taylor expansion around the stationary point $\boldsymbol{u}^*$:

$$\delta J(\boldsymbol{u}^* + \delta\boldsymbol{u}) = \delta J(\boldsymbol{u}^*) + \frac{\partial(\delta J)}{\partial \boldsymbol{u}}\delta\boldsymbol{u} + \frac{1}{2}\delta\boldsymbol{u}^T\frac{\partial^2(\delta J)}{\partial \boldsymbol{u}^2}\delta\boldsymbol{u} \tag{3-63a}$$

$$\boldsymbol{u} = \begin{bmatrix}\dot{\boldsymbol{w}}^T & \dot{\boldsymbol{\beta}}^T\end{bmatrix}^T \tag{3-63b}$$

This expansion is exact for the cost function δJ, because the cost function is a quadratic equation. If the third term in the equation results in a positive value for every $\delta \boldsymbol{u}$, the stationary point is a minimum. The stationary point is thus a minimum if the Hessian $\frac{\partial^2 \delta J}{\partial \boldsymbol{u}^2}$ is positive definite, which requires that all the eigenvalues of the Hessian are positive (Lay, 2012). This approach is similar to one-dimensional optimization where the second derivative is used. The Hessian of this minimization problem is found to be:

$$\frac{\partial^2(\delta J)}{\partial \boldsymbol{u}^2} = \begin{bmatrix} 2\boldsymbol{A} & \boldsymbol{C}^T \\ \boldsymbol{C} & 2\boldsymbol{B} \end{bmatrix} \tag{3-64}$$

It could not be proved that the Hessian is positive definite in general, however, it can be shown that it should be positive definite. There is no derivative of the parameters and weights that leads to a maximum residual, because the derivative could increase toward infinity while the residual increases. This indicates that there is no bound on the maximum residual. In addition, it also not logical that the square of the residual will have an unbounded minimum, because there is only one shape that the PDF should have. Therefore, it is expected that the stationary point that is obtained is always or at least in most practical cases, a minimum.

3-5-4 Kernel Selection

In theory any function can serve as a kernel for this method, however, it must be a function that has a total integral of 1, is positive on its domain and can be used to model a PDF. The following considerations must be taken into account when selecting a kernel:

1. Initial distribution - The PDF approximation must be able to represent the initial distribution. This can either performed by a weighted summation of multiple kernels or the kernel itself can represent the initial distribution. For example, using a single Gaussian PDF as a kernel can be used to model the initial PDF in an exact way.
2. Flexibility - The kernel must be flexible in a sense that its parameters can be evolved in time such that the shape of the modeled PDF can change in a way that it can accurately describe the exact PDF. This means that the kernel must contain parameters that can change the location, the width or skewness of the kernel.
3. Complexity - The equations that govern the evolution of the parameters and weights are defined by a set of integrals (Equation (3-61)) that are ideally solved analytically. Therefore, the complexity or form of the functional form of the kernels influence the computational effort and accuracy.

3-5-5 The LSQKD Equations

The parameters and weights are solved using a set of ODEs defined by Equations (3-47). These equations are defined by a set of integrals defined in Equations (3-61). To provide more insight in the method, the contents of these matrices are provided in this section.

The $\boldsymbol{A}, \boldsymbol{B}, \boldsymbol{C}$ matrices are only dependent on the kernels K_i and the weights w_i. For a case where two kernels are used the matrices are defined as:

$$\boldsymbol{A} = \int_{-\infty}^{\infty} \begin{bmatrix} K_1^2 & K_1 K_2 \\ K_2 K_1 & K_2^2 \end{bmatrix} d\boldsymbol{X_G} \tag{3-65}$$

$$\boldsymbol{B} = \int_{-\infty}^{\infty} \begin{bmatrix} w_1^2 K_{1,\beta_1}^2 & w_1^2 K_{1,\beta_1} K_{1,\beta_2} & w_1 w_2 K_{1,\beta_1} K_{2,\beta_3} & w_1 w_2 K_{1,\beta_1} K_{2,\beta_4} \\ w_1^2 K_{1,\beta_2} K_{1,\beta_1} & w_1^2 K_{1,\beta_2}^2 & w_1 w_2 K_{1,\beta_2} K_{2,\beta_3} & w_1 w_2 K_{1,\beta_2} K_{2,\beta_4} \\ w_1 w_2 K_{2,\beta_3} K_{1,\beta_1} & w_1 w_2 K_{2,\beta_3} K_{1,\beta_2} & w_2^2 K_{2,\beta_3}^2 & w_1 w_2 K_{2,\beta_3} K_{2,\beta_4} \\ w_1 w_2 K_{2,\beta_4} K_{1,\beta_1} & w_1 w_2 K_{2,\beta_4} K_{1,\beta_2} & w_1 w_2 K_{2,\beta_4} K_{2,\beta_3} & w_2^2 K_{2,\beta_4}^2 \end{bmatrix} d\boldsymbol{X_G} \tag{3-66}$$

$$\boldsymbol{C} = 2 \int_{-\infty}^{\infty} \begin{bmatrix} K_{1,\beta_1} & 0 \\ K_{1,\beta_2} & 0 \\ 0 & K_{2,\beta_3} \\ 0 & K_{2,\beta_4} \end{bmatrix} \begin{bmatrix} w_1 K_1 & w_1 K_2 \\ w_2 K_1 & w_2 K_2 \end{bmatrix} d\boldsymbol{X_G} \tag{3-67}$$

These integrals are only dependent on the weights and the kernels, so for some kernels, these integrals can be solved analytically. Solving these integrals analytically is highly advantageous, because otherwise a large number of integrals need to be solved numerically for every state derivative (Equation (3-47)) computation that is performed by the integrator.

The vectors $\boldsymbol{D}$ and $\boldsymbol{E}$ are not only dependent on the kernels, but also on the dynamical model. These integrals can generally not be performed analytically, so numerical integration is required to define the right-hand side of Equation (3-47).

3-5-6 Limitations

An analysis of the method revealed several limitations of the method that will be discussed in this section. The first limitation of the method is that an exact uniform distribution is not possible. This can be explained by using the function definition of an exact uniform distribution, which is:

$$K(x) = \begin{cases} \frac{1}{2h} & -h < x - \mu < h \\ 0 & \text{otherwise} \end{cases} \tag{3-68}$$

The center μ of the uniform distribution is only observed in the boundaries of the function, but not in the function itself. The LSQKD method determines the change in the center μ by using the chain rule in the residual:

$$\frac{\partial K(x)}{\partial \mu} \frac{\partial \mu}{\partial t} \tag{3-69}$$

If the derivative of function to center $\frac{\partial K(x)}{\partial \mu}$ is equal to zero, the derivative of the center to time is multiplied with zero. This means that the time derivative of μ is not included in the equations anymore, so it cannot be solved for.

Another limitation of the method is that the initial conditions of two kernels with the same function cannot be the same. The reason for this is that the $\boldsymbol{A}$ and $\boldsymbol{B}$ matrices become

singular. Physically this means that the optimization process does not know which of the two functions should change shape and location, because the functions are identical. In addition, the matrix $\boldsymbol{B}$ becomes singular if one of the weights is equal to zero. These limitations makes the use of multiple kernels more difficult, since the initial distribution also needs to be modelled by the kernels. For example, two Gaussian kernels cannot be used with one of the weights equal to zero. The only option would be to use to almost identical Gaussian kernels to model an initial Gaussian distribution.

Chapter 4

Preliminary Analysis

This chapter describes a preliminary analysis and research on the methods that are possibly used for statistical impact prediction of the Delta-K rocket body. The test cases described here are used to evaluate the LSQKD method and the DPP method, and to test their capabilities and limitations. The chapter starts with an analysis on the uncertainty analysis methods and its applicability to decay and entry problems in Section 4-1. After that a test case is discussed for a planar atmospheric entry trajectory in Section 4-2.

4-1 Method Analysis and Selection

The DPP method and the LSQKD method were selected, because they are potentially be useful for statistical impact prediction. These methods were analyzed using several test cases to evaluate their usefulness for atmospheric entry problems and to verify the methods. The results of this analysis are summarized in this section, the details of the analysis are presented in Appendix B and Appendix C and Section D-2.

4-1-1 One-dimensional Test Model

In the research of Pantano and Shotorban (2007) the LSQKD method was presented and several simulations were performed with the following one-dimensional state-derivative model:

$$\begin{aligned} \dot{x} &= ax^2 + bx + c \\ \text{with } & b^2 - 4ac > 0 \end{aligned} \tag{B-1}$$

The results obtained in the research are reconstructed and the performance of the LSQKD method was compared with the DPP method and MC in Appendix B. One of the results is shown in Figure 4-1, which is also presented in the paper of Pantano and Shotorban (2007).

The figure shows the evolution of the PDF of the state in time obtained from an analytical solution of the DPP method, and an approximate solution obtained using the LSQKD method with one Gaussian kernel. The figure shows that the Gaussian kernel varies such that the LSQKD solution closely approximates the exact solution.

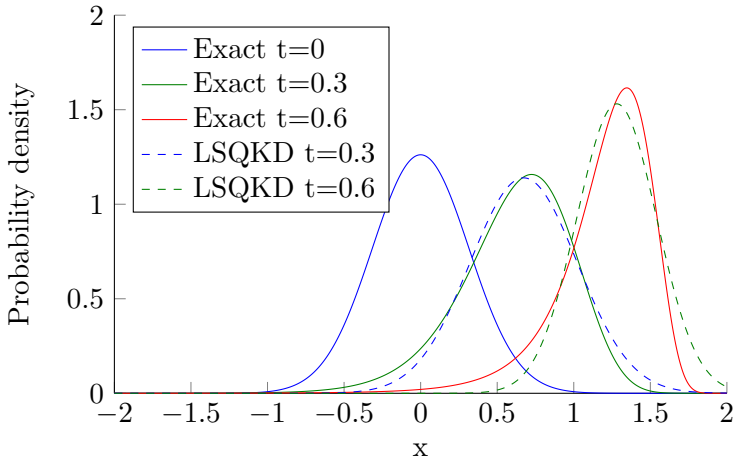

Figure 4-1: A reconstruction of the probability density evolution as described in the research of Pantano and Shotorban (2007) with initial Gaussian distribution with $\mu(0) = 0$ and $\sigma(0) = \sqrt{0.1}$.

- Accuracy - The accuracy of the LSQKD method is dependent on the number of kernels, because a larger number of kernels can generally model an arbitrary PDF more accurately. The simulations showed that using two kernels resulted in more accurate results than with only one kernel, because any assymetry of the PDF cannot be modeled using only one symmetric Gaussian kernel. However, no feasible solution could be obtained for a larger number of kernels due to limitations of the method. Therefore, the LSQKD method could not provide an accuracy that is similar to MC or the DPP method.
- Distributions - The simulations were performed using two different distributions for the initial state. The simulations with an initially Gaussian distribution resulted in more accurate results than the simulations with an initial state that is uniformly distributed. This could be attributed to the selection of the kernels, because the kernels that were required to model the initial distribution as a uniform distribution could not change its shape such that an accurate solution could be obtained. Since no better alternatives could be found for the kernels, no accurate solutions could be obtained for this case.
- Computational effort - The computational effort of the LSQKD method was similar to the DPP method and the MC method for the cases with a Gaussian initial distribution. However, the computation time of the LSQKD method was about three times larger than the other methods for the uniform distribution cases. The reason is that the integrals (Equation (3-61)) that define the ODEs could not be evaluated analytically. Therefore, $(4N)^2 + 4N$ integrals need to be determined using numerical quadrature during every state-derivative computation. For the Gaussian initial distribution, only $3N$ numerical integrals needed to be calculated for every state-derivative computation.
- DPP method - A numerical DPP simulator was developed that solves Equations (3-29) and the results were compared with the analytical solution. it was found that solving

the integral in Equation (3-27) using numerical quadrature could not produce accurate results. However, introducing the PDF correction factor Ω, such that this integral is solved by the numerical integrator, resulted in highly accurate results, because the variable stepsize integrator controls the error of this factor.

4-1-2 Two-dimensional Test Model

Several simulations were performed using a two-dimensional state derivative model to investigate the influence of correlation. A numerical DPP simulator and a MC simulator were developed and verified. The LSQKD method was not used for this test, because it was concluded that the method cannot provide sufficient accuracy. The LSQKD method will be further discussed in Section 4-1-3. The details of the analysis with the two-dimensional state derivative model are discussed in Appendix C. The following two-dimensional state-derivative model was used for this test case:

$$\dot{\boldsymbol{x}} = \begin{pmatrix} \dot{x} \\ \dot{y} \end{pmatrix} = \begin{pmatrix} ay \sin\left(\frac{2\pi x}{T}\right) \\ b \sin\left(\frac{2\pi x}{T}\right) \end{pmatrix} \qquad (\text{C-1})$$

One of the results that is obtained using the DPP simulator is shown in Figure 4-2. The figure shows the initial distribution of the state, which is a uniform distribution with correlation that is modelled using a Gaussian copula (Section A-4). The figure shows that the probability density function gets a periodic shape after propagation due to the sine functions in the state-derivative model. The figure also shows that the concentrations of higher probability that are caused by the correlation have an effect on the propagated PDF. These results were verified with the MC simulator.

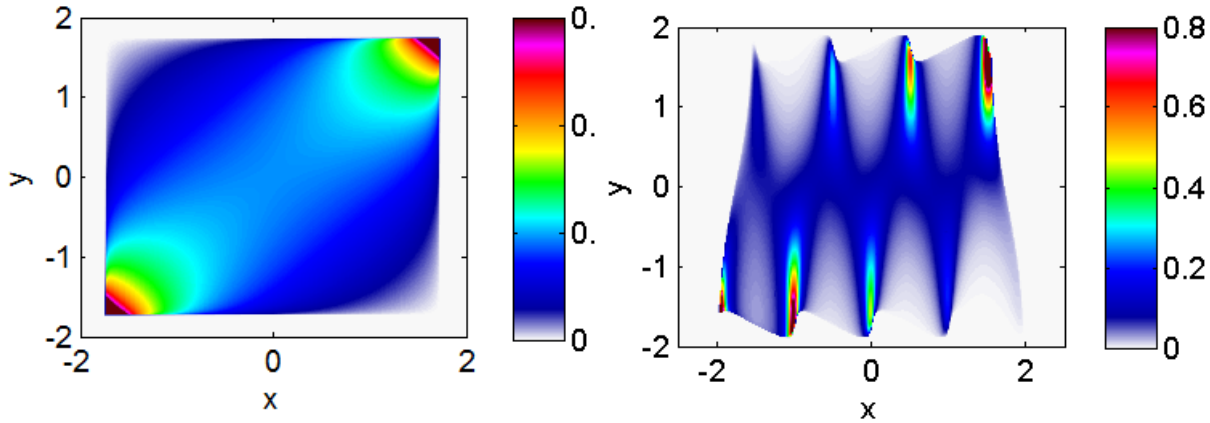

(a) $t = 0$ **(b)** $t = 0.2$

Figure 4-2: The probability density function of the state at $t = 0$ and at $t = 0.2$ for $a = b = T = 1$ obtained using the DPP simulator. The probability density is indicated by the colors.

- Correlation - Copulae (Section A-4) were used to model the initially uniform distributions with correlation and it was shown that a Gaussian copula can represent the correlation in the random variables. The simulations also showed that the shape of

the PDF is largely affected by an initial correlation between the variables, which suggests that correlation cannot be neglected when modelling the distribution of a random variable.

- Propagation method - The simulations were performed using a numerical DPP simulator that could propagate the state backwards or forward in time. It was found that when propagating the state backwards in time, the sampling grid should be defined such that rapid changes in the value of the PDF can observed. A too coarse grid will result in inaccuracies in these areas. When propagating the state forward in time, it was found that the distribution of the datapoints is partially determined by the PDF itself. This means that areas with higher probability density will contain more datapoints than areas with lower probability density. So it might be dificult to obtain accurate information about the PDF for areas where the probability density is low.

  To obtain accurate impact time windows with a high probability band, for example, 99.73% probability, accurate information of the PDF is necessary at the edges of the PDF, which is where the probability density is low. Forward propagation may induce inaccuracies at the edges of the PDF, so the accuracy of the impact time window can be affected. Therefore, a hybrid method that uses both backward and forward time propagation can ideally provide more accurate results. Such a method would use forward propagation to obtain accurate information at the regions of high probability density and backward propagation to obtain accurate information at the regions low probability density.

  These problems are also present for MC, because a small number of samples is present at the edges of the PDF. Therefore, a large number of samples is required to obtain accurate information about the edges of the PDF, because the small number of samples at the edge of the PDF have a large effect on the 99.73% impact time window.

- Concentration - It is observed that the probability density flows towards certain regions, which is shown in Figure 4-2. The figure shows that the joint PDF gets more concentrated even though the marginal distributions of x or y (Figure C-4) do not necessarily show these concentrations. This shows that the joint PDF can have much more complex features than marginal distributions of each state alone.

4-1-3 The LSQKD Method

The test cases and further analysis on the LSQKD method have revealed features and limitations of the method. This section describes the applicability of the LSQKD method to atmospheric entry problems.

The one-dimensional case showed that the accuracy of the LSQKD method is limited. Reasonably accurate results were obtained for the initial Gaussian distribution, but for an initial uniform distribution, the accuracy is not sufficient and a large computational effort was observed compared to the other methods.

The two-dimensional test case showed that correlation causes concentrations and features in the PDF that are difficult to model using kernels that can be used in a computationally efficient way. A hypothetical solution of the LSQKD solution compared to a DPP solution

obtained in Appendix C is shown in Figure 4-3. The hypothetical LSQKD solution is a PDF that is composed of nine Gaussian kernels. Comparing the figures, one can see that the hypothetical solution approximates the DPP solution. However, the accuracy is limited and the band of higher probability density around $y = 0$ is not observed in the LSQKD solution.

In the one-dimensional test case it was observed that no solution could be obtained for the LSQKD method with more than two kernels and the computational-effort increases with increasing number of kernels. This shows that it is difficult to obtain a solution using a higher number of kernels. Therefore, it is expected that the hypothetical solution in Figure 4-3 is not possible or a large computational effort is required to obtain such a solution. Considering that the distribution of the initial state can be uniform or contain considerable correlations, it is expected that the accuracy of the LSQKD method is lower than the other methods for higher dimensional problems.

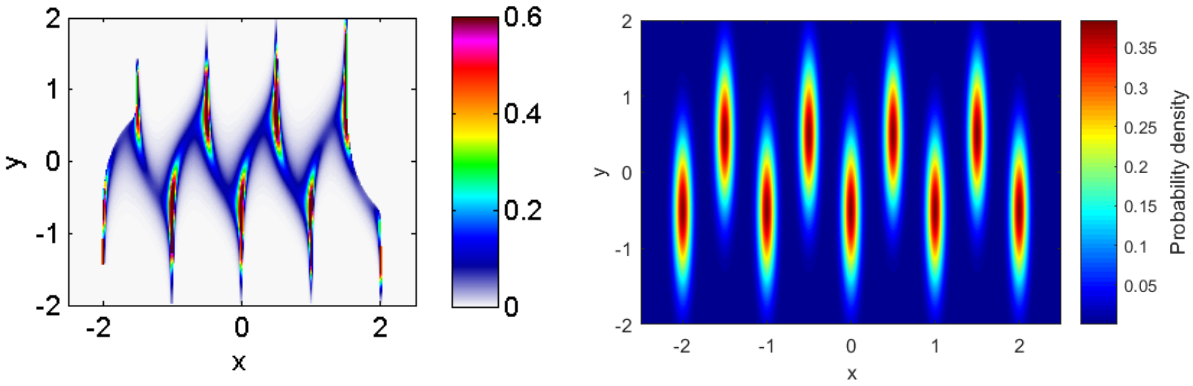

(a) DPP solution

(b) Example of LSQKD solution

Figure 4-3: Comparison of DPP solution and an example of a LSQKD solution using nine Gaussian kernels.

In an attempt to obtain more accurate results using the LSQKD method, the two-dimensional test case described in the research of Pantano and Shotorban (2007) was analyzed. In Section 3-5, it was explained that the LSQKD method allows the state variables to be seperated in global and local variables. The PDF is then approximated for the global variables and the distribution for the local variables can be solved in an exact way. With such a method, the accuracy of the method could be largely improved.

The equations were derived for the case where only one of the two states is a global variable. The resulting differential equations are PDEs in contrast to ODEs, which are obtained for the case were all states are globally approximated. The PDEs derived in Section IV.A.2 in the paper of Pantano and Shotorban (2007) are derived to investigate the use of this method and presented in Section D-2. It was found that this method is not suitable for Statistical Impact Prediction, because the terms in the PDEs cannot be derived analytically. This means that numerical quadrature is required to obtain the terms of the PDEs for every state-derivative computation. Therefore, it is expected that the computational time of such a method will be even larger then when all states are globally approximated.

Based on these considerations, it is expected that the LSQKD method will result in less accurate results with more computational effort for statistical impact prediction. Therefore, no further research is performed on this method.

4-2 Two-Dimensional Atmospheric Entry

This section describes a test that was performed using the DPP method for an atmospheric entry trajectory in a single plane.

4-2-1 Dynamical Model

The following equations of motion are used to simulate a two-dimensional atmospheric entry trajectory (Mooij, 2014):

$$\dot{R} = V \sin\gamma \tag{4-1a}$$

$$\dot{V} = -\frac{\rho V^2 S C_D}{2m} - g\sin\gamma \tag{4-1b}$$

$$\dot{\gamma} = \frac{L}{mV} - \frac{g}{V}\cos\gamma\left(1 - \frac{V^2}{gR}\right) \tag{4-1c}$$

These equations describe a planar entry trajectory for a non-rotating planet. The atmospheric density ρ is calculated using the exponential atmosphere model and the gravitational acceleration g is calculated using the central gravity model.

Uncertainty is present in the initial state of the vehicle, which leads to uncertainty its trajectory. The uncertainty in the initial state is presented using a PDF of the state at the initial time. The evolution of the PDF in time, so the stochastic evolution of the state in time, can be solved using the DPP method (Section 3-4). This method requires that an extra state Ω is solved, which is the summation of partial derivatives of the state derivative model:

$$\dot{\Omega} = \frac{\partial \dot{R}}{\partial R} + \frac{\partial \dot{V}}{\partial V} + \frac{\partial \dot{\gamma}}{\partial \gamma} = -\frac{\rho V S C_D}{m} + \frac{g}{V}\sin\gamma\left(1 - \frac{V^2}{gR}\right) \tag{4-2}$$

Using Equations (4-1) and Equation (4-2), the PDF of the state can be propagated in time using using Equation (3-29).

Adding uncertainty in other variables

The model described in the previous section can only be used for uncertainty in the initial state. However, uncertainty can be present in the constants and other dependent variables as well. For instance, some examples are provided that explain how to include uncertainty in other variables. For example, the uncertainty in the atmospheric density can also be included by adding a state variable X_ρ:

$$\rho = X_\rho \rho_0 \exp\left(-\beta h\right) \tag{4-3a}$$

$$\dot{X}_\rho = 0 \tag{4-3b}$$

$$\frac{\partial \dot{X}_\rho}{\partial X_\rho} = 0 \tag{4-3c}$$

where X_ρ is a (random) atmospheric density factor that is used to add uncertainty in the atmospheric density. This random factor is then added as a state variable using its state derivative. For this example, the value of X_ρ is constant, so the evolution of X_ρ does not need to be solved. In addition, the state derivative of Ω does not change, so apart from the fact the the dimension of the initial PDF is increased, this causes no increase in complexity. The distribution of X_ρ stays constant and only affects the other distributions.

In this example it is assumed that the uncertainty in the atmospheric density is constant throughout the trajectory. However, the uncertainty can also be dependent on the altitude h or other variables, which is generally the case for atmosphere models. The uncertainty can then be modeled using a random function $X_\rho(h)$:

$$\rho = X_\rho(h) \cdot \rho_0 \exp\left(-\beta h\right) \tag{4-4a}$$

$$\dot{X}_\rho = \frac{dX_\rho(h)}{dh}\frac{dh}{dt} = \frac{dX_\rho(h)}{dh} V \sin\gamma \tag{4-4b}$$

$$\frac{\partial \dot{X}_\rho}{\partial X_\rho} = \frac{\partial}{\partial X_\rho}\left(\frac{dX_\rho(h)}{dh}\right) V \sin\gamma \tag{4-4c}$$

With uncertainty dependent on altitude, the atmospheric density factor also needs to be propagated in time to obtain a solution. In addition, the extra term described by Equation (4-4c) needs to be added to the derivative of Ω (Equation (4-2)).

Another example is by adding uncertainty in the mass of the body, resulting in the following state derivative model:

$$\dot{m} = 0 \tag{4-5}$$

Similarly to an atmospheric density factor that is constant, the uncertainty in the mass will not add any terms to the derivative of Ω.

4-2-2 The Evolution of Uncertainty

A preliminary analysis on the evolution of uncertainty is performed using a MC simulation with $N = 10,000$ samples to show how the uncertainty in the state variables evolve in time. A ballistic trajectory is simulated from an initial altitude of 80 km and an initial flight-path angle of -10 and an initial velocity of 7.2 km/s. The uncertainty in each state is modelled by a Gaussian distribution without correlation and the following standard deviations:

$$\begin{pmatrix}\sigma_R\\ \sigma_V\\ \sigma_\gamma\end{pmatrix} = \begin{pmatrix}1.0 \text{ m}\\ 50.0 \text{ m/s}\\ 10^{-3} \text{ rad}\end{pmatrix} \tag{4-6}$$

In Figure 4-4, the distributions of the altitude and velocity are shown for various epochs. The figures show that the distributions move towards a lower altitude and a smaller velocity.

In the first part of the trajectory the dispersion in the altitude increases, because the different velocities cause different aerodynamic accelerations. At an altitude of approximately 40 km, the dispersion in the altitude starts to decrease, because the atmospheric density starts to

increase more rapidly. The distribution of the altitude thus diverges for the first part and converges for the second part.

The distribution of the velocity converges twice during the trajectory. In the first part of the trajectory, the differences in the atmospheric density are small, so the aerodynamic accelerations cause a slight convergence of the velocity. At an altitude of approximately 40 km, the atmospheric density is significantly larger and the dispersion in the altitude is large, so the difference in deceleration causes that the distribution of the velocity to diverge. At lower altitudes, the decelerations cause that the velocity converges towards the terminal velocity for each trajectory.

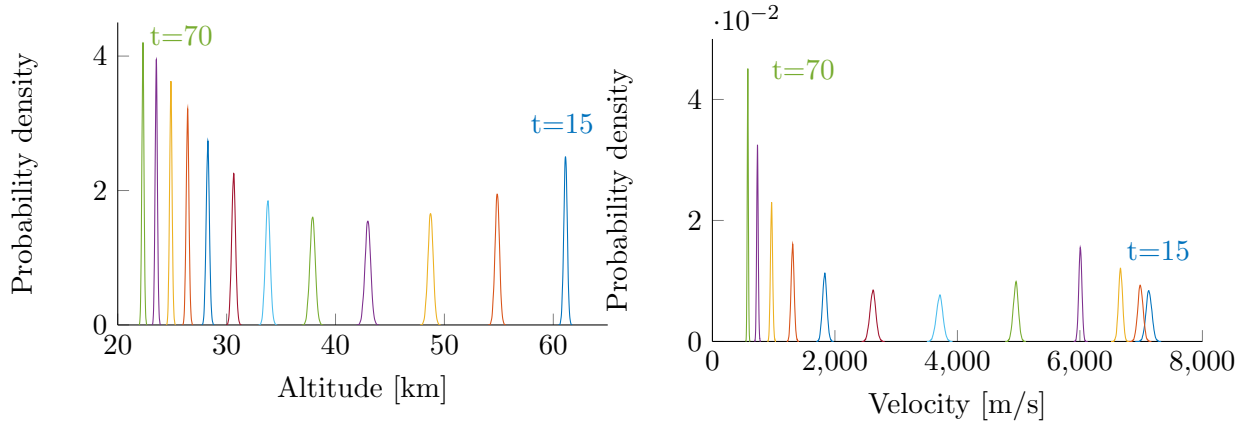

Figure 4-4: Illustration of the marginal distributions of the altitude and velocity obtained from 10,000 MC samples at $t = 15$ to $t = 70$ with steps of 5.

This example shows that the marginal distributions diverge for the first part of the trajectory and converges for the final part of the trajectory. Therefore, it is expected that the of the PDF correction factor Ω is positive and increases for the first part of the trajectory and negative and decreasing for the final part of the trajectory. In Figure 4-5, the evolution of Ω and $\dot{\Omega}$ is shown as a function of time and the state variables. The figure shows that Ω only decreases, which means that the joint PDF converges during the whole trajectory. This is a different result than expected from the marginal distributions.

It can be explained, because no random noise is present that increases the uncertainty. As a result, the state variables, whos evolution is completely governed by Equation (4-1), get highly correlated. Therefore, the volume of the joint PDF becomes smaller and the values of the PDF become larger, so Ω becomes negative and decreases. The fact that the joint PDF converges will be confirmed in Section 4-2-3.

The fact that the dispersion of the joint PDF, which is the three-dimensional PDF of all state variables, decreases does not mean that the dispersion in the marginal distributions also decreases. This was also shown in Appendix C, where joint PDFs are shown that are concentrated, but the marginal PDF are not necessarily concentrated.

Figure 4-5 also shows the evolution of $\dot{\Omega}$ and the two terms that are present in Equation (4-2). The figure shows that the evolution of Ω is mostly governed by the aerodynamic drag, which becomes larger with decreasing altitude. When the velocity becomes small the second term, which is governed by the velocity becomes more important. The reason that the aerodynamic

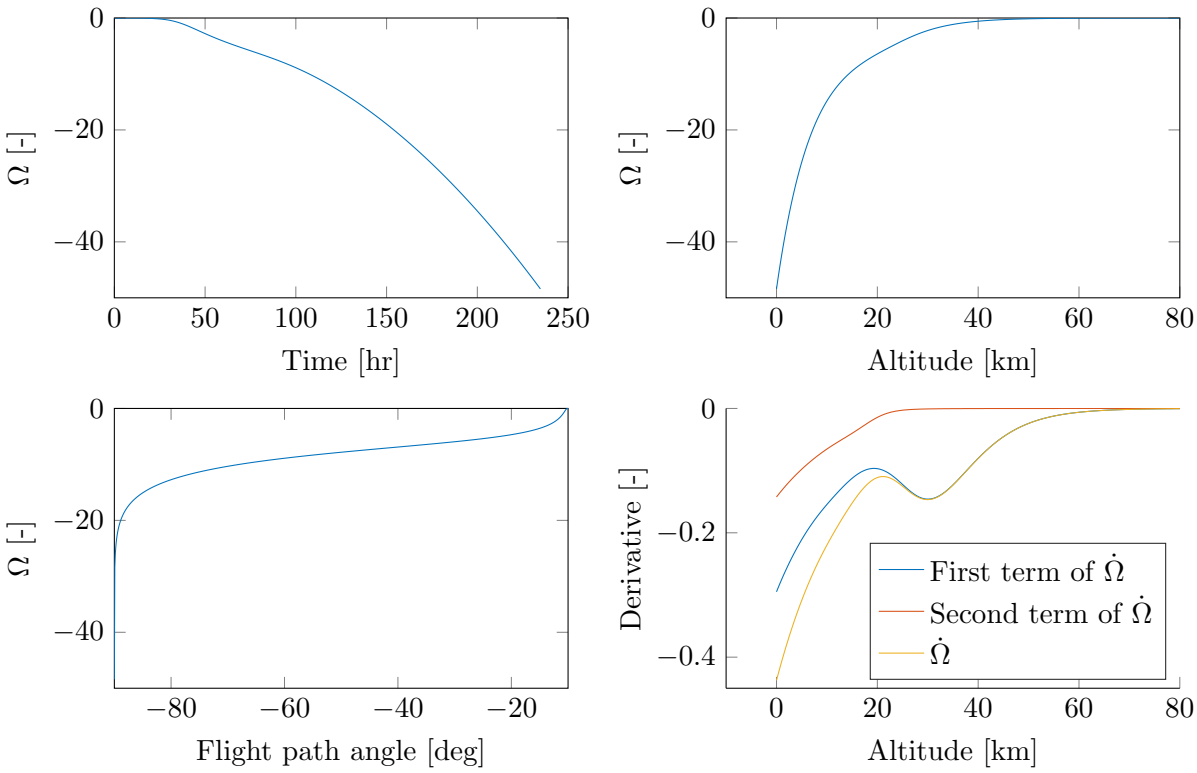

Figure 4-5: The evolution of Ω and $\dot{\Omega}$ as a function of time and the state variables.

drag causes Ω to decrease so rapidly, is because it decelerates the body, so the dispersion in velocity and altitude becomes smaller.

4-2-3 Direct PDF Propagator Results

To test the DPP method a simulation was performed with Gaussian uncertainty on the initial state without uncertainty in the other parameters. The PDF of the initial state is modeled by a three-dimensional Gaussian PDF with the same parameters as described in Equation (4-6).

The same initial state was used as described in Section 4-2-2. The initial state was sampled using a pseudo-random number generator, which generated 2000 samples with a uniform distribution within a region bounded by four times the standard deviation of the initial state. Each initial state was propagated in time using the equations of motion (Equation (4-1)). Simultaniously Ω was solved (Equation (4-2)) and used to calculate the probability density using Equation (3-29). In only 0.4 seconds of simulation time, the result displayed in Figure 4-6 were obtained.

The PDF is a three-dimensional function, so the function value, the probability density is indicated by the colors. Because the PDF values vary largely, the $\log_{10}$ of the PDF value is indicated by the colors. The figure shows that the probability density is the highest near the center of the data and the value of the PDF decreases almost in a radially symmetric way. This symmetry originates from the initial distribution, which is Gaussian, thus symmetric.

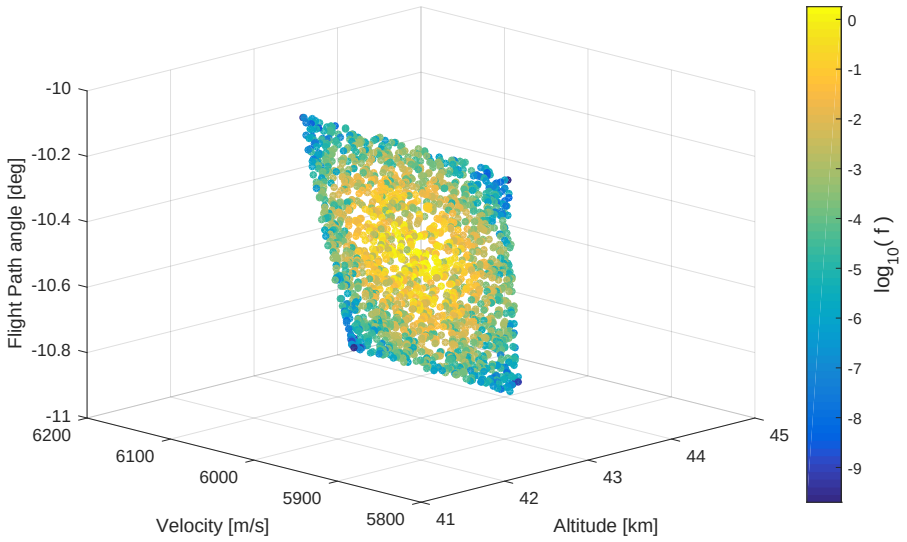

Figure 4-6: 2000 datapoints of the PDF of the state at $t = 30$ s generated using the DPP method. The color denotes the $\log_{10}$ of the probability density f.

Observing the figure carefully one can observe that the datapoints all lie in a plane. This is more clearly seen in Figure 4-7, which is a sideview of the same data. The initial state is uniformly sampled before propagation, so a scatter view of these samples will thus be a rectangular three-dimensional grid, a box-like shape. The figure shows an almost linear relation between the datapoints, which shows that the states get highly correlated after propagation.

In Figure 4-8, a scatter plot of the data is shown for in the final part of the trajectory. The figure shows that the correlation between the states increase with time. In addition, a second test is performed with a larger uncertainty in the initial states:

$$\begin{pmatrix} \sigma_R \\ \sigma_V \\ \sigma_\gamma \end{pmatrix} = \begin{pmatrix} 40.0 \text{ m} \\ 50.0 \text{ m/s} \\ \sqrt{10^{-3}} \text{ rad} \end{pmatrix} \tag{4-7}$$

The result for this case are shown in Figure 4-9. The figure shows that the data is dispersed in a more complex way than the results in Figure 4-6, which makes it more difficult to process the data. In the following sections, the methods and results will be discussed to obtain valuable information from these data samples.

4-2-4 Data Processing

A three-dimensional scatter view of the PDF contains a lot information about the distribution of the state and the correlation between the state variables. However, it is difficult to interpret such a plot or to obtain a statistic. Therefore, marginal distributions are generated, which represent the distribution of a subset or just one of the state variables.

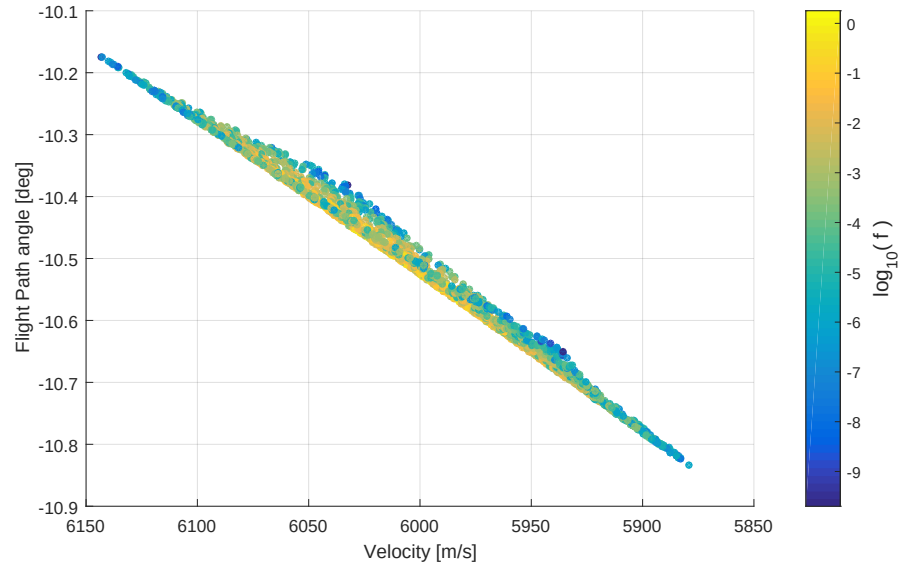

Figure 4-7: 2000 datapoints of the PDF of the state at $t = 30$ s generated using the DPP method. Sideview of the three-dimensional datapoints.

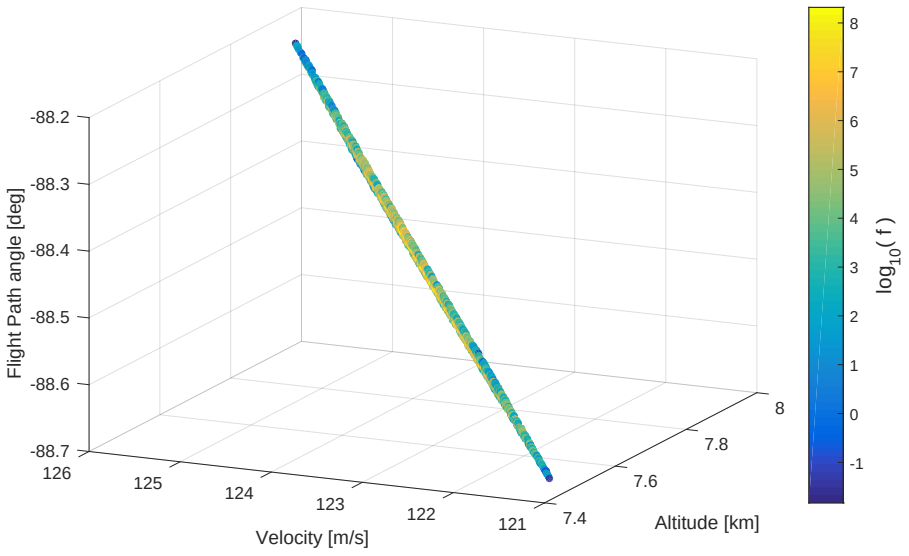

Figure 4-8: 2000 datapoints of the PDF of the state at $t = 150$ s generated using the DPP method for the small uncertainty case. The color denotes the $\log_{10}$ of the probability density f.

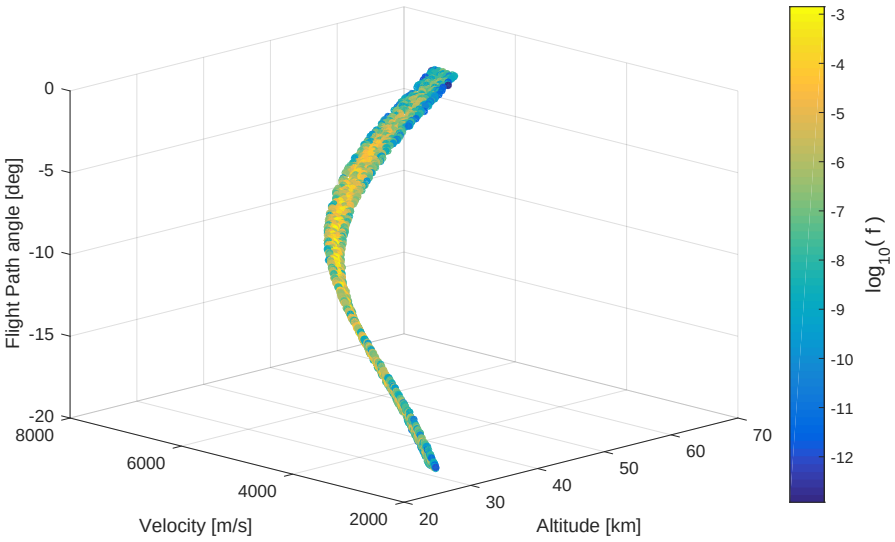

Figure 4-9: 2000 datapoints of the PDF of the state at $t = 30$ s generated using the DPP method for the large uncertainty case. The color denotes the $\log_{10}$ of the probability density f.

The DPP method results in a scattered dataset of points on the underlying PDF, however the functional expression of the PDF cannot be readily be obtained. Ideally, such a functional expression of the PDF is used to analytically integrate the function and obtain an expression of the marginal PDF. If an analytical definition is not possible, the function needs to be integrated numerically to obtain the marginal PDF. However, numerical integration is challenging for a larger number of dimensions. One of the goals of this research is to apply the method to a decay and entry problem that involves 12 or 13 state variables and uncertainty in the atmospheric density. This means that the PDF of the state will have a dimension of 13 or 14. Therefore, a potential method needs to be applicable for this large number of dimensions.

A functional definition of a multi-dimensional function is generally obtained using a curve fitting process, which involve a Radial Basis Function (RBF) or multi-variate splines. Multi-variate splines are multi-variate polynomials that are bounded by a certain range. Meshing techniques like triangulation are generally used to generate the region on which the splines are defined. This method provides accurate results for low-dimensional functions, but the method becomes challenging for high dimensions.

A method that is less sensitive to the dimensionality problem is to use RBFs to interpolate or approximate the data. The values of these functions are in principle dependent on the radial distance from their origin. The function approximation is then described as a weighted summation of RBFs (Lazzaro and Montefusco, 2002):

$$\tilde{f}(\boldsymbol{x}) = \sum_{i=1}^{N} c_i \phi(r) \tag{4-8a}$$

$$r = ||\boldsymbol{x} - \boldsymbol{x}_i|| \tag{4-8b}$$

where $\boldsymbol{x}_i$ is one of the independent variables of the data and $\phi(r)$ is the RBF. The approximation $\tilde{f}(\boldsymbol{x})$ essentially is a weighted summation of functions that are located at the datapoints $\boldsymbol{x}_i$. The coefficients c_i are chosen such that the function $\tilde{f}$ interpolates the values y_i of the PDF:

$$\tilde{f}(\boldsymbol{x}_i) = y_i \tag{4-9}$$

The coefficients can be solved directly by solving a system of linear equations (Lazzaro and Montefusco, 2002):

$$\boldsymbol{A}\boldsymbol{c} = \boldsymbol{y} \quad \text{with} \quad \boldsymbol{y} = \begin{pmatrix} y_1 \\ \vdots \\ y_n \end{pmatrix} \quad , \quad \boldsymbol{c} = \begin{pmatrix} c_1 \\ \vdots \\ c_n \end{pmatrix} \tag{4-10a}$$

$$\boldsymbol{A} = \begin{bmatrix} \phi(\boldsymbol{x}_1 - \boldsymbol{x}_1) & \phi(\boldsymbol{x}_1 - \boldsymbol{x}_2) & \dots & \phi(\boldsymbol{x}_1 - \boldsymbol{x}_n) \\ \phi(\boldsymbol{x}_2 - \boldsymbol{x}_1) & \phi(\boldsymbol{x}_2 - \boldsymbol{x}_2) & \dots & \phi(\boldsymbol{x}_2 - \boldsymbol{x}_n) \\ \vdots & \vdots & \ddots & \vdots \\ \phi(\boldsymbol{x}_n - \boldsymbol{x}_1) & \phi(\boldsymbol{x}_n - \boldsymbol{x}_2) & \dots & \phi(\boldsymbol{x}_n - \boldsymbol{x}_n) \end{bmatrix} \tag{4-10b}$$

where $\boldsymbol{y}$ is a vector of interpolation values y_i. This system has a unique solution for the coefficients if the interpolation matrix $\boldsymbol{A}$ is unique, which is the case if there are N distinct datapoints for specific RBFs. One of the commonly used RBF that results in a unique solution is the Gaussian RBF:

$$\phi(r) = \exp\left(-sr^2\right) \tag{4-11}$$

where s is a scaling parameter. Similarly to Kernel Density Estimation (KDE), the scaling parameter has an influence on the accuracy of the solution. From the equation it can be derived that the value of the function drops faster for a larger value of s.

The influence of the scaling parameter on the accuracy of the interpolator is shown in Figure 4-10. These figures are generated by interpolating three datapoints of a Gaussian distribution using Gaussian RBFs. The left figure illustrates that with only three datapoints, the function can be succesfully interpolated because the RBF interpolation and the Gaussian distribution overlap. However, if the scaling parameter is chosen too large, the interpolation is significantly less accurate, which is shown in the right figure. Therefore, it seems optimal to choose a large scaling parameter. However, a too small scaling parameter can cause numerical issues, because the system of equations that is solved to obtain the coefficients becomes ill conditioned. This can be explained by the fact that if the RBFs reduce very slowly with distance, each RBF provides an almost equal amount to each datapoint, so a large number of functions will be used to interpolate the value at each datapoint.

As one can see from Figure 4-10, the scaling parameter determines the width of each RBF. One can imagine that if the multi-dimensional data samples $\boldsymbol{x}_i$ are of different orders of magnitude for each dimension, the scaling should also be different for each dimension. If a radially symmetric RBF is used with one scaling parameter, the approximation of the function can contain errors in the dimensions for which the scaling parameter is not a suitable choice. Considering that the state variables are very different in orders of magnitude, it is expected that these problems will occur when reconstructing the PDF. Therefore, a RBF is used that is not radially symmetric, but accounts for the different scale for each dimension of the data:

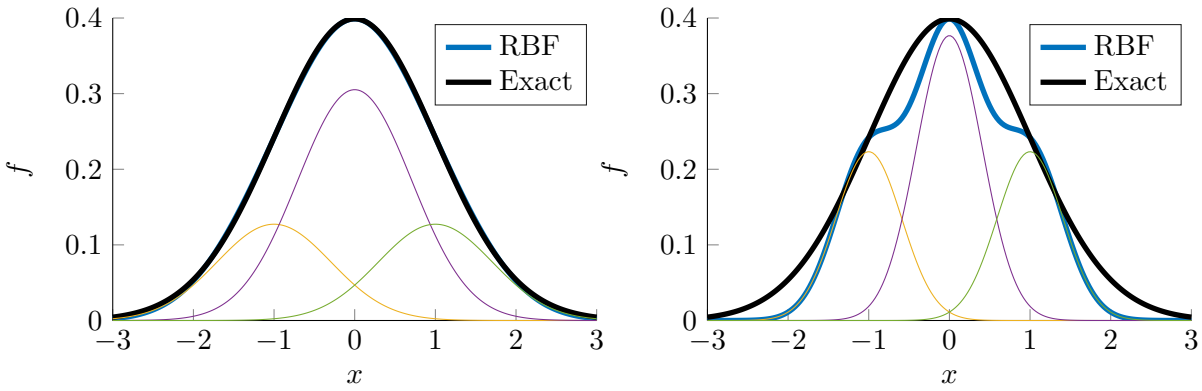

Figure 4-10: Illustration of RBF interpolation with $s = 1$ (left) and $s = 3$ (right).

$$\tilde{f}(\boldsymbol{x}) = \sum_{i=1}^{N} c_i \phi\left(\frac{x_1 - x_{1,i}}{\sigma_{x_1}}\right) \phi\left(\frac{x_2 - x_{2,i}}{\sigma_{x_2}}\right) \dots \phi\left(\frac{x_{N_s} - x_{N_s,i}}{\sigma_{x_{N_s}}}\right) \tag{4-12a}$$

where σ_{x_j} are the standard deviation of the data samples $\boldsymbol{x}_i$ for each dimension j. Essentially, this function is a multiplication of RBFs scaled with the standard deviation of the data samples for that particular dimension. Each RBF also contains a scaling parameter to control the solution.

This function definition is most suitable for data, which do not contain relations between the independent variables, because no relations are included in the function definition. If there is no relation between the independent variables the data is considered orthogonal. However, a large benefit of this representation is that an analytical expression for the marginal distributions can be obtained.

Results

The data presented in Figure 4-6 were used to obtain marginal distributions of the PDF using RBF interpolation. A Gaussian RBF was used to generate the marginal distributions, but no results could be obtained that were close to the solution obtained using Monte Carlo. The marginal distribution showed large oscillations and even became negative, which is not allowed for a PDF. The reason for this is that the interpolation matrix becomes ill conditioned, because Gaussian PDFs extent over all the data, so they all have an influence on the function value at each datapoint. As a result the solution becomes unstable.

In the research of Lazzaro and Montefusco (2002), it is acknowledged that this instability occurs for large datasets with globally supported RBFs. The use of compactly supported RBFs, which are only defined within a certain region, could partially overcome this problem. However, no significant improvement was obtained.

Because interpolation could not provide a stable and accurate result, additional attempts to obtain an accurate marginal distribution were performed using a Least-Squares optimization process, which included constraints. The definition of the RBFs allowed to compute the total integral of the function, so the coefficients are constraint such that the total integral of the

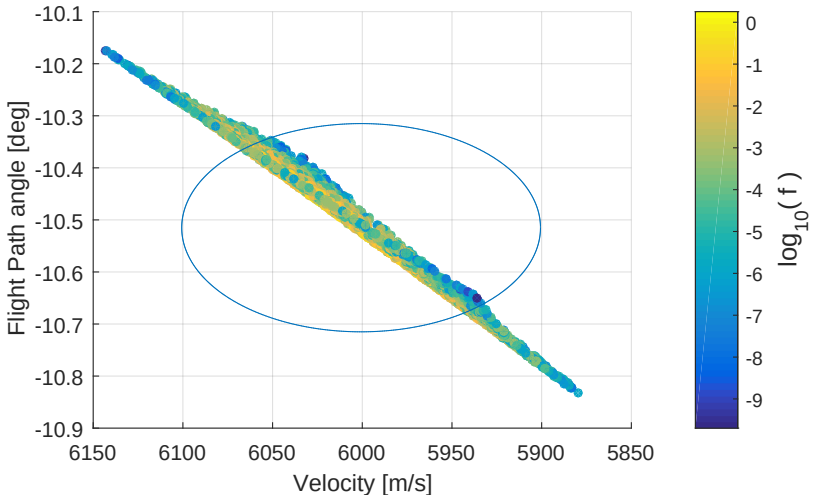

Figure 4-11: Data obtained from the DPP method and the bounds of a radial basis function that is used to approximate the function.

function is equal to one. The resulting marginal distribution still showed large oscillations and negative values, so a next test was performed in which the coefficients were constraint to be larger than zero. Although the distribution was positive, the oscillations did not reduce to a satisfactory level. In addition, a last test was performed in which the location of the RBFs and the scaling parameters were included in the optimization, but no satistfactory result was obtained.

The reason that these function fits were highly inaccurate is that the relations in the data are too large to obtain an accurate approximation of the function using the chosen representation. In Figure 4-11 the data are plotted with the bounds of a possible RBF that is used to approximate the data. Since the function only has a non-zero value at these datapoints, the RBF extents outside the range of the function. A possible solution would be to rotate this function such that it alligns with the data, however, this would require that the relation between the data is known. In Figure 4-9 it is shown that the plane of the data rotates, so for each RBF the local slope of the data needs to be determined. Considering the fact that the main problem of this research consists of 14 states with maybe even more complex relations in the data, this method will not be feasible to approximate the PDF.

These difficulties with fitting a large dataset of multi-dimensional data were also found in fundamental research on these numerical methods. In a recent study of Allasia et al. (2014), a new method is presented to integrate a function presented by scattered data. The relative integration errors that were obtained using the method are in the order of 0.01 for a function with 3 dimensions and a maximum error of 0.7 was observed with a function of 10 dimensions. This error is relatively large considering that the total integral of a PDF is 1. One could thus expect that it is very difficult to obtain an accurate marginal distribution using scattered data of a PDF with 14 dimensions.

4-2-5 The Binning Method

In the research of Halder and Bhattacharya (2011) an approximate method is used to generate marginal distributions. This method produces a histogram-like PDF that is obtained by determining the mean value of the PDF in each bin and subsequently normalizing the distribution. In an ideal situation where all the samples are uniformly distributed in the domain and the enclosed volume of the samples in each bin are equal, the function will approach the exact solution for an increasing number of samples. In this situation, the method is identical to Monte Carlo integration, which also approaches the exact solution for an increasing number of samples.

It is essential to understand that by binning the data, information is removed from the data. The location of the samples within the bin and the distribution of the data within the bin is not accounted for. Even though the initial state is uniformly sampled, the output states are not uniformly distributed, because the propagation process changes this distribution. In addition, the enclosed volume of the samples in each bin is generally not equal. This means that the assumptions that make the method valid are violated. Nevertheless, the output states are fairly uniformly distributed, as shown in Figure 4-6, so it is expected that reasonably accurate approximate results can be obtained.

Marginal distribution of the altitude that are obtained using this method are shown in Figure 4-12 and Figure 4-13 for the two cases discussed in Section 4-2-3 . The red line corresponds to the reference solution, which is a kernel density estimate obtained using Monte Carlo data. The orange line corresponds to a RBF interpolation solution of the bin values. The figures show that the binning method indeed approximates the exact solution, but the shape of the PDF is not similar. The binning method solution shows features that are not present in the reference solution.

The problem that the enclosed volume of the data in each bin is not equal can be partially mitigated by multiplying the method with the enclosed volume of the samples in each bin. If the samples are uniformly distributed in the enclosed volume, the method would then be equal to Monte Carlo integration. A measure of the enclose volume of the data in each bin can be obtained by determining the standard deviations for the data. Multiplying these standard deviations gives a measure of the enclose volume. This method will be employed in Chapter 9 to obtain results for statistical impact prediction.

4-2-6 Direct PDF Propagation vs Monte Carlo

The major advantage of the DPP method is that it propagates the uncertainty in an exact way. Since Monte Carlo needs a large number of samples to obtain an accurate result, it is thus expected that the DPP method can obtain a better solution with fewer samples. However, because it was found that it is difficult to accurately process the data that are obtained from the DPP method, an approximate method is used to process the data. Therefore, the accuracy of this approximate method needs to be evaluated.

An impact time distribution is obtained using 10^4 samples obtained from a MC simulation, which is used as a reference to compare with the DPP results. The DPP method is used to generate 2000 datapoints, which can be used to generate an impact time distribution using the binning method. Increasing the number of samples further for the DPP method is not

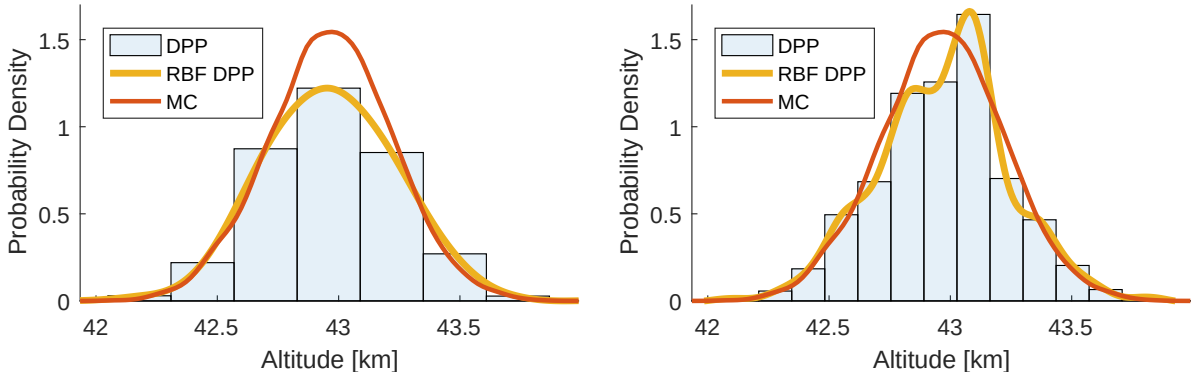

Figure 4-12: Marginal distributions of the altitude for the small-uncertainty case at $t = 30$ for 10 and 20 bins.

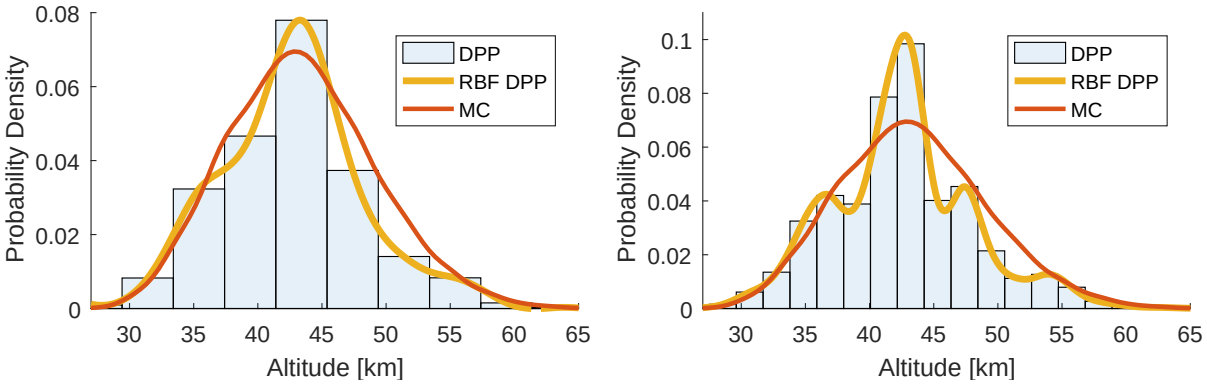

Figure 4-13: Marginal distributions of the altitude for the large-uncertainty case at $t = 30$ for 10 and 20 bins.

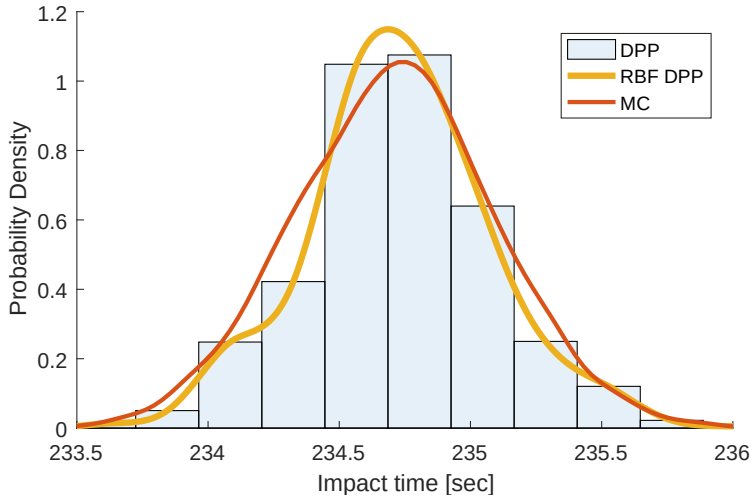

Figure 4-14: Impact time distributions for the small-uncertainty case generated using 10^4 Monte Carlo samples (orange) and 2000 DPP samples using 15 bins.

logical, because the benefit of the method is that a significantly fewer samples are required to obtain accurate results. These distributions are shown in Figure 4-14. The figure shows that the results obtained with both methods are similar.

In Figure 4-15 the results are shown for two simulations with the two uncertainty models discussed in Section 4-2-3. A distribution is shown that is obtained from 100 MC samples and a distribution is shown that is obtained using 100 DPP samples. The distributions obtained using MC simulations are very similar, so even for 100 samples an accurate result is obtained with the MC method. However, the result that is obtained from the DPP method is not similar to the reference solution. The width of the distribution is correctly approximated, but the shape of the distribution is clearly inaccurate.

The results were obtained with the same computation time, so this shows that the DPP method does not yield a more accurate solution within the same computation time if the binning method is used to post-process the data. Furthermore, the binning method results in an impact time window that is approximately the same, but the shape of the distribution could be totally inaccurate.

4-3 Conclusions

The analysis on the methods and the atmospheric entry problem described in this chapter has lead to a number of conclusions:

- The one-dimensional test cases showed that the numerical DPP method provides accurate results.
- Several limitations of the LSQKD method were found and it was concluded that the method cannot provide a sufficient accuracy for atmospheric entry problems.

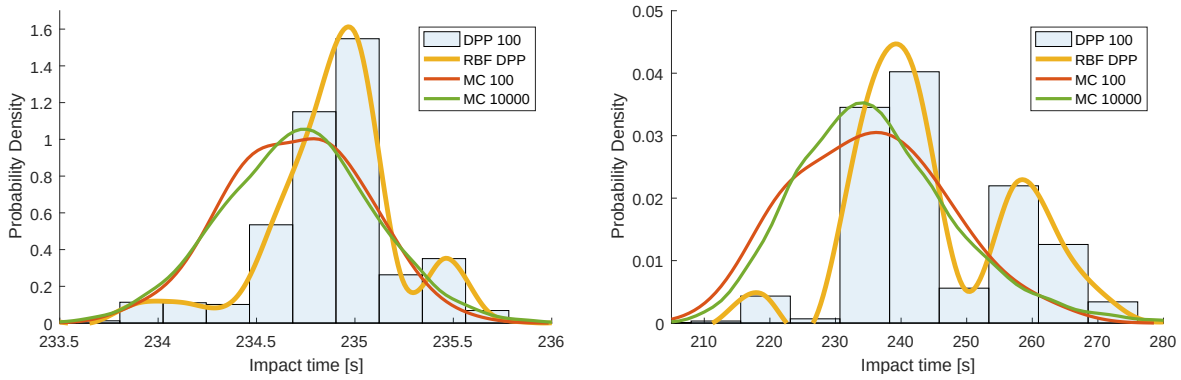

Figure 4-15: Impact time distributions of small-uncertainty case(left) and large-uncertainty case(right) obtained from 100 DPP samples and 100 and 10^4 MC samples.

- The DPP method results in scattered data of a multi-dimensional PDF, which are difficult to process.
- The binning method that is used in the research of Halder and Bhattacharya (2011) to process the DPP data is from a theoretical point of view incorrect. The method provides approximate results that approaches the true solution for some cases, but not all cases.

Chapter 5

Flight Dynamics and Models

This chapter describes the flight dynamics model that is used to simulate atmospheric entry trajectories. The chapter starts by explaining the reference frames (Section 5-1) and state variables (Section 5-2) after which the computation of angles are discussed in Section 5-3. The equations of motion, which are solved to determine the trajectory of the Delta-K rocket body will be discussed in Section 5-4. Several models are required in the equations of motion to determine the influence of the environment on the rocket body. The aerodynamic model is described in Section 5-5, the gravity model is discussed in Section 5-6, the atmosphere model is discussed in Section 5-7 and the Earth's shape and rotation model is discussed in Section 5-8.

5-1 Reference Frames

The state of the body and additional parameters are defined with respect to a reference frame. The reference frame that are used for the calculations are discussed in this section.

Earth Centered Inertial Reference Frame (I-frame)
This reference frame is a pseudo-inertial reference frame, because the velocity of the Earth is not exactly constant. The reference frame is defined using $J2000$ epoch, which is at 1.5 January 2000 (Montenbruck and Gill, 2001). This reference frame is shown in Figure 5-1.

Origin	Center of mass of the Earth.
X_I-axis	Intersects the point where the vernal equinox and the mean equator intersect.
Y_I-axis	Points in the direction of the angular velocity vector of the Earth.
Z_I-axis	Completes the right handed reference frame.

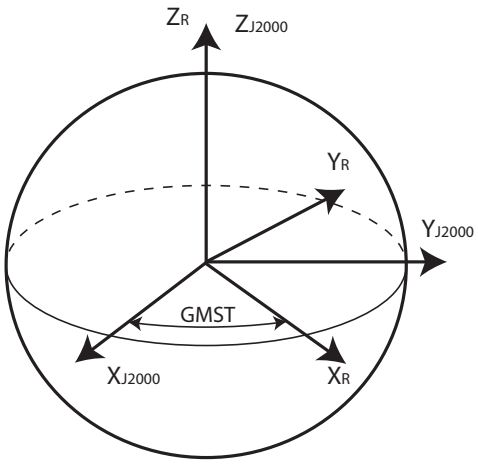

Figure 5-1: J2000 Reference frame and the R frame.

Earth Fixed Rotating Reference Frame (R-frame)
This frame is co-rotating with the Earth with a rotational velocity ω_E provided in Section 5-8.

Origin	Center of mass of the Earth.
X_R-axis	Directed towards a reference meridian of the Earth, called the Greenwich meridian.
Y_R-axis	Completes the right handed reference frame.
Z_R-axis	Directed towards the North parallel to the Earth's spin axis.

Vertical frame (V-Frame)
The frame is oriented such that locally horizontal plane is formed with respect to the Earth.

Origin	At the center of mass of the spacecraft or body of interest.
X_V-axis	This axis is placed in the local meridian plane. This axis points in the north direction.
Y_V-axis	Completes the right handed reference frame. This axis points in the east direction.
Z_V-axis	Directed towards the center of mass of the Earth. This axis points in the downward direction.

Body reference frame (B-Frame)
The body frame is fixed to the Delta-K rocket body and used to model the attitude of the body. The axis coincide with the principle axis of inertia.

Origin	At the center of mass of the spacecraft or body of interest.
X_B-axis	Directed in the forward direction and lies in the plane of symmetry of the Delta-K rocket body.
Y_B-axis	This axis is directed such that it coincides with the large pressure spheres of the Delta-K body, which is the same the definition used by Ronse (2013)
Z_B-axis	Completes the right handed reference frame.

Trajectory reference frame (T-Frame)
A frame related the direction of the velocity. No distinction is made between airspeed and groundspeed, because it is assumed that there is no wind.

Origin	At the center of mass of the spacecraft or body of interest.
X_T-axis	Pointing in the direction of the velocity with respect to the Earth.
Y_T-axis	Completes the right handed reference frame.
Z_T-axis	Placed in the vertical plane and is directed downwards.

Aerodynamic reference frame (A-Frame)
This reference frame is alligned with the opposite direction of the aerodynamic forces.

Origin	At the center of mass of the spacecraft or body of interest.
X_A-axis	In the direction of the velocity with respect to the Earth, and opposite to the drag force.
Y_A-axis	Completes the right handed reference frame.
Z_A-axis	Directed in the opposite direction of the aerodynamic lift force.

Frame transformations between these reference frames are performed using the transformations that are specified in Mooij (2014).

5-2 State Variables

The state of the body is described by a set of state variables. These state variables are described in this section.

5-2-1 Translational State

The position of the Delta-K rocket body is described using a set of spherical coordinates. These variables are prefered over other options, because they are the variables of interest for impact prediction. Transforming PDFs to a different set of variables, as described in Section 3-3, is a difficult task and can be infeasible for some transformations. Therefore, it is highly advantageous if no additional transformations are required after propagating the PDF of the state.

The position of the body is defined using a radius R that is the distrance between the body and the center of mass of the Earth. A longitude angle τ, which is defined as the angle between the local meridian and the prime meridian or Greenwich meridian, positively defined in the direction of motion of the Earth. The latitude δ is defined as the angle between the equatorial plane and the radius vector.

$$\boldsymbol{r} = \begin{pmatrix} R \\ \tau \\ \delta \end{pmatrix} \tag{5-1}$$

The velocity vector of the body is composed of the velocity components defined in the V-frame:

$$\boldsymbol{V}_G = \begin{pmatrix} V_R \\ V_\tau \\ V_\delta \end{pmatrix} \tag{5-2}$$

These components are displayed in Figure 5-2. Because the V-frame is rotating with the Earth, the velocity is a ground velocity. The heading angle χ and flight path angle γ define the direction of the velocity of the body. These angles can be calculated using the following equations (Mooij, 1994):

$$V_G^2 = V_\delta^2 + V_\tau^2 + V_R^2 \tag{5-3a}$$

$$\gamma_g = \arcsin\left(\frac{V_R}{V_g}\right) \tag{5-3b}$$

$$\chi_g = \arctan\left(\frac{V_\tau}{V_\delta}\right) \tag{5-3c}$$

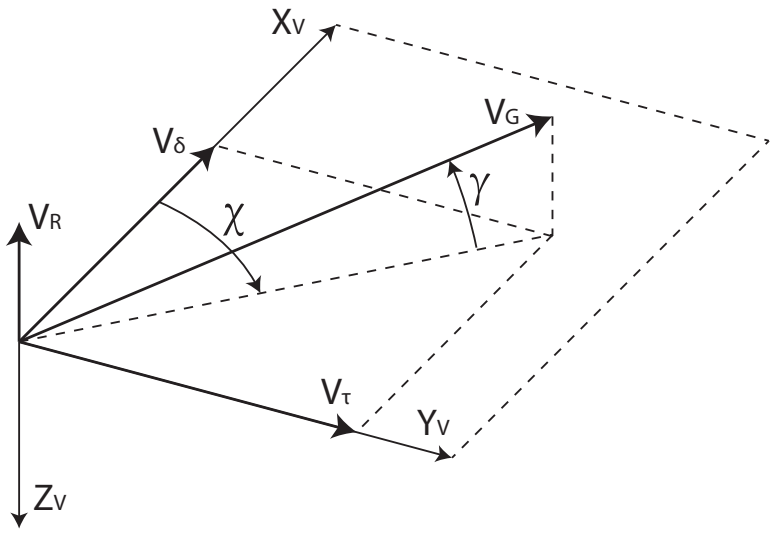

Figure 5-2: Local vertical local horizontal reference frame with velocity components.

5-2-2 Rotational State

The rotational state of the body is defined using the attitude and the rotational velocity. The attitude of the body is defined as the orientation of the body frame with respect to the Earth inertial frame. The attitude can thus be defined as a transformation matrix $\boldsymbol{C}_{I,B}$ between the body frame and the Earth inertial frame.

This rotation matrix can be defined using Euler angles, quaternions or other parameters. Quaternions are used during this thesis, because the kinematic equations do not include a singularity and they are linear.

Quaternions are defined using Euler's theorem, which states that any rotation can be described by one angular rotation about the Euler eigenaxis. The quaternion vector is defined using this axis and the angle of rotation θ:

$$\boldsymbol{q} = \begin{pmatrix} q_1 \\ q_2 \\ q_3 \\ q_4 \end{pmatrix} = \begin{pmatrix} e_1 \sin(\theta/2) \\ e_2 \sin(\theta/2) \\ e_3 \sin(\theta/2) \\ \cos(\theta/2) \end{pmatrix} \tag{5-4}$$

where e_1, e_2, e_3 are the components of the Euler eigenvector. The Euler eigenaxis has, by definition, a unit length, so the following constraint must hold for the quaternion vector:

$$q_1^2 + q_2^2 + q_3^2 + q_4^2 = 1 \tag{5-5}$$

These quaternion elements represent the attitude of the body, given that the constraint is satisfied. These elements can be converted to a direction cosine matrix $\boldsymbol{C}_{I,B}$ to perform transformations:

$$\boldsymbol{C}_{I,B} = \begin{bmatrix} 1-2(q_2^2+q_3^2) & 2(q_1q_2+q_3q_4) & 2(q_1q_3-q_2q_4) \\ 2(q_2q_1-q_3q_4) & 1-2(q_1^2+q_3^2) & 2(q_2q_3+q_1q_4) \\ 2(q_3q_1+q_2q_4) & 2(q_3q_2-q_1q_4) & 1-2(q_1^2+q_2^2) \end{bmatrix} \tag{5-6}$$

which represents the orientation of the B-frame with respect to the I-frame. The rotational velocity ω of the body is expressed in the body frame and consists of three components:

$$\boldsymbol{\omega} = \begin{pmatrix} \omega_1 \\ \omega_2 \\ \omega_3 \end{pmatrix} \tag{5-7}$$

5-3 Reference Angles

Several reference angles are required to perform the computations. The calculation of the aerodynamic angles and the angle between the inertial frame and the Earth fixed frame are discussed in this section.

5-3-1 Aerodynamic Angles

The aerodynamic angles angle of attack, α, angle of sideslip, β, and bank angle, σ, are required to determine the aerodynamic forces expressed in the used reference frame. These angles are defined as a set of Euler angles defining the orientation of the aerodynamic reference frame to the body frame.

The aerodynamic angles can be obtained from the transformation matrix between the body frame and the trajectory frame $\boldsymbol{C}_{T,B}$. This matrix can be determined using the following frame transformations (Mooij, 1994):

$$\boldsymbol{C}_{T,B}(\alpha,\beta,\sigma) = \boldsymbol{C}_{T,V}(\gamma,\chi)\boldsymbol{C}_{V,B}(\tau,\delta,t,\boldsymbol{q}) = \boldsymbol{C}_{T,A}(\sigma)\boldsymbol{C}_{A,B}(\alpha,\beta) \tag{5-8a}$$

$$\boldsymbol{C}_{V,B}(\tau, \delta, t, \boldsymbol{q}) = \boldsymbol{C}_{V,R}(\tau, \delta)\boldsymbol{C}_{R,I}(\theta_G)\boldsymbol{C}_{I,B}(\boldsymbol{q}) \tag{5-8b}$$

The aerodynamic angles are extracted from this frame transformation matrix using the following equations:

$$\alpha = \arctan\left(\frac{\boldsymbol{C}_{T,B}(1,3)}{\boldsymbol{C}_{T,B}(1,1)}\right) \tag{5-9a}$$

$$\beta = \arcsin\left(\boldsymbol{C}_{T,B}(1,2)\right) \tag{5-9b}$$

$$\sigma = -\arctan\left(\frac{\boldsymbol{C}_{T,B}(3,2)}{\boldsymbol{C}_{T,B}(2,2)}\right) \tag{5-9c}$$

5-3-2 Vernal Offset / Greenwich Mean Sidereal Time

The vernal offset is the angle between the Earth inertial reference frame and the Earth fixed reference frame. This parameter is important for the attitude dynamics of the body, because the attitude is defined with respect to the inertial reference frame.

The rotation of the Earth and time are closely related, because some time systems that are used are based on the rotation of the Earth. Universal Time (UT1) is the time system that is currently used as a mean solar time scale. This time system is defined such that the average length of the solar day equals 24 hours. The UT1 time system is defined using the Greenwich Mean Sidereal Time (GMST), which is defined as the mean sidereal time at the Greenwich meridian. The GMST can be used to determine the vernal offset angle, however the TLE data is published with a julian day fraction, which corresponds to a UT1 time value. Therefore, the GMST can be calculated using the UT1 time (Montenbruck and Gill, 2001):

$$\begin{aligned}\mathrm{GMST}_{sec} = \; & 24110.54841 + 8640184.812866 \cdot T_0 \\ & + 1.002737909350795 \cdot \mathrm{UTl} + 0.093104 \cdot T^2 - 6.2 \cdot 10^{-6} \cdot T^3\end{aligned} \tag{5-10a}$$

$$T_0 = \frac{\mathrm{JD}(0^{\mathrm{h}}\mathrm{UT1}) - 2451545}{36525} \tag{5-10b}$$

$$T = \frac{\mathrm{JD}(\mathrm{UT1}) - 2451545}{36525} \tag{5-10c}$$

where T_0 equals the amount of centuries since the $J2000$ epoch at 0 hr UT1 and T equals the amount of centuries since the $J2000$ epoch at the current time. This equation calculates the GMST in seconds, which can be converted to the vernal offset angle θ_G using the following equation:

$$\theta_G = 2\pi \mod (\mathrm{GMST}, 86400) \tag{5-11}$$

Using these equations, it can be found that the vernal offset is equal to $\theta_G = 280.46$ deg at the $J2000$ epoch.

5-4 Equations of Motion

The evolution of the state variables, thus the trajectory of the Delta-K body, is governed by the equations of motion. The state of the body is described by the following set of state variables:

$$\boldsymbol{X} = \boldsymbol{F}(\boldsymbol{X}) \tag{5-12a}$$

$$\boldsymbol{X} = \begin{pmatrix} R & \tau & \delta & V_R & V_\tau & V_\delta & q_1 & q_2 & q_3 & q_4 & \omega_1 & \omega_2 & \omega_3 \end{pmatrix}^T \tag{5-12b}$$

The equations of motion are differential equations that govern the evolution of the state variables in time. The equations of motion that are used to solve the trajectories of the Delta-K body are discussed in the following subsections.

5-4-1 Translational State

The position of the body is described using spherical coordinates and they are related to the velocity of the body using the following kinematic equations (Mooij, 1994):

$$\frac{dR}{dt} = V_R \tag{5-13a}$$

$$\frac{d\tau}{dt} = \frac{V_\tau}{r\cos\delta} \tag{5-13b}$$

$$\frac{d\delta}{dt} = \frac{V_\delta}{r} \tag{5-13c}$$

The dynamic equations relate the external forces with the velocity of the body:

$$\frac{dV_R}{dt} = -\frac{F_{z,V}}{m} + 2\omega_E V_\tau \cos\delta + \omega_E^2 R\cos^2\delta + \frac{V_\tau^2 + V_\delta^2}{R} \tag{5-14a}$$

$$\frac{dV_\tau}{dt} = \frac{F_{y,V}}{m} - 2\omega_E \left(V_R\cos\delta - V_\delta\sin\delta\right) + \frac{V_\tau}{R}\left(V_\delta\tan\delta - V_R\right) \tag{5-14b}$$

$$\frac{dV_\delta}{dt} = \frac{F_{x,V}}{m} - 2\omega_E V_\tau \sin\delta - \omega_E^2 R\sin\delta\cos\delta - \frac{V_\tau^2\tan\delta + V_\delta V_R}{R} \tag{5-14c}$$

The external forces in these equations are described by a force vector $\boldsymbol{F}_V$ expressed in the V-frame. This force vector is composed of an aerodynamic force $\boldsymbol{F}_{A,V}$ and a gravitational force $\boldsymbol{F}_{G,V}$:

$$\boldsymbol{F}_V = \begin{pmatrix} F_{x,V} \\ F_{y,V} \\ F_{z,V} \end{pmatrix} = \boldsymbol{F}_{G,V} + \boldsymbol{F}_{A,V} \tag{5-15}$$

The gravitational force $\boldsymbol{F}_G$ is determined using the gravity model (Section 5-6).

where the frame transformation matrix $\boldsymbol{C}_{V,R}$ is used as described in Section 5-1. The aerodynamic force $\boldsymbol{F}_A$ is determined using the aerodynamic model (Section 5-5). This force is expressed in the aerodynamic frame and also transformed to the V-frame:

$$\boldsymbol{F}_{A,V} = \boldsymbol{C}_{V,AG}(\gamma,\chi,\sigma)\boldsymbol{F}_{A,AG} \tag{5-16a}$$

$$\boldsymbol{C}_{V,AG} = \boldsymbol{C}_{V,TG}(\gamma, \chi)\boldsymbol{C}_{TG,AG}(\sigma) \tag{5-16b}$$

The flight-path angle γ and the heading angle χ are calculated using Equation (5-3b) and Equation (5-3c). The bank angle σ is derived using a series of frame transformations described in Section 5-1. In these equations of motion it is assumed that there is no wind, so the airspeed is equal to the ground speed. Furthermore, the velocity components are expressed in the V-frame, so they are defined with respect to the rotating Earth.

5-4-2 Rotational State

The attitude of the body evolves in time due to the rotation of the body. The attitude of the body is described by quaternions, which are propagated in time using the following kinematic equations (Mooij, 1994):

$$\begin{pmatrix} \dot{q}_1 \\ \dot{q}_2 \\ \dot{q}_3 \\ \dot{q}_4 \end{pmatrix} = \frac{1}{2} \begin{bmatrix} q_4 & -q_3 & q_2 \\ q_3 & q_4 & -q_1 \\ -q_2 & q_1 & q_4 \\ -q_1 & -q_2 & -q_3 \end{bmatrix} \begin{pmatrix} \omega_1 \\ \omega_2 \\ \omega_3 \end{pmatrix} \tag{5-17}$$

The moments that act on the body cause an angular acceleration, which can be calculated using the following equation (Mooij, 1994):

$$\dot{\boldsymbol{\omega}} = I^{-1}(\boldsymbol{M_B} - \boldsymbol{\omega} \times I\boldsymbol{\omega}) \tag{5-18}$$

$$\dot{\boldsymbol{\omega}} = \begin{pmatrix} (M_1 + (I_{22} - I_{33})\omega_2\omega_3)/I_{11} \\ (M_2 + (I_{33} - I_{11})\omega_2\omega_3)/I_{22} \\ (M_3 + (I_{11} - I_{22})\omega_2\omega_3)/I_{33} \end{pmatrix} \tag{5-19}$$

where $\boldsymbol{M}_B$ is a vector of moments acting on the body defined in the body-fixed frame. Only the aerodynamic moments are taken into account, because other moments are much smaller in magnitude. The aerodynamic moment is calculated using the aerodynamic model (Section 5-5).

5-5 Aerodynamic Model

The aerodynamic forces and moments on the Delta-K rocket body are modeled using an aerodynamic database that is used to derive aerodynamic coefficients. The aerodynamic forces are defined in the aerodynamic frame and calculated using the following equations:

$$\boldsymbol{F}_{A,A} = \frac{1}{2}\rho V_g^2 \boldsymbol{C}_{F,A} S_{ref} \tag{5-20a}$$

$$\boldsymbol{C}_{F,A} = \begin{pmatrix} C_D \\ C_S \\ C_L \end{pmatrix} \tag{5-20b}$$

The aerodynamic moments are calculated in the body frame:

$$\boldsymbol{M}_A = \frac{1}{2}\rho V_g^2 \boldsymbol{C}_{M,B} S_{ref} L_{ref} \tag{5-21a}$$

$$\boldsymbol{C}_{M,B} = \begin{pmatrix} C_l \\ C_m \\ C_n \end{pmatrix} \tag{5-21b}$$

The aerodynamic database is table of aerodynamic coefficients as a function of the angle of attack α, angle of sideslip β and the Mach number M. This database was generated in the work of Ronse (2013). The angle of attack, angle of sideslip and Mach number are sampled from a rectangular grid with the properties described in Table 5-1. For each of these datapoints, the aerodynamic coefficients are provided in the database.

Table 5-1: Properties of the aerodynamic database.

		Minimum	**Maximum**	**Datapoints**	**Spacing**
Angle of attack	α	$-\pi$	$+\pi$	30	12.41 deg
Angle of sideslip	β	$-\pi/2$	$\pi/2$	15	12.86 deg
Mach number	M	10	48	20	2

In the research of Ronse (2013), two aerodynamic databases were generated, one for the continuum flow regime and one for the rarefied flow regime. Based on the Knudsen number Kn, it is determined if the body is in the continuum flow regime, transition regime or the rarefied flow regime. The Knudsen number is calculated using the following equation:

$$K_n = \frac{\lambda}{L_{ref}} \tag{5-22}$$

A bridging function $F(Kn)$ is used to calculate the aerodynamic coefficients in the transition regime. In the research of Ronse (2013), it was found that the shuttle bridging function was the most accurate compared to wind tunnel data. Using the shuttle function, the aerodynamic coefficient C_X in the transition regime can be calculated using the following equations:

$$F(Kn) = \frac{C_X - C_{X_{MN}}}{C_{X_{FM}} - C_{X_{MN}}} \tag{5-23a}$$

$$F(Kn) = \begin{cases} 0 & \text{if } Kn \leq 10^{-3} \\ \sin^2\left(\pi \frac{3+\log_{10}(Kn)}{8}\right) & \text{if } 10^{-3} < Kn < 10 \\ 1 & \text{if } Kn \geq 10 \end{cases} \tag{5-23b}$$

where $C_{X_{MN}}$ is the coefficient in the continuum regime and $C_{X_{FM}}$ is the coefficient in the free molecular regime.

The following properties of the Delta-K body were used to generate the aerodynamic database and to calculate the aerodynamic force and moment:

$$S_{ref} = 0.85^2\pi \text{ m}^2$$

$$L_{ref} = 6 \text{ m}$$

The coefficients are defined on a multi-dimensional rectangular grid defined using the properties specified in Table 5-1. Therefore, linear interpolation is used to determine the aerodynamic coefficients for each occuring orientation.

5-6 Gravity Model

The major causes of a body to enter the atmosphere of a planet is the graviational acceleration. Therefore, accurate predictions of the trajectory and the impact location require a gravity model that is sufficiently accurate.

The major part of the gravitational acceleration is modeled using the central gravity field model, which models the gravity field as the gravity field of a point mass. This means that the gravitational acceleration is only directed towards the center of the Earth and only dependent on the radial distance from the center of the Earth.

This model can be improved using Spherical Harmonics, which can be used to account for the non-spherical mass distribution of the Earth. The spherical harmonics model of the Earth contains a large number of terms to account for local variations in the gravity field. Of these terms, the J_2 term has the most important contribution, which is about 400 times larger than the others. A simple integration of the maximum acceleration caused by the J_2 term results in an error in the impact location of 50 km, which means that the other gravity terms cause errors in the order of meters. Therefore, it is decided that only the J_2 gravity term is included in the gravity field model. The gravitational acceleration can be calculated using the following equation (Mooij, 1994):

$$\boldsymbol{a}_{G,V} = \frac{\mu}{R^2} \begin{pmatrix} -3J_2 \left(\frac{R_e}{R}\right)^2 \sin\delta\cos\delta \\ 0 \\ 1 - \frac{3}{2}J_2 \left(\frac{R_e}{R}\right)^2 (3\sin^2\delta - 1) \end{pmatrix} \tag{5-24}$$

The gravitational constant of the Earth is equal to (WGS, 2000):

$$\mu_{Earth} = 398600.4418 \text{ km}^3/\text{s}^2$$

The J_2 constant of the gravity field is defined as (WGS, 2000):

$$J_2 = 1082.629821313305 \cdot 10^{-6}$$

5-7 Atmosphere Model

The NRLMSISE-00 atmosphere model is used to provide the atmosphere properties to the trajectory simulator. This model is chosen, because an extensive analysis has shown that the model accurately represents the Earths atmosphere for a variety of conditions (Picone et al., 2002). In addition, the research of Ronse (2013) showed that accurate impact predictions could be obtained using this model.

The NRLMSISE-00 atmosphere model is an empirical model of the atmosphere that provides the atmospheric properties in all the altitude regimes. The model is an improvement on the Mass Spectrometer Incoherent Scatter class of models. The model is derived by fitting parametric equations to an extensive database covering a large variety of conditions and locations in the atmosphere. The required input parameters are displayed in Table 5-2. As shown in the table, the model is dependent on the location, time and solar activity, which influences the solar flux and geomagnetism. The Solar activity and geomagnetic index are obtained from Kelso (2016). The model outputs the temperature, the total mass density and the number densities for each constituent shown in Table 5-3.

Table 5-2: Input parameters of the NRLMSISE-00 atmosphere model.

Input	**Symbol**	**Unit**
Longitude	τ	deg
latitude	δ	deg
Altitude	h	m
Daily solar flux	$F_{10.7}$	W/m^2
81-day average daily flux	$\bar{F}_{10.7}$	W/m^2
Geomagnetic index	A_P	
Day of year	-	day
Seconds of day (UT1)	-	s
Local apparent Solar time	lst	hr

Picone et al. (2002) have performed an extensive comparison of the NRLMSISE-00 model with the MSISE-90 and Jacchia-70 models and concluded that the NRLMSISE-00 model is an improvement on these models. In the comparison it was also found that the NRLMSISE-00 model overestimates the density for lower altitudes and underestimates the density at higher altitudes. However, the bias that was obtained is very small.

The composition of the atmosphere is such that it exists of multiple particles with different properties. The composition of the atmosphere is provided by the NRLMSISE-00 model by providing the number density of each molecule. The number density is defined as the number of molecules per unit volume and is related to the mass density ρ by the mass of a single particle m (Chapman and Cowling, 1970):

$$n = \frac{\rho}{m} \tag{5-25}$$

The mean molar mass can be calculated using the number density of each constituent n_i and the molar mass of each molecule M_i (Cengel and Boles, 2004):

$$M = \frac{1}{n_m} \sum M_i n_i \tag{5-26}$$

where n_m is the summation of the number densities of the molecules in the gas mixture.

The speed of sound is calculated using the following equation(Regan and Anandakrishnan, 1993):

$$a = \sqrt{\gamma R T} \tag{5-27}$$

Where the temperature T is obtained from the NRLMSISE-00 model and the specific heat ratio γ is set to 1.4. The specific heat ratio actually varies with altitude, but it varies only little and the effect is relatively small. Therefore, it is chosen to use a constant value of the specific heat ratio. The specific gas constant R can be obtained by dividing the absolute gas constant R_{abs} with the mean molar mass M:

$$R = \frac{R_{abs}}{M} \tag{5-28}$$

where R_{abs} is equal to (NIST, 2016):

$$R_{abs} = 8.3144598 \text{ J/mol K}$$

The mean free path λ is used to determine in which aerodynamic regime the body is in. The mean free path is defined as the mean distance between collisions of a molecule. It is calculated using the following equation (Chapman and Cowling, 1970; Regan and Anandakrishnan, 1993):

$$\lambda = \left(\sqrt{2}\pi\sigma^2 n\right)^{-1} \tag{5-29}$$

where σ is the molecule diameter and n is the number density of the gas. The molecular diameter of each constituent in the atmosphere is provided in Table 5-3[1]. The mean free path is calculated by using the average number density $\bar{n}$ and the weighted average of the particle diameter $\bar{\sigma}$ where the number densities are used as weights ((Regan and Anandakrishnan, 1993)):

$$\bar{n} = \frac{1}{N}\sum_{i=1}^{N} n_i \tag{5-30a}$$

$$\bar{\sigma} = \sum_{i=1}^{N} \frac{n_i \sigma_i}{n_{tot}} \tag{5-30b}$$

Table 5-3: Molecule diameter σ for the constituents in the atmosphere (Ronse, 2013).

Constituent	σ [pm $= 10^{-12}$ m]
Ar	340
H	260
He	256
N_2	370
O_2	358
N	290
O	280

The local solar time is computed by adding the solar time difference between the greenwich meridian and the current location using the longitude τ:

$$t_{LS} = \text{GMST}_{\text{hrs}} + \frac{\pi}{12}\tau \tag{5-31}$$

[1]National Physical Laboratory: `http://www.kayelaby.npl.co.uk/general_physics/2_2/2_2_4.html`; date accessed: 15-08-2016

5-8 Earth Shape and Rotation Model

The shape of the Earth is such that the radius is larger at the Equator than at the poles. Therefore, the Earth's surface can be approximated using an oblate spheroid model. The radius from the center of the Earth to the Earth's surface can then be approximated using the following equation (WGS, 2000):

$$R_S = R_E \left(1 - e \sin^2 \delta\right) \tag{5-32}$$

where R_E is the equatorial radius and e is the ellipticity of the Earth. The following values are used to model the Earth's surface (WGS, 2000):

$$R_E = 6378.137 \text{ km}$$
$$e = 3.3528 \cdot 10^{-3}$$

The rotational velocity ω_E of the Earth is assumed to be constant and set to (WGS, 2000):

$$\omega_E = 7.292115 \cdot 10^{-5} \text{ rad/s}$$

Chapter 6

Uncertainty Model

Uncertainty is present in the impact predictions, because uncertainty is present in the initial state of the rocket body and the models that are used to propagate this state in time. An accurate model of the uncertainty in the initial states and environment models is required, to obtain accurate statistics and probability measures. Uncertainty is considered in the initial translational state and rotational state, and in the atmospheric density that is generated using the NRLMSISE-00 model (Section 5-7), because it has been shown that accurate predictions can be made when considering only uncertainty in these parameters (Ronse, 2013). This chapter starts with describing the uncertainty model for the translational state in Section 6-1. Subsequently, the uncertainty model of the rotational state (Section 6-2), and the uncertainty model of the atmospheric density (Section 6-3) are discussed. The chapter is concluded with a discussion on how these model are connected form a joint uncertainty model (Section 6-4), and a discussion on the uncertainty in the uncertainty model (Section 6-5).

6-1 Translational state

The uncertainty in the initial translational state is modelled by statistically evaluating the error of the TLEs that are used to generate the initial position. This section describes how the uncertainty model of the translational state is derived.

In the research of Ronse (2013) it was assumed that the initial position has a uniform distribution and a covariance matrix was used to model the correlation structure between the variables. In the research of Yim and Chung (2012) two covariance matrices were derived, which were used in the research of Ronse (2013) to define the covariance matrix of the Delta-K body. The two covariance matrices were derived using TLEs of a rocket body and a satellite at 700 km altitude. The covariance matrix of the Delta-K body was derived by taking the average of the two matrices.

It was observed that the two covariance matrices that were used to derive the final covariance matrix have some elements that have an opposite sign. Therefore, taking the average of the two matrices will cause that some elements cancel each other out. Such an operation

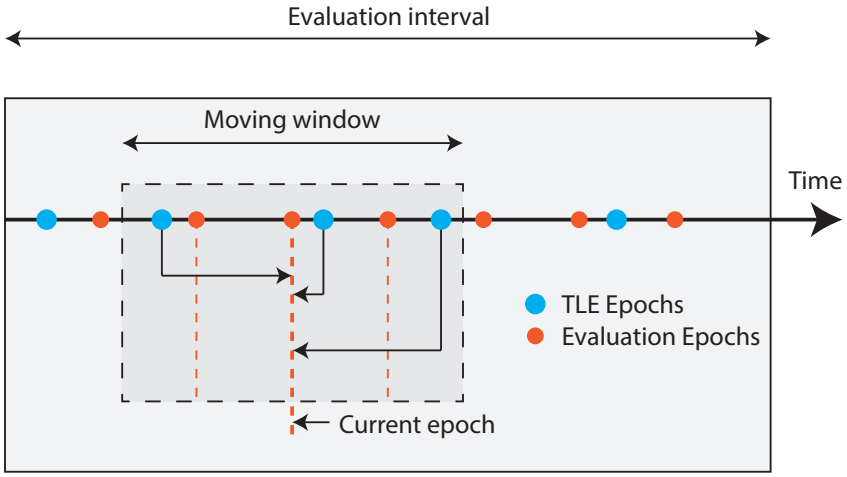

Figure 6-1: Visualization of TLE propagation for the TLE Pair-Wise Differencing method.

cannot be performed, because the two original matrices clearly show a correlation in some elements, which are not present in the average of the two matrices. In addition, the simulations of the decay of the Delta-K body start at 200 km in the simulations in this research. A covariance matrix derived at 700 km altitude may not be representative for the error at 200 km. Therefore, it is concluded that this covariance matrix cannot be used to model the initial uncertainty.

6-1-1 TLE Pair-Wise Differencing

The TLEs are generated using an orbit fitting proces using observations of the translational state of the body. Ideally, one needs the observations to model the uncertainty in the TLE. However, the process that is used to derive the TLEs and the original data is not known. Therefore, a method called TLE pair-wise differencing is used to obtain data that can be used to derive an uncertainty model. A similar method is also used by Osweiler (2006); Yim and Chung (2012).

The method uses the Simplified General Perturbations-4 (SGP4) model to propagate several TLEs to a certain epoch at which the results are compared to determine the uncertainty in the TLEs. An illustration of the method is shown in Figure 6-1. As shown in the figure, a certain evaluation interval is chosen in which the error in the TLEs is determined. Several evaluation epochs are defined on this interval at which the TLEs are compared. A moving window is defined, which is centered on the current epoch at which the TLEs are compared. All the TLEs that are available within this window are propagated towards the current epoch and the results are pair-wise substracted to determine the error. This process is performed for all the evaluation epochs within the evaluation interval (Geul et al., 2016).

The errors that are obtained at each evaluation interval are combined to obtain an estimate of the statistical distribution of the error in the initial state.

Considerations and Settings

To generate an accurate uncertainty model of the initial state using TLE pair-wise differencing, several considerations needs to be taken into account. One must realize that propagating the TLEs in time, also propagates the uncertainty in the initial state, which is similar to the methods discussed in Chapter 3. This means that the propagation process changes the uncertainty in the state.

Because the TLEs are propagated in time, the uncertainty in the state will increase. Therefore, if a large moving window width is chosen, large propagation times are allowed and the uncertainty of the state is changed during the propagation time. The initial uncertainty cannot be directly reconstructed, because the propagation process has changed the correlation structure and the magnitude of the uncertainty. Simulations have confirmed that the uncertainty increases with increasing propagation time, so the moving window width needs to be chosen as small as possible considering that the window contains enough TLEs to perform the comparison.

The choice of the evaluation epochs is important, because the errors can depend on the position of the body in its orbit (Geul et al., 2016). This dependence is caused by perturbations that are dependent on the location of the body and other parameters that are dependent on the location. Therefore, the evaluation epochs need to be chosen at approximately the same location as the initial state. One can choose to evaluate the differences only at the TLE epochs, however, this would result in a small number of available evaluation epochs. It was found that most TLEs are published when the body crosses the equator. Therefore, the evaluation points are selected at the ascending node of each orbit. The descending nodes cannot be used as evaluation points, because the direction of flight is then opposite with respect to the Earth compared to the ascending node.

An evaluation interval of 15 days was chosen, because the average of the altitude within this period was about 180 km. Furthermore, it was observed that the errors obtained from TLEs that are forward propagated in time and backward propagated in time are different (Geul et al., 2016). It was found that the errors are larger when propagating backward, because of the instability of the equations of motion. The differencing is performed by substracting all possible combinations of the TLEs at the evaluation epoch. Therefore, after performing the differencing is performed the dataset is doubled by adding all differences multiplied with -1. This counteracts the assymmetry in the data that originates from the difference in numerical stability between forward and backward propagating.

Scaling

The data that are obtained from differencing are not directly representative for the uncertainty in the TLEs, because the propagation process changes the uncertainty in the state. Data obtained by the differencing method was compared with data obtained using Global Positioning System (GPS) solutions for the GOCE satellite[1] . The observed correlation structure was similar, but the magnitude of the errors is not similar, which is caused by the propagation process.

[1]This comparison is performed in the research of Geul et al. (2016) with GPS solutions obtained by Bock et al. (2011).

Therefore, the differencing method is used to provide the correlation structure of the uncertainty and the errors are scaled such that the standard deviation of the errors are the same as for the GOCE satellite determined with GPS. In the research of Yim and Chung (2012) it was shown that the standard deviations of the errors of a rocket body and a satellite are similar in magnitude. Therefore, it is expected that even though the GOCE satellite has a different shape than the Delta-K rocket body, this method will result in a more accurate uncertainty model than using TLE differencing alone.

The errors are scaled such that the standard deviation of the data is equal to the standard deviation for the TLEs of GOCE:

$$\begin{pmatrix} \sigma_R \\ \sigma_S \\ \sigma_W \\ \sigma_{V_R} \\ \sigma_{V_S} \\ \sigma_{V_W} \end{pmatrix} \begin{pmatrix} 102.2 \text{ m} \\ 4245.0 \text{ m} \\ 62.9 \text{ m} \\ 4.6532 \cdot 10^{-3} \text{ m/s} \\ 1.137 \cdot 10^{-4} \text{ m/s} \\ 5.6581 \cdot 10^{-5} \text{ m/s} \end{pmatrix} \tag{6-1}$$

where the values are standard devations of the errors expressed in the orbital frame, which corresponds to the radial R, along-track S and cross-track W direction. After scaling the results are converted to the state variables (Section 5-2) that are used in the simulators.

Results

The data were generated multiple times using different settings to establish the settings that result in the most accurate representation of the uncertainty. For each rocket body that is simulated, the settings were adjusted such that the moving window is as small as possible to reduce the influence of the propagation process. A PDF was modelled using different moving windows and the smallest moving window was chosen such that a larger moving window would not change the distribution significantly. For most cases this resulted in a moving window of 0.7 days that contained around 800 error samples. These error samples are used to form probability distributions for the uncertainty model.

An example of the samples that are generated for TLE-3 (moving window of 0.6 days) is shown in Figure 6-2. The correlation matrix that corresponds to the figure is shown in Table 6-2. The samples that are obtained in the orbital frame are converted to the state variables that are described in Section 5-2. The standard deviation of these samples is shown in Equation (6-2). The correlation matrix of the initial translational state is provided in Table 6-1.

$$\begin{pmatrix} \sigma_R \\ \sigma_\tau \\ \sigma_\delta \\ \sigma_{V_R} \\ \sigma_{V_\tau} \\ \sigma_{V_\delta} \end{pmatrix} = \begin{pmatrix} 185.42 \text{ m} \\ 4.44 \cdot 10^{-4} \text{ rad} \\ 7.78 \cdot 10^{-4} \text{ rad} \\ 5.62 \text{ m/s} \\ 0.097 \text{ m/s} \\ 0.0631 \text{ m/s} \end{pmatrix} \tag{6-2}$$

From Figure 6-2 it can be derived that the distribution of the errors is approximately Gaussian. Observing these errors reveals two clear features in the data. There is a strong correlation

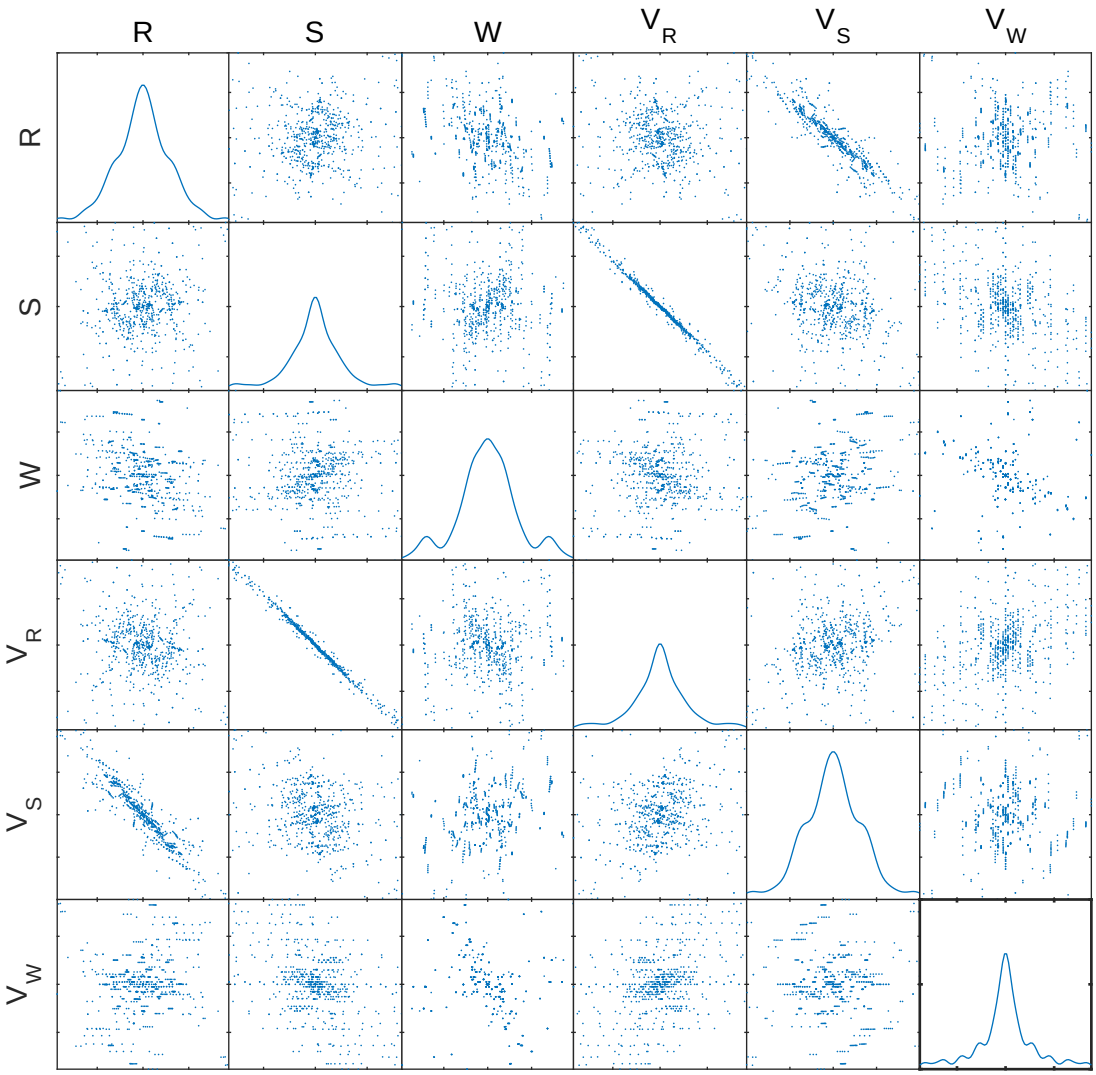

Figure 6-2: Data samples obtained for TLE 3 (Norad ID 28130) with a moving window size of 0.6 days.

Table 6-1: Correlation matrix of TLE-3.

	R	δ	τ	V_τ	V_δ	V_R
R	1.000	0.034	0.047	0.049	-0.892	-0.605
δ		1.000	0.999	0.999	-0.228	-0.498
τ			1.000	1.000	-0.245	-0.505
V_τ				1.000	-0.247	-0.511
V_δ					1.000	0.681
V_R						1.000

Table 6-2: Correlation matrix of errors in orbital frame of TLE-3.

	R	S	W	V_R	V_S	V_W
R	1.000	0.165	-0.319	-0.167	-0.984	0.036
S		1.000	-0.156	-0.997	-0.318	0.296
W			1.000	0.158	0.305	-0.330
V_R				1.000	0.321	-0.313
V_S					1.000	-0.095
V_W						1.000

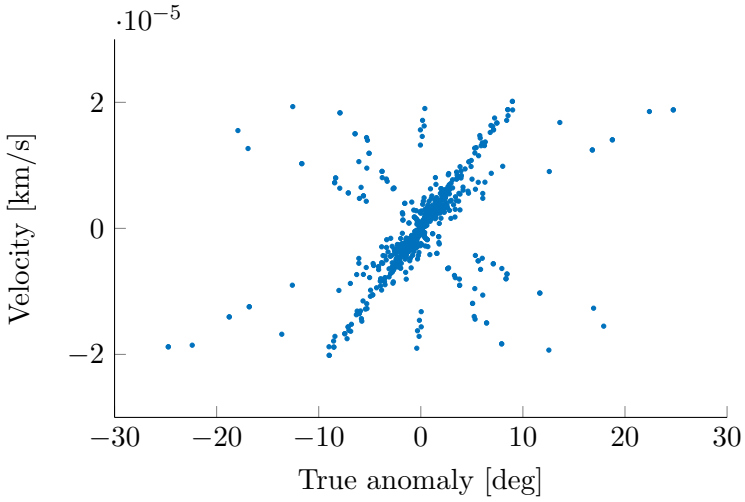

Figure 6-3: True anomaly error vs velocity error (TLE 3).

between the along-track velocity V_S error and the radial position R error and between the radial velocity V_R error and the along track position S error.

The radial position and the along track velocity error are strongly correlated, because the orbital velocity is related with the radial position by the vis-viva equation:

$$V^2 = \mu(2/r - 1/a) \tag{6-3}$$

The correlation between the along-track position error and the radial velocity error can be attributed to the error in the true anomaly and argument of perigee. For an orbit with a slight eccentricity, the radial velocity varies with true anomaly, so it is expected that the true anomaly and the velocity are correlated. Figure 6-3 clearly shows the correlation between these variables. Therefore, the along-track position error is also strongly correlated with the radial velocity, because the true anomaly is strongly related with the along-track position.

Remarks

After producing the results in Chapter 9, it was found that an error was made in the calculation of the samples for the spherical coordinates representation. The standard deviation of the velocity (Equation (6-2)) in the vertical frame is large compared to the standard deviation

obtained from GOCE (Equation (6-1)), which is expressed in the orbital frame. Because the data is scaled before converting the samples to the spherical frame, the errors should have the same order of magnitude. Unfortunately, an error was made in this conversion process that resulted in standard deviations of the velocity components that are a factor 1000 larger than the standard deviation obtained from GOCE.

The error originates from the fact that the conversions are seperately performed for each sample. Therefore, samples that are substracted to obtain an error are transformed using two slight different transformation matrices. As a result the errors greatly increase or cancel out. The error is corrected and new samples were obtained with a moving window of 0.8. A corrected uncertainty model for TLE-3 was obtained with the following standard deviation:

$$\begin{pmatrix} \sigma_R \\ \sigma_\tau \\ \sigma_\delta \\ \sigma_{V_R} \\ \sigma_{V_\tau} \\ \sigma_{V_\delta} \end{pmatrix} = \begin{pmatrix} 103.5 \text{ m} \\ 3.27 \cdot 10^{-4} \text{ rad} \\ 5.67 \cdot 10^{-4} \text{ rad} \\ 0.27 \text{ m/s} \\ 7.59 \cdot 10^{-3} \text{ m/s} \\ 3.05 \cdot 10^{-4} \text{ m/s} \end{pmatrix} \tag{6-4}$$

In the research of Ronse (2013), it was found the uncertainty in the initial velocity has the least impact on the impact time distributions, so it is expected that the impact of the error is small. Ten additional MC simulations have been performed with the corrected uncertainty model to confirm that the error does not have a significant impact on the obtained results. The newly obtained impact time distributions were compared with the earlier obtained impact time distributions and it was found that the distributions exactly match. For the two worst cases, a difference of 5% was observed in the impact time window. However, because only a small number of samples are located at the edges of the PDF the reliability of a 99.73% probability impact time window is limited. This shows that the errors do not have a significant impact on the results and the conclusions that are made. Furthermore, it confirms that the initial uncertainty in the velocity has only a small effect on the impact time distributions.

6-1-2 Probability Distribution Modeling

The data obtained from the TLE pair-wise differencing method is used to model the uncertainty in the TLEs. Only using the covariance matrix of the data to model the distribution as a Gaussian distribution could result in an incorrect uncertainty model, because the distribution could be different and non-linear correlations may be present that are not represented by the correlation matrix or covariance matrix. Therefore, a non-parametric method called KDE (Section 3-2) is used such that no assumptions are made about the distribution of each state and the correlations.

At every datapoint a kernel (function) is placed with a certain window width h. These kernels have an integral of 1. The PDF of the translational state is then obtained by taking the sum of the kernels divided by the number of kernels:

$$f_{X_1 \ldots X_N}(x_1, \ldots, x_N) = \frac{1}{N} \sum_{i=1}^{N} K_{i, X_1 \ldots X_N}(x_1, \ldots, x_N, h) \tag{6-5}$$

The kernels that are used for modelling the PDF are Gaussian distributions without correlation. The window width has a large influence on the shape of the PDF, so the window width is selected using a process called cross-validation.

Because the Gaussian kernels are uncorrelated, the PDF can be written as the multiplication of independent uni-variate Gaussian PDFs:

$$f_{X_1 X_2}(x_1, x_2) = \frac{1}{N} \sum_{i=1}^{N} K_{i, X_1}(x_1, h_1) K_{i, X_2}(x_2, h_2) \tag{6-6}$$

Because of this property, a marginal distribution can easily be obtained:

$$f_{X_1}(x_1) = \frac{1}{N} \sum_{i=1}^{N} K_{i, X_1}(x_1, h_1) \tag{6-7}$$

This property can be used to sample the distribution in a numerically efficient way for a MC simulation.

Uncertainty Model and Validation

With the data obtained by the TLE pair-wise differencing method, only the bandwidth of the kernels needs to be chosen such that the model accurately fits the data. A bandwidth that is too small results in oscillations in the PDF, which is called an overfit. A bandwidth that is too large results in a PDF that is much smoother than the actual distribution of the data. Therefore, it needs to be chosen such that it does not overfit or oversmooth the data.

A way to test if the model is overfitted is to derive the model using two different datasets and verify that they produce approximately the same results. This model validation technique is called cross-validation (Geisser, 1993). The bandwidth of the kernel is obtained by calculating the optimal bandwidth and multiplying it with a factor, such that the model is not overfitted or oversmoothed.

In Figure 6-4 two models are shown that are each derived using half of a total dataset of 766 samples. The bandwidth of the kernels is chosen as 1.5 times the optimal bandwidth for these models. The figure shows that the two models are similar. In Figure 6-5, two different models are shown that use the same datasets using a bandwidth that is equal to the optimal bandwidth. These models clearly show more features than the previous one, however, the two models are less similar.

The model with a bandwidth 1.5 times the optimal bandwidth is chosen, because the two models are more similar. It is possible that this oversmooths the function, but an oversmoothening results in a more conservative result, because the probability density covers a larger area.

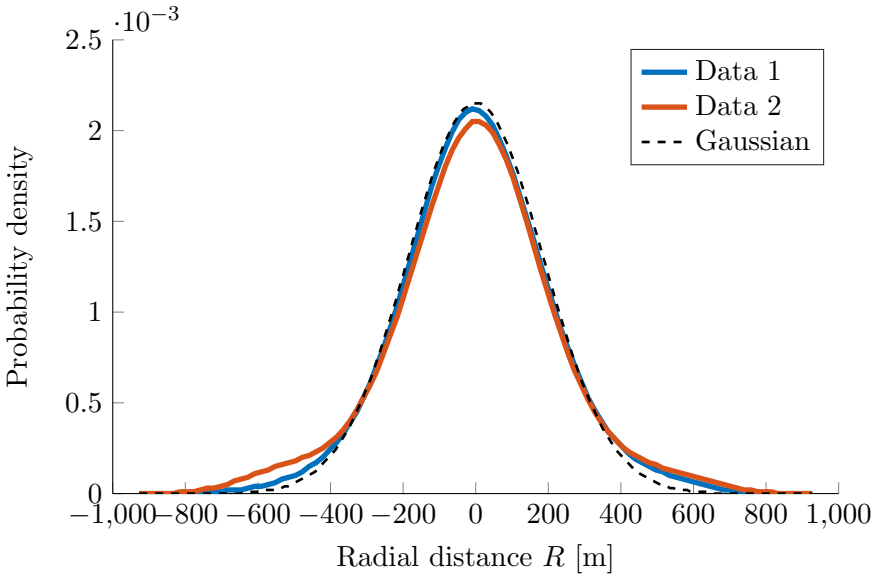

Figure 6-4: Uncertainty model of the radial distance using two different datasets with $h = 1.5h_{opt}$ (TLE-3).

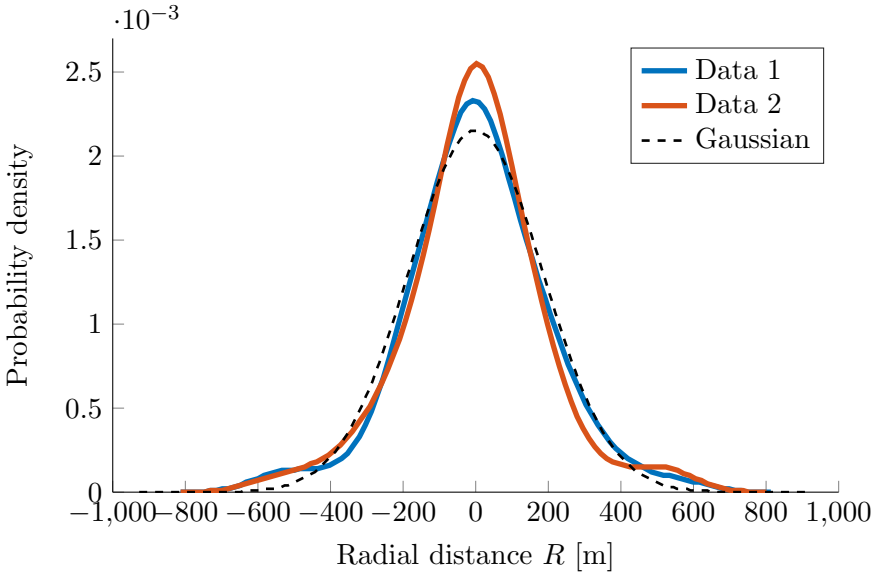

Figure 6-5: Uncertainty model of the radial distance using two different datasets with $h = h_{opt}$ (TLE-3).

6-2 Rotational state

This section describes the uncertainty model of the rotational state, which involves the initial attitude and the initial rotational velocity. In the derivations it is assumed that the rotational state is uncorrelated to the translational state and the atmospheric density. This assumption is made, because no information is available of these correlations. It is further assumed that the attitude and rotational velocity is uncorrelated, because no information of this correlation is available.

6-2-1 Attitude

A research performed by Ronse (2013) found that no information is available about the initial attitude of the rocket bodies. Therefore, it is assumed that the rocket body can have any orientation and each orientation is equally probable, which will be called a uniform random attitude.

Uniform Random Attitude Sampling

Since the attitude is modeled using the axis of the body frame, these vectors should be distributed such that they have a uniform random orientation. A uniform random attitude is obtained by transforming an arbitrary unit vector using a random transformation matrix $\boldsymbol{C}$ such that the vector is uniformly distributed over the surface of a unit sphere. Such a distribution is shown in Figure 6-6. The random transformation matrix is obtained by using a normal transformation matrix and inserting random attitude parameters. For example, consider a vector that coincides with the Z axis and that is rotated using the matrix $\boldsymbol{C}$:

$$\begin{pmatrix} X \\ Y \\ Z \end{pmatrix} = \boldsymbol{C} \begin{pmatrix} 0 \\ 0 \\ 1 \end{pmatrix} \tag{6-8}$$

The distribution of the attitude parameters should be such that the marginal distribution of X, Y and Z will be uniform on $[-1, 1]$, so each orientation will be equally probable. Evaluating Equation (6-8) will find that the resulting vector will be equal to the third column of the transformation matrix, however, for a true random uniform attitude all elements of the transformation matrix should have a uniform distribution on $[-1, 1]$. The distributions of the attitude parameters are constrainted by the fact that the length of the resulting random vector must be equal to the length of the initial vector. This is always satisfied if valid attitude parameters are used, because the transformation matrix is orthonormal.

If the attitude is represented using Euler angles and the transformation is performed as described in Equation (6-8), the following relation can be obtained between the Euler angles and the X, Y, Z coordinates:

$$\begin{pmatrix} X \\ Y \\ Z \end{pmatrix} = \begin{pmatrix} -\sin\theta_y \\ \sin\theta_x \cos\theta_y \\ \cos\theta_x \cos\theta_y \end{pmatrix} \tag{6-9}$$

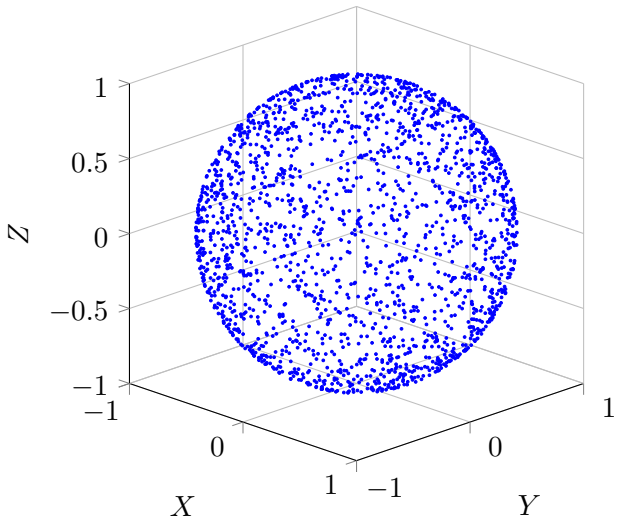

Figure 6-6: 2000 random uniform attitude samples generated using quaternions.

The distributions of each of the Euler angles θ_i should be such the distribution of X, Y and Z are uniform. In the research of Ronse (2013), it was shown that θ_x was sampled from a uniform distribution on $[-\pi, \pi]$ and θ_y should be sampled using:

$$\theta_y = \arcsin u \tag{6-10}$$

where u is a sample of a random variable U with a uniform distribution on $[-1, 1]$. Using the X component of Equation (6-9), it can be derived (using Equation (3-10)) that if X is a uniform distribution on $[-1, 1]$, the PDF of θ_y should be:

$$f_{\theta_y} = \begin{cases} \frac{\cos\theta_y}{2} & -\frac{\pi}{2} < \theta_y < \frac{\pi}{2} \\ 0 & \text{otherwise} \end{cases} \tag{6-11}$$

Using the inverse CDF $F^{-1}_{\theta_y}$ to sample θ_y corresponds to Equation (6-10), so this proves that the sampling method used in the research of Ronse (2013) was correct. Note that sampling the Euler angles uniformly would result in a concentration of attitudes near the poles, so a non uniform random orientation.

Uniform Random Attitude Quaternions

Quaternions will be used to represent the attitude in this research, so a model of the initial PDF is required that results in a uniform random attitude. Performing the transformation in Equation (6-8) results in the following vector:

$$\begin{pmatrix} X \\ Y \\ Z \end{pmatrix} = \begin{pmatrix} 2(q_1 q_3 - q_2 q_4) \\ 2(q_2 q_3 + q_1 q_4) \\ 1 - 2(q_1^2 + q_2^2) \end{pmatrix} \tag{6-12}$$

A random uniform attitude is obtained by sampling the quaternions using Equation (6-13) with random samples u that are uniformly distributed on $[0, 1]$ (Kirk, 1992).

$$\begin{pmatrix} q_1 \\ q_2 \\ q_3 \\ q_4 \end{pmatrix} = \begin{pmatrix} \sqrt{1-u_1}\sin(2\pi u_2) \\ \sqrt{1-u_1}\cos(2\pi u_2) \\ \sqrt{u_1}\sin(2\pi u_3) \\ \sqrt{u_1}\cos(2\pi u_3) \end{pmatrix} \tag{6-13}$$

Figure 6-6 was derived using the sampling method described by Equation (6-13). A histogram of X, Y and Z were plotted using a large number of samples, which confirmed that the distributions are uniform. Furthermore, sampling the attitude using the method described by Ronse (2013) results in the same distribution of samples, so this verifies that this sampling method results in a uniform random attitude. Using Equation (6-13) it can be derived that the quaternion constraint is fulfilled.

To model a uniform random attitude using quaternions, a joint PDF of the quaternions needs to be found that results in a uniform distribution of X, Y and Z. It is important that the normality constraint of quaternions (Equation (5-5)) is not violated. Therefore, it is chosen to model the PDF of the attitude using q_1, q_2 and q_3, while q_4 is defined using the other three quaternions.

Figure 6-7 shows 2000 samples of quaternions that result in a random uniform attitude. The figure clearly shows that the joint distribution of q_1, q_2 and q_3 is uniform within a unit sphere. The figure shows that there is no statistical correlation between the variables, so the PDF can be represented by a constant value, which is equal to 1 divided by the volume of the sphere. Since, the sphere is a unit sphere, the joint PDF is defined as:

$$f_{q_1q_2q_3}(q_1, q_2, q_3) = \begin{cases} \frac{3}{4\pi} & q_1^2 + q_2^2 + q_3^2 \leq 1 \\ 0 & \text{otherwise} \end{cases} \tag{6-14}$$

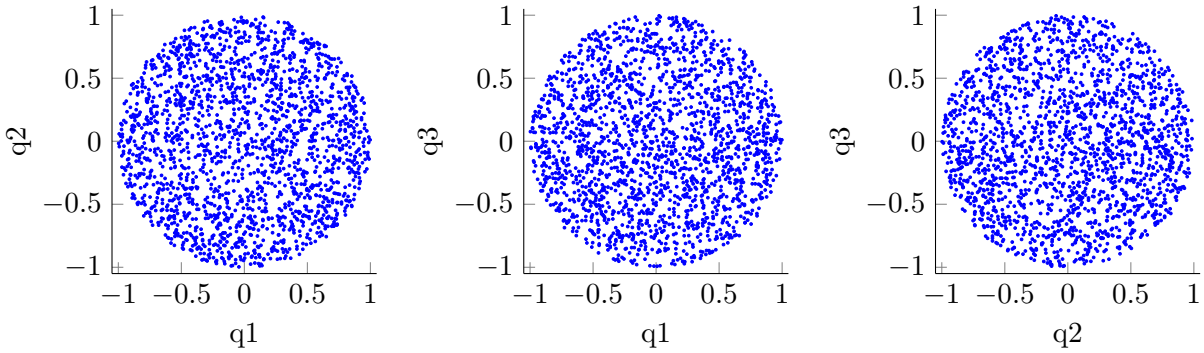

Figure 6-7: 2000 samples of random quaternions that are distributed such that a random uniform attitude is obtained.

Verification

Because the distribution of the uniform random attitude quaternions is derived from a corresponding sampling method, the distribution needs to be verified. Using the joint PDF it can

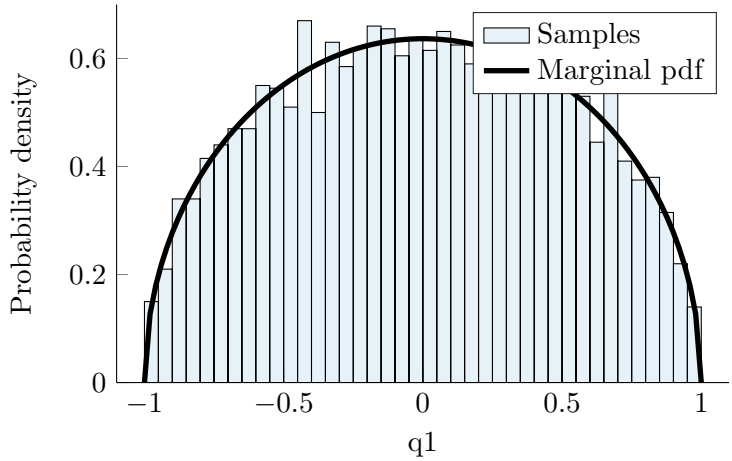

Figure 6-8: Histogram of 4000 quaternion samples and derived marginal PDF of q_1.

be derived by integration (Section A-3) that the marginal PDFs of q_1, q_2 and q_3 are:

$$f_{q_i}(q_i) = \begin{cases} \frac{2\sqrt{1-q_i^2}}{\pi} & -1 < q_i < 1 \\ 0 & \text{otherwise} \end{cases} \tag{6-15}$$

To verify the PDF, a histogram of 4000 uniform random attitude quaternions are sampled and shown in Figure 6-8. The figure shows that the derived marginal PDF corresponds to the samples. This indicates that the derived joint PDF (Equation (6-14)) is correct.

To further verify the joint PDF, the marginal PDFs are derived from Equation (6-13). This derivation is performed without using the joint PDF, so it can be used to show that the derived joint PDF is correct. The distribution of the first quaternion is derived by splitting the equation in two factors a and b:

$$q_1 = a \cdot b = \sqrt{1-u_1}\sin(2\pi u_2) \tag{6-16}$$

The distribution of both factors is determined and the distribution of the multiplication of these two random variables will result in the distribution of the first quaternion. The distribution of the first factor a is found using static PDF transformations as described in Section 3-3, resulting in:

$$a = \sqrt{1-u} = S(u) \tag{6-17a}$$

$$f_U(u) = \begin{cases} 1 & 0 < u < 1 \\ 0 & \text{otherwise} \end{cases} \tag{6-17b}$$

$$S^{-1}(x) = 1 - x^2 \tag{6-17c}$$

$$\frac{d}{dx}\left(S^{-1}(x)\right) = -2x \tag{6-17d}$$

$$f_A(a) = \begin{cases} |-2a| & 0 < 1-a^2 < 1 \\ 0 & \text{otherwise} \end{cases} = \begin{cases} -2a & -1 < a < 0 \\ 2a & 0 < a < 1 \\ 0 & \text{otherwise} \end{cases} \tag{6-17e}$$

The distribution of the second factor b is derived using the same method, resulting in:

$$b = S(u) = \sin(2\pi u) \tag{6-18a}$$

$$f_U(u) = \begin{cases} 1 & 0 < u < 1 \\ 0 & \text{otherwise} \end{cases} \tag{6-18b}$$

$$S^{-1}(x) = \frac{\arcsin(x)}{2\pi} \tag{6-18c}$$

$$\frac{d}{dx}\left(S^{-1}(x)\right) = \frac{1}{2\pi\sqrt{1-x^2}} \tag{6-18d}$$

$$f_B(b) = \begin{cases} \left|\frac{1}{2\pi\sqrt{1-b^2}}\right| & 0 < \frac{\arcsin(b)}{2\pi} < 1 \\ 0 & \text{otherwise} \end{cases} = \begin{cases} \frac{1}{2\pi\sqrt{1-b^2}} & -1 < b < 1 \\ 0 & \text{otherwise} \end{cases} \tag{6-18e}$$

The limits of the distribution are changed due to the inverse of the sine function. Evaluating only the arcsin does not give this result, but one must keep in mind that we actually use the inverse of the sin. The inverse of the sin cannot be defined in a function beyond $y > \pi/2$, however $y = \sin(2\pi x)$ has a solution for x if $y > \pi/2$. Because $\sin(2\pi u)$ has a range of $[-1, 1]$, the limits of the distribution are changed to -1 and 1.

The distribution of q_1 is found by deriving the distribution of z where $z = ab$. The distribution of z is derived using a convolution of the PDFs of a and b as described in Section 3-3-2:

$$\begin{aligned} f_z(z) &= \int_{\sqrt{z^2}}^{1} 2x \frac{1}{2\pi\sqrt{1-\left(\frac{z}{x}\right)^2}\,|x|} dx + \int_{-1}^{\sqrt{z^2}} -2x \frac{1}{2\pi\sqrt{1-\left(\frac{z}{x}\right)^2}\,|x|} dx \\ &= \frac{\sqrt{x^2-z^2}}{\pi}\Bigg|_{x=\sqrt{z^2}}^{x=1} + \frac{-\sqrt{x^2-z^2}}{\pi}\Bigg|_{x=-1}^{x=\sqrt{z^2}} \\ &= \frac{2\sqrt{1-z^2}}{\pi} \end{aligned} \tag{6-19}$$

The first distribution is defined on $[-1, 1]$, but the second distribution is only defined if $x^2 > z^2$, because the square root is only defined for positive values, so the integration bound of x is set to $\sqrt{z^2}$.

Changing the variable name z to q_1 will result in the distribution of q_1:

$$f_{q_1}(q_1) = \begin{cases} \frac{2\sqrt{1-q_1^2}}{\pi} & -1 < q_1 < 1 \\ 0 & \text{otherwise} \end{cases} \tag{6-20}$$

Using the same methodology, the marginal PDFs of the other quaternions are derived, which are identical to the marginal PDF of q_1. This proves that the joint PDF results in the correct marginal PDF for each quaternion. The correlation structure between the quaternions is not mathematically proven, but the obtained samples clearly show that the joint PDF accurately describes the desired distribution.

6-2-2 Rotational Velocity

In the research of Ronse (2013), an analysis was performed on the rotational velocity of the Delta-K rocket body. Data of the rotational velocity of these bodies was obtained for 10 cases and it was concluded that the orientation of the rotation vector is arbitrary and the magnitude of the rotational velocity was in the range of $[0, \frac{2\pi}{60}]$ rad/s. Therefore, the uncertainty in the rotational velocity is modelled such that the vector has a random uniform orientation and the length of the vector is uniformly distributed.

The random uniform orientation can be obtained in a similar way as described in Section 6-2-1. Because the length of the vector is not constant, the distributions of each component of the vector are not uniform. The joint distribution is derived using the general spherical coordinate representation (r, θ, ϕ) to express each component of the rotational velocity vector:

$$\boldsymbol{\omega} = \begin{pmatrix} \omega_1 \\ \omega_2 \\ \omega_3 \end{pmatrix} = \begin{pmatrix} \cos\theta\cos\phi \\ \cos\theta\sin\phi \\ \sin\theta \end{pmatrix} r \tag{6-21}$$

The length of the vector is governed by r, so r is uniformly distributed on $[0, \omega_{\max}]$ and the angles are distributed such that the vector $\boldsymbol{\omega}$ has a random uniform orientation. Figure 6-9a contains samples of the rotational velocity vector that are sampled using these properties. The figure clearly shows that probability density is inversely propertional to the length of the vector or radius r.

Consider such samples in three dimensions, one can draw several spheres with a radius r that contain a number of samples on its surface. Because the radius is uniformly distributed, each sphere will have the same number of samples on its surface. The smaller spheres will contain much more samples per unit area than the larger spheres. Therefore, the probability density will be inversely proportional to the area of a sphere, which is $4\pi r^2$. Because each orientation is equally likely, the distribution is only dependent on the radius of the sphere, so it is expected that the joint PDF is of the form $1/r^2$. If the PDF integrated over its volume should result in one, so this form is integrated over its volume:

$$\int_0^{2\pi}\int_0^{\pi}\int_0^{\omega_{\max}} \frac{1}{r^2} r^2 \sin\theta dr d\theta d\phi = 4\pi\omega_{\max} \tag{6-22}$$

Using this result, it can be derived that the PDF is described by Equation (6-23):

$$f_{r,\theta,\phi}(r,\theta,\phi) = \begin{cases} \frac{1}{4\pi\omega_{\max} r^2} & 0 < r \leq \omega_{\max} \\ 0 & \text{otherwise} \end{cases} \tag{6-23}$$

The marginal distribution of the radius r is derived to prove that the radius is uniformly distributed, resulting in:

$$f_r(r) = \int_0^{2\pi}\int_0^{\pi} = f_{r,\theta,\phi} d\theta d\phi = \begin{cases} \frac{1}{\omega_{\max}} & 0 < r \leq \omega_{\max} \\ 0 & \text{otherwise} \end{cases} \tag{6-24}$$

This equations shows that the marginal distribution of the radius is uniform. The marginal distribution of θ and ϕ cannot be obtained, because the integral of $1/r$ diverges for $r \to 0$. However, the distribution is only dependent on the radius, so the distribution is spherically symmetric and each direction is equally likely. This means that the derived PDF can be used to represent a random rotational velocity, with a uniformly distributed magnitude and random orientation.

Now that a joint PDF has been found that results in the desired properties, the joint PDF of the rotational velocity can be derived by changing the variables:

$$f_{\boldsymbol{\omega}}(\boldsymbol{\omega}) = \begin{cases} \frac{1}{4\pi\omega_{max}\left(\omega_1^2+\omega_2^2+\omega_3^2\right)} & 0 < \omega_1^2 + \omega_2^2 + \omega_3^2 \leq \omega_{max}^2 \\ 0 & \text{otherwise} \end{cases} \tag{6-25}$$

Note that this PDF is not defined if $\|\boldsymbol{\omega}\|$ is zero. This PDF has an integral of 1 over its domain and the vector $\boldsymbol{\omega}$ has a length that is uniformly distributed on $(0, \omega_{max}]$. Figure 6-9 shows a comparsion of samples generated using the desired distributions and the corresponding PDF of the rotational velocity. Comparing the figures it can be concluded that the PDF represents the correct distribution of the samples.

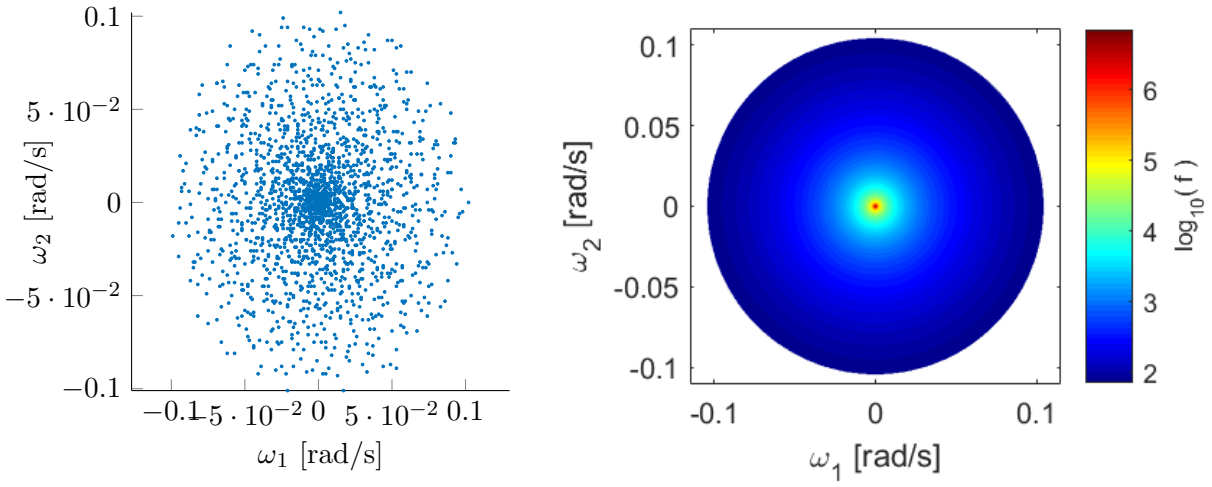

(a) Samples

(b) Marginal PDF

Figure 6-9: Comparison of 2000 rotational-velocity samples uniformly distributed on $[0, 3]$ with the marginal PDF of ω_1 and ω_2.

6-3 Atmospheric Density

In the research of Ronse (2013), the NRLMSISE-00 model was used and uncertainty in the atmospheric density was modeled using a uniform distribution. However, no justification for this distribution was given. Therefore, the uncertainty in the atmospheric density and its distribution is investigated.

The distribution of the error in the MSIS-86 model is analyzed in the research of Bezdek (2007) by comparing the model predictions with data obtained from an accelerometer mounted on a satellite within an altitude range of $230 - 750$ km. The research concluded that the natural logaritm of the ratio of the observed density to the predicted density has a normal distribution. The same conclusion was made in the research of Prag (1983) using data in the altitude range of $120 - 200$ km. Furthermore, in the report of Picone et al. (2002), the NRLMSISE-00 model was presented and it was indicated that a previous study performed by Hedin (1988) also showed that the ratio of observed density to the predicted density has a lognormal distribution.

Because the NRLMSISE-00 model is based on the MSIS model, it is expected that the statistical properties of the error are the same, so the uncertainty will be modeled using a lognormal distribution. This means that the ratio of observed density ρ_O to the computed density using the model ρ_M has a lognormal distribution:

$$Y_\rho = \ln(X_\rho) \sim N(\bar{Y}_\rho, \sigma^2_{Y_\rho}) \tag{6-26a}$$

$$X_\rho = \frac{\rho_O}{\rho_M} \tag{6-26b}$$

The relative error thus also has a lognormal distribution, because it can be defined using the following ratio:

$$\frac{\Delta\rho}{\rho_M} = X_\rho - 1 \tag{6-27}$$

The distribution of the atmospheric density ρ can be defined using the density ratio X_ρ:

$$\rho(P) = \Delta\rho + \rho = X_\rho \rho_M(P) \tag{6-28}$$

The model is dependent on several parameters P, so the uncertainty in the model can also vary with these parameters. In the research of Picone et al. (2002), it is shown that the statistical properties of the error changes with altitude. To simplify the uncertainty model it is assumed that the distribution of the atmospheric density ratio is constant throughout the atmosphere. This is a reasonable assumption, because errors in the atmosphere model are caused by a physical process that is not only locally present in the atmosphere. For example, if the effect of solar activity is different than predicted by the model, it is likely that this happens to a whole region instead of locally.

The PDF of the atmospheric density ratio X_ρ is defined using a lognormal distribution (Montgomery and Runger, 2014):

$$f_{X_\rho}(x) = \frac{1}{x\omega\sqrt{2\pi}} \exp\left(-\frac{(\ln x - \theta)^2}{2\omega^2}\right) \tag{6-29}$$

The parameters θ and ω are the mean and standard deviation of the normal distribution and related to the mean and standard deviation of the random variable X by:

$$\mu_x = \exp\left(\theta + \omega^2/2\right) \tag{6-30a}$$

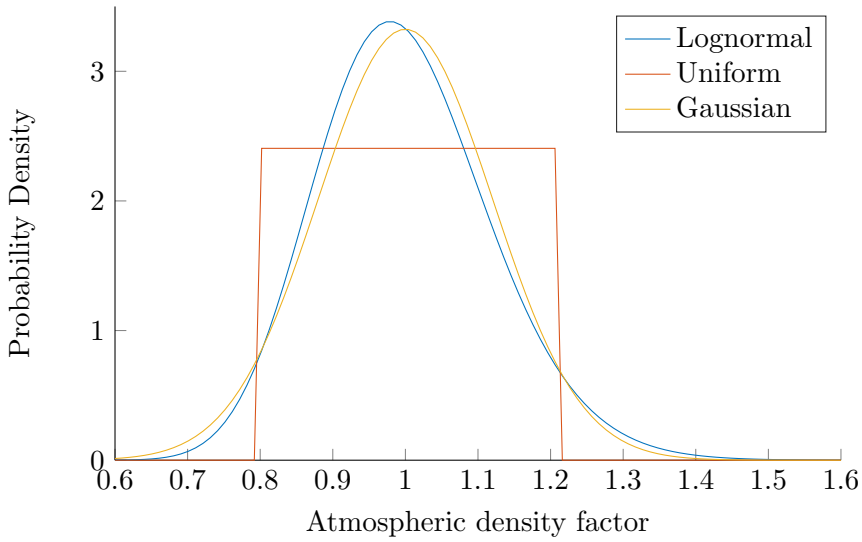

Figure 6-10: Comparison of three different distributions with $\mu = 1$ and $\sigma = 0.12$.

$$\sigma_x^2 = \exp\left(2\theta + \omega^2\right)\left(e^{\omega^2} - 1\right) \tag{6-30b}$$

The mean and standard deviation of the density ratio X_ρ are known, so these values need to be converted to θ and ω using:

$$\theta = \ln\left(\frac{\mu_x}{\sqrt{\frac{\sigma_x^2}{\mu_x^2} + 1}}\right) \tag{6-31}$$

$$\omega^2 = \ln\left(\frac{\sigma_x^2}{\mu_x^2} + 1\right) \tag{6-32}$$

An analysis on the accuracy of the NRL Mass Spectrometer and Incoherent Scatter Radar (NRLMSISE-00) model performed by Ronse (2013) concluded that the following mean and standard deviation accurately represents the uncertainty in the model:

$$\mu_x = 1 \quad ; \quad \sigma_x = 0.12$$

$$\theta = -7.149 \cdot 10^{-3} \quad ; \quad \omega = 1.196 \cdot 10^{-1}$$

The distribution of the atmospheric density factor X_ρ is shown in Figure 6-10. For comparison, a Gaussian and uniform distribution are plotted with the same standard deviation and mean. The figure shows that the lognormal distribution with these parameters is approximately equal to the Gaussian distribution, but is slightly skewed. The figure also shows that for the lognormal distribution, the uncertainty is more concentrated near the median and the width of the distribution is larger than a uniform distribution.

6-3-1 Correlation

The error in the atmospheric density originates from two sources: error in the atmosphere model itself and error in the position that is used to calculate the atmospheric density. In

addition, the aerodynamic drag is determined using the atmospheric density, so it is expected that the error in the atmospheric density is correlated with the error in the translational state of the rocket body. Ideally, the correlation between the two variables is found using the data that are used to model the atmospheric density, but these data are not available. Therefore, a survey is performed to obtain information about the correlation of the atmospheric density and the translational state.

In the research of Wright and Woodburn (2004), it was shown that the atmospheric density and the translational state are indeed correlated. An orbit-estimation procedure was used to obtain the atmospheric density, ballistic coefficient and the translational state. The research showed that correlations are present, which is logical because the orbit is used to estimate the atmospheric density. Because the NRLMSISE-00 model is partially based on atmospheric density data derived from orbit predictions, it is assumed that these data are also applicable to the uncertainty model for this research.

The research showed that the atmospheric density is negatively correlated ($\rho = -0.4$) with the intrack position and positively correlated ($\rho = 0.4$) with the radial velocity and that the atmospheric density is not correlated with the intrack velocity and radial position.

Consider a spacecraft moving through the atmosphere in a part where the atmospheric density is lower than expected, it is then more probable that the velocity of the spacecraft is smaller than expected. This would mean that the intrack velocity and atmospheric density are negatively correlated. This correlation was not observed, which shows that the error in the velocity of the spacecraft is governed by other effects than the atmospheric density, like the fitting process. A possible explanation could be that the atmospheric density and the velocity difference are too small to cause these effects. Nevertheless, the intrack position is more influenced by the error in the atmospheric density, because the intrack position error accumulates over time. Therefore, one would expect that a negative correlation can be observed between the error in the intrack position and the atmospheric density.

If the atmospheric density is lower than expected, it is more probable that the altitude or radial position is higher than expected, which means that there is a negative correlation between the atmospheric density and the altitude. This correlation was not observed, which shows that the radial position error is more influenced by other effects than the atmospheric density. A possible explanation can be that the gradient of the atmospheric density with respect to altitude is small, so the difference is too small to observe these effects. Nevertheless, a correlation can be observed between the atmospheric density and the radial velocity. This correlation could be explained, because a larger atmospheric density, would most probably result in a downward motion, which means that there is a negative correlation between the atmospheric density and radial velocity.

It is expected that there is no correlation between the cross-track position and velocity and the atmospheric density, because a cross-track maneuver requires a large ΔV. The error in the atmospheric density is small, so it does not cause any error in the cross-track position and velocity.

The expected correlations agree with the results from the research of Wright and Woodburn (2004), except that a positive correlation of 0.4 was observed between the atmospheric density and the radial velocity. A possible explanation was provided by James Woodburn[2], which

[2]Private communication with James Woodburn, Chief Orbital Scientist at Analytical Graphics, Inc. (email dd. 25-03-2016).

indicated that the orbit estimation procedure can result in less obvious relationships between the state variables. For example, the correlation between the intrack velocity and radial position originates from the fact that the estimator wants to conserve the orbital period. In addition, in the orbit estimation process the ballistic coefficient and atmospheric density are estimated simultaniously, which could complicate the correlations between the state variables.

Because only one source of information is available and the correlations cannot be readily explained, the correlation between the atmospheric density and the translational state is not included in the uncertainty model. An additional reason is that this correlation would increase the complexity of the PDF, because a copula (Section A-4) may be required to model the correlation, which increases the complexity of the sampling method (Section 7-1).

6-4 The Joint Distribution Model

The uncertainty model is defined by combining the uncertainty models of the translational state, the rotational state and the atmospheric density in a model of the joint distribution. It is assumed that the translational state, rotational state and the atmospheric density are uncorrelated. The joint PDF can thus be defined by multiplying the PDFs of these components:

$$f_{rVq\omega\rho}(\boldsymbol{r}, \boldsymbol{V}, \boldsymbol{q}, \boldsymbol{\omega}, \rho) = f_{rV}(\boldsymbol{r}, \boldsymbol{V}) f_q(\boldsymbol{q}) f_\omega(\boldsymbol{\omega}) f_{X_\rho}(X_\rho) \tag{6-33}$$

6-5 Uncertainty in the Uncertainty Model

The uncertainty model is defined using the knowledge that is obtained during the thesis project. However, it is important to consider that the uncertainty model is an estimate of the true uncertainty. This section discusses some considerations on the accuracy of the estimate of the uncertainty model.

The uncertainty model of the translational state is obtained by propagating TLEs using the SGP4 model. This process influences the uncertainty in the translational state that is propagated, so the correlation structure that is obtained is influenced by this process. Nevertheless, research has shown that it provides a good estimate of the true uncertainty (Geul et al., 2016; Yim and Chung, 2012).

The estimate of the uncertainty model of the rotational state is based on a small amount of data. In addition, no physical considerations are taken into account when defining this uncertainty model. For example, the rotational velocity of the body can be stable around some axis of rotation and can be unstable around another axis. In addition, energy-dissipation processes can be present that make some rotational motion more probable than others. Furthermore, torques that are present, like the gravity gradient torque, can make some orientations of the rocket body more probable than others. Because impact predictions are sensitive to the initial rotational state, the inaccuracies in this model could have a large influence.

The uncertainty in the atmospheric density is considered independent of location or time. However, the research of Picone et al. (2002) has shown that there is a dependence on altitude.

Because the atmosphere model is dependent on time and Solar activity properties, uncertainty in these properties can also influence the uncertainty in the atmospheric density uncertainty.

Other parameters that are not included in the uncertainty model can also have a large influence on the impact predictions. For example, uncertainty in the aerodynamic coefficients is not modelled, which has a similar linear influence on the aerodynamic drag as the atmospheric density. Because the atmospheric density has a large influence on the impact predictions, it is expected that uncertainty in the aerodynamic coefficients will also have a large influence on the impact predictions.

6-6 Conclusions and Recommendations

The research performed on the uncertainty model has lead to the following conclusions:

- The uncertainty in the initial translational state (TLEs) can be obtained from the TLE pair-wise differencing method. The random samples that are generated by the method need to be scaled with factors derived from external data, because the propagation process influences the magnitude of the errors. However, the method can provide the correlation structure of the initial translational state. The random samples generated by the method can be used to perform KDE, which results in a PDF of the initial translational state (Equation (6-5)). This model needs to be verified using cross-validation to prevent overfitting of the PDF.
- In the research of Geul et al. (2016), an improved method is presented that can be used to derive the uncertainty in the TLEs. It is recommended to implement this method in future research on statistical impact prediction, because it does not require any scaling or outlier removal.
- A random uniform attitude can be obtained using quaternions sampled using Equation (6-13). The PDF of random uniform attitude quaternions is described by Equation 6-14.
- The initial rotational velocity has a uniform random orientation and a uniformly distributed magnitude. The PDF that describes this uncertainty model is described by Equation (6-25).
- The uncertainty in the atmospheric density should be modelled using a lognormal distribution. Using a uniform distribution underestimates the dispersion in the error of the atmospheric density model.
- Correlations between the atmospheric density and the translational state are present, but they are not included in the uncertainty model, because only one source is available that supports this result and the correlation structure is not fully understood. A more detailed analysis is required to obtain information about these correlations, which could be performed by performing orbit fitting.

Chapter 7

Statistical Impact Prediction Methods

Impact predictions will be performed using two statistical methods: The Monte Carlo method and the Direct PDF propgation method. These methods will be used to generate impact time distributions and impact time windows. The methods to obtain these distributions are discussed in this chapter. The Monte Carlo method is discussed in Section 7-1 and the Direct PDF propagation method is discussed in Section 7-2.

7-1 Monte Carlo Method

The MC method, discussed in Section 3-1, is used to propagate the uncertainty in the state of the Delta-K rocket body. The uncertainty will be propagated by sampling the initial state and the atmospheric density factor and propagating these samples. The propagated samples are used to estimate the PDF of the impact time using kernel density estimation, as explained in Section 3-2.

7-1-1 Sampling Method

The random samples of the initial state are obtained by sampling random uniform samples and applying the inverse transform method (Section 3-1-2) to obtain samples with the correct distribution. The uniformly distributed samples are obtained using a pseudo-random number generator or a Sobol sampler. For the Sobol sampler, the uniform samples cannot be generated seperately for the translational state and the rotational state. This would lead to correlations, because the samples are a obtained using a deterministic sequence. Therefore, the Sobol samples are generated for all the random variables at once.

The PDF of the translational is a summation of Gaussian PDFs, which are independent. Random samples are drawn from this distribution by seperately generating a random sample from each of these Gaussian distributions using the inverse transform method. Only an integer multiple of the number of Gaussian distributions is sampled, such that an equal number of

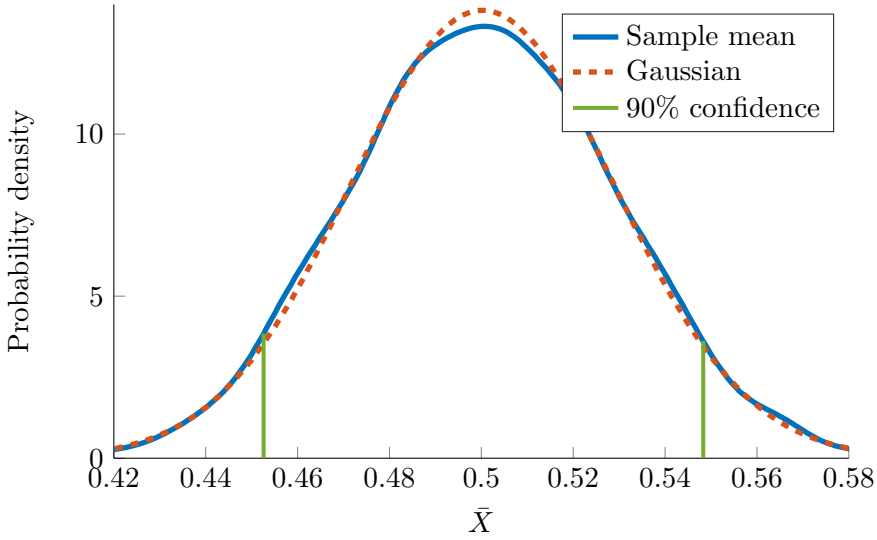

Figure 7-1: Illustration of sample mean bootstrapping using $N = 100$ uniform samples on $[0, 1]$ and $N_B = 10^4$ estimates of the sample mean.

samples is generated from each Gaussian distribution. This eliminates the need for a selection process to select, which from Gaussian distribution will be sampled.

Uniform random attitude samples are generated by sampling random quaternions using Equation (6-13). Subsequently, the rotational velocity is sampled by generating a random oriented vector using Equation (6-12) and a seperate set of uniform random attitude quaternions. This vector is then multiplied by uniformly distributed samples distributed on $[0, \omega_{max}]$.

The atmospheric density factor X_ρ is sampled by directly applying the inverse transform method to the lognormal distribution specified in Section 6-3.

7-1-2 Statistic Estimation

The impact time distributions that are generated are used to obtain statistics of the random impact time, for example, an impact time window or the mean or median. Considering that these distributions are generated using random samples, these statistics are also random. The reason is that if the MC simulations are performed with another set of samples generated from the same distributions, the resulting impact time distribution will be slightly different. Therefore, it is important that the randomness of the statistic is also evaluated and a measure of the precision of the estimate of the statistic is given. The estimate of a statistic is called a point estimate (Montgomery and Runger, 2014).

Consider the mean μ of a random variable X, a point estimate of the mean is the sample mean $\bar{X}$, which can be calculated using N samples:

$$\bar{X} = \frac{x_1 + \cdots + x_N}{N} \tag{7-1}$$

To show the randomness of the sample mean, the sample mean is calculated $N_B = 10^4$ times by subsequently sampling 100 uniformly distributed samples. These 10^4 estimates of the sample

mean can be used to form a probability distribution of the sample mean, which is shown in Figure 7-1. The figure shows that the sample mean is approximately normally distributed. Due to the central limit theorem, this distribution will approach a normal distribution for $N \to \infty$. Because the point estimate of the mean (sample mean) is random, the true mean can only be defined using a confidence level. The figure shows that the true mean lies within the interval $[0.453, 0.548]$ with 90% probability or a 90% confidence level. This interval is derived from the CDF and corresponds to a cumulative probability of 0.05 and 0.95. This method, which used iteratively estimating a statistic, is called bootstrapping.

The process of bootstrapping can be applied to obtain a confidence interval for any statistic of the distribution. In general bootstrapping is performed by subsequently generating N bootstrap samples from the distribution of X and estimating the value of the statistic using these samples. If this is performed N_B times, the estimates can be used to form a probability distribution of the statistic and a confidence interval can be derived from the CDF of the estimates.

If the distribution of the random variable is not known, the data samples can then be used as a population and the bootstrap samples can be sampled directly from the sample population. For the MC simulations only data samples are obtained, so the samples are drawn from the MC samples.

7-1-3 Impact Time Window Estimation

The MC simulations result in samples of the impact time that are used to estimate the impact time distribution using KDE, which is discussed in Section 3-2. From these distributions, an impact time window is generated, which represents the time window in which the Delta-K body is expected to impact the Earth's surface with 99.73% probability. This impact time window can be derived by using the CDF of the impact time and determining the impact time at a cumulative probability of 0.135 and 99.865.

Because the impact time distribution is generated using random samples, any statistic generated from this distribution is also random. Therefore, the impact time window bounds are random statistics and a bootstrapping technique is used to determine the impact time window with a certain confidence level. N samples are randomly drawn from the impact time samples obtained from the MC simulations. The impact time distribution is generated from these samples and the 99.73% probability bounds are determined from this distribution. This is repeated N_B times to obtain a large number of estimates of the probability bounds.

The distribution of the probability bounds is found by performing a KDE on the estimates. The CDF of the probability bounds is used to determine a 99.73% confidence interval for the probability bounds. The most outer bounds then represent the impact window with a probability of 99.73% and a confidence level of 99.73%. This means that it can be said with 99.73% confidence that the probability of impact in this window is 99.73%. An example of an impact time distribution is shown in Figure 7-2. The figure shows the 99.73% probability window and the same probability window with 99.73% confidence level. The figure shows that the same probability window with a 99.73% confidence level is larger than the window without any confidence level. These values for the probability window and confidence level are chosen such that the impact windows can be compared with the impact windows generated in the research of Ronse (2013).

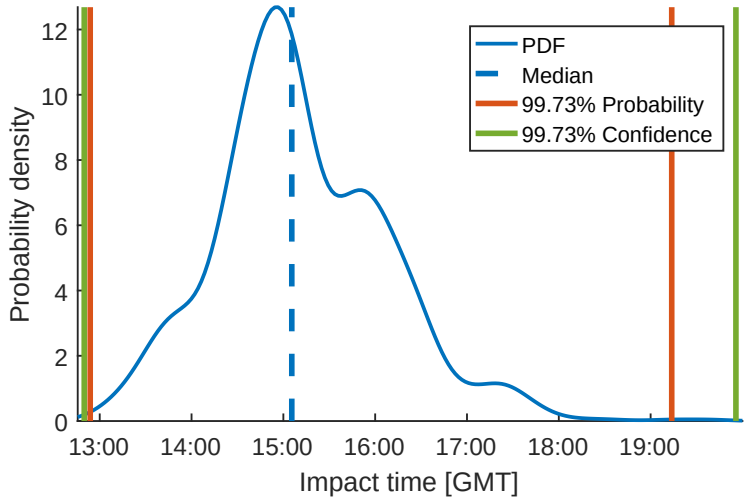

Figure 7-2: Example of an impact time distribution for TLE 10-3 (Norad ID 29109).

7-2 Direct PDF Propagation

The DPP method is used to determine the evolution of uncertainty in the state in time. The uncertainty is modeled using a PDF of the initial state (Section 6-4), which is propagated in time to obtain information about the uncertainty in the future. As explained in Section 3-4, the initial PDF is sampled and the state and probability density is propagated in time for each sample.

A schematic view of this method is shown in Figure 7-3. The figure shows schematically how a value of the PDF φ is calculated using a sample of $\boldsymbol{X}_0$. The initial state is uniformly sampled using a Sobol sampler or a pseudo-random number generator (Section 3-1-1), and for each sample the trajectory of the state and Ω is solved. The bounds of the uniform samples are defined by a multiple of the standard deviation of the distribution of each state such that a probability band of the distribution is sampled that is close to 100%.

The state $\boldsymbol{X}$ is forward propagated in time, because no stable solutions could be obtained for backward time propagation of the state of the uncontrolled rocket body, which is explained in Section 8-1. Therefore, the result of the DPP method is a scattered dataset of values of the state $\boldsymbol{X}$ at several epochs t and a corresponding probability density value.

Because the DPP method can only propagate the PDF of the initial state, any uncertainty in parameters in the state derivative model that are not state variables can only be included if the parameters are added to the state vector. Therefore, the uncertainty in the atmospheric density, which is modeled by a factor X_ρ, is included by including X_ρ as a state variable:

$$\boldsymbol{X}_{new} = \begin{pmatrix} \boldsymbol{X} \\ X_\rho \end{pmatrix} \tag{7-2}$$

The atmospheric density factor X_ρ stays constant troughout the trajectory, so the state derivative model is defined as:

$$\dot{X}_\rho = F_{X_\rho} = 0 \tag{7-3}$$

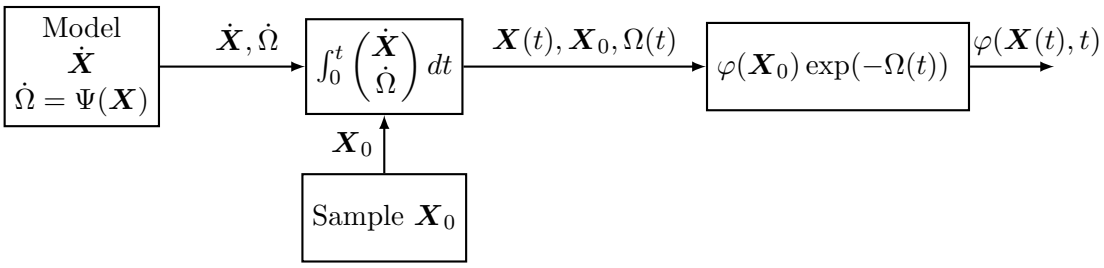

Figure 7-3: Schematic presentation of the DPP method.

7-2-1 The Model of Omega

The DPP method requires that a PDF correction factor Ω is added to the state derivative model, which is defined by:

$$\dot{\Omega} = \sum \frac{\partial F_i}{\partial X_i} \tag{7-4}$$

To derive $\dot{\Omega}$, the derivative of the state derivatives to the state variables need to be derived. These derivatives are zero for the kinematic part of the translational state:

$$\frac{\partial F_R}{\partial R} = \frac{\partial F_\delta}{\partial \delta} = \frac{\partial F_\tau}{\partial \tau} = 0 \tag{7-5}$$

The derivatives of the dynamic part of the translational state model are derived to be:

$$\frac{\partial F_{V_R}}{\partial V_R} = -\frac{\partial F_{z,V}/m}{\partial V_R} \tag{7-6a}$$

$$\frac{\partial F_{V_\tau}}{\partial V_\tau} = \frac{\partial F_{y,V}/m}{\partial V_\tau} + \frac{1}{r}\left(V_\delta \tan\delta - V_r\right) \tag{7-6b}$$

$$\frac{\partial F_{V_\delta}}{\partial V_\delta} = \frac{\partial F_{x,V}/m}{\partial V_\delta} - \frac{V_r}{r} \tag{7-6c}$$

The derivatives of the state derivatives of the quaternions are also zero:

$$\frac{\partial F_{q_i}}{\partial q_i} = 0 \quad \forall i \in [1,2,3,4] \tag{7-7}$$

The derivatives of $\dot{\omega}$ to ω are also zero, but only if $\boldsymbol{I}$ is a diagonal matrix:

$$\frac{\partial F_{\omega_n}}{\partial \omega_n} = 0 \quad \forall n \in [1,2,3] \quad \text{if} \quad I_{ij} = 0 \quad \forall i,j \in [1,2,3] \text{ if } i \neq j \tag{7-8}$$

which is the case for the inertia tensor of the Delta-K rocket body (Section 2-4). The derivative of the state derivative of the atmospheric density factor is also zero:

$$\frac{\partial F_{X_\rho}}{\partial X_\rho} = 0 \tag{7-9}$$

Using these equations, the state derivative of Ω is defined as:

$$\dot{\Omega} = -\frac{1}{m}\frac{\partial F_{z,V}}{\partial V_R} + \frac{1}{m}\frac{\partial F_{y,V}}{\partial V_\tau} + \frac{1}{r}\left(V_\delta \tan\delta - V_r\right) + \frac{1}{m}\frac{\partial F_{x,V}}{\partial V_\delta} - \frac{V_r}{r} \tag{7-10}$$

The partial derivatives of the forces with respect to each velocity component only contain the aerodynamic force, because the gravitational force is only dependent on the position of the body. The aerodynamic force expressed in the V frame is calculated using the following equation:

$$\boldsymbol{F}_{A,V} = \boldsymbol{C}_{V,AG}\boldsymbol{F}_{A,A} = \boldsymbol{C}_{V,AG}(\gamma(\boldsymbol{V}), \chi(\boldsymbol{V}), \sigma(\boldsymbol{V}))\frac{1}{2}\rho \boldsymbol{V}^2 S \boldsymbol{C}_{F,A}(\alpha(\boldsymbol{V}), \beta(\boldsymbol{V}), M(\boldsymbol{V})) \tag{7-11}$$

The aerodynamic force $\boldsymbol{F}_{A,V}$ is directly dependent on the velocity components and indirectly dependent on the velocity trough the transformation matrix $\boldsymbol{C}_{V,AG}$ and the aerodynamic coefficients $\boldsymbol{C}_{F,A}$ are a function of the velocity components. Therefore, the derivative of the aerodynamic force to the velocity components V_i are derived using the product rule of differentiation:

$$\frac{\partial \boldsymbol{F}_{A,V}}{\partial V_i} = \frac{\partial \boldsymbol{C}_{V,AG}}{\partial V_i}\boldsymbol{F}_{A,A} + \boldsymbol{C}_{V,AG}\frac{\partial \boldsymbol{C}_{F,A}}{\partial V_i}\frac{1}{2}\rho \boldsymbol{V}^2 S + \boldsymbol{C}_{V,AG}\rho V_i S \boldsymbol{C}_{F,A} \tag{7-12}$$

where the derivative of the transformation matrix to the velocity components is given by:

$$\frac{\partial \boldsymbol{C}_{V,AG}}{\partial V_i} = \frac{d\boldsymbol{C}_{V,AG}}{d\chi}\frac{d\chi}{dV_i} + \frac{d\boldsymbol{C}_{V,AG}}{d\gamma}\frac{d\gamma}{dV_i} + \frac{d\boldsymbol{C}_{V,AG}}{d\sigma}\frac{d\sigma}{dV_i} \tag{7-13}$$

and the derivative of the aerodynamic coefficients to the velocity components is given by:

$$\frac{\partial \boldsymbol{C}_{F,A}}{\partial V_i} = \frac{d\boldsymbol{C}_{F,A}}{d\alpha}\frac{d\alpha}{dV_i} + \frac{d\boldsymbol{C}_{F,A}}{d\beta}\frac{d\beta}{dV_i} + \frac{d\boldsymbol{C}_{F,A}}{dM}\frac{dM}{dV_i} \tag{7-14}$$

The derivative of the Mach number to each velocity component is derived to be:

$$\frac{dM}{dV_i} = \frac{V_i}{\|\boldsymbol{V}\|a} \tag{7-15}$$

These expressions are derived using the symbolic manipulation software Maple® and implemented in the DPP simulator. The derivatives of the aerodynamic coefficients to the aerodynamic angles and Mach number are derived numerically, because an aerodynamic database is used that depends on these parameters (Section 5-5). The derivatives are determined using the three-point midpoint rule (Burden and Faires, 2011):

$$\frac{df(x)}{dx}(x_0) \approx \frac{f(x_0 + h) - f(x_0 - h)}{2h} \tag{7-16}$$

where h is the stepsize and $f(x)$ is the function that is differentated at x_0. The error E of this numerical differentiation method is bounded by (Burden and Faires, 2011):

$$E \leq \frac{\epsilon}{h} + \frac{h^2 M}{6} \tag{7-17}$$

where ϵ is the numerical epsilon, the first part of the error is the rounding error, the second part is the truncation error and M is an unknown constant dependent on the third derivative of the function. This equation shows that the truncation error decreases with decreasing stepsize and the rounding error increases with decreasing stepsize. An approximate optimal value can be derived by finding the minimum of the error bound, resulting in:

$$h_{opt} \approx \sqrt[3]{\frac{3\epsilon}{M}} \tag{7-18}$$

Because the value of M is not known, the following stepsize is used:

$$h = x_0 \sqrt[3]{\epsilon} \tag{7-19}$$

This stepsize is scaled using the value x_0, because the errors will scale with the value of the function. The relative error for this differentiation rule is $O(h^2)$, so with a machine epsilon of $\epsilon \approx 10^{-16}$, the relative error will be $O(10^{-11})$.

7-2-2 Impact Prediction

The output of the DPP method is a scattered dataset that contains the value of the PDF as a function of the state and time. This dataset is used to obtain a PDF of the impact time. Considering that the output of the DPP represents a PDF of the state for several time values, distributions of state and time at impact are obtained by determining the conditional distribution (Section A-3):

$$f_{R=R_s(\delta),\boldsymbol{X}^*,t}(\boldsymbol{X}^*, t) = \frac{f_{\boldsymbol{X},t}(R = R_s(\delta), \boldsymbol{X}^*, t)}{A} \tag{7-20}$$

where $\boldsymbol{X}^*$ is the state vector without the radius R and A is a factor to normalize the PDF. This conditional distribution can be used to compute marginal distributions of time and location (δ, τ).

The time t is added to the PDF, such that impact-time distributions can be generated. The DPP method keeps the integral of the PDF constant in time, so the resulting distribution is not normalized by the standard procedure that is used to compute a conditional distribution and must be normalized after the computation.

In Section 4-2 it was shown that an accurate reconstruction of a multi-dimensional PDF is difficult to obtain using scattered data for a high-dimensional PDF. Therefore, the binning method, described in Section 4-2-5, will be employed to compute the impact-time distributions.

Chapter 8

Simulation and Verification

This chapter explains the simulators that are developed during this thesis and the verification proces. The chapter starts with a discussion on backward time propagation in Section 8-1, because this concept is used in several simulators. Subsequently, the simulators are discussed in Section 8-2, and the verification and validation process of these simulators is discussed in Section 8-3. The chapter is concluded with an analysis on the convergence and accuracy of the numerical integration process in Section 8-4.

8-1 Backward Time Propagation

Backward propagation is a technique to propagate the state backward in time. This can be used to find the initial conditions of a state $\boldsymbol{x}$ at a given moment in time. As discussed in Section 4-1, this technique is useful for the DPP method.

An atmospheric entry trajectory is the solution of an initial value problem, because the future trajectory of the body is fully determined by the current state of the body if uncertainties are not taken into account. This means that the problem can be defined as an initial value problem of the form:

$$\dot{\boldsymbol{x}} = \boldsymbol{f}(\boldsymbol{x}(t), t) \quad , \quad \boldsymbol{x}(t_0) = \boldsymbol{x_0} \tag{8-1}$$

where $\boldsymbol{f}(\boldsymbol{x}(t), t)$ is the state derivative model of the body. The solution to this problem is generally found using a numerical integrator that propagates the state $\boldsymbol{x}(t)$ forward in time. However, in some applications it may be useful to determine the state history $\boldsymbol{x}(t)$ or the initial condition $\boldsymbol{x}_0$ if only the final condition is known. This means that we want to find the solution of a final value problem:

$$\dot{\boldsymbol{x}} = \boldsymbol{f}(\boldsymbol{x}(t), t) \quad , \quad \boldsymbol{x}(t_f) = \boldsymbol{x_f} \tag{8-2}$$

In other words, one is interested in the initial conditions that leads to the given conditions at the final time t_f. Regular numerical integrators cannot be used to solve this problem,

because they are designed to solve initial value problems. However, the final value problem can be restated as an initial value problem using several transformations. The state $\boldsymbol{x}'(t')$ is introduced that is related with the state $\boldsymbol{x}(t)$ by the following definition:

$$\boldsymbol{x}'(t') = \boldsymbol{x}(t) \tag{8-3}$$

where t' is defined as:

$$t' = t_f - t \tag{8-4}$$

These definitions basically mean that the trajectory of the state $\boldsymbol{x}$ is equal to the trajectory of the transformed state $\boldsymbol{x}'$ if the time is reversed. So if the trajectory of $\boldsymbol{x}'$ is known, the trajectory of the state $\boldsymbol{x}$ can be derived using these definitions.

Inserting the relation between the state variables (Equation (8-3)) and the relation between t' and t (Equation (8-4)) into the initial value problem (Equation (8-1)) results in the following differential equation:

$$\frac{d\boldsymbol{x}'(t')}{dt'}\frac{dt'}{dt} = \boldsymbol{f}(\boldsymbol{x}'(t'), t_f - t') \tag{8-5}$$

Inserting the derivative of the reversed time variable t' to t results in the following differential equation:

$$\frac{d\boldsymbol{x}'(t')}{dt'} = -\boldsymbol{f}(\boldsymbol{x}'(t'), t_f - t') \tag{8-6}$$

Given the relation between the state $\boldsymbol{x}(t)$ and the reversed state $\boldsymbol{x}'(t')$ (Equation (8-3)), the initial condition can be determined:

$$\boldsymbol{x}'(0) = \boldsymbol{x}(t_f) = \boldsymbol{x}_f \tag{8-7}$$

Combining the differential equation of the reversed state $\boldsymbol{x}'$ and this initial condition yields the final value problem of $\boldsymbol{x}(t)$ defined as an initial value problem of $\boldsymbol{x}'(t')$:

$$\frac{d\boldsymbol{x}'(t')}{dt'} = -\boldsymbol{f}(\boldsymbol{x}'(t'), t_f - t') \quad , \quad \boldsymbol{x}'(0) = \boldsymbol{x}_f \tag{8-8}$$

This initial value problem can be solved using a numerical integrator to find the initial condition $\boldsymbol{x}_0$ that corresponds to a value of $\boldsymbol{x}(t)$. One can observe from the equation that if the state derivative model $\boldsymbol{f}$ is not directly dependent on time, multiplying the state derivative with minus one is sufficient. However, the NRLMSISE-00 model is dependent on time, so inversion of the time should be accounted for.

8-1-1 Stability

Solving a final value problem as an initial value problem can introduce stability problems. The following example will be used to illustrate these problems:

$$\dot{x} = ax \quad , \quad x(t_0) = x_0 \tag{8-9a}$$

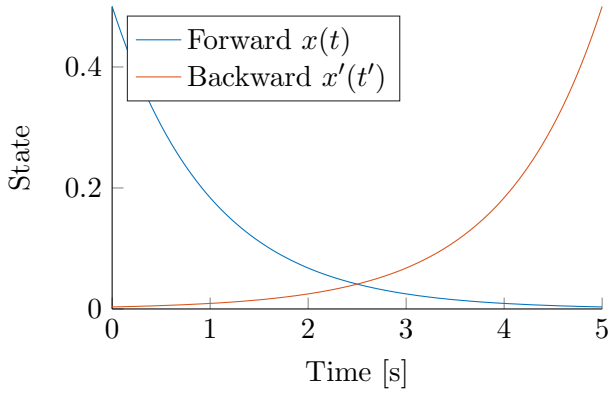

Figure 8-1: Illustration of forward and backward time propagation of x subject to $\dot{x} = -x$ with $x_0 = 0.5$.

$$\dot{x'} = -ax' \quad , \quad x(t_f) = x'(0) = x_f \tag{8-9b}$$

The equations show that the ODE is simply transformed by adding a minus sign, such that the final value problem is converted to an initial value problem. Solving both equations will yield the same outcome if x_f corresponds to x_0. The only difference is that the second equation is solved with backward time propagation. This means the state transformation condition (Equation (8-3)) holds for this case.

Consider the example shown in Figure 8-1, which uses a model with a value $a < 0$ and $x_0 > 0$. The figure shows that forward propagation results in a stable trajectory that converges to zero and backward propagation results in an unstable trajectory of x'. Because, backward time propagation results in an unstable trajectory, solving this trajectory can cause numerical issues. This means that solving the final value problem can cause numerical issues that are not present in the initial value problem. Especially when the original ODE is stiff, for example, when a has a large negative value, the transformed ODE has a large positive derivative so the transformed ODE is highly unstable.

8-1-2 Atmospheric Entry

To verify that backward propagation can be used to determine atmospheric entry trajectories several test cases were performed. A first test was performed that simulated the ballistic entry trajectory of an Apollo capsule using the model obtained from Mooij (2014). A 3 DoF simulation was performed with a gravity model that includes only the J_2 coefficient, an oblate spheroid earth model and the US76 atmosphere model. The test involved propagating the initial conditions forward from an altitude of 80 km to an altitude of 5 km after which, the final conditions were used in a backward propagation.

A plot of the altitude and velocity is shown in Figure 8-2. The plot shows the state as a function of flight time, which corresponds to t when propagating forward in time and to t' when propagation backward in time. As one can see in the figure, the trajectories resulting from forward and backward propagation seem identical. The absolute difference between the two trajectories is calculated and shown in Figure 8-3 as a function of the actual time. This figure clearly shows that the error between the two trajectories is very small. The error is

the largest at $t = 0$, which is logical because this is the final point of the backward time propagator so the numerical error is accumulated to this point.

It is important to consider that the final state is obtained using forward propagation, which introduces error. This final state is used as the initial condition of the backward propagator, so the error in the final state is also included when propagating the state backward in time. Therefore, a test was performed to obtain a more accurate final state and propagate this state backward in time. This isolates the errors of the backward propagator by truncating the step size of the forward propagator. It was observed that the errors are similar in magnitude, so no improvement was obtained. This is a logical result, because the first results were obtained using a Runge-Kutta 5(6) (RK5(6)) integrator with the tolerances set to 10^{-15}, which is close to the numerical roundof error.

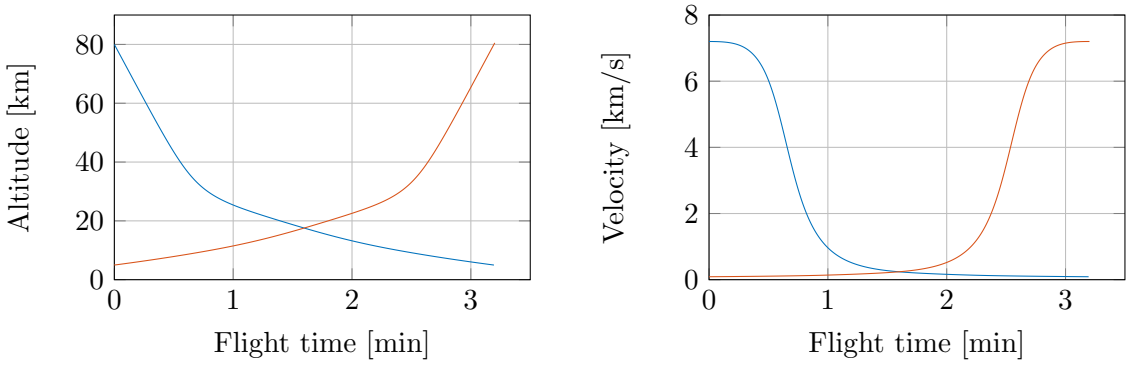

Figure 8-2: Example trajectory of an Apollo capsule obtained using forward(blue) and backward(red) propagation.

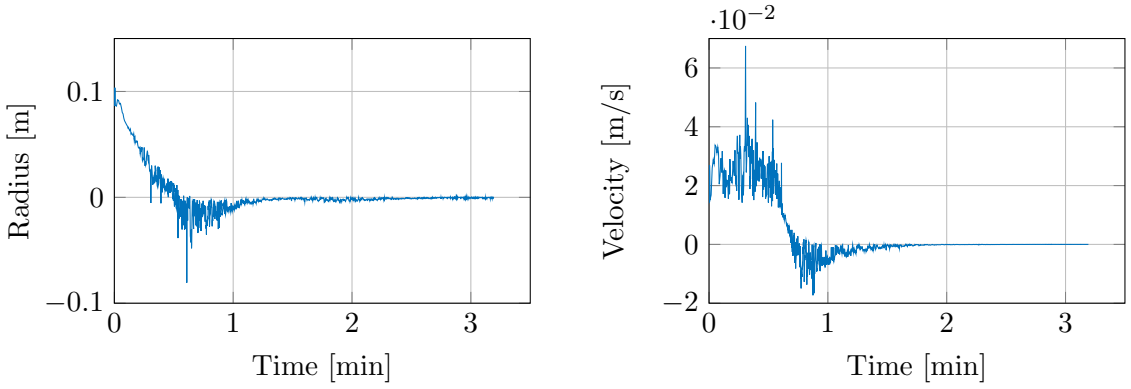

Figure 8-3: Absolute error of the radius and velocity for a 3 DoF simulation.

A similar test was performed with a 6 DoF simulator using the full model described in Chapter 5. The simulator was used to propagate the state forward in time until an altitude of 10 km after which it is propagated backward in time. The absolute error in the radius and velocity is shown in Figure 8-4. The figure shows that the errors that are obtained are larger than for the 3 DoF case. However, the errors are still quite small compared to the uncertainty in the initial state (Section 6-1).

This example shows that backward time propagation can be used for 6 DoF entry trajectory

simulations. However, the backward time propagator could not obtain a solution within a reasonable amount of computation time when the state was propagated to the Earths surface. This can be explained by looking at the velocity profile of the trajectory, which is similar to the velocity profile of the 3 DoF simulation (Figure 8-2). When propagating the state forward in time, the velocity decreases until it reaches the terminal velocity, which is a stable trajectory. However, when propagating the state backward in time, the velocity has an unstable trajectory, because the velocity increases rapidly due to aerodynamic forces. Furthermore, the flight-path angle is already $-89.4°$ at 10 km and approaches $-90°$ at the end of the trajectory, so the heading angle approaches a singularity. This causes numerical problems, because the flight direction becomes undefined. A physical explanation could be that a large number of entry trajectories can end in a vertical falling trajectory that are approximately the same at the end of the trajectory. Therefore, propagating such a trajectory backwards is very sensitive to errors in the initial phase.

As a result, a small error in backward time propagation of the final state, results in a large error in the initial state. Even if a solution could be obtained, the step size should be very small to obtain an accurate solution. Therefore, backward time propagation will not be used for the DPP method for impact prediction, because the reliability cannot be guaranteed.

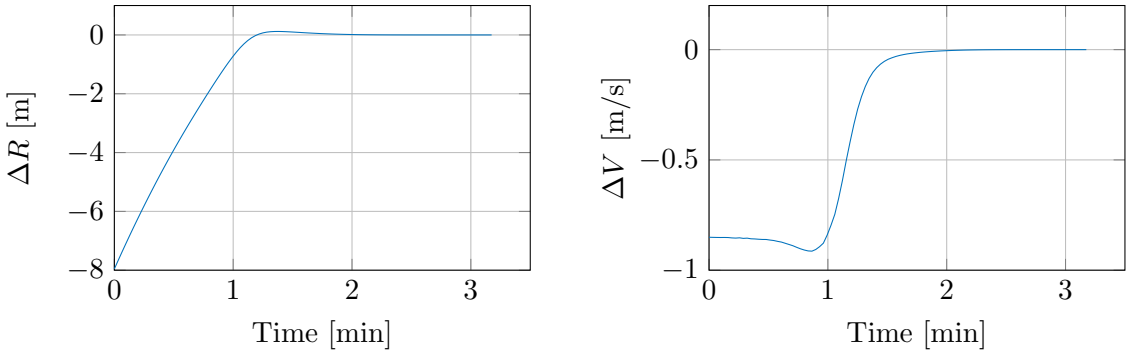

Figure 8-4: Absolute error of the radius R and velocity V for a 6 DoF simulation.

8-1-3 Direct PDF Propagation

Backward time propagation is a useful technique for the DPP method, because the value of the PDF can be solved at a specified grid of $\boldsymbol{x}$ at a specific time. Transforming the final value problem to an initial value problem results in the following system of ODEs:

$$\frac{d\boldsymbol{X}'}{dt'} = -\boldsymbol{F}(\boldsymbol{X}'(t'), t_f - t') \quad \text{with} \quad \boldsymbol{X}'(0) = \boldsymbol{x}_f \tag{8-10a}$$

$$\frac{d\Omega}{dt} = \Psi(\boldsymbol{X}'(t')) \quad \text{with} \quad \Omega(t_0) = 0 \tag{8-10b}$$

The PDF correction factor Ω is not solved in a reverse way, because only the initial condition of Ω is known. However, the state $\boldsymbol{X}'(t')$ can directly be used, because it is equal to the

state $\boldsymbol{X}(t)$. The numerical integrator considers the two different time variables t' and t as the same. This means that the timestep in t' of the state $\boldsymbol{X}$ is equal to the timestep in t for Ω.

After performing the integration, the reversed time value t' will be equal to t_f, so the initial state is obtained:

$$\boldsymbol{X}'(t' = t_f - t_0) = \boldsymbol{X}_0 \tag{8-11}$$

Simultaneously the time $t = t_f$ for Ω, so the PDF correction factor $\Omega(t_f)$ is known at the final time. The value of $\boldsymbol{X}_0$ and $\Omega(t_f)$ can be used in Equation (3-29) to obtain the value of the PDF at the final time and $\boldsymbol{X}$.

8-2 Simulators

Several simulators were developed that are used to test the methods and perform the simulations that are required for the research. These simulators are discussed in this section.

8-2-1 External Software

The simulators and other software components are programmed in C++ and make use of several libraries that are used for scientific computing. These libraries are:

TU Delft Astrodynamics Toolbox (Tudat) The Tudat[1] is a C++ library that contains a large number of functions and classes that can be used to solve general problems related to Astrodynamics. The following functions are used from this library:

- Variable stepsize numerical integrators - The Runge-Kutta 5(6) or Runge-Kutta 7(8) integrators are used to integrate the equations of motion (Section 5-4).
- Reference frame transformations (Section 5-1)
- Multi-linear interpolator: To interpolate the aerodynamic database (Section 5-5).
- Gravity model: Central gravity model and the J_2 gravity model (Section 5-6).
- Atmosphere models: C++ wrapper of C code of the NRLMSISE-00 model and the US Standard Atmosphere 1976 (Section 5-7).

The following functions have been developed for the Tudat library:

- Kernel Density Distribution Estimator: A multi-dimensional estimator (Section 3-2).
- Radial Basis Function Interpolator (Chapter 4).
- Hermite Interpolator
- Space weather data file reader: Is used to provide input for the NRLMSISE-00 atmosphere model. (Section 5-7).
- Probability distributions: Multi-dimensional Gaussian, Multi-dimensional Uniform, Lognormal and Gaussian Copulae (Section A-4)

[1] `http://tudat.tudelft.nl/projects/tudat`; date accessed: 15-08-2016

- Numerical Quadrature: Trapezoid integrator
- Random Sampler for correlated samples

Eigen Eigen[2] is a C++ library that can be used to perform linear algebra operations. This library is used for all the linear algebra operations.

Boost The Boost[3] library contains a large number of functions. This library is used for memory management, time keeping and random number generation.

GSL The GNU Scientific Library (GSL)[4] contains a large number of mathematical routines. This library is used for the probability distributions and quasi-random number generation.

Jsoncpp The Jsoncpp library[5] is used to process config and input files, which completely control all simulators.

NRLMSISE-00 The C source code[6] is used with a C++ wrapper of the NRLMSISE-00 model provided by Tudat.

8-2-2 Trajectory Simulator

A trajectory simulator is developed that can be used to simulate an atmospheric decay and entry trajectory. The simulator uses the equations defined in Chapter 5 to propagate the translational and rotational state of the body.

The trajectory simulator is programmed in C++ and is developed using object-oriented programming. A trajectory simulator module is programmed that contains all the module, which are shown in Figure 8-5. The simulator is build using the following modules:

Integrator The Runge-Kutta integrator of Tudat is linked to the state derivative model and is used to propagate the state $\boldsymbol{X}$ in time.

State derivative The state derivative model uses the state $\boldsymbol{X}$, other dependent variables $\boldsymbol{p}$, and the models, described in Chapter 5, to calculate the derivative of the state.

Body The body contains all information about the state of the Delta-K rocket body including the properties of the body that are used in the models. The state of the body is updated by the integrator every integration step and all dependent variables are updated by this module.

Settings The simulator settings is used to vary the models that are used, the settings of the models and the physical constants that are used. The integrator settings contains all settings for the numerical integrator.

[2] `https://eigen.tuxfamily.org/dox/`; date accessed: 15-08-2016
[3] `http://www.boost.org/`; date accessed: 15-08-2016
[4] `https://www.gnu.org/software/gsl/`; date accessed: 15-08-2016
[5] `https://github.com/open-source-parsers/jsoncpp`; date accessed: 15-08-2016
[6] `https://github.com/magnific0/nrlmsise-00`; date accessed: 15-08-2016

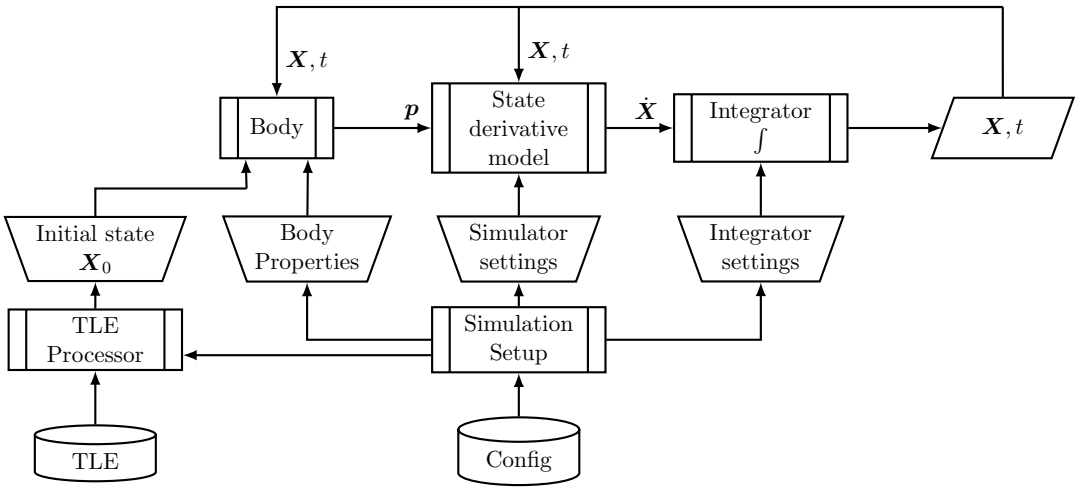

Figure 8-5: Software architecture of the trajectory simulator.

Body properties The config file provides the mass, inertia tensor, aerodynamic reference length and aerodynamic reference surface of the Delta-K rocket body. These properties are saved in the body module and are used in the state derivative model.

Simulation setup The simulation setup module uses a Json config file to provide all the settings and input parameters for the models, and the initial state of the Delta-K rocket body.

TLE Processor The TLE processor reads the TLE file and uses the TLE to initialize the SGP4 simulator. The output of the SGP4 simulator is an initial state in cartesian coordinates in the inertial frame, which is converted to the state variables described in Section 5-2.

The output of the numerical integrator is the state of the Delta-K rocket body at a specific time. The body module uses this state and time to update the dependent variables. A software architecture of this calculation process is shown in Figure 8-6. The following dependent variables are calculated in this process:

- Altitude h.
- Mach number M.
- Aerodynamic angles α, β, σ (Section 5-3).
- Flight-path angle γ and heading angle χ (Section 5-3).

The equations of motion are used to compute the state derivative in the state derivative model. A software architecture for this process is shown in Figure 8-7. The following models are used in to provide input to the equations of motion:

Earth model The model of the Earth contains the rotational velocity of the Earth ω_E and is used to compute the surface radius R_s (Section 5-8).

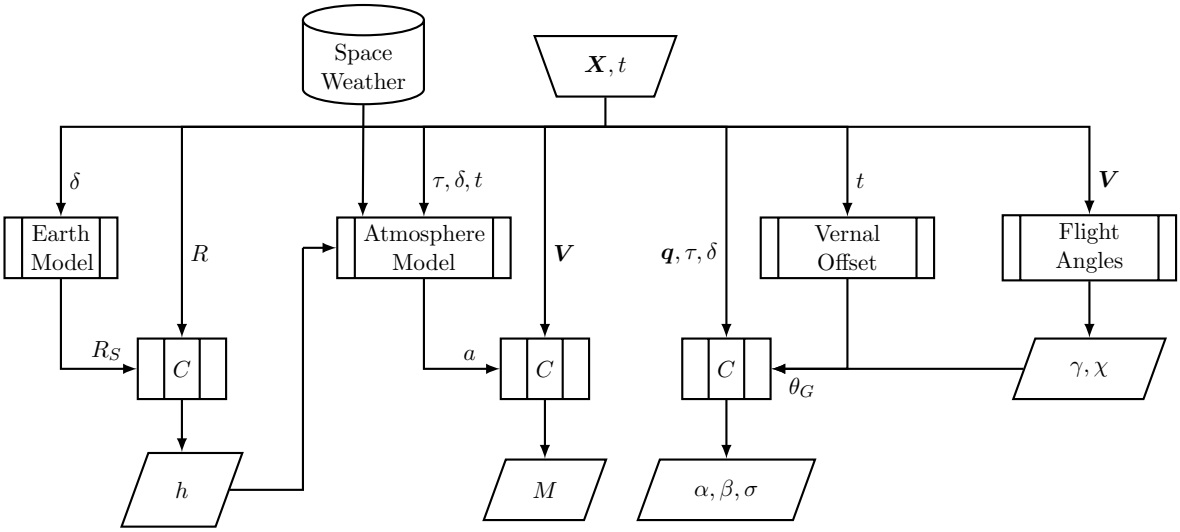

Figure 8-6: Software architecture of the dependent variable calculations inside the body.

Aerodynamic model This model is used to calculate the aerodynamic forces and moments. The aerodynamic database is linearly interpolated using the angle of attack α, the angle of sideslip β and the Mach number M to obtain the aerodynamic coefficients. The knudsen number is calculated using the mean free path λ and is used to provide aerodynamic coefficients for the transient flow regime (Section 5-5).

Atmosphere model The atmosphere model (NRLMSISE-00) is used to calculate the atmospheric density ρ and the speed of sound a. A space-weather datafile is obtained from Kelso (2016) and the solar activity parameters are extracted that corresponds to the current time. This datafile provides input for the NRLMSISE-00 model. A C version of the original Fortran source code release of the NRLMSISE-00 model, and a C++ wrapper provided by Tudat are used to provide (Section 5-7).

Gravity model The gravity model is used to calculate the gravity force (Section 5-6).

8-2-3 Monte-Carlo Simulator

The MC simulator uses the trajectory simulator to simulate a large number of trajectories (Section 7-1). These trajectories originate from different initial conditions that are obtained using random sampling. A software architecture of the MC simulation is shown in Figure 8-8. The modules that are shown in the architecture have the following functions:

TLE Processor The TLE processor provides the initial state for the random sampler. A more detailed description of the TLE processor is provided in Section 8-2-2.

Uncertainty Model The uncertainty model contains all the information about the uncertainty in the initial state and the atmospheric density factor as specified in Chapter 6.

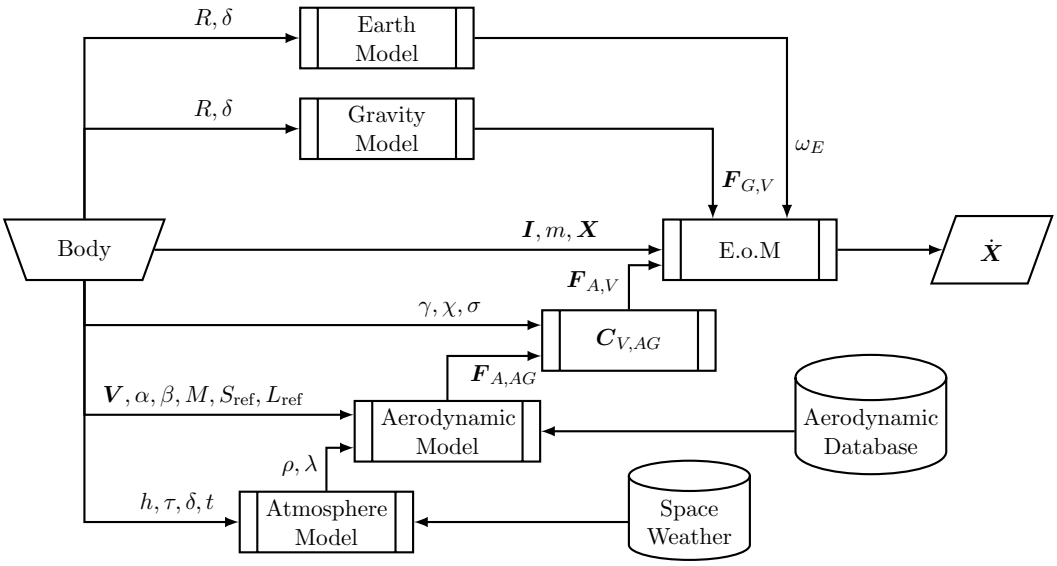

Figure 8-7: Software architecture of the state derivative calculation.

Random Sampler The random sampler generates uniformly distributed random samples using a Mersenne Twister implemented in the Boost library (Section 8-2-1) or using Sobol sampling implemented in the GSL library. These uniform samples are used to generate samples of the initial state and the atmospheric density factor.

Trajectory Simulator The trajectory simulator is used to simulate a trajectory for all the initial state samples $(\hat{\boldsymbol{X}}_0, \hat{X}_\rho)$ generated by the random sampler. The trajectory simulator described in Section 8-2-2 is used to simulate the trajectories until impact ($h = 0$ km). The output is a dataset of state variables at impact and the impact time.

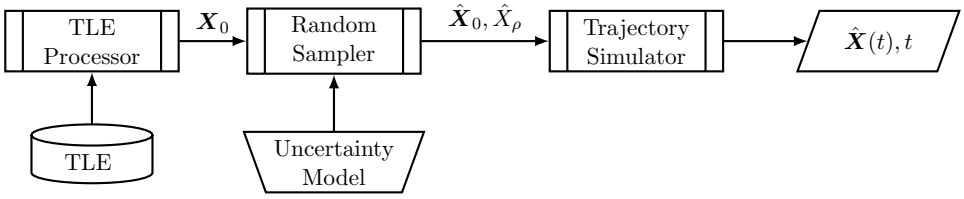

Figure 8-8: Software architecture of the Monte Carlo simulation.

8-2-4 DPP Simulator

The DPP simulator uses the trajectory simulator to propagate the PDF of the state as described in Section 7-2. A software architecture is shown in Figure 8-9. A more detailed description of the simulator is provided below. The process shown in the figure is repeated for all the samples that are generated.

TLE Processor The TLE processor provides the initial state for the random sampler. A more detailed description of the TLE processor is provided in Section 8-2-2.

Sampler The sampler uses a pseudo-random generator or a Sobol sampler to generate uniform samples of the initial state $\hat{\boldsymbol{X}}_0$ and the atmospheric density factor. The bounds of uniform samples can be adjusted by any multiple of the standard deviation of the data.

Uncertainty Model The uncertainty model contains all the information about the uncertainty in the initial state and the atmospheric density factor as specified in Chapter 6. The module is an implementation of Equation (6-33).

Initial State Distribution The initial state distribution module is an implementation of the PDFs that are derived in Chapter 6. The probability distributions are implemented by the Boost library and used in the software.

Trajectory Simulator The trajectory simulator described in Section 8-2-2 is used to simulate the trajectories. The trajectory simulator is used with the DPP mode setting on, such that Ω is also included in the state derivative model and propagated in time. For each sample $\hat{\boldsymbol{X}}_0$, a trajectory is simulated, which results in the state $\hat{\boldsymbol{X}}(t)$, and $\Omega(t)$ is determined.

DPP This module calculates the value of the PDF $\varphi(\hat{\boldsymbol{X}}(t), t)$ that corresponds to the output state $\hat{\boldsymbol{X}}(t)$ using $\Omega(t)$ and the PDF of the initial state $\varphi(\hat{\boldsymbol{X}}_0)$. The output of the simulator is a dataset of the state (including the atmospheric density factor), time and a corresponding probability density value.

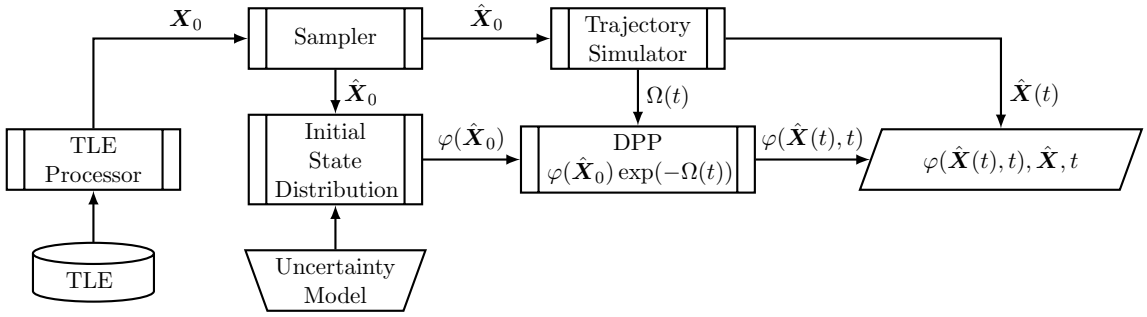

Figure 8-9: Software architecture of the DPP simulation.

8-3 Verification and Validation

A series of tests is performed to verify and validate the developed software. Unit tests are performed to test each individual function in which the solution of the software is compared with an exact solution. Additionally, system tests are performed to test the simulator as a whole. This ensures that the interfaces work correctly and all models are properly setup and linked. The system tests that are performed are described in this section.

8-3-1 Trajectory simulator

The trajectory simulator is verified by performing four system test, which are discussed in this section. These tests verify that the models are correclty implemented and its interfaces.

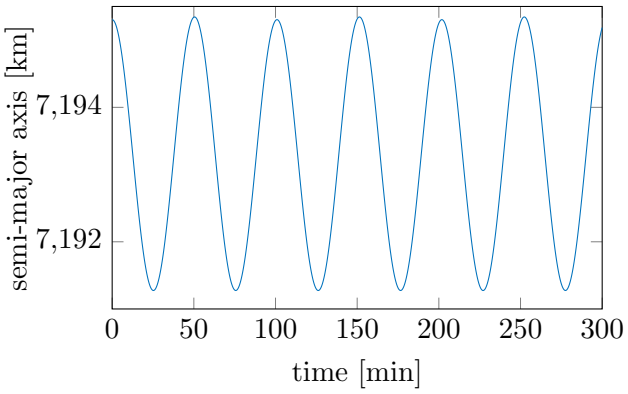

Figure 8-10: Variation in semi-major axis versus time.

Kepler orbit - A simulation was performed without atmosphere model and an initial velocity vector that should result in a circular orbit. The simulator results exactly matches with a circular orbit. This test verifies the implementation of the translational equations of motion, the central gravity model implementation and the interface with the gravity model.

Earth repeat-orbit - A simulation was performed with the J_2 perturbed gravity model. The inclination $i = 28°$ and semi-major axis $a = 7195.304$ km were selected such that a circular Earth-repeat orbit was obtained. An orbit was obtained that repeats its ground track every 14 orbits for each day. The error in longitude that was observed was a maximum of 0.1 degrees, which can be attributed to numerical errors. In addition, the variations in the orbital elements were tested with the expected variations described in Wakker (2015). It was observed that the variation in semi-major axis and inclination exactly matches the expected variations. The variation in the semi-major axis is shown in Figure 8-10. The minimum semi-major axis due to the J_2 perturbation was calculated $a_{min} = 7191.25$ km and it was observed that it matches with a maximum error of 0.4%.

A three DoF ballistic Apollo entry was simulated and compared with the solution obtained by Mooij (2014). The following properties were used to perform the simulation:

$$\begin{aligned} K = \frac{mg}{C_D S} &= 2806 \text{ N/m}^2 \\ m &= 4976 \text{ kg} \\ C_D &= 1.45 \\ S_{\text{ref}} &= 12 \text{ m} \\ V_E &= 7,200 \text{ m/s} \end{aligned}$$

An analytical and numerical solution were obtained, which are shown in Figure 8-11. The analytical solution is obtained by assuming an exponential atmosphere model with $\rho_0 = 1.225$ kg/m^3 and a scale height $H_s = 6950$ m. The numerical solution is obtained using a three DoF simulation with a central gravity field model and the US Standard Atmosphere 1976 model. The left figure is obtained with an initial flight path angle of $\gamma_E = -10°$ and the right figure is obtained with an initial flight path angle of $\gamma_E = -20°$. The figures shows that the numerical solution and analytical solution are similar. Furthermore, the figure exactly matches with the result obtained in Mooij (2014). This test verifies the implementation of the

models, but more importantly, this test verifies the interfaces between the atmospheric model, the aerodynamic model and the equations of motion, and the interface between the gravity model and the equations of motion. Even though different atmospheric and gravity models are used in the final simulations, the interfaces are verified, so if the models are verified, the simulator can be assumed verified.

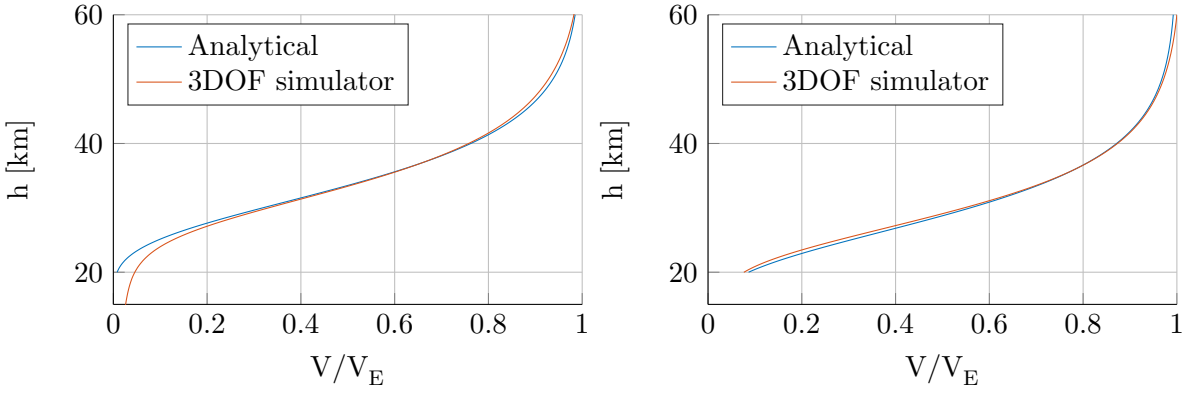

Figure 8-11: Altitude velocity plot of the 3 DoF ballistic Apollo entry simulation with $\gamma_E = -10°$ (left) and $\gamma_E = -20°$ (right).

The 6 DoF simulator was verified using the following tests:

- A simulation was performed with the atmospheric density set to zero and a constant angular rate about one of the axis. A kepler orbit was obtained and it was observed that the variation of the quaternions exactly matches with an analytical solution obtained from Equation (5-4):

$$q_i = e_i \sin(\omega_i t/2) \tag{8-12}$$

- A simulation was performed with the atmospheric density set to zero and a constant angular rate about all axis. A kepler orbit was obtained and it was verified that the angular momentum stays constant.

These tests show that the rotational state model is correctly implemented and that the rotational state model is uncoupled from the translational state model.

8-3-2 Monte-Carlo Simulator

The MC simulator is only a wrapper around the trajectory simulator and adds a random sampler. Therefore, this simulator can be verified by verifying the interfaces and the random sampler. The random sampler of the MC simulator is tested by generating random samples and comparing a KDE of the samples with the distributions that are used to perform the sampling. In addition, the MC simulator is validated by comparing the results of the simulator with the results obtained by Ronse (2013).

8-3-3 Direct PDF Propagation Simulator

The DPP simulator uses the verified trajectory simulator with the parameter Ω added to the state-derivative model. The model of $\dot{\Omega}$ is verified by performing a simulation where the model of $\dot{\Omega}$ is derived using numerical differentiation, and using an analytical expression. The results will be further discussed in Section 9-1.

The initial PDF is verified by using the developed software to generate the distributions and to verify this result with the desired distributions. The kernel density distribution generator is verified with the kernel density function of Matlab®. The random sampler is verified by comparing the samples with the desired distribution of the samples. Subsequently, the DPP simulator is verified by testing if the correct probability density is calculated by the method.

8-4 Numerical Integration Accuracy, Stability and Convergence

The trajectory simulator uses a Runge-Kutta variable stepsize integrator to perform the simulations. Several simulations were performed with different integrator settings to test the convergence of the simulator and define the settings that will be used in the simulations.

Several tests are performed with different tolerance settings and it was found that for some cases, large descrepancies between the trajectories were observed. In Figure 8-12, one of these cases is shown in which the integrator clearly does not yield identical results. It was found that all the impact points lie on the same ground track for these cases, so the dispersion is governed by a dispersion in flight time. The maximum difference in impact location for this case is 50 degrees in longitude, which corresponds to about 0.15 hrs of difference in flight time.

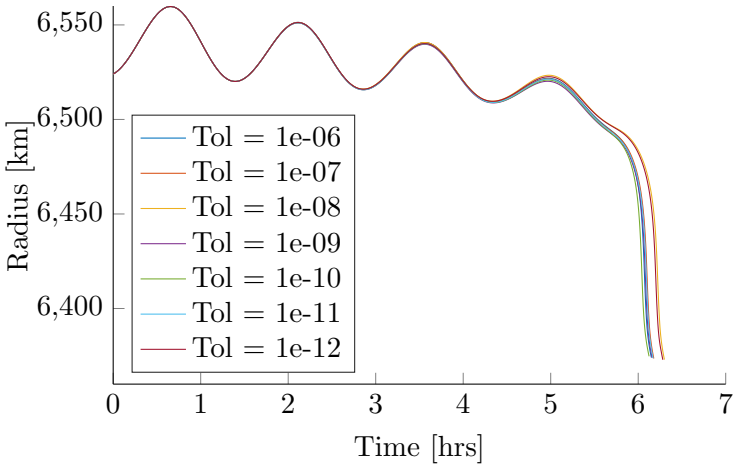

Figure 8-12: Simulations with different error tolerances using TLE 3.

Since these trajectories result from identical initial conditions, the discrepancies are purely due to numerical issues. An analysis was performed and no relation between dispersion of the trajectories and the translational state could be found. Therefore a Monte Carlo analysis was performed to determine the influence of the rotational state on the numerical dispersion.

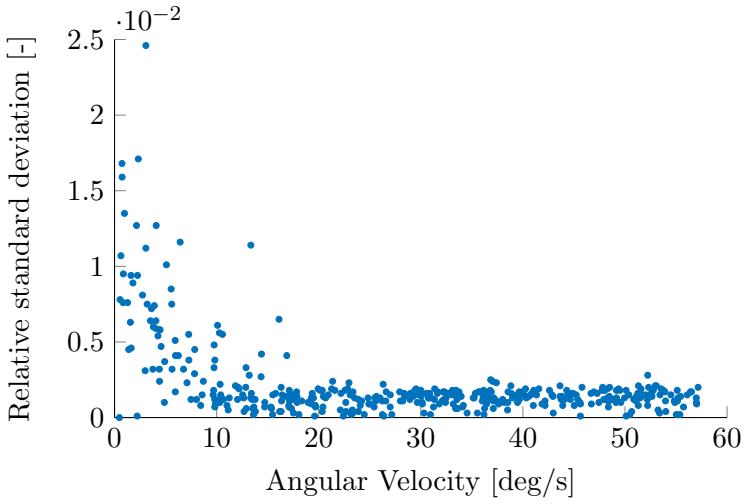

Figure 8-13: Dispersion (standard deviation) of the flight time due to varying integrator tolerances relative to the flight time as a function of angular velocity.

A total of 400 simulations were performed with a random initial attitude and random initial angular velocity. Each of these simulations was performed 7 times for integrator tolerances from 10^{-6} to 10^{-12}. The dispersion in flight time was calculated for these cases by taking the standard deviation of the impact time obtained from different tolerance settings, resulting in 400 dispersion measures related to varying initial rotational states. Also no relation was found between the initial aerodynamic angles and the dispersion in impact time.

However, as shown in Figure 8-13, there is a clear relation between the initial angular velocity and the dispersion in impact time. The figure shows the relative standard deviation, which is the standard deviation of the flight time divided by the flight time, versus the angular velocity. One can clearly observe that the dispersion increases greatly for small angular velocities.

An explanation for this result can be that when the angular velocity is small, the rotational state of the body is more affected by perturbations in the aerodynamic moments. These numerical perturbations can cause a different evolution of the attitude in time, which results in a different trajectory. Because the rotational state in the decay phase is important for the impact prediction (Ronse, 2013), this can result in a large dispersion of the trajectories.

It was further found that the flight time was not correlated with the integrator tolerance, so the impact time seems to behave randomly with respect to the integrator tolerance. This means that one cannot say that a higher tolerance results in a more accurate result, because no convergence is observed when the tolerance is increased. This shows that the problem is inherently sensitive.

The numerical sensitivity of the problem causes errors in the flight time of the body. However, the uncertainty in the state and atmospheric density has a much larger influence on the impact time, which can be much larger than 50% of the flight time as shown in Chapter 9. As shown in Figure 8-13, the maximum dispersion that was observed is about 2.5% of the flight time, so it is not expected to have a large impact on the impact time distribution. To verify the impact on the results, an impact time distribution was generated for each integrator setting using the data with a random rotational state. These impact time distributions are used to

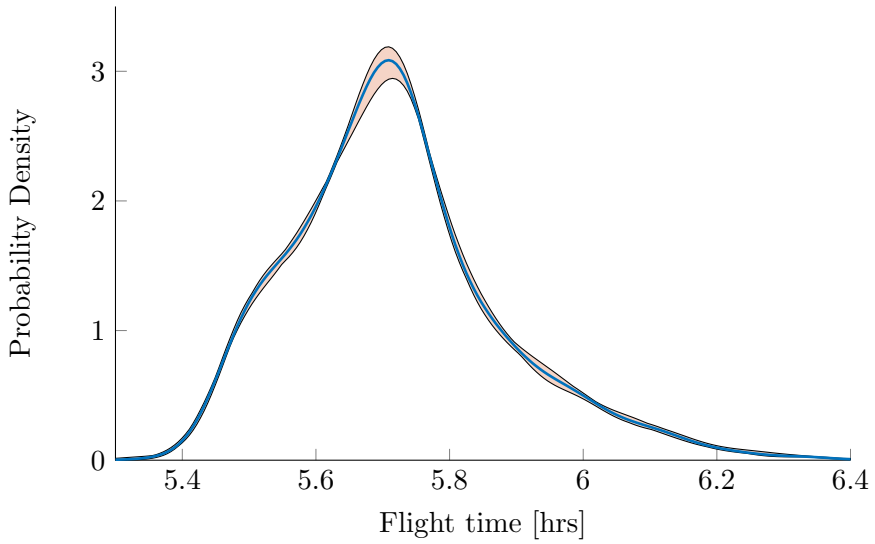

Figure 8-14: Impact time distribution with dispersion due to numerical descrepancies.

determine a dispersion band caused by numerical inaccuracies or sensitivity. In Figure 8-14, one can see the mean impact time distribution of these distributions and the dispersion band due to numerical inaccuracies. The figure shows that the inaccuracies hardly affect the shape of the distribution.

All simulations showed that the dispersion of the impact points due to numerical sensitivity decreases with decreasing maximum stepsize. The simulations showed that the stepsize only reaches the maximum stepsize in the decay phase, so this means that errors introduced during the decay phase accumulate in the trajectory and result in a larger dispersion. In addition, in the final part of the trajectory, the flight path angle approaches -90 degrees, so the heading angle becomes singular. This causes numerical issues, so the minimum stepsize needed to be truncated such that solutions could be obtained. A plot of the flight path angle versus the numerical stepsize showed that the stepsize is only truncated by the minimum stepsize when the flight path angle is close to $-90°$. This confirms that these numerical issues are caused by the singularity. These numerical issues are a consequence of the state variables that are used, because velocity components in the vertical frame are defined using the heading angle, which becomes singular.

Furthermore, a total of 40 trajectories were simulated using different tolerance settings and maximum stepsize. It was observed that the RK7(8) integrator resulted in faster solutions than the RKF5(6) integrator for the same integrator settings. Because no convergence of the solution was observed with respect to integrator tolerance, the integrator tolerance cannot be selected based on any accuracy treshold. Based on these observations, the integrator settings that are chosen, which are provided in Table 8-1.

Table 8-1: Integrator settings

Integrator	RKF7(8)
Absolute tolerance	10^{-9}
Relative tolerance	10^{-9}
Minimum stepsize	10^{-4} s
Maximum stepsize	1 s

It must be noted that only the relative tolerance is actively used to control the error in the Runge-Kutta Fehlberg integrator of Tudat. The absolute tolerance only serves as a minimum absolute tolerance, which is used when the state approaches zero.

Chapter 9

Results

The developed simulators are used to perform statistical impact predictions of the Delta-K rocket body. The results of these simulations are discussed in this chapter. The performance of the DPP method for statistical impact prediction is compared with the MC method in Section 9-1. Impact time distributions are derived for several cases of the Delta-K rocket body in Section 9-2. A statistical validation is performed on these impact time distributions and a comparison is performed with the TIPs and the impact time distributions generated in the research of Ronse (2013).

9-1 Direct PDF Propagation

One of the goals of the research is to apply the direct PDF propagation method to statistical impact prediction of the Delta-K rocket body. The results that were obtained with the DPP simulator are presented in this section.

9-1-1 The Evolution of Omega

As explained in Section 7-2 , the DPP method simulates a large number of trajectories and simultaniously solves the PDF correction factor Ω for each trajectory. Because this parameter indicates shape changing of the PDF, the evolution of Ω using Equation (7-10) is investigated before executing the full method. This parameter governs the evolution of the probability density of that sample. A value of Ω that is higher than zero means that the probability density of that sample is decreased and a value that is lower than zero means that the probability density is increased. This generally means that the PDF gets more concentrated for a negative value of Ω.

Figure 9-1 shows the evolution Ω in time for initial conditions obtained using TLE 3 (Table 2-1). The figure shows that Ω oscillates with a small amplitude for the first part of the trajectory. In this part, the evolution is dominated by the term:

$$\frac{1}{r}\left(V_\delta \tan\delta - V_r\right)$$

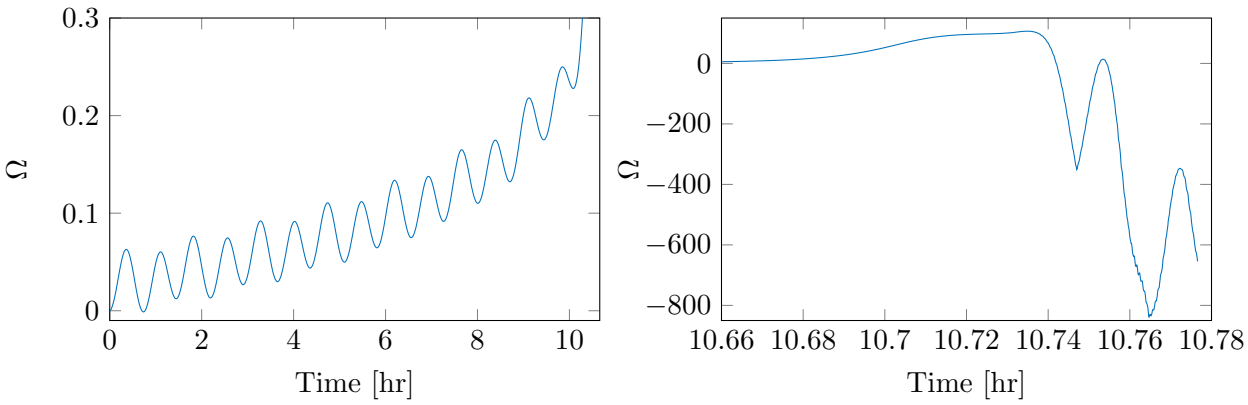

Figure 9-1: Evolution of Ω in time plotted for the complete trajectory. (TLE 3)

because the forces acting on the body are relatively small and V_δ is large for this part of the trajectory. The oscillations of Ω correspond to the oscilations in $V_\delta \tan \delta$. During the final phase of the trajectory, the value of Ω blows up and rapidly decreases to a value around -800. Unfortunately, the probability density is determined by multiplying the initial value of the PDF with $\exp(-\Omega)$ (Equation (3-29)) and the return value of $\exp(800)$ from a computer equals infinity, clearly a value, which is not acceptable. In addition, strange jumps are observed in the value of Ω that are unlikely.

Nevertheless, it is expected that Ω oscilates during the decay phase and increases when the entry phase starts. During the first part of the entry phase, the uncertainty in the initial conditions cause the uncertainty to grow as a result of the varying atmospheric density and errors in the velocity. The body accelerates, so the dispersion in velocity and position gets larger. The PDF thus gets wider, so Ω should increase such that the PDF values become smaller. Subsequently, when the aerodynamic accelerations get larger, the velocity decreases and the PDF becomes smaller, so the sample values of the PDF should increase and Ω should decrease. For example, the velocity can be expressed in the body frame, which allows to directly calculate the aerodynamic angles from the velocity components.

Instability

The instability of Ω shown in Figure 9-1, which occurs in the final part of the trajectory were investigated. A first explanation is that this instability occurs due to errors in the equations that define $\dot{\Omega}$, which is used to propagate Ω. However, these simulations were also performed without analytical expressions for the derivatives of the forces to the velocity and instead used numerical differentiation to determine these terms, which produced similar unstable behavior. In addition, the analytical expressions for $\dot{\Omega}$ are derived using the symbolic manipulation software Maple®, which makes it unlikely that errors in the equations are present. Becaue similar results were obtained using numerical differentiation, it is expected that the instability is not caused by errors in the derived equations. Therefore, an analysis has been performed to find the cause of this unstable behavior.

In Figure 9-2, the value of Ω is plotted versus altitude and flight-path angle. The figure shows that Ω becomes unstable in the lower part of the atmosphere. The instability starts

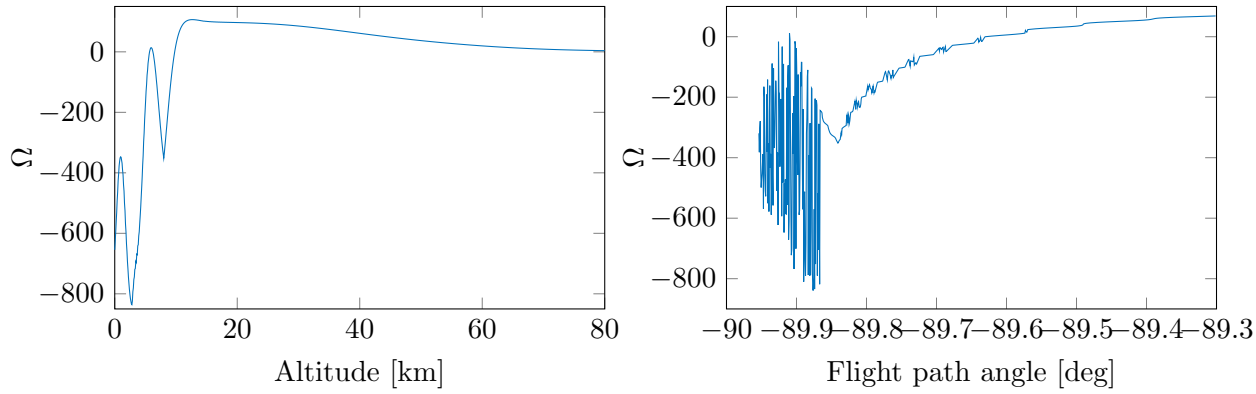

Figure 9-2: Evolution of Ω as a function of altitude and flight-path angle. (TLE 3)

around 7 km altitude, which corresponds to a flight-path angle of 89.5°. The value of Ω becomes more unstable as the altitude decreases and the flight-path angle approaches −90°. At this moment in the trajectory, the body is in almost vertical flight, so the heading angle approaches a singularity and starts to oscillate rapidly. The heading angle is used to calculate the aerodynamic angles, so the aerodynamic forces change rapidly. This does not mean that the magnitude changes rapidly, but any of the individual components of the aerodynamic force, because the direction changes.

The reason that Ω becomes unstable is clearly seen in Figure 9-3. The figure shows the aerodynamic acceleration in the X direction of the V frame as a function of the north velocity for the final part of the trajectory. The derivative of Ω is defined using the derivative of this aerodynamic acceleration to the north velocity (Equation (7-10)). Observing the figure, one can see that the slope becomes largely negative for some parts and jumps in the slope occur periodically. These jumps are also shown in the plot of Ω as a function of the flight-path angle (Figure 9-2). At the end of the trajectory, the north velocity becomes small and a circle-like trajectory in the acceleration-velocity phase space occurs. As a result the derivatives become very large and even undefined at several points in time.

The instabilities that are observed are a consequence of the choice of the state variables that are used. A different set of state variables that mitigates these problems would be preferred such that Ω is defined using terms that do not result in these problems. Using the velocity V, flight-path angle γ and the heading angle χ instead would not solve this problem, because the heading angle becomes singular. A better choice would be to use three cartesian velocity components defined in the inertial frame or the body frame. These state variables need to be chosen such that the aerodynamic angles are determined without any dependence on the flight-path angle or heading angle.

9-1-2 Avoiding the Instability

A test has been performed to avoid the problems discussed in the previous section, by setting the derivatives of the east and north velocity to zero at the moment where the flight-path angle reaches −89.5 degrees, which corresponds to 7 km altitude and an approximate horizonal velocity of around 0.5 m/s. This limits the flight-path angle to this value, so that the instability is prevented. As a result the derivatives to these velocity terms also needs to be

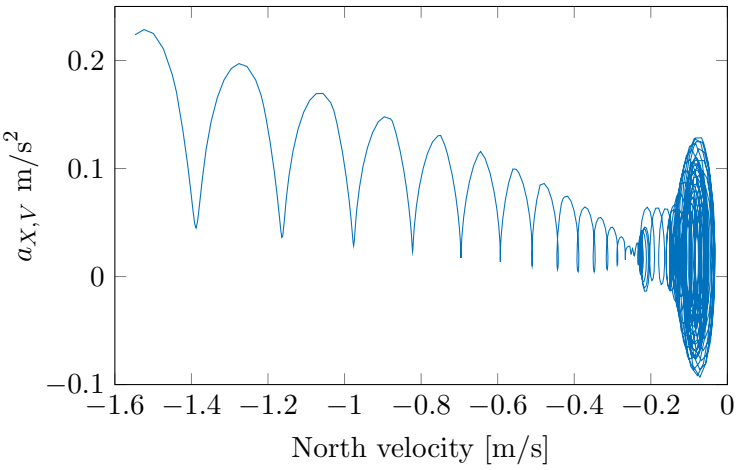

Figure 9-3: Evolution of the aerodynamic acceleration in the X direction of the V frame as a function of the north velocity starting from $t = 10.735$ hrs.

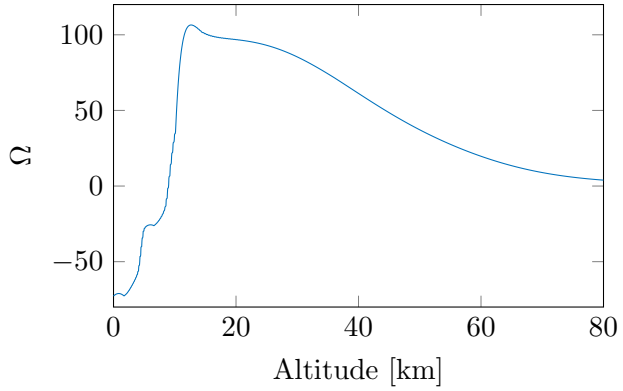

Figure 9-4: Evolution of Ω as a function of altitude for a trajectory with a truncated flight-path angle at $\gamma = -89.5$ deg.

set to zero in $\dot{\Omega}$ (Equation (7-10)). Because the horizontal velocity is small, this will only have a margina effect on the impact location and impact time.

The result for Ω is plotted as a function of altitude in Figure 9-4. The value of Ω then goes to around -60, which is a value that can be used for the calculations. The jumps in the figure are a result of truncating the flight-path angle. Figure 9-4 shows that a solution could be obtained for impact predictions by truncating the flight-path angle. However, it must be considered that the accuracy of the results are influenced by the truncation of the flight-path angle. Because the aerodynamic forces are large at the end of the trajectories this can have a significant impact.

9-1-3 Time Distributions

The DPP simulator is used to propagate the PDF of the initial state to the final state for several cases. Unfortunately, no accurate solutions could be obtained for the PDF at the Earth's surface, because for about 10% of the simulations the value of Ω became even smaller

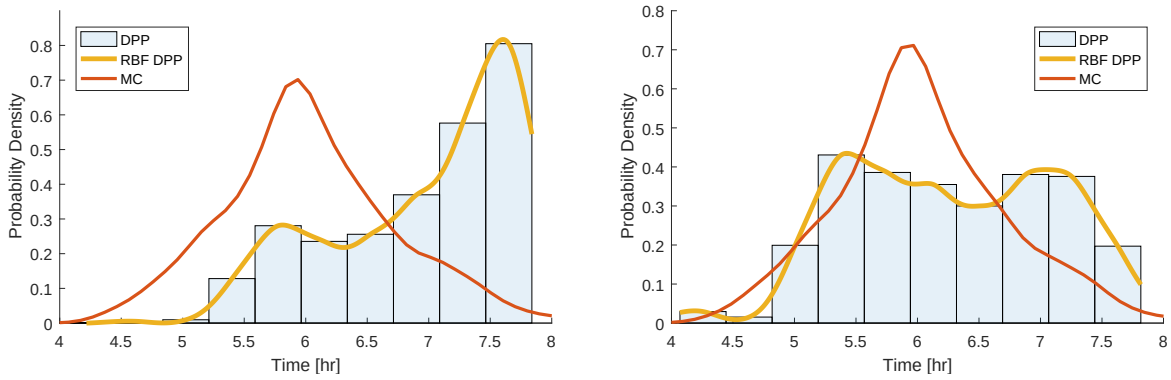

Figure 9-5: Marginal PDFs of the time at an altitude of 50 km(left) and 70 km(right) obtained using the binning method with 766(697 with outlier removal) samples and Monte Carlo (red line).

than −800. This shows that the numerical instabilities already cause problems earlier in the trajectory. Because of these problems no accurate results could be obtained for altitudes below 50 km.

Therefore, the data of the DPP method are used to derive distributions of the time at an altitude of 50 and 70 km. Figure 9-5 shows the two time distributions obtained at these altitudes using the standard binning method described in Section 4-2-5.

The distributions are derived by taking the mean of the probability density in each bin and subsequently normalizing the distribution. The red line corresponds to a kernel density estimate based on approximately 2500 Monte Carlo samples, which is used as a reference. The bars are the result of the binning method and the orange line represents a RBF interpolation of the binvalues. An outlier removal method is applied to the DPP data before constructing the distribution, because the dispersion in Ω was large and outliers caused that the mean for each bin was biased. Without performing any outlier removal, the results were highly inaccurate. The outlier removal method removed any samples that were located outside the 5σ range. Observing Figure 9-5, it can be concluded that the distributions do not match, so the binning method produces inaccurate results for this case.

The binning method does not really integrate the data, because the dispersion of the data could be different in each bin. Therefore, the binning method could be improved by multiplying each value of the bin with a measure of the enclosed volume of the data in that bin. The measure that is used is the product of the standard deviation for each state (dimension) that are not included in the marginal. This method basically assumes that the enclosed volume is a hypercube. As was observed in Section 4-2, the dispersion of the data is strongly correlated, so assuming that the enclosed volume is a hypercube produces inaccurate results. A better measure can be obtained if the standard deviations of the principle components are used instead of the states itself. In Figure 4-7, it was observed that there are linear relations in the dispersion of the data. Using the principle components, which are a linear combination of the states that result in a maximum variance of the data, a better measure of the enclosed volume can be obtained. The results of applying these weights are shown in Figure 9-6.

The deficiency of the binning method can be partially attributed to the number of datapoints, because on average only 70 datapoints are used in each bin. In addition, the datapoints are

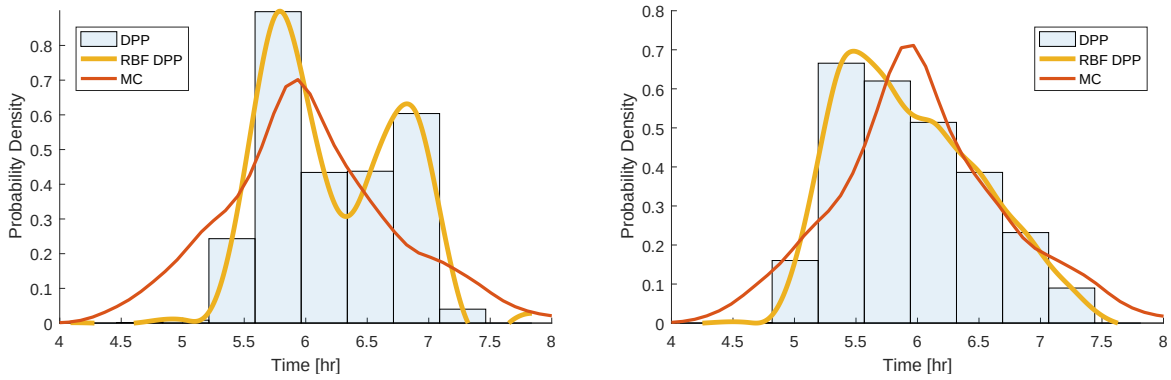

Figure 9-6: Marginal PDFs of the time at an altitude of 50 km(left) and 70 km(right) obtained using the binning method with 766(697 with outlier removal) samples and Monte Carlo (red line).

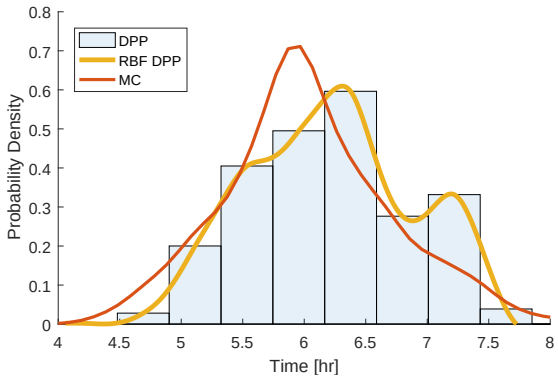

Figure 9-7: Marginal PDFs of the time at an altitude of 70 km obtained using the binning method with 2298 samples and Monte Carlo (red line).

not uniformly distributed, so the bins in the center contain up to 180 datapoints and the bins at the edges contain only 6 datapoints. With such a small number of datapoints, the method cannot produce accurate results. As explained in Section 4-2-5, the binning method corresponds to a MC integration process if the datapoints are uniformly distributed and the mean is multiplied with the enclosed volume of the data. Because the convergence of the sample mean to the true mean is dependent on the number of samples (Section 3-1), it is expected that no accurate result can be obtained. Furthermore, an accurate marginal distribution can only be obtained if the mean of the data in each bin is multiplied with an accurate measure of the enclosed volume of the data, which is difficult to obtain.

An additional simulation is performed with 2298 DPP samples to investigate if the performance of the binning method converges to a satisfactory level. The result of this simulation is shown in Figure 9-7 for an altitude of 70 km. Comparing Figure 9-7 with Figure 9-6 it cannot be concluded that the results are improved. This result is expected, because MC integration generally requires a significantly large number of samples to obtain accurate estimates.

The observed computation time for the DPP method is approximately a factor two larger than for MC for the same number of samples. This can be attributed to the fact that the DPP method requires that an extra ODE (for Ω) needs to be solved, which drives the stepsize

of the numerical integrator. It must be noted that this is not a fair comparison, because numerical issues were observed for the solution of Ω.

Conclusion

The simulations with the DPP simulator have revealed several features and drawbacks of the DPP method, which resulted in the following conclusions:

- Stability issues when propagating Ω in time can cause large inaccuracies in the PDF obtained by the DPP method.
- The state variables should be chosen such that there is no dependence on the flight-path angle or heading angle in the model of Ω to avoid numerical issues.
- The binning method does not produce accurate results unless a large number of DPP samples are provided. It is expected that more samples are required than with a MC simulation to obtain the same accuracy. The DPP method can only be used for statistical impact prediction if the marginal distributions are calculated using a more accurate method than the binning method.

Because no accurate results could be obtained with the DPP simulator, the MC simulator is used to derive the impact time distributions of the Delta-K rocket bodies.

9-2 Statistical Impact Predictions

Several statistical impact predictions are performed using the MC simulator (Section 8-2) and the uncertainty model described in Chapter 6. The samples that are obtained from this simulator are used to estimate the PDF of the impact time using KDE (Section 3-2). A total of 119 valid TLEs could be used to perform a MC simulation and could be compared to true impact points provided by the Joint Space Operation Center (JSPOC) obtained from space-track.org[1].

For 31 different cases described in Table 2-1, the distributions could be compared with the TIP window and with the results of Ronse (2013). The distributions are obtained using 2000 Monte Carlo simulations. The random samples are obtained using Sobol sampling as discussed in Section 3-1-1, because this results in a faster convergence than pseudo-random sampling. The obtained distributions are displayed in appendix E. In Figures E-1 to E-4, the results are shown for the uncertainty model described in Chapter 6. In Figures E-5 to E-8, the results are shown that are obtained with a modified uncertainty model that will be described later. The following features are indicated in these plots:

- The predicted impact-time PDF obtained using KDE.
- The predicted median of the impact time.

[1] `https://www.space-track.org/`; date accessed: 15-08-2016

- An impact-time window that represents the 99.73% probability band around the median with a 99.73% confidence level. The probability band represents the window, in which the Delta-K rocket body is expected to impact with 99.73% probability. The confidence level is derived using the bootstrapping method discussed in Section 7-1-2. The confidence level represents the probability that the derived window is accurately estimated based on the MC data. This does not mean that it is a measure of the accuracy of the probability window, but it is a measure of the accuracy of the statistical method that is used to derive the probability window.
- The TIP epoch and window.
- The true impact-time.

For all derived impact-time distributions, it is observed that the true impact time lies within the 99.73% probability impact-time window. However, for one of the cases the true impact time is not located within the TIP window, which indicates that the performance of the predictions are better than TIPs. The accuracy of the impact time distribution is much lower at the edges of the distributions than around the mean, because only a small number of samples are located at the edges of the PDF. Thererfore, the accuracy of the derived 99.73% impact-time windows is limited. The accuracy of the derived impact-time distributions is evaluated in the following subsections.

9-2-1 Statistical Validation

The results can be validated with a statistical method that tests if the impact-time distributions match with the observations, the true impact points. For a total of 119 TLEs, a MC simulation was performed and the impact-time distribution was derived and compared with the true impact point. In Figure 9-8 a graphical representation of the method is shown. Inserting the true impact points in the predicted CDF of the impact time, results in a cumulative probability value. The cumulative probabilities should be uniformly distributed if the distribution matches with the observations.

Figure 9-8 shows an impact point that corresponds to a probability band of 60%. If the predicted impact-time distributions are accurate, 60% of the cases should have a probability band lower than 60%. The probability band of the true impact point is determined for all cases and the distribution of this probability band is shown in Figure 9-9. The ideal result would match with a uniform CDF on $[0, 1]$, which is also plotted in the figure.

The figure shows that the results that are obtained all result in a probability band that is higher than the number of cases observed in that band. This means that the width of the probability band is underestimated, thus the impact-time windows are underestimated. Ideally, one wants that the values of the plot are always higher than the uniform plot, because this means that all probability bands are wider than they should be and the impact-time window is conservative.

To investigate the accuracy of the derived impact time distributions further, an additional analysis is performed. The cumulative probability of the true impact points are used instead of the probability bands, which corresponds to a value of 0.8 in the example of Figure 9-8. The distribution of these cumulative probabilities contains more information on the accuracy

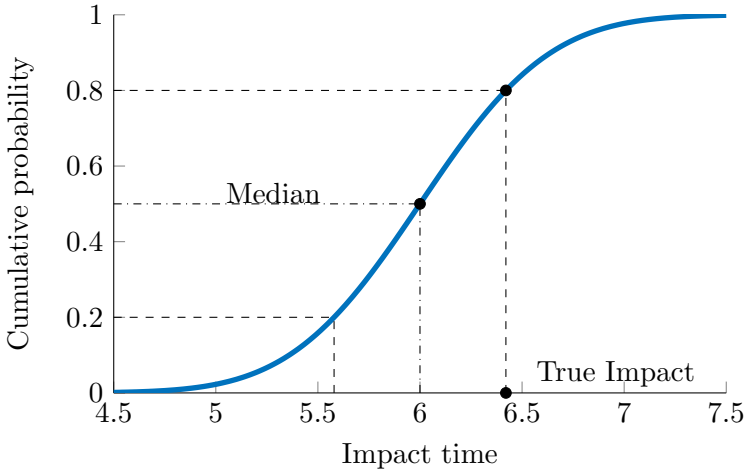

Figure 9-8: Illustration of a CDF and a 60% probability band of the true impact point centered around the median.

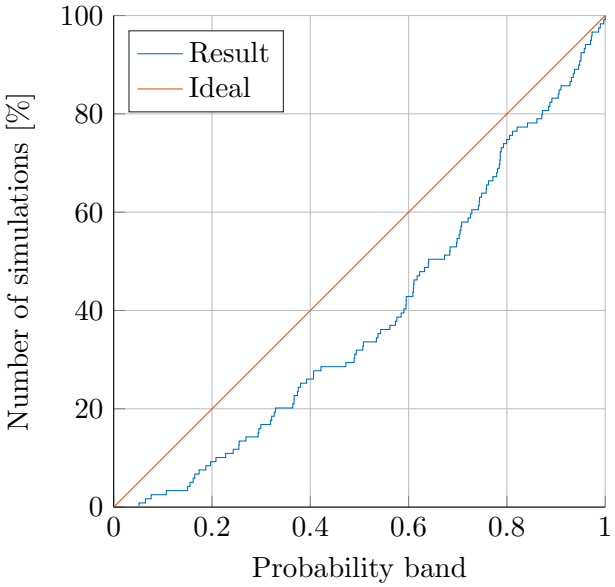

Figure 9-9: Number of simulations versus the probability band of the true impact point centered around median for 119 Monte Carlo simulations.

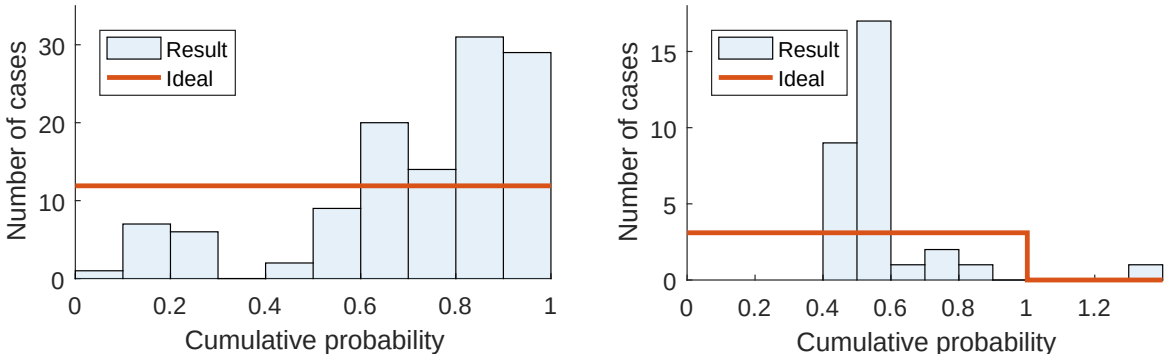

Figure 9-10: Histogram of the cumulative probability that is obtained from inserting the true impact point in the generated CDF (left) and inserting it in a uniform distribution using the TIP window.

of the predictions. For example, if most of these cumulative probabilities have a value that is lower than 0.5 it means that the median generally overpredicts the impact time.

A PDF of the cumulative probability of the true impact points is shown in Figure 9-10. If the derived impact time distributions exactly matches with the true impact points, this PDF should be uniformly distributed, which can be derived from Equation (3-2). The figure clearly shows that the distribution is not uniform, which means that the derived impact time distributions do not exactly match with the observed impact points. This is an expected result, because only if the uncertainty model is and the statistical methods are a 100% correct, this result could be obtained. Furthermore, only 119 true impact points were used to derive this figure, which is not enough to prove that the shape of the impact time distribution is entirely correct.

Furthermore, the figure shows that most cumulative probabilities have a larger value than 0.5. This means that most impact locations are located at a later time than the predicted median. The mean cumulative probability of the impact points is equal to 0.73, which means that the derived distributions largely underpredict the impact time.

The observed bias in the impact time is consistent with the atmospheric density generated by the NRLMSISE-00 atmosphere model, because an analysis performed by Picone et al. (2002) showed that the model overestimates the atmospheric density for lower altitude regions. In addition, in the research of Picone et al. (2002) a standard deviation of 0.17 is presented for the atmospheric density factor for altitudes between 120 and 200 km. This value is larger than the value of 0.12, which was used for these simulations and derived by Ronse (2013), so it could explain why the probability bands are generally underpredicted.

A second series of MC simulations is performed using a standard deviation of 0.17 and a mean of 0.93 for the atmospheric density factor, which were obtained from Picone et al. (2002). A total of 31 MC simulations were performed and the impact-time distribution was compared to the true impact point. The cumulative probability of the true impact points are calculated with a 99.73% confidence level using bootstrapping (Section 7-1-2) to obtain a more reliable result. The mean cumulative probability for these results is bounded by $[0.5, 0.56]$, so the bias is almost removed using this modified uncertainty model. This shows that the bias was mainly caused by the atmosphere model.

The CDF of the probability bands is shown in Figure 9-11. From the figure it can be derived

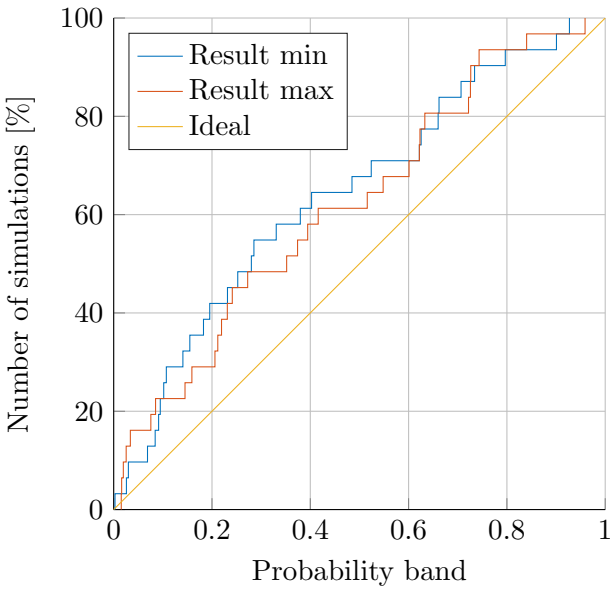

Figure 9-11: Number of simulations versus the probability band of the true impact point centered around median for 31 Monte Carlo simulations with a different uncertainty model for the atmospheric density.

that every probability band is overestimated, because more impact points are located in each probability band than the probability distributions predict. Therefore, statistical impact windows generated from these distributions overestimate the true window, which is preferred over underestimated windows. This result is expected, because the standard deviation of 0.17 that is used for for the atmospheric density factor is larger than the standard deviation of 0.12, which is used for the first results.

A PDF of the cumulative probability of the impact points is shown in Figure 9-12. The figure shows that most true impact points are located near the mean, so it confirms that the bias in the predictions is largely reduced. Furthermore, the figure shows that the figure shows that less than expected impacts are observed at the edges of the distributions, because the lowest and highest cumulative probability bin contain less true impact points than the ideal value. This confirms that the probability bands are generally overestimated.

These results show that the impact-time window is consistent with the observed impact points, but it cannot be concluded that the shape of the distribution is also correct. A significantly larger number of verification samples is required to make such a conclusion.

Important to note is that the better performance of the simulations with a different uncertainty model does not mean that the previous uncertainty model of the atmospheric density is less accurate. The better performance could also be attributed to the fact that uncertainty is present in other parameters that is now accounted for by making the uncertainty in the atmospheric density larger. For example, the uncertainty in aerodynamic coefficients could be a source of large influence.

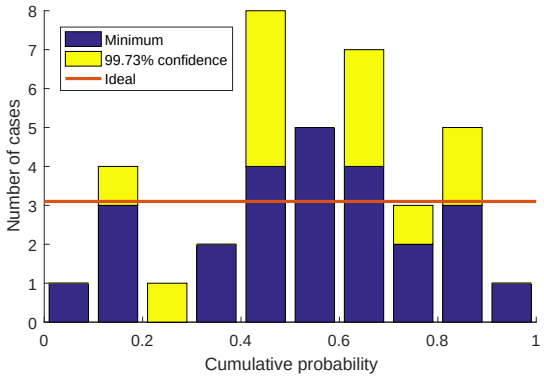

Figure 9-12: Histogram of the cumulative probability that is obtained from inserting the true impact point in the generated CDF with a different uncertainty model for the atmospheric density.

9-2-2 Comparison with TIP

Figure 9-10 shows a histogram of the cumulative probability of the true impacts for the predictions of this research and the TIP predictions. The figure for the TIP predictions is generated by assuming that the distribution is uniform within the TIP window. The figure shows that most of the true impact points are close to TIP epochs, but that one of the true impact points is located outside of the TIP window. This indicates that the TIP distribution is more concentrated around the median than a uniform distribution. The mean cumulative probability is equal to 0.57, so it is close to the TIP epoch, which means that a bias of 7% of true impact point with respect to the TIP epoch is observed.

The window size of the distributions obtained with the original uncertainty model are in 21 of the 31 cases smaller than the TIP windows. On average the obtained windows are 7% smaller than the TIP windows. However, in Section 9-2-1 it was found that the impact windows are underpredicted, so it cannot be concluded that these results are better than the TIPs.

Assuming that the TIP window corresponds to a 3σ value of a Gaussian distribution results in the histogram shown in Figure 9-13. The figure shows that the cumulative probability of the impact points is more uniform than assuming that the TIP distribution is uniform. The figure also shows that the high probability bands are underestimated, which originates from the case where the impact point is located outside the TIP window. Furthermore, it shows that the TIP results are also biased, because the mean cumulative probability is equal to 0.62. This means that the TIP predictions also generally underestimate the impact time.

For the modified uncertainty model, the histogram of the cumulative probability shown in Figure 9-12 was obtained. Comparing the figure with the histograms obtained from the TIP window (Figure 9-13 and Figure 9-10), one can conclude that the impact window generated using the MC predictions is more conservative than the TIP window. This is based on the fact that the larger probability bands are overestimated with the MC simulations and for one of the cases, the true impact point was observed outside the TIP window.

For the results with the modified uncertainty model only 6 of the 31 impact windows are smaller than the TIP window and the impact windows are on average 29% larger than the TIP window.

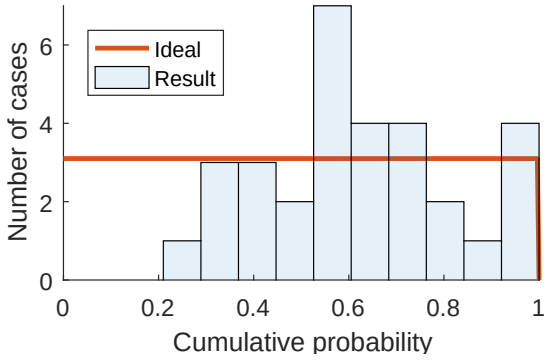

Figure 9-13: Histogram of the cumulative probability that is obtained from inserting the true impact point in a Gaussian CDF obtained using the TIP window.

The smallest mean cumulative probability value of the impact points for the TIP prediction is 0.57, which is a larger bias than the bias that was observed for the MC simulations with the modified uncertainty model. The reason that a smaller bias was obtained could also be because the impact windows are larger, so it cannot be concluded that the predictions that are performed are better.

It must be noted that the comparison with the TIPs is not a fair comparison, because it is not known how these windows are obtained and what probability band is assigned to these windows. Furthermore, only 31 TIPs were used to perform the comparison and in only one case, the impact point was not located in the impact window. This number is too small to conclude that the accuracy of the TIPs is higher or lower than the predictions performed in this research.

9-2-3 Comparison with Ronse

In the research of Ronse (2013), a similar validation process was performed. The result of this validation process is shown in Figure 9-14. The plot shows that the probability bands are overestimated close to the median and the probability bands are underestimated further away from the median. This means that the 99.73% probability impact window that was generated, actually is an impact window with a probability of impact that is smaller than 99.73%.

For the MC simulations with the nominal uncertainty model it was observed that for 50% of the cases, the impact-time window was larger than the impact-time windows generated by Ronse (2013). The shape of the distributions is obtained in this research is also less flat than the distributions obtained by Ronse (2013). The bias in the predictions of Ronse (2013) could not be evaluated, because the predicted median is not provided. For the simulations with the modified uncertainty model, the impact windows are all larger than the windows obtained in the research of Ronse (2013).

In the research of Ronse (2013), a sensitivity analysis has shown that uncertainty in the initial translational only has a minor effect on the uncertainty in impact time, so it is most likely that the difference is caused by the different uncertainty model of the atmospheric density. Considering that a uniform distribution was used to model the uncertainty in the

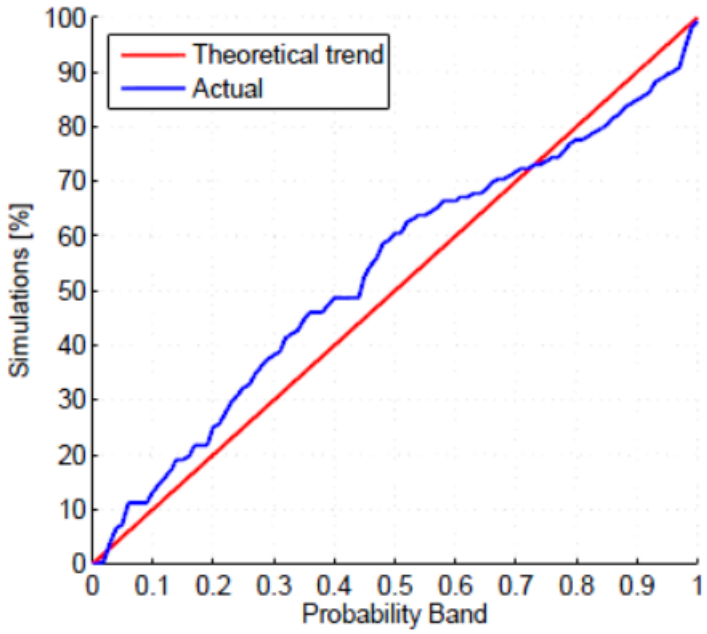

Figure 9-14: Number of simulations versus the probability band of the true impact point centered around median for 152 Monte Carlo simulations performed by Ronse (2013).

atmospheric density, the difference with the result in Figure 9-9 can be explained. Figure 6-10 shows that the uncertainty of a lognormal distribution is more concentrated than the uniform distribution, however it extends beyond the bounds of the uniform distribution. Therefore, using a uniform distribution instead of a lognormal distribution results in a distribution that is too wide (or flat) near the median up to the 70% probability band and results in higher probability bands that are too small, which is also observed in the validation plot of Ronse (2013).

The influence of the atmospheric density is clearly shown in Figure 9-15. The figure shows that there is a high correlation ($\rho = -0.85$) between the atmospheric density and the impact time, which confirms the sensitivity of the flight time to atmospheric density uncertainty. In addition, the bounds of a uniform distribution with the same standard deviation are displayed in the figure. The figure shows that a considerable number of datapoints are located outside these bounds and they increase the flight time window. As a result the distribution of the impact time is wider than when the uncertainty in the atmospheric density is modelled using a uniform distribution. This shows that using a uniform distribution instead of a lognormal distribution underestimates the possible impact-time window.

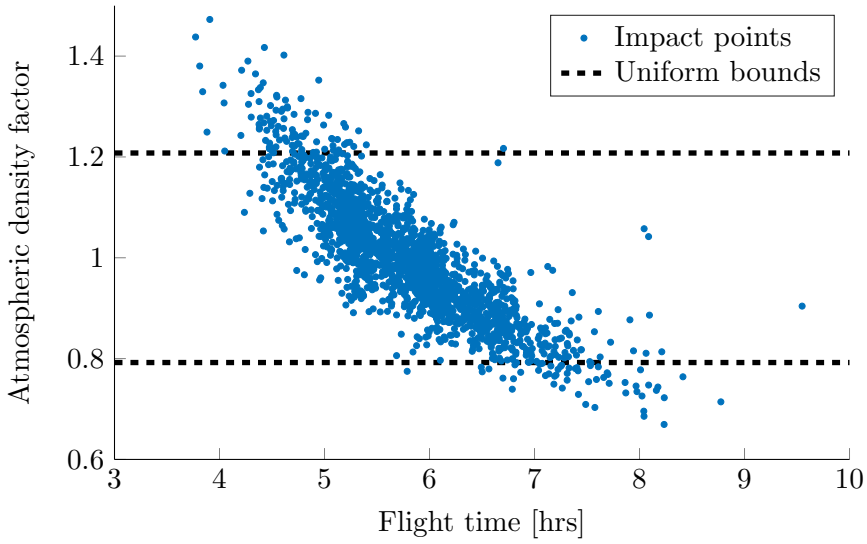

Figure 9-15: Scatter plot of the atmospheric density factor that is used in the simulation and flight time of the body. 1940 samples obtained from a Monte Carlo simulation with TLE 27.

Chapter 10

Conclusions and Recommendations

The research performed during this thesis work has lead to a number of insights, opportunities and limitations. This chapter discusses the conclusions that are drawn from the obtained results in the research and discusses recommendations for further research.

10-1 Conclusions

The research performed for this thesis work is driven by the following research question:

Can we improve the accuracy of statistical predictions of the impact location or impact time of objects that enter the atmosphere?

The research has shown that improvements to the uncertainty model and improvements to the statistical methods can lead to more accurate statistical predictions of the impact location or impact time of space debris. With the available data it could not be proven that the improved uncertainty model leads to more accurate statistical predictions, because a large amount of data is required to prove that the obtained impact-time distributions have the correct shape. Nevertheless, the statistical validation has shown that the statistical predictions obtained in this research lead to more conservative results than the method of Ronse (2013) or TIPs with the consequence that the impact windows are larger. Unfortunately, using direct methods to propagate uncertainty in the state of the Delta-K rocket body did not lead to more accurate results than the MC method.

Research has been performed on several areas that are related to impact predictions. The following conclusions have been drawn from this research:

The LSQKD Method

- The results have shown that using two kernels to represent the PDF of the state results in a higher accuracy than when using only one kernel.

- The accuracy of the LSQKD method depends on the degree of non-linearity of the state derivative model and degrades with time.
- The method is limited in the number of kernels that can be used to model the PDF of the state. During this research, solutions could only be obtained for a maximum of two kernels.
- The computation time increases largely when the integrals that define the LSQKD equations cannot be solved analytically beforehand. Therefore, this method can only outperform other methods when the expressions that are purely based on the kernels can be analytically derived.
- The LSQKD method, in its current form, cannot provide a similar accuracy for atmospheric entry problems compared with the MC method or the DPP method.

Uncertainty Model

- The uncertainty model should be defined such that the correct probability distributions are used for each random variable. In addition, correlation between random variables cannot be neglected, because correlation concentrates the uncertainty.
- The TLE pair-wise differencing method can be used to define the correlation structure of uncertainty in the initial translational state variables. The dispersion of the uncertainty cannot be obtained from this method, but must be obtained from other sources.
- Kernel density estimation can be used to model a PDF based on observations of the errors. Cross-validation can be used to validate the model derived using the kernel density estimation.
- A uniform random attitude can be described by quaternions uniformly distributed in a quaternion sphere of three of the four quaternions.
- The uncertainty in the atmospheric density model should be modeled using a lognormal distribution. Using a uniform distribution with the same standard deviation results in an underestimation of the impact-time window and results in overestimation of the probability bands up to 70% around the median.
- The bias in the uncertainty of the atmospheric density cannot be neglected in the uncertainty model, because it results in a bias in the impact-time distribution.

Numerical Integration

- The simulations have shown that backward time propagation can be performed on uncontrolled atmospheric entry trajectories.
- Backward time propagation can suffer from stability issues if the propagation is performed until the Earths surface for uncontrolled atmospheric entry problems. A different set of state variables could mitigate these issues.

- Numerical issues can arise in the integration of an uncontrolled entry trajectory when the flight-path angle approaches $-90°$ if dependencies on the heading angle are present.
- Atmospheric decay trajectories that start with an initial rotational velocity that is small are more sensitive to the settings of the numerical integrator, because a body with a small rotational velocity is more sensitive to perturbations. As a result, there is a relatively large dispersion in trajectories that are obtained with different integrator settings.

Direct PDF Propagation

- The numerical integral that needs to be solved for each trajectory, $\int \Psi$ in Equation (3-27), should be converted to an ODE, which can be solved using the numerical integrator. Hereby, the numerical integrator can be used to control the accuracy.
- Backward time integration can be used to obtain the value of the PDF at a certain location. However, the accuracy of such a solution depends on the state derivative model, because instabilities can cause large inaccuracies.
- Propagating uncertainty in all states where only one of the initial states contains uncertainty cannot be performed in a conventional way as described in Section 3-4.
- The binning method that is used in the research of Halder and Bhattacharya (2011) (Section 4-2-5) to process the DPP data leads to inaccuracies that are too large to perform accurate statistical impact predictions.
- Describing the velocity of an uncontrolled body using east and north velocity, or flight-path angle and heading angle, results in singularities in the derivative of Ω near the Earth's surface, which causes that no accurate results can be obtained for statistical impact prediction.
- When selecting the state variables to describe the trajectory and the PDF that is propagated, it is important to consider singularities that can occur in the derivative of Ω.
- The Direct Probability Density Function Propagation (DPP) can in theory outperform a Monte Carlo analysis. However, if the data from the DPP cannot be processed in an accurate way, the MC method will outperform the DPP method. No method was found to process the data that could provide the necessary accuracy.

Statistical Impact Prediction

- An accurate uncertainty model is required to obtain accurate impact predictions, because the distribution of any random variable has an effect on the distribution of the impact time. The research has shown that the distribution of the atmospheric density has a large influence on the impact-time distributions.
- The statistical validation process should also be performed using a bootstrapping method to provide the validation data with a confidence level.

10-2 Recommendations

Based on the performed research, several recommendations are defined for future research:

Uncertainty Model

- Investigate the uncertainty in TLEs more closely. A more accurate uncertainty model could be obtained using other methods as described in Geul et al. (2016).
- Investigate the uncertainty in the atmospheric density more closely, because using a different uncertainty model for the atmospheric density resulted in more conservative results than the results obtained by Ronse (2013). In the research of Picone et al. (2002), it is shown that the uncertainty in the atmospheric density is dependent on altitude and solar activity. The uncertainty model could be improved by including these dependencies.
- Investigate the correlation structure between the error in the initial position obtained by the TLEs and the atmospheric density model. Only one paper was found that presented results on the correlation based on an orbit fitting process. An idea would be to execute an orbit fitting process to investigate which correlations will originate.
- Investigate the uncertainty in the rotational state more closely, because it is an important parameter for the impact predictions (Ronse, 2013). In the research of Ronse (2013), it was assumed that the rotation axis is uniformly distributed, which is also used in this research. However, the theory on rotational motion and perturbations, for example, gravity-gradient torque could show that a uniform distribution is unlikely. An idea would be to start with a uniform distribution and to propagate it in time, to investigate how the distribution evolves in time.
- Perform a statistical impact-prediction analysis with uncertainty in more parameters. For example, the aerodynamic coefficients are generated using a panel method, which could contain errors that are non-neglible. The aerodynamic coefficients have a similar effect on the aerodynamic drag as the atmospheric density, so it is expected that uncertainty in these parameters has a large influence on the impact-time distributions. In addition, the inertia tensor can be uncertain due to unused fuel in the rocket body. Because the rotational state has a large influence on the impact time, uncertainty in this parameter could also have a large influence.

Uncertainty Propagation Methods

- It would be valuable to test the DQMOM method for these problems since literature has shown that it is very computationally efficient and representing distributions using the Dirac delta function makes it easy to compute marginal distributions. This can potentially overcome the problems of data processing that are observed for the DPP method. It must be noted that the method might not be feasible for atmospheric entry problems due to the Hausdorff moment problem (Section 2-3).

Direct PDF Propagation

- Investigate the performance of the method using a different set of state variables. However, take into account that transforming distributions is a difficult task, so it is recommended to use the variables of interest as state variables.
  - A possible feasible set of state variables would be to represent the velocity as Cartesian components expressed in the inertial frame or body frame.
- Investigate the performance of the method on controlled atmospheric entry problems. The controller influences the uncertainty, so the performance of the method could be totally different.

Statistical Impact Prediction

- Perform statistical impact predictions with more test cases, such that more TIPs can be used to compare the accuracy. This could result in stronger conclusions about the performance of the method and the TIP predictions.
- Investigate the effect of higher order gravity terms on the impact predictions. Simulations performed by J. Geul[1] showed that these terms can have an influence on impact-time distributions.
- Investigate the effect of the uncertainty model on the statistical impact predictions more closely. This research has shown that the shape of the distribution also has a large influence on the impact-time distributions.
- Investigate the effect of gravity gradient torque on the impact predictions. The rotational state has a large influence on the impact predictions, so this torque could have a significant effect.

[1] Private communication with J. Geul d.d. 05-08-2016.

Bibliography

Allasia, G., Cavoretto, R., and Rossi, A. D., "Multidimensional Lobachevsky Spline Integration on Scattered Data," *Applied Mathematics & Information Sciences*, Vol. 8, No. 1, 2014, pp. 145–151.

Anderson, J. D., *Fundamentals of Aerodynamics*, McGraw-Hill, 2001.

Attar, P. J. and Vedula, P., "Direct quadrature method of moments solution of the Fokker-Planck equation," *Journal of Sound and Vibration*, Vol. 317, 2008, pp. 265–272.

Bezdek, A., "Lognormal distribution of the observed and modelled neutral thermospheric densities," *Studia Geophysica et Geodaetica*, Vol. 51, No. 3, 2007.

Bock, H., Jäggi, A., Meyer, U., Visser, P., van den IJssel, J., van Helleputte, T., Heinze, M., and Hugentobler, U., "GPS-derived orbits for the GOCE satellite," *Journal of Geodesy*, Vol. 85, No. 11, 2011, pp. 807–818.

Bowman, A. W. and Azzalini, A., *Applied Smoothing Techniques for Data Analysis*, Oxford University Press Inc., New York, 1997.

Burden, R. L. and Faires, J. D., *Numerical Analysis*, Brooks/Cole, Cengage Learning, 9th ed., 2011.

Casella, G. and Berger, R. L., *Statistical Inference*, Duxbury Press, 1990.

Cengel, Y. A. and Boles, M. A., *Thermodynamics An Engineering Approach*, McGraw-Hill, 5th ed., 2004.

Chapman, S. and Cowling, T., *The mathematical theory of nonuniform gases*, Cambridge University Press, 3rd ed., 1970.

Cheatwood, F. M. and Desai, P. N., "Entry Dispersion Analysis for the Genesis Sample Return Capsule," *Journal of Spacecraft and Rockets*, Vol. 38, No. 3, May-June 2001, pp. 345*350.

Dekking, F., Kraaikamp, C., Lopuhaa, H., and Meester, L., *A Modern Introduction to Probability and Statistics*, Springer, 2005.

Desai, P. N., Braun, R. D., Powell, R. W., Engelund, W. C., and Tartabini, P. V., "Six-Degree-of-Freedom Entry Dispersion Analysis for the METEOR Recovery Module," *Journal of Spacecraft and Rockets*, Vol. 34, No. 3, May-June 1997, pp. 334–340.

Desai, P. N., Mitcheltree, R. A., and Cheatwood, F. M., "Entry Dispersion Analysis for the Stardust Comet Sample Return Capsule," *Journal of Spacecraft and Rockets*, Vol. 36, No. 3, 1999, pp. 463–469.

Desai, P. N., Schoenenberger, M., and Cheatwood, F. M., "Mars Exploration Rover Six-Degree-of-Freedom Entry Trajectory Analysis," *Journal of Spacecraft and Rockets*, Vol. 43, No. 5, 2006, pp. 1019–1025.

Gardiner, C., *Handbook of Stochastic Methods*, Springer, 2004.

Geisser, S., *Predictive Inference: An Introduction*, Springer science bussiness media, B.V., 1993.

Gelb, A., *Applied Optimal Estimation*, The M.I.T. Press, 1974.

Geul, J., Mooij, E., and Noomen, R., "TLE Uncertainty Estimation using Weighted differencing," To be published: Advances in Space Research, 2016.

Glasserman, P., *Monte Carlo Methods in Financial Engineering*, Springer, 2004.

Haberman, R., *Applied Partial Differential Equations*, Pearson Education International, 2003.

Halder, A. and Bhattacharya, R., "Dispersion Analysis in Hypersonic Flight During Planetary Entry Using Stochastic Liouville Equation," *Journal of Guidance, Control and Dynamics*, Vol. 34, No. 2, March - April 2011, pp. 459–474.

Hedin, A. E., "High altitude atmospheric modeling," NASA, Nasa technical memorandum 100707, 1988.

Hogg, R. V., McKean, J. W., and Craig, A. T., *Introduction to Mathematical Statistics*, Pearson Education International, 6th ed., 2005.

Kelso, T., "EOP and Space Weather Data," https://www.celestrak.com/SpaceData/, 2016.

Kirk, D., editor, *Graphics Gems III - A Collection of Practical Techniques for the Computer Graphics Programmer*, AP Professional, 1992.

Klinkrad, H., *Space Debris Models and Risk Analysis*, Springer, 2006.

Kurowicka, D. and Cooke, R., *Uncertainty Analysis with High Dimensional Dependence Modelling*, John Wiley & Sons, Ltd, 2006.

Lasoata, A. and Mackey, M. C., *Chaos, Fractals and Noise - Stochastic Aspects of Dynamics*, Vol. 97 of Applied Mathematical Sciences 97, Springer, 2nd ed., 1994.

Lay, D. C., *Linear Algebra and its applications*, Pearson Education, Inc., 4th ed., 2012.

Lazzaro, D. and Montefusco, L. B., "Radial basis functions for the multivariate interpolation of large scattered data sets," *Journal of Computational and Applied Mathematics*, Vol. 140, 2002, pp. 521–536.

Li, S. T. and Hammond, J. L., "Generation of Pseudorandom Numbers with Specified Univariate Distributions and Correlation Coefficients," *IEEE Transactions on Systems, Man, and Cybernetics*, Vol. 5, 1975, pp. 557–561.

Marchisio, D. L. and Fox, R. O., "Solution of population balance equation using the direct quadrature method of moments," *Journal of Aerosol Science*, Vol. 36, July 2004, pp. 43–73.

Montenbruck, O. and Gill, E., *Satellite Orbits Models, Methods and Applications*, Springer, 2001.

Montgomery, D. C. and Runger, G. C., *Applied Statistics and Probability for engineers*, Wiley, 6th ed., 2014.

Mooij, E., *The motion of a vehicle in a planetary atmosphere*, Delft University Press, December 1994.

Mooij, E., "Re-entry Systems - Draft Lecture Notes course AE4070B," TU Delft, September 2014.

Moore, R. E., *Interval Arithmetic and Automatic Error Analysis in Digital Computing*, Ph.D. thesis, Stanford University California, 1962.

Moore, R. E., "Risk Analysis witwith Monte-Carlo methods," Inst. fur Angewandte Math., University of Freiburg, FRG, Tech. Rep. 84/1, 1984.

Niedereiter, H., *Random Number Generation and Quasi-Monte Carlo Methods*, Society for Industrial and Applied Mathematics, 1992.

NIST, "Fundamental physics constants," http://physics.nist.gov/cgi-bin/cuu/Value?r, 2016.

Osweiler, V. P., *Covariance Estimation and Autocorrelation of Norad Two-line Element Sets*, MSc. thesis, Air Force Institute of Technology, March 2006.

Pantano, C. and Shotorban, B., "Least-squares dynamic approximation method for evolution of uncertainty in initial conditions of dynamical systems," *Physical Review E*, Vol. 76, No. 6, December 2007, pp. 066705.

Picone, J. M., Hedin, A. E., and Drob, D. P., "NRLMSISE-00 empirical model of the atmosphere: Statistical comparisons and scientific issues," *Journal of Geophysical Research*, Vol. 107, No. A12, 2002, pp. SIA 15–1SIA 15–16.

Portelli, C., Salotti, L., Anselmo, L., Lips, T., and Tramutola, A., "BeppoSAX equatorial uncontrolled re-entry," *Advances in Space Research*, Vol. 34, 2004.

Prabhakar, A., Fisher, J., and Bhattacharya, R., "Polynomial Chaos-Based Analysis of Probabilistic Uncertainty in Hypersonic Flight Dynamics," *Journal of Guidance, Control and Dynamics*, Vol. 33, No. 1, January - February 2010, pp. 222–234.

Prag, A. B., "A Comparison of the MSIS and Jacchia-70 Models with Measured Atmospheric Density Data in the 120 to 200 km Altitude Range." The Aerospace Corporation El Segundo, CA 90245, Technical report a500821, 1983.

Queen, E. M., Cheatwood, F. M., Powell, R. W., and Braun, R. D., "Mars Polar Lander Aerothermodynamic and Entry Dispersion Analysis," *Journal of Spacecraft and Rockets*, Vol. 36, No. 3, May-June 1999, pp. 421–428.

Regan, F. J. and Anandakrishnan, S. M., *Dynamics of Atmospheric Re-entry*, American Institute of Aeronautics and Astronautics, 1993.

Ridolfi, G., *Space Systems Conceptual Design - Analysis methods for engineering-team support*, Ph.D. thesis, Delft University of Technology, http://repository.tudelft.nl/islandora/object/uuid:abb30ba0-5307-4592-aa4f-6016c0cd85f8, April 2013.

Rochelle, W. and Johnson, J. M. N., "Analysis of reentry survivability of UARS spacecraft," *Advances in Space Research*, Vol. 34, 2004.

Rohatgi, V. K. and Saleh, A. K. E., *An Introduction to Probability and Statistics*, John Wiley & Sons, Ltd, 2nd ed., 2001.

Römgens, B., Mooij, E., and Naeije, M., "Satellite Collision Avoidance Prediction Using Verified Interval Orbit Propagation," *Journal of Guidance, Control and Dynamics*, Vol. 36, No. 3, May-June 2013, pp. 821–832.

Ronse, A., *Statistical Impact Prediction of Decaying Objects*, MSc. thesis, TU Delft, March 2013.

Shotorban, B., "Dynamic least-squares kernel density modeling of Fokker-Planck equations with application to neural population," *Physical Review E*, Vol. 81, No. 4, April 2010, pp. 046706.

Silverman, B., *Density Estimation for Statistics and Data Analy*, Chapman and Hall, 1998.

Song, P. X.-K., "Multivariate Dispersion Models Generated from Gaussian Copula," *Scandinavian Journal of Statistics*, Vol. 27, No. 2, 2000, pp. 305–320.

Terejanu, G., Singla, P., Singh, T., and Scott, P. D., "Uncertainty Propagation for Nonlinear Dynamic Systems Using Gaussian Mixture Models," *Journal of Guidance, Control and Dynamics*, Vol. 31, No. 6, November-December 2008, pp. 1623–1633.

Thomopoulos, N. T., *Essentials of Monte Carlo Simulation*, Springer, 2013.

Wakker, K. F., *Fundamentals of Astrodynamics*, Delft University of Technology, http://repository.tudelft.nl/islandora/object/uuid:3fc91471-8e47-4215-af43-718740e6694e, 2015.

Watkins, D. S., *Fundamentals of Matrix Computations*, John Wiley & Sons, Inc., 2nd ed., 2002.

WGS, "Department of Defense World Geodetic System 1984," Department of Defense, Tech. rep., 2000.

Wright, J. R. and Woodburn, J., "Simultaneous Real-Time Estimation of Atmospheric Density and Ballistic Coefficient," 2004.

Xu, Y., "Nonlinear Robust Stochastic Control for Unmanned Aerial Vehicles," *Journal of Guidance, Control and Dynamics*, Vol. 32, No. 4, July-August 2009, pp. 1308–1319.

Xu, Y., "Nonlinear Stochastic Control for Space Launch Vehicles," *Aerospace and Electronic Systems*, January 2011, pp. 98–108.

Yim, H. and Chung, D., "Validation on Residual Variation and Covariance Matrix of USSTRATCOM Two Line Element," *Journal of Astronomy and Space Sciences*, Vol. 29, No. 3, 2012, pp. 287–293.

Appendix A

Probability Theory

The statistical analysis of uncertainty makes use of definitions and knowledge of probability theory. This section discusses several mathematical tools and relations, which are used in the methods used in this research. The chapter starts with discussing theory on uni-variate (single) random variables A-1. Thereafter, statistical relations between random variables are discussed in Section A-2. Multi-variate (multiple) random variables are discussed in Section A-3. The chapter is concluded with a discussion on Copulae in Section A-4, which are used to model statistical relations between random variables.

A-1 Uni-Variate Random Variables

An example of a random variable is a measurement of the local temperature. The instruments that are used do not measure the temperature in an exact way, so a random error is present. The error is thus a random variable, so information about the error is obtained using statistical methods. For example, it can be derived that the error has a maximum value of 0.1 K with a probability of 90%. This means that in ideally, 10% of the cases, the error is larger.

The random variable can be described in a more general way using a probability distribution. A probability distribution contains all information of how the probability is distributed over the possible values of the random variable. From this distribution it can be derived what the maximum error is with 95% probability and with 99% probability, and many other statistics of the random variable.

The probability distribuiton of a random variable X can be described by a Probability Density Function (PDF), which has the following properties:

$$f(x) \geq 0 \tag{A-1a}$$

$$\int_{-\infty}^{\infty} f(x)dx = 1 \tag{A-1b}$$

$$P(a \leq X \leq b) = \int_a^b f(x)dx \tag{A-1c}$$

where P is the probability of X to have a value in the range $[a, b]$. A Cumulative Distribution Function (CDF) can be derived by integrating the PDF:

$$F(x) = P(X \leq x) = \int_{-\infty}^{x} f(u)du \tag{A-2a}$$

$$f(x) = \frac{d}{dx}\left(F(x)\right) \tag{A-2b}$$

An example of a probability distribution is a uniform distribution. The PDF of a uniform distribution is described by the following equations:

$$f(x) = \begin{cases} \frac{1}{b-a} & a \leq x \leq b \\ 0 & \text{otherwise} \end{cases} \tag{A-3a}$$

$$\sigma^2 = \frac{(b-a)^2}{12} \tag{A-3b}$$

$$\mu = \frac{b+a}{2} \tag{A-3c}$$

$$a = \mu - \sigma\sqrt{3} \tag{A-3d}$$

$$b = \mu + \sigma\sqrt{3} \tag{A-3e}$$

which show that the distribution has a constant probability density within a certain bound. Another commonly used distribution is the Gaussian or normal distribution. The Gaussian PDF is described by the following equation:

$$f(x) = \frac{1}{\sigma\sqrt{2\pi}} \exp\left(-\frac{(x-\mu)^2}{2\sigma^2}\right) \tag{A-4}$$

Two examples of a probability distribution of a temperature measurement are shown in Figure A-1. The figure shows a PDF of a uniform distribution and a Gaussian distribution with $\mu = 283$ K and $\sigma = 0.5$ K. The area under these curves correspond to a probability value, so the total area under both curves equals one.

Several statistical properties of a random variable can be calculated using the PDF of the random variable. The expected value $E(X)$, expectance or mean μ_X of a random variable X can be calculated using the following equation:

$$\mu_X = E(X) = \int_{-\infty}^{\infty} xf(x)dx \tag{A-5}$$

The variance $V(X)$ is a measure of the dispersion of the distribution:

$$\sigma_X^2 = V(X) = \int_{-\infty}^{\infty} (x-\mu)^2 f(x)dx \tag{A-6}$$

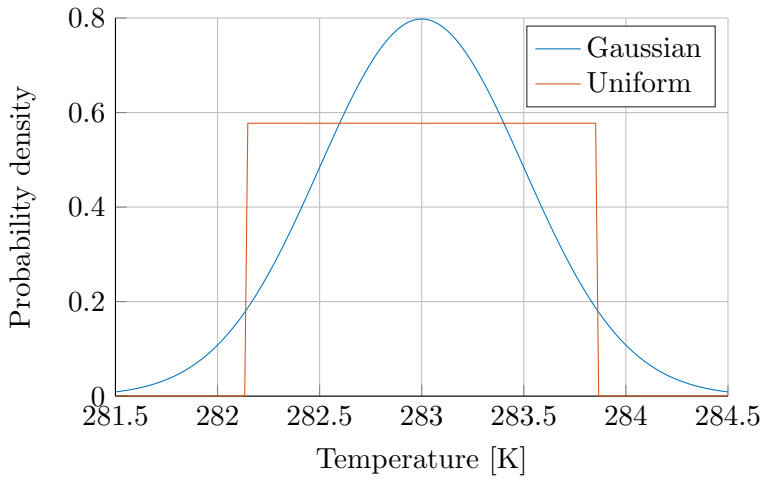

Figure A-1: Example of a PDF of a temperature measurement ($\mu = 283$ K , $\sigma = 0.5$ K).

More information can be obtained by using the moments of the distribution. The moment k'_n of X is calculated using (Casella and Berger, 1990; Rohatgi and Saleh, 2001):

$$k'_n = E(X^n) \tag{A-7}$$

The n^{th} central moment of X is given by:

$$k_n = E(X - \mu)^n \tag{A-8}$$

These moments can be used to obtain more information about the shape of the distribution. For example, the skewness can be used to measure the assymetry of the distribution and the kurtosis can be used to measure the peakiness of a distribution. The skewness k_3 and kurtosis k_4 can be calculated using (Hogg et al., 2005):

$$k_3 = \frac{E[(X - \mu)^3]}{\sigma^3} \tag{A-9}$$

$$k_4 = \frac{E[(X - \mu)^4]}{\sigma^4} \tag{A-10}$$

A-2 Covariance and Correlation

Most applications of probability theory do not consider only one random variable, but multiple random variables that can have a statistical relation. These variables are not only random, but they can also have a relation. An example is shown in Figure A-2, which is not based on any data. The figure shows 1000 measurements of the atmospheric density and the temperature. The figure shows that both measurements are random, but they also have a statistical relation, because the samples are slightly aligned.

This is an example of two random variables that have a negative correlation. This means that if the atmospheric density has a larger value, it is more probable that the temperature has a lower value. This is an example of a linear statistical dependence between the random

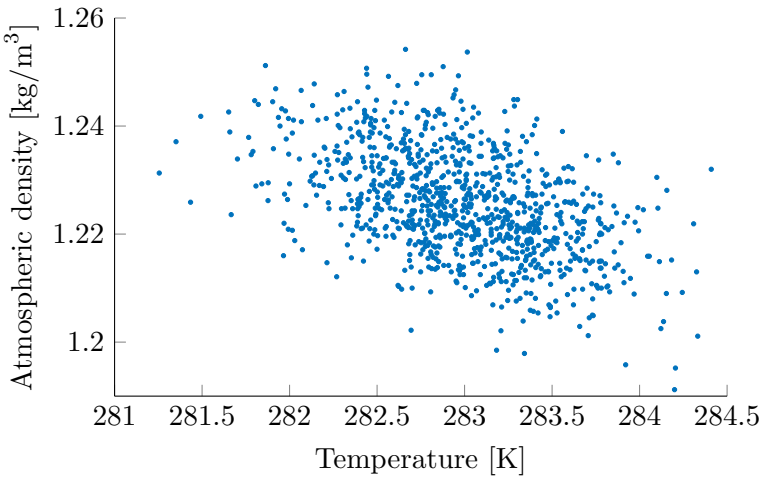

Figure A-2: Example of samples of simultanious measurements of the atmospheric density ρ and the temperature T ($\mu_T = 283$ K , $\mu_\rho = 1.225$ kg/m^3, $\sigma_T = 0.5$ K, $\sigma_\rho = 0.01$ kg/m^3, $\rho = -0.5$).

variables. A measure of the linear relation between two random variables is the covariance σ_{XY}:

$$\sigma_{XY} = E[(X - \mu_X)(Y - \mu_Y)] = E[XY] - \mu_X \mu_Y \tag{A-11a}$$

$$\sigma_{XY} = \int_{-\infty}^{\infty} xyf(x,y)dxdy - \mu_X \mu_Y \tag{A-11b}$$

where μ_X and μ_Y are the means of the random variables X and Y and $f(x,y)$ is the joint probability PDF, which will be described in the Section A-3. This distribution describes the probability distribution of each random variable and the statistical relation between them. If only, a number of samples are available of these random variable, like in Figure A-2. The covariance can be calculated using the samples x_i, y_i of the random variables X, Y (Kurowicka and Cooke, 2006):

$$S(X,Y) = \sum_{i=1}^{N} (x_i - \bar{X})(y_i - \bar{Y}) \tag{A-12}$$

where $\bar{X}, \bar{Y}$ are the sample mean of the random variables X and Y. These can be calculated using:

$$\bar{X} = \frac{\sum_{i=1}^{N} x_i}{N} \tag{A-13}$$

The relation between two random variables is important when studying the distribution of a combination of two random variables, for example $Z = X + Y$. The variance of Z is not only dependent on the variance of X and Y, but also on the covariance σ_{XY} (Dekking et al., 2005):

$$V(X+Y) = \sigma_X^2 + \sigma_Y^2 + 2\sigma_{XY} \tag{A-14}$$

The covariance is a number, which cannot be easily interpreted, because its magnitude is dependent on the variance of each variable. Therefore, the covariance is mostly transformed to a correlation, which is defined as:

$$\rho(X,Y) = \frac{\sigma_{XY}}{\sigma_X \sigma_Y} \tag{A-15}$$

where σ_X and σ_Y are the standard deviations of the random variables X and Y. This parameter is called the Pearson correlation coefficient or product moment correlation coefficient and it is a measure of linear dependence between the variables. If the random variables X and Y are linearly independent, the product-moment correlation coefficient will be zero. However, random variables are not always independent if the covariance value is zero. For example, non-linear dependence can be present that yields no linear dependence. The product moment correlation has a maximum range bounded by $-1 \leq \rho \leq 1$.

Another measure of the linear dependency between two variables is the Spearman or Rank correlation coefficient ρ_r. This coefficient is a product-moment coefficient that uses the ranks of the variables X and Y instead of the samples instead. Defining the rank R of X and the rank S of Y, the following equation can be used to calculate the rank coefficient (Kurowicka and Cooke, 2006):

$$\rho_r(X,Y) = \frac{\sum_{i=1}^{N}(R_i - \bar{R})(S_i - \bar{S})}{\sqrt{\sum_{i=1}^{N}(R_i - \bar{R})^2}\sqrt{\sum_{i=1}^{N}(S_i - \bar{S})^2}} \tag{A-16}$$

The rank correlation has several properties that gives it an advantage over the product-moment correlation. The rank correlation always exist and does not depend on the marginal distribution, which means that if a number of samples are given and the distribution of these samples is changed, the rank correlation doesn't change.

In general, the rank correlation and product-moment coefficient are different, but these coefficients are equal for uniformly distributed variables. A relationship between the product-moment correlation and rank correlation can be found for normally distributed variables (Kurowicka and Cooke, 2006):

$$\rho(X,Y) = 2\sin\left(\frac{\pi}{6}\rho_r(X,Y)\right) \tag{A-17}$$

In general multiple random variables can have linear relations with each other. These linear dependencies can be expressed using a covariance matrix $\boldsymbol{\Sigma}$, which contains the variance and covariance of all the random variables:

$$\boldsymbol{\Sigma} = E\left[(\boldsymbol{X} - \boldsymbol{\mu_X})(\boldsymbol{X} - \boldsymbol{\mu_X})^T\right] \tag{A-18a}$$

$$\boldsymbol{\Sigma} = \begin{bmatrix} \sigma_{X_1}^2 & \sigma_{X_1X_2} & \dots & \sigma_{X_1X_N} \\ \sigma_{X_1X_2} & \sigma_{X_2}^2 & \dots & \sigma_{X_2X_N} \\ \vdots & \vdots & \ddots & \vdots \\ \sigma_{X_1X_N} & \sigma_{X_2X_N} & \dots & \sigma_{X_N}^2 \end{bmatrix} \tag{A-18b}$$

Using Equation (A-15), the covariance matrix can be transformed to a correlation matrix R :

$$\boldsymbol{R} = \begin{bmatrix} 1 & \rho(X_1,X_2) & \dots & \rho(X_1,X_N) \\ \rho(X_1,X_2) & 1 & \dots & \rho(X_2,X_N) \\ \vdots & \vdots & \ddots & \vdots \\ \rho(X_1,X_N) & \rho(X_2,X_N) & \dots & 1 \end{bmatrix} \tag{A-19}$$

The covariance matrix and correlation matrix are defined using the correlation between all random variables. Because the values in the matrix provides measures for the dependence

between a pair of variables, the matrix must be consistent. This means that no contradictory correlations can be present, otherwise the matrix is invalid. A valid covariance matrix is positive definite (Kurowicka and Cooke, 2006).

A-3 Multi-Variate Distributions

In general, there can be nonlinear relations between the random variables. For example, the circular velocity and the radius of an orbit are related due to orbital mechanics. Therefore, studying only the variance and covariance of the random variables does not provide a full image of the statistical relation between the random variables. Therefore, multi-variate probability distributions are used to model the statistical dependence.

A PDF that describes the probability density distribution of multiple variables is called a joint PDF. The properties of a joint PDF are similar to the properties of a uni-variate PDF. The normalization condition for an N dimensional PDF is defined as:

$$\int_{-\infty}^{\infty} \cdots \int_{-\infty}^{\infty} f_{X_1 \ldots X_N}(x_1, \ldots, x_N) dx_1 \ldots dx_N = 1 \tag{A-20}$$

A joint PDF $f_{X_1 \ldots X_N}$ of the random variables can be used to investigate any statistical relation between the variables and the distribution of each variable. The distribution of a subset of the random variables is called a marginal probability distribution. This marginal distribution is obtained by integrating over all the random variables that are not included in the marginal distribution (Montgomery and Runger, 2014):

$$f_{X_1,\ldots,X_{N_C}} = \int_{-\infty}^{\infty} f_{x_1,\ldots,x_N} dx_{N_C+1} \ldots dx_N \tag{A-21a}$$

$$\boldsymbol{X} = \begin{bmatrix} X_1 & \ldots & X_{N_C} & \ldots & X_N \end{bmatrix}^T \tag{A-21b}$$

Such a marginal distribution can be used to identify the statistical relation between two variables or to investigate the distribution of a single variable. Consider a multi-variate Gaussian PDF, the marginal distribution of each variable is then also a Gaussian distribution.

If several random variables $X_1 \ldots X_N$ are statistically independent and the marginal distributions f_{X_i} are known, the joint distribution can be obtained by multiplying the invidual PDFs (Montgomery and Runger, 2014):

$$f_{X_1,\ldots,X_N} = f_{X_1} f_{X_2} \cdots f_{X_N} \tag{A-22}$$

For statistical impact prediction, one is interested in the probability distribution of the random state variables and time at impact. This means that one is interested in probability distributions with the condition that the altitude $h = 0$ km. If the joint distribution of the state and time is known, such a conditional distribution can be derived. A conditional distribution is a distribution of a subset of the random variables when the value of one or multiple of the random variables is known. A conditional PDF is obtained using the following equation (Montgomery and Runger, 2014):

$$f_{X_1 \ldots X_{N_C} | x_{N_C+1} \ldots x_N}(x_1, \ldots, x_{N_C}) = \frac{f_{X_1 \ldots X_N}(x_1, \ldots, x_N)}{f_{X_{N_C+1} \ldots X_N}(x_{N_C+1}, \ldots, x_N)} \tag{A-23}$$

A multi-variate Gaussian distribution is fully defined using a covariance matrix and a mean vector. However, for uniformly distributed random variables the joint distribution with correlation is not uniquely defined, because different methods exist to model the correlation between the uniformly distributed random variables. Therefore, copulae are used to model the correlation structure between uniformly distributed random variables. The bivariate PDF of uniformly distributed random variables with correlation is described by:

$$f_{XY} = \begin{cases} 1 & \text{if } (x, y) \in [0, 1] \\ 0 & \text{otherwise} \end{cases} \tag{A-24a}$$

$$F_{XY} = \begin{cases} xy & \text{if } (x, y) \in [0, 1] \\ 0 & \text{otherwise} \end{cases} \tag{A-24b}$$

Because each random variable is uniformly distributed, it means that the marginal distributions of each random variable are uniform distributions. In general, uniformly distributed variables can also be correlated. A joint PDF of correlated uniformly distributed random variables can be constructed using Copulae.

A-4 Copulae

The DPP method requires that the uncertainty in the state is modelled as a PDF. Therefore, a method is required to model a joint uniform distribution, which is discussed in this section.

Copulae are functions that can be used to model a joint PDF of a multi-variate random variable. Such a function can be used to derive a joint PDF, which describes the distribution of the random variables and the correlation structure. A copula links the marginal distributions of the random variables, while adding any specified correlation structure. A copula C uses the marginal CDFs $F_{X_i}(x_i)$ to construct a joint CDF:

$$F_{X_1 \dots X_N}(x_1, \dots, x_N) = C\left(F_{X_1}(x_1), \dots, F_{X_N}(x_N)\right) \tag{A-25}$$

An example of a joint PDF obtained using a Gaussian copula is shown in Figure A-3. The marginal distributions of the random variables X and Y are uniform distributions, while a correlation is clearly observed in the joint PDF. The figure shows a copula with a positive correlation, because if the value of X is close to one, it is more probable that the value of Y is close to one and it is less probable that the value of Y is close to zero. If no correlation is present between the uniformly distributed random variables, the figure would show a flat surface.

A joint PDF can be derived by taking the derivative of Equation (A-25):

$$f_{X_1 \dots X_N}(x_1, \dots, x_N) = c\left(F_{X_1}(x_1), \dots, F_{X_N}(x_N)\right) f_{X_1}(x_1) \dots f_{X_N}(x_N) \tag{A-26a}$$

$$c = \frac{\partial^N C}{\partial F_{X_1}(x_1) \dots \partial F_{X_N}(x_N)} \tag{A-26b}$$

where c is called the copula density. The joint PDF $f_{X_1 \dots X_N}$ is thus defined using the marginal CDFs F_{X_i} and marginal PDFs f_{X_i} and the copula density. This means that the copula density

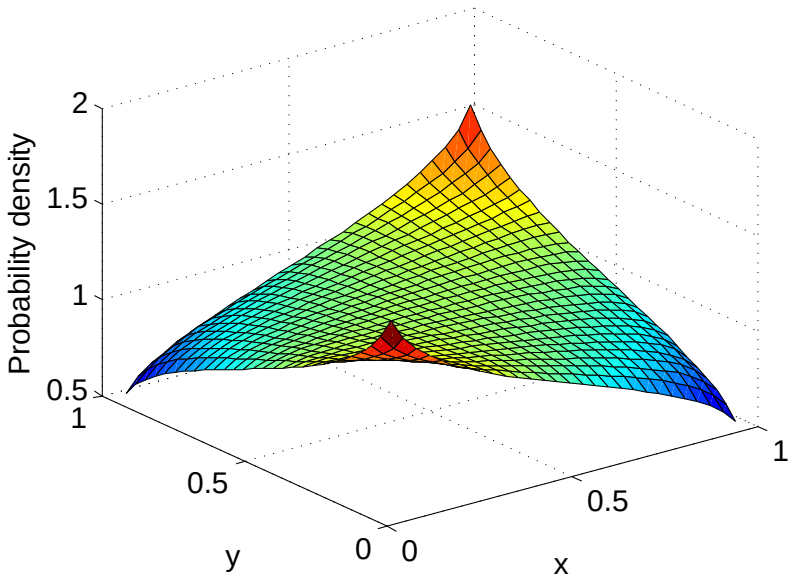

Figure A-3: Example of a joint PDF using a Gaussian copula with uniform marginals of X and Y.

basically merges the marginal distributions to obtain a joint distribution, which can included correlation.

Copulae are constructed using the following properties. Consider a variable X with CDF $F_X(x)$, a random variable U with a uniform distribution on $[0, 1]$ can then be constructed using (Kurowicka and Cooke, 2006):

$$U = F_X(X) \tag{A-27}$$

This means that any variable can be transformed to a uniform distribution with bounds $(0, 1)$ by inserting it into its CDF. Similarly, the inverse transformation can also be performed (Dekking et al., 2005):

$$X = F_X^{-1}(U) \tag{A-28}$$

A copula is a distribution defined on $[0, 1]^N$ with uniform marginal distributions. As one can see in Equation (A-25), the marginal CDFs are used as input variables for the copula. It can be derived that the random variable X is transformed to a uniform variable using the CDF and Equation (A-28). This means that the copula uses uniformly distributed input variables to represent the joint distribution. However, the variables itself can have an arbitrary distribution.

A-4-1 Gaussian Copula

A copula can be constructed using different methods and one of these methods is using an N-dimensional distribution function H and its marginals H_i (Song, 2000):

$$C\left(u_1, \ldots, u_N\right) = H(H_1^{-1}(u_1), \ldots, H_N^{-1}(u_N)) \tag{A-29}$$

where u is a uniformly distributed variable with $u \in [0,1]$. Observing the equation, one can conclude that the uniformly distributed variables U_i are transformed to another distribution using the inverse function and again transformed to a uniform distribution. The construction of such a copula is thus based on the properties given in Equations (A-28) , (A-27). An example of such a copula is the Gaussian copula (Kurowicka and Cooke, 2006):

$$C_{Gauss}(u_1, \ldots, u_N) = \Phi_G\left(\Phi^{-1}(u_1), \ldots, \Phi^{-1}(u_N)\right) \tag{A-30}$$

where Φ_G is the multi-variate normal CDF and Φ the uni-variate normal CDF. In principle, the Gaussian copula can be used to link random variables with any distribution. However, the Gaussian copula will be used to model the PDF of uniformly distributed correlated variables for this research.

Considering a random variable X uniformly ditributed on $[0,1]$ and its marginal PDF $f_{X_i} = 1$ and marginal CDF $F_{X_i} = x_i$, a Gaussian copula can be used to derive the joint PDF (Song, 2000):

$$f_{X_1 \ldots X_N}(x_1, \ldots, x_N) = c_{Gauss}\left(F_{X_1}(x_1), \ldots, F_{X_N}(x_N)\right) \tag{A-31a}$$

$$f_{X_1 \ldots X_N}(x_1, \ldots, x_N) = \frac{1}{\sqrt{|\boldsymbol{\Sigma}|}} \exp\left(-\frac{1}{2}\boldsymbol{y}^T(\boldsymbol{\Sigma}^{-1} - \boldsymbol{I})\boldsymbol{y}\right) \tag{A-31b}$$

$$\boldsymbol{y} = \Phi^{-1}(\boldsymbol{x}) \tag{A-31c}$$

where $\boldsymbol{\Sigma}$ is the covariance matrix. A plot of a bivariate Gaussian copula is shown in Figure A-3.

A-4-2 The Multi-variate Uniform PDF

The PDF defined in Equations (A-31) is based on the fact that $\boldsymbol{X} \in [0,1]^N$, however the uniform distributions in general have different bounds.

$$F_{X_i}(x_i) = \begin{cases} 0 & x_i - \mu_i < -\sigma_i\sqrt{3} \\ \frac{x_i - \mu_i + \sigma_i\sqrt{3}}{2\sqrt{3}\sigma_i} & -\sigma_i\sqrt{3} \leq x_i - \mu_i \leq \sigma_i\sqrt{3} \\ 1 & x_i - \mu_i > \sigma_i\sqrt{3} \end{cases} \tag{A-32a}$$

$$f_{X_i}(x_i) = \begin{cases} 0 & x_i - \mu_i < -\sigma_i\sqrt{3} \\ \frac{1}{2\sqrt{3}\sigma_i} & -\sigma_i\sqrt{3} \leq x_i - \mu_i \leq \sigma_i\sqrt{3} \\ 1 & x_i - \mu_i > \sigma_i\sqrt{3} \end{cases} \tag{A-32b}$$

The joint PDF of uniformly distributed random variables $\boldsymbol{X}$ with arbitrary bounds can be obtained by using these distributions as specified in Equation (A-26a):

$$f_{X_1 \ldots X_N}(x_1, \ldots, x_N) = \frac{1}{\prod_{i=1}^{N}(b_i - a_i)\sqrt{|\boldsymbol{R}|}} \exp\left(-\frac{1}{2}\boldsymbol{y}^T(\boldsymbol{R}^{-1} - \boldsymbol{I})\boldsymbol{y}\right) \tag{A-33a}$$

$$y_i = \Phi^{-1}(F_{X_i}(x_i)) \tag{A-33b}$$

where $\boldsymbol{R}$ is the correlation matrix, $F_{X_i}(x_i)$ is defined using Equation (A-32) and x_i is uniformly distributed on $[a_i, b_i]$.

Important to notice is that the Gaussian copula (or distribution) uses the product-moment correlation to define the PDF. However, the copula transforms the uniformly distributed random variables $\boldsymbol{X}$ to random variables $\boldsymbol{Y}$ that are normally distributed. This transformation changes the product-moment correlations, but the rank correlations remain the same. This means that the correlation matrix of $\boldsymbol{X}$ also needs to be converted to the product-moment correlation matrix of $\boldsymbol{Y}$. These transformations are schematically shown in Figure A-4. The rank correlation and the product-moment correlation are equal for uniform distribution and the rank correlation is independent of the marginal distribution, thus the product-moment correlation matrix $\boldsymbol{R}^U$ of $\boldsymbol{X}$ is equal to the rank correlation matrix $\boldsymbol{R}_r^G$ of $\boldsymbol{Y}$. Therefore, the correlation matrix can directly be transformed using Equation (A-17).

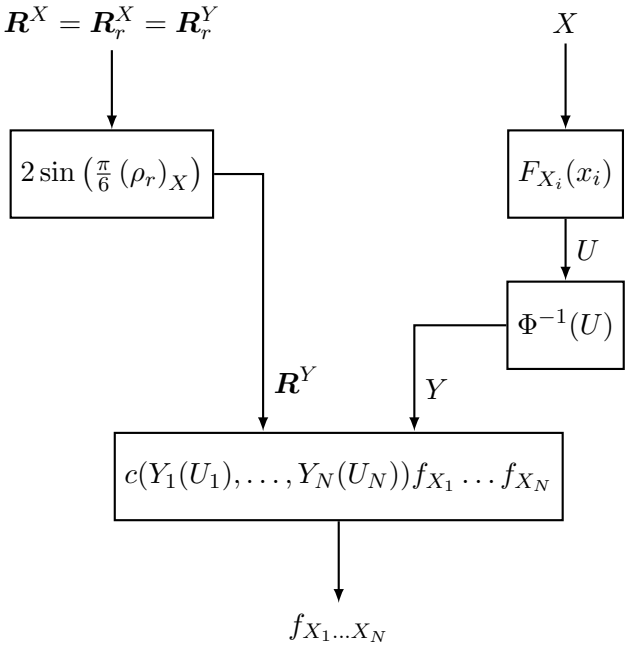

Figure A-4: Transformation of uniformly distributed random variable X and corresponding correlation matrix $\boldsymbol{R}^X$.

A-4-3 Example

The joint uniform PDF described by Equation (A-33) is used to generate the underlying bivariate PDF of the samples that are drawn in the research of Ronse (2013). Figure A-5 shows a comparison of a Gaussian copula and samples used by Ronse (2013). The probability density is presented by colors, note that the colorbar is truncated at a value of 0.01 so that figure can be better compared. Otherwise the value would go to infinity in the upper right and lower left corners of the PDF. The figure shows that the samples and the shape of the PDF are similar. Furthermore, the areas of higher probability density correspond to the areas with a higher number of samples. This shows that the PDF represents the correct distribution of the generated samples.

The method of Ronse (2013) was based on the research of Li and Hammond (1975). This method converts the variables to a Gaussian distribution, correlates the variables and converts the variables back to a uniform distribution, which is similar to this sampling method. This is equivalent to how the Gaussian copula correlates the random variables. Therefore, one can conclude that a Gaussian copula represents the joint PDF corresponding to the sampling method.

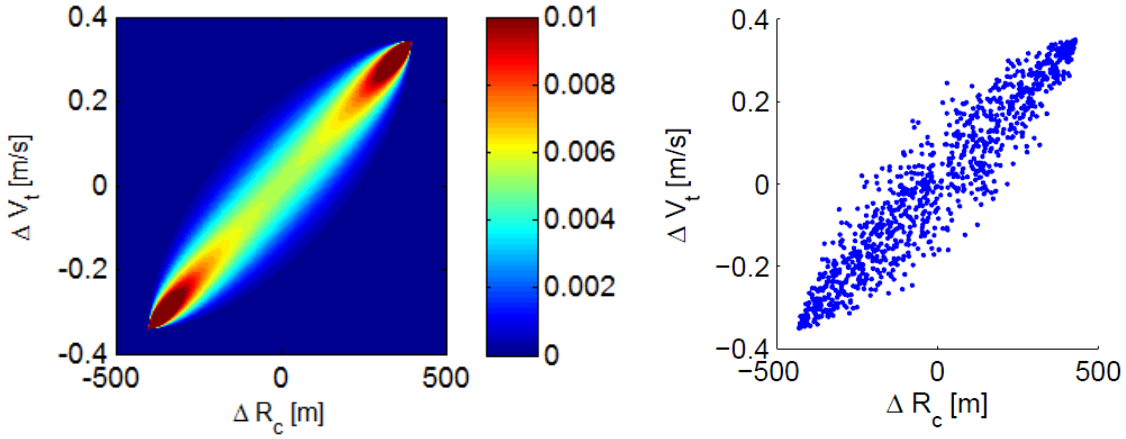

(a) Joint PDF.

(b) Samples.

Figure A-5: Comparison of joint PDF constructed using a Gaussian copula with samples generated in the research of Ronse (2013).

Appendix B

One-Dimensional Test Case

This chapter will describe research that has been performed on a one-dimensional test case. The goal of this research is to learn about the capabilities and limitations of the methods. A second goal is to get an indication of the (relative) performance of the methods. The chapter will start by explaining the dynamical model (Section B-1) that will be used for the simulations. Subsequently, analytical solutions are discussed in Section B-2. The research goals and setup is discussed in Section B-3. After that the development and verification of the simulators is discussed in Section B-4-1 and the results and conclusions will be discussed in Section B-5.

B-1 Dynamical model

The dynamical model that will be used in the simulations is described in this section. The model that was selected is presented in Equation (B-1). This model is selected, because it is non-linear, the evolution of the PDF has an analytical solution and an example is provided in the research of Pantano and Shotorban (2007), which can be used to verify the simulator. This model was also used as an example in the research of Halder and Bhattacharya (2011).

The dynamical model is one-dimensional differential equation, which governs the evolution of the variable x in time t.

$$\begin{aligned} \dot{x} &= ax^2 + bx + c \\ \text{with } & b^2 - 4ac > 0 \end{aligned} \tag{B-1}$$

The equation is a non-linear quadratic equation that contains constants, which can be varied to obtain models with different characteristics.

To understand how the PDF will change over time it is required to know how the state x evolves when originating from different initial conditions. This can be derived using a plot of the derivative as a function of the state, of which an example is displayed in Figure B-1. The figure shows that there are two roots, which are points where the derivative of the state

is equal to zero. The gray arrows in the figure display the trajectories that the state x will follow if it starts somewhere along the curve.

The arrows can be explained as follows. If the initial state is smaller than the left root, the state derivative will be negative, so the state will continue to decrease. If the initial state is in between the first two roots, the derivative will be positive and eventually decrease to zero when the state approaches the value of the right root. If the initial state is larger than the value of the right root, it will also converge towards the right root. When the initial state starts in any of these roots, it will not change it value, because the state derivative is equal to zero. It can thus be said that the left root is unstable and the right root is stable. When the derivative decreases as the state approaches the stable root, it can be concluded that the solution will asymptotically approach the stable root.

As one can observe from Equation (B-1), the constants of the dynamical model will be selected such that the equation has real roots. This is beneficial for the derivations. Several examples of the evolution of the state x are shown in Figure B-2. The figure shows several trajectories originating from different initial states. The figure shows that the state does not change if it originates from $x_0 = 1$ or $x_0 = 5$, which correspond to the roots of the dynamical model that is used. The figure further shows that the trajectories converge to $x = 5$, which is the stable root and diverge from $x = 1$, which is the unstable root.

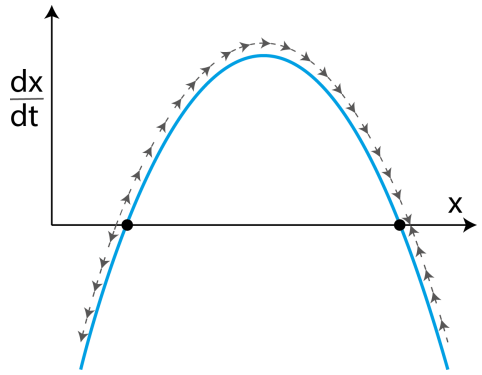

Figure B-1: State derivative vs state plot to illustrate the behaviour of the state over time.

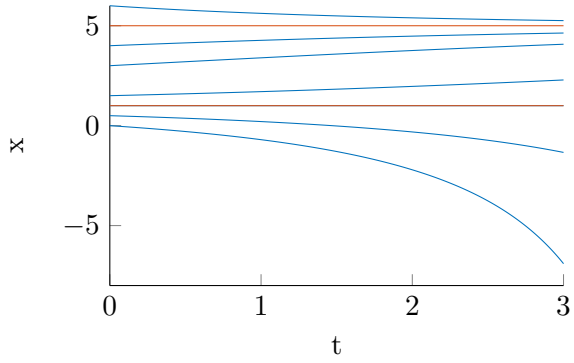

Figure B-2: Example trajectories originating from different initial states with model $\dot{x} = -0.1x^2 + 0.6x - 0.5$ (roots: $x = 1, x = 5$).

B-2 Probility Density Evolution

The evolution of uncertainty in a state can be propagated by defining the intial state using a PDF and propagating the PDF in time. This PDF can be propagated in time using Equation (3-27). An exact solution for the trajectory of x can be obtained using the model described by Equation (B-1):

$$x(x_0, t) = -\frac{1}{a}\left(\frac{ar_1x_0e^{\gamma t} + r_1r_2e^{\gamma t} - ar_2x_0 - r_1r_2}{ax_0e^{\gamma t} + r_2e^{\gamma t} - x_0a - r_1}\right) \tag{B-2}$$

This solution can be solved for the initial condition x_0 as a function of x and time t, which is required to solve the PDF evolution in time.

$$x_0(x,t) = \frac{1}{a}\left(\frac{ax(r_2e^{\gamma t} - r_1) + r_1r_2(e^{\gamma t} - 1)}{ax(1 - e^{\gamma t}) - r_1e^{\gamma t} + r_2}\right) \tag{B-3}$$

where the following constants are used:

$$D = \frac{b^2}{4} - ac > 0 \tag{B-4a}$$

$$r_1 = b/2 + \sqrt{D} \tag{B-4b}$$

$$r_2 = b/2 - \sqrt{D} \tag{B-4c}$$

$$\gamma = r_1 - r_2 = \sqrt{b^2 - 4ac} \tag{B-4d}$$

The PDF $\varphi(x,t)$ can be solved as a function of time using:

$$\varphi(x,t) = \varphi(x_0,0)\exp\left(-\int_0^t \Psi(x(t))dt\right) \tag{B-5a}$$

$$\Psi(x(t)) = \frac{dF}{dx} = 2ax(t) + b \tag{B-5b}$$

If the exact solutions x_0 and x are substituted and the integral is evaluated the following solution is obtained:

$$\begin{aligned}\varphi(x,t) = \frac{\varphi(x_0,0)}{\gamma^2}\exp\Bigg(&bt + \frac{2r_1}{\gamma}\ln\left[x_0a(e^{-\gamma t} - 1) - r_2 + r_1e^{-\gamma t}\right] \\ &- \frac{2r_2}{\gamma}\ln\left[x_0a(1 - e^{\gamma t}) + r_1 + r_2e^{\gamma t}\right]\Bigg)\end{aligned} \tag{B-6}$$

This equation provides the exact solution of the PDF $\varphi(x,t)$ in time. Examples of such a solution are provided in the upcoming sections.

B-3 Research Setup

Several simulations are performed to investigate the performance of the methods and the influence of the PDF model on the accuracy of the LSQKD method.

B-3-1 Simulation setup

The simulations will be performed using the following dynamical model.

$$\dot{x} = a\left(-x^2 + 8x - 7\right) \tag{B-7}$$

This model contains two roots at $x = 1$ and $x = 7$, where $x = 7$ is the stable root, and the maximum state derivative is equal to:

$$\dot{x}_{max} = 9a$$

The constant a scales the state derivative so it can be changed to investigate the effect of faster or slower dynamics.

Four initial distributions will be used in the simulations, i.e., two Gaussian and two uniform distributions, and stable and unstable solutions will be considered. A summary of the initial distributions is given in Table B-1. The stable solutions correspond to the converging trajectories shown in Figure B-2, which converge to the stable root. The unstable solutions correspond to the diverging trajectories in the figure.

Table B-1: Initial distributions that will be used in the simulations.

	Uniform	Gaussian
Stable	$[2; 5]$	$\mu = 3$, $\sigma = 1$
Unstable	$[-2; 0]$	$\mu = -1$, $\sigma = 2$

In addition, the number of kernels will be varied in the simulations.

B-3-2 Kernel selection

The true PDF will be approximated by a weighted summation of kernels. Therefore, a proper selection of these kernels is important. A Gaussian kernel is used for the cases where the initial distribution is a Gaussian distribution. Using such a kernel the initial distribution can be accurately modelled. The cases with an initial distribution that is uniform requires different kernels.

Initial Distribution: Uniform

The LSQKD method is limited in a way that it cannot represent an exact uniform distribution. Therefore, several options are considered that can approximate a uniform distribution. The first option is to use two approximate step functions, which could have the following functional form:

$$K_1(x, \mu, h, \alpha) = \frac{1}{4h}\left(\frac{x - \mu + h}{\sqrt{\alpha + (x - \mu + h)^2}} - \frac{x - \mu - h}{\sqrt{\alpha + (x - \mu - h)^2}}\right) \tag{B-8}$$

where the center of the distribution is defined by μ, the width of the distribution is $2h$ and α is a tuning parameter. This function is also refered to as the square root block kernel. The tuning parameter α determines how closely the function will match a uniform distribution. In the following limit case, the kernel results in a uniform distribution:

$$\lim_{\alpha \to 0} \left(K_1(x, \mu, h, \alpha)\right) = \begin{cases} \frac{1}{2h} & -h < x - \mu < h \\ 0 & \text{otherwise} \end{cases} \tag{B-9}$$

A similar function can be created using an exponential function:

$$K_2(x,\mu,h,\alpha) = -\frac{\alpha}{2\ln(\exp(-\alpha h))}\left(\frac{1}{1+\exp(\alpha(x-\mu+h))}+\frac{1}{1+\exp(-\alpha(x-\mu-h))}-1\right) \tag{B-10}$$

which is referred to as the exponential block kernel. This function has the same properties as the other approximate function, however, the tuning parameter α has to be large to approximate the uniform distribution accurately:

$$\lim_{\alpha\to\infty}\left(K_2(x,\mu,h,\alpha)\right) = \begin{cases}\frac{1}{2h} & -h < x-\mu < h \\ 0 & \text{otherwise}\end{cases} \tag{B-11}$$

More approximate uniform distributions can be derived using the arctan and tanh functions and absolute values, however these functions result in expressions that are more difficult to implement in the LSQKD method. In Figure B-3 an example is shown of these two approximate uniform distributions. The figure shows that the descrepancy between a uniform distribution and the function is small, so these functions are a valid choice.

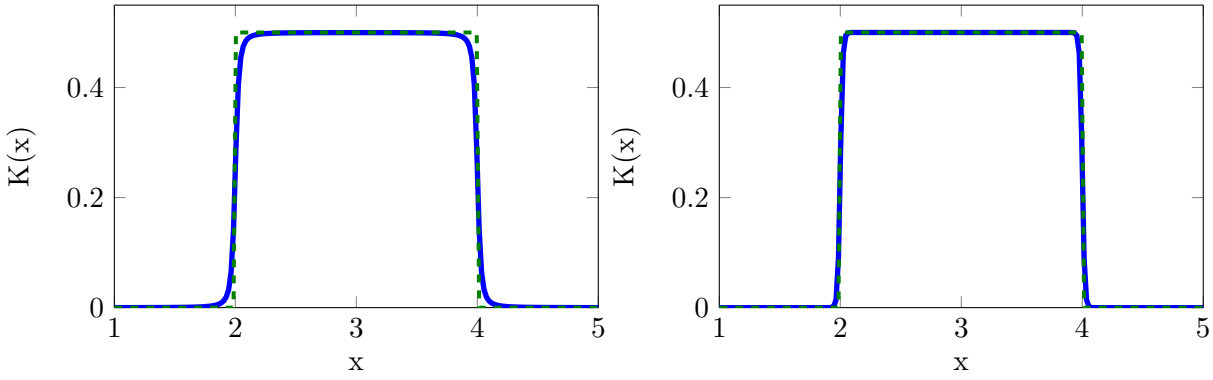

Figure B-3: Approximate block function $K_1(x)$ with $\mu = 3$, $h = 1$ and $\alpha = 10^{-3}$ and $K_2(x)$ with the same parameters except $\alpha = 10^2$.

Another option would be to use two functions which can form a uniform distribution when they are combined with equal weights:

$$\boldsymbol{P} = \begin{pmatrix} f(x) \\ 1-f(x)\end{pmatrix} \tag{B-12}$$

Using this method requires a larger number of kernels than the other functions, so a single function is preferred. A third option is to use a polynomial of the form:

$$K_3 = \begin{cases}\frac{1}{h}\left(1-\left(\frac{x-\mu}{h}\right)^{2N}\right) & -h < x-\mu < h \\ 0 & \text{otherwise}\end{cases} \tag{B-13}$$

with a large value of N such that it gets a block like shape. Since derivatives of the kernels are used, it is expected that numerical problems occur due to the large power in the function.

B-4 Simulator development and verification

Several simulators are developed that each implement one of the methods that will be compared. The simulators that are developed are:

Sim-21-1 Monte Carlo simulator - Generates a large number of trajectories using the model (Equation (B-1)) and the initial distribution.

Sim-21-2 Exact DPP simulator - Exact probability density function propagator. This simulator implements the analytical solution (Equation (B-6)) for the evolution of the probability density function.

Sim-21-3 Numerical DPP simulator - This propagates the PDF numerically using the DPP method. A system architecture of this simulator is displayed in Figure B-4. The difference with the exact DPP simulator is that $x_0(x,t)$ and Ω are solved numerically. Such a simulator is developed, because analytical solutions does not always exist. The state x is propagated backwards to obtain the corresponding $x_0(x,t)$, as explained in Section 8-1.

Sim-21-4 LSQKD simulator - Propability density function propagator, which provides the evolution of the kernel shape parameters. This simulator is developed such that any number of kernels can be used. Even though an analytical solution exists for one Gaussian kernel, a numerical method is implemented to generalize the simulator.

These simulators are developed using C++, the Tudat, Boost and Eigen libraries, which are discussed in Section 8-2-1. The numerical integrators or ODE solvers of the Tudat library are used to integrate the trajectories. The Boost library is used to generate random numbers for the MC simulator and the Eigen library is used for all the linear algebra applications.

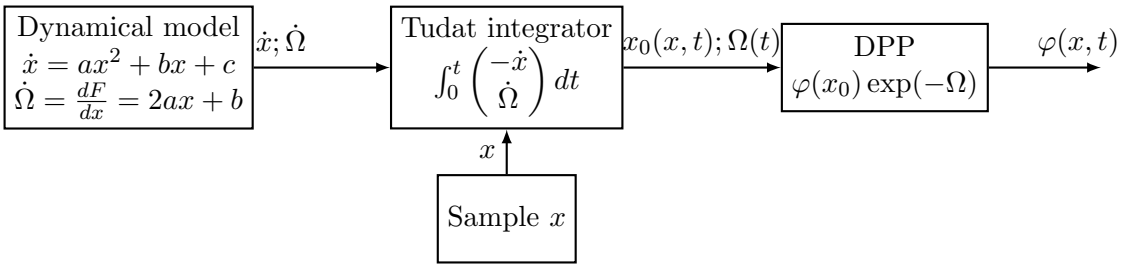

Figure B-4: System architecture of the numerical DPP simulator

B-4-1 Verification

The simulators are verified by performing unit and system tests. The unit tests confirm whether the individual components are correctly implemented and the system tests check the simulator as a whole. For each component of the simulator a test is performed that uses an exact solution to test if the correct output is provided.

System test

The simulators are verified by comparing the results with the exact solution and with the other simulators. The exact solution is verified using results from the paper and knowledge about the dynamical model as described in Section B-1. The first system test that is performed, reconstructs the results in the paper of Pantano and Shotorban (2007). The second system test is performed using an initial distribution, which is uniform for which no reference is available.

Initial distribution Gaussian
The dynamical model that was used in the research of Pantano and Shotorban (2007) will be used for the first system test. The goal of this system test is to reconstruct the results in the paper and to verify the simulators. The dynamical model for these tests will be:

$$\dot{x} = -x^2 + x + 2 \tag{B-14}$$

This dynamical model has a root at $x = -1$ and $x = 2$, of which $x = 2$ is the stable root and the other is an unstable root. This means that it can be expected that if the initial PDF is located in between these two roots, it will move towards $x = 2$.

Figure B-5 displays the solution obtained using the LSQKD simulator and the exact solution. The figures illustrate that the probability density converges towards the second (stable) root ($x = 2$) as time evolves, as can be expected. The figure also displays an exact replication of the figure described in the paper of Pantano and Shotorban (2007). This shows that the simulator provides accurate results.

The DPP numerical simulator was compared with the exact solution and the absolute error of the PDF ranged from 10^{-3} to 10^{-9} with a mean error of $1.3 \cdot 10^{-4}$. This verifies that the correct solution is obtained with the numerical simulator. Furthermore, the integral of PDF obtained using the exact solution simulator and the DPP numerical simulator had an error of at most 10^{-4}.

A kernel density estimate of samples generated by the MC simulator also resulted in a PDF that was similar to the exact solution. Over the range of the whole PDF, the absolute error varied between 10^{-5} to 10^{-2} with a mean of $3 \cdot 10^{-3}$.

Another system test, which was also performed in the research of Pantano and Shotorban (2007), was performed using a different initial mean $\mu(0) = -2$. The results of this test are plotted in Figure B-6. The figure is an exact match with the figure presented in the paper, except for the LSQKD curve for $t = 0.15$. The LSQKD simulator was not able to reproduce the curve for $t = 0.15$ presented in the paper. This can be attributed to numerical issues, because two different solutions for $t = 0.3$ could be obtained by changing the tolerance and initial stepsize. The solution of the paper ($\mu = -4.99$,$\sigma = 2.40$) was only obtained with one specific integrator setting. Every other setting resulted in the solution ($\mu = -5.37$, $\sigma = 2.82$). A comparison showed that the second solution approximates the exact solution better, because the integrated error is lower and the mean of the PDF is closer to the exact value of $\mu = -6.33$.

The DPP simulator and the MC simulator resulted in an exact match with the exact solution.

Initial distribution uniform
A second system test is performed to verify that the LSQKD simulator with the uniform

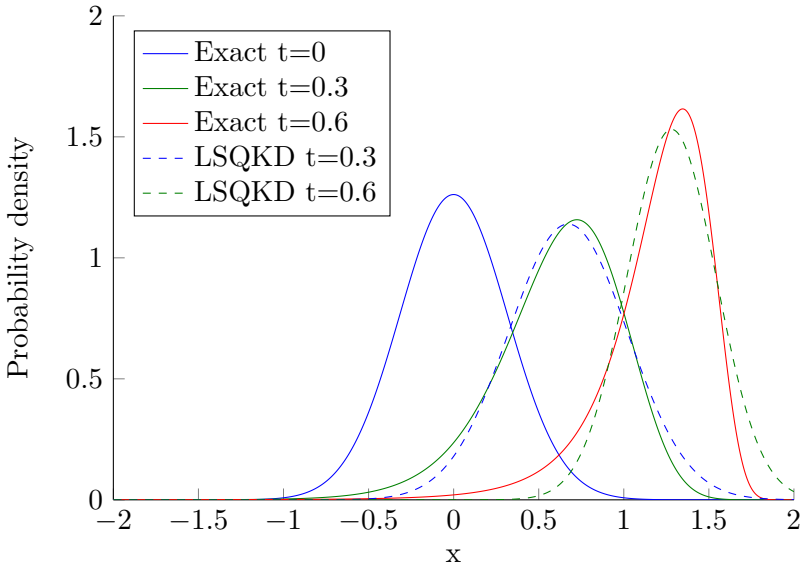

Figure B-5: A reconstruction of the probability density evolution as described in the research of Pantano and Shotorban (2007) with initial Gaussian distribution with $\mu(0) = 0$ and $\sigma(0) = \sqrt{0.1}$.

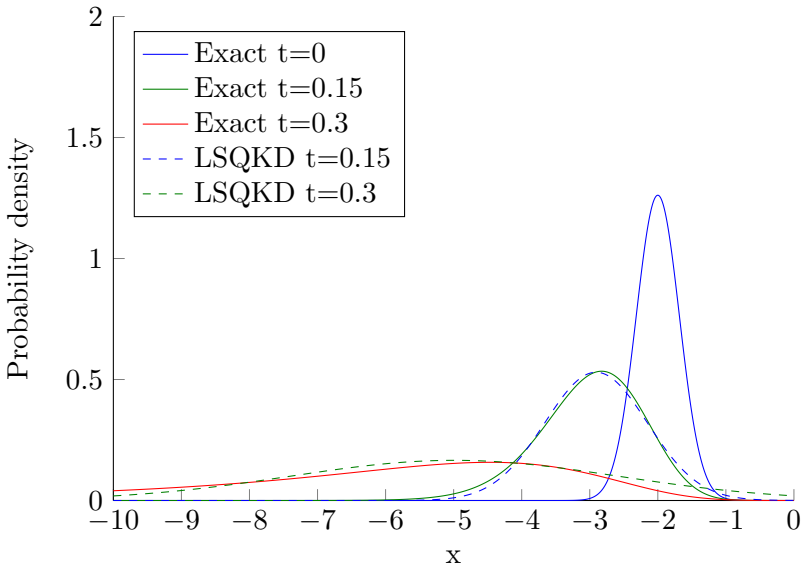

Figure B-6: An approximate reconstruction of the probability density evolution as described in the research of Pantano and Shotorban (2007) with initial Gaussian distribution with $\mu(0) = -2$ and $\sigma(0) = \sqrt{0.1}$.

kernel works correctly. The dynamical model that is used during this simulations is:

$$\dot{x} = x^2 - \frac{1}{2}x - \frac{1}{2} \tag{B-15}$$

This model has a root at $x = 1$ and $x = -0.5$, with the latter root as the stable root. The model has a minimum state derivative of $\dot{x}_{min} = -9/16$, so it is less dynamic than the model of the first system test. The initial distribution is a uniform distribution with a mean of 0.5 and a width of 1.

The exact solution of the evolution of the PDF is displayed in Figure B-7. The figure shows that the probability density converges towards $x = -0.5$, which is expected because this is the stable root of the dynamical model. The numerical DPP simulator and the MC simulator combined with KDE resulted in the same distributions.

Several tests were performed with the LSQKD simulator and the square root block kernel with varying number of kernels. The results are displayed in Figure B-8. As one can see in the figure, a single kernel is not sufficient to approximate the PDF. However, the approximation becomes increasingly accurate with an increasing number of kernels. It is clearly seen that the solution follows the behavior of the dynamical models, because it converges towards the root at $x = 0.5$.

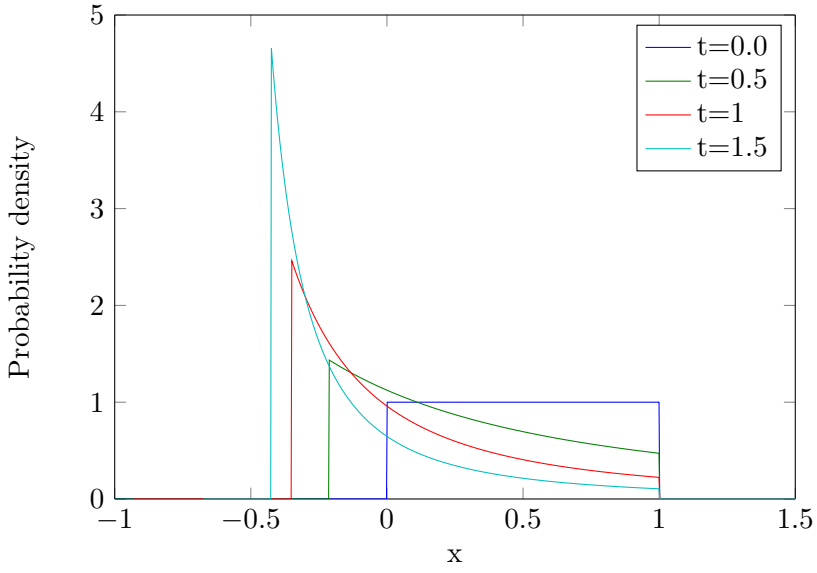

Figure B-7: Exact solution of the evolution of the PDF the state x with an initially uniform PDF.

B-5 Results

The results of the simulations for the test cases described in Table B-1 are presented and discussed in this section.

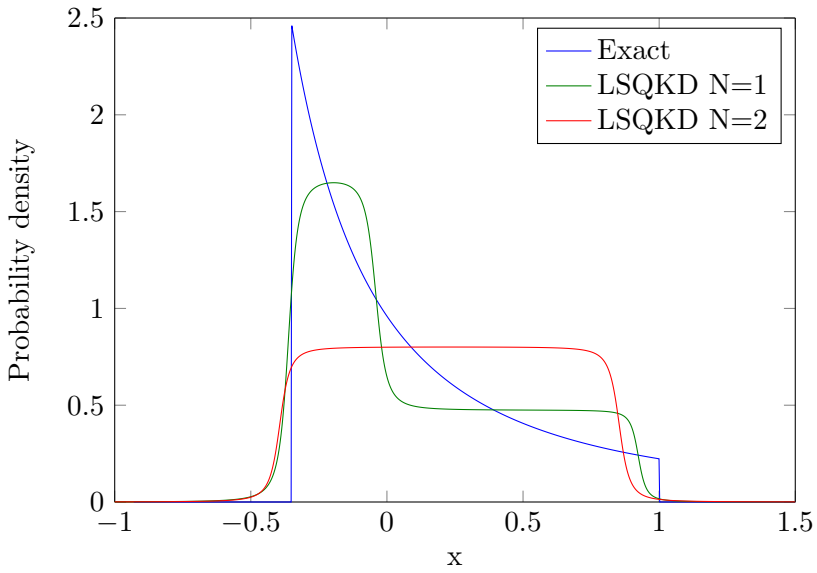

Figure B-8: Exact solution and LSQKD solution with N square root block kernels at $t = 1.0$.

B-5-1 Gaussian initial distribution

Two test cases involve an initial distribution that is Gaussian, of which one represents stable behavior and the other unstable.

The exact solution and the LSQKD solution where one Gaussian kernel is used to model the PDF are shown in Figure B-9. The figure clearly shows that the LSQKD solution is close to the exact solution, the skewness of the PDF is not included because only one Gaussian kernel is used. Therefore, an another simulation is performed using two Gaussian kernels, which is shown in Figure B-10. The figure shows that the LSQKD solution matches the exact solution more closely than with one Gaussian kernel. Some performance parameters are calculated for these cases and presented in Table B-2. The Mean Integrated Square Error (MISE), the error in variance and mean are much lower and in particular an improvement in the skewness is observed. Furthermore, the kurtosis is lower and closer to the exact value.

In addition, it can be observed from the figures that the error increases over time. This is a logical result, because the non-linearity of the model becomes more important and the Gaussian kernels cannot fully account for the non-linear behavior.

Table B-2: Comparison of performance parameters for $t = 1.5$.

	MISE	Mean	Variance	Skewness	Kurtosis	Computation time [s]
LSQKD N=1	0.0219	5.6219	0.6308	-0.01	7.32	1.340
LSQKD N=2	0.0043	5.3735	0.9267	-1.06	4.5	5.313
Exact	0	5.172	1.1283	-1.19	4.75	-

Further simulations were performed with a large number of kernels, however no accurate solution could be obtained. This originates from the fact that the matrices $\boldsymbol{A}$ and $\boldsymbol{B}$ (Equation (3-61)) become singular for certain settings. This can be explained by the determinants of

these matrices, which have the following form for N kernels:

$$\det(\boldsymbol{A}_N) = \frac{k_A}{\pi^{N/2}} \tag{B-16a}$$

$$\det(\boldsymbol{B}_N) = \frac{k_B \prod_{i=1}^{N} w_i^4}{\pi^N} \tag{B-16b}$$

where the constant k is a numerical values depending on the parameters (μ, σ) of the kernel. This value approaches zero as the kernel parameters approach each other, which is required to model an initial distribution. It has been observed that k also approaches zero as the number of kernels (with approximately the same parameters) is increased. Furthermore, the weights w_i, which are by definition smaller than 1, cause that the determinant rapidly approaches zero for an increasing number of kernels. This will lead to numerical problems, which make it unfeasible to obtain an accurate solution. Because this problem originates from the PDF and the LSQKD method, it is independent of the dynamical model.

As shown in Table B-2, the computation time required by the LSQKD simulator was low. It was found that computation time was highly dependent on the number of datapoints that was used to computate the integrals to define the vectors $\boldsymbol{D}$ and $\boldsymbol{E}$ (Equation (3-61)). For a large number of datapoints it was observed that the computation time varies with $3N$, which is the number of integrals that need to be evaluated for every state-derivative calculation. For a smaller number of datapoints, the growth rate was higher than $3N$, so the integral evaluation has a smaller influence.

The computation time of the numerical DPP simulator was in the order of a few seconds and the MC simulations were performed in around 40 seconds for 10^4 datapoints. The LSQKD solution was thus obtained faster than the MC, but not faster than the DPP simulator. The computation time for the DPP method is not provided, because it is dependent on the number of datapoints that are simulated. No fair comparison can be made, because the DPP simulator almost exactly matches the exact solution, so with only a small number of datapoints a highly accurate result can be obtained.

Another simulation was performed where the initial distribution is located in the unstable region of the dynamical model. A less dynamic dynamical model was used with a factor a of $1/20$. The performance of the methods was similar as in the stable case discussed before.

B-5-2 Uniform initial distribution

Several simulations were performed using an initial uniform distribution. The solution with only one kernel resulted in a PDF that is a block with a height that is approximately equal to the mean of the true PDF.

A more accurate solution is obtained with two kernels, which is shown in Figure B-11. The figure shows that LSQKD method produces the most optimal solution for the chosen kernels that are used. However, due to the choice of the kernels the shape of the distribution cannot be accurately represented. Some performance parameters for these cases are shown in Table B-3. The table shows that the LSQKD solution is much better for two kernels than for one kernel, however, the skewness and kurtosis values also show that the shape of the distribution does not match the exact solution. No solutions could be obtained with $N \geq 3$ kernels, due to numerical issues as discussed earlier for the initial Gaussian distribution case.

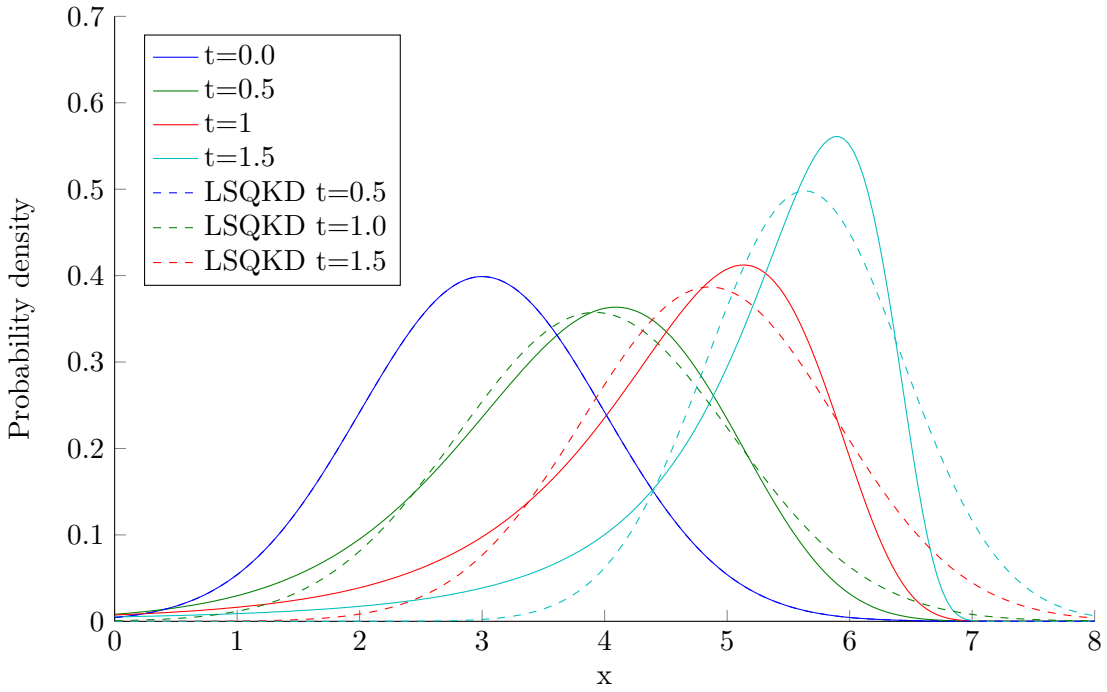

Figure B-9: PDFs of x at various time instances. The solid lines represent the exact solution and the dashed lines represent the LSQKD solution using one Gaussian kernel.

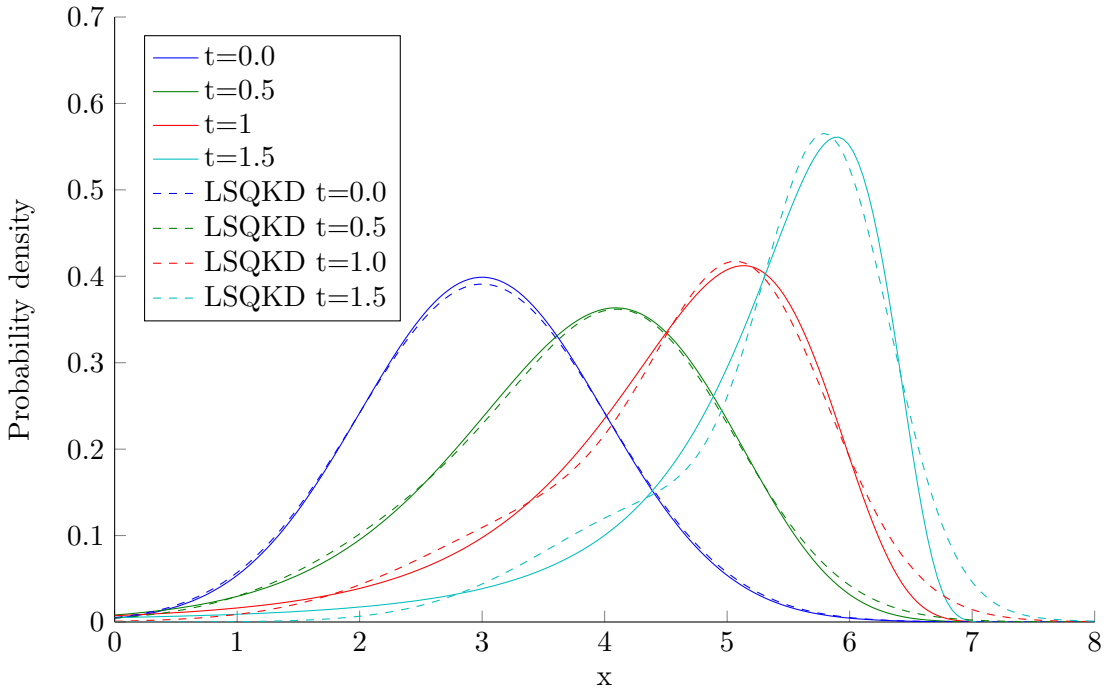

Figure B-10: PDFs of x at various time instances. The solid lines represent the exact solution and the dashed lines represent the LSQKD solution using two Gaussian kernels with $\mu_1(0) = 2.8$,$\mu_2(0) = 3.2$,$\sigma_1(0) = \sigma_2(0) = 1$.

The computation time for these cases is also much larger than for the results obtained with the initial Gaussian distribution (Table B-2). This originates from the fact that all the integrals in the LSQKD equations were integrated using numerical quadrature. Since the DPP simulator and the MC simulator resulted in more accurate results within 5 seconds, the LSQKD method does not outperform the other methods for this case.

Table B-3: Comparison of performance parameters for $t = 1.5$.

	MISE	Mean	Variance	Skewness	Kurtosis	Computation time [s]
Exact	0	5.73	0.38	-2.49	15.21	-
LSQKD N=1	0.1171	5.42	0.42	0.00	10.13	5.4
LSQKD N=2	0.032	5.67	0.43	-1.80	10.60	17.5

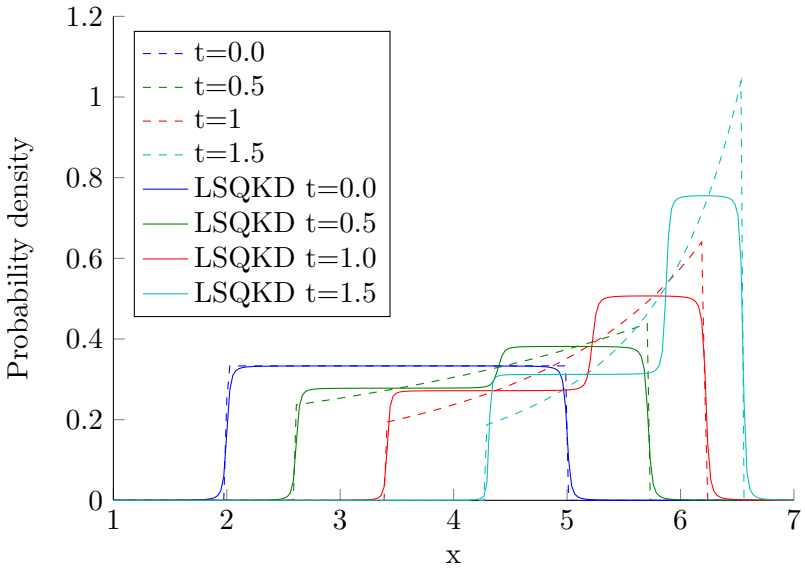

Figure B-11: PDFs of x at various time instances using two sqrt block kernels with $w_1(0) = w_2(0) = 0.5$, $\mu_1(0) = 2.75$, $\mu_2(0) = 4.25$, $h_1(0) = h_2(0) = 0.75$, $\alpha_1(0) = \alpha_2(0) = 10^{-3}$.

B-6 Conclusions

The development of the simulators and the simulations have lead to a number of issues and new insight in the method, which were used to form the following conclusions.

It was found that the LSQKD method is capable of approximating a PDF that transforms due to nonlinear dynamics. Furthermore, the simulation cases showed that the use of two kernels instead of one kernel increases the accuracy significantly and is useful to account for nonlinear behavior.

An inherent limitation of the method is that the method cannot provide feasible solutions for a larger number of kernels than two. This can be explained by the fact that as the number of kernels increases, the change in the PDF due to the change of one kernel approaches to zero.

This means that difference in the performance of the optimal solution and other solutions becomes less, which causes that the method cannot find (choose) an optimal solution.

The method is limited such that an exact uniform distribution cannot be modeled. Several approximate block functions were found that can be used to approximately model a uniform distribution. The disadvantage is that no analytical solutions of the $\boldsymbol{A}$,$\boldsymbol{B}$ and $\boldsymbol{C}$ matrices could be found for these functions. This means that the a minimum of $9N^2$ integrals have to be evaluated for a kernel with two parameters, which increases with the number of parameters. As a result, the computation time is much larger than with Gaussian kernels for which analytical expressions are available.

There was no difference in accuracy observed in the solutions with stable and unstable dynamics. However, the "speed" of the dynamics does have an influence due to numerical issues. Fast dynamical models are generally more challenging to integrate, which is also the case with this method.

The computation time of the LSQKD method and the numerical DPP method have the same order of magnitude. However, for kernels, which do not have an analytical solution of the $\boldsymbol{A}$,$\boldsymbol{B}$ and $\boldsymbol{C}$ matrices, the computation time of the LSQKD was about a factor three larger. This indicates that the LSQKD method is not as efficient as expected. Because the LSQKD method requires that significantly less ODEs need to be solved to obtain a solution, it was expected that the computational-effort of the method is lower than the other methods. Because, the integrals (Equation (3-61)) that define the LSQKD equations cannot generally be obtained analytically, the benefit in computational-effort was not observed.

Because this test was performed with a one-dimensional dynamical model, the advantage of the LSQKD could not be truly tested. It is expected that a much better computational-effort ratio with the DPP method is obtained, when performing simulations for a multi-dimensional model. This is based on the fact that the number of ODEs that need to be solved in the LSQKD method is a function of the estimation parameters, which do not grow rapidly with the number of dimensions.

In addition, it must be noted that the code of the simulators that have been developed was not fully optimized. Therefore, a fair comparison in computation time cannot be performed. Nevertheless, a comparison of the simulation time is valuable to get an indication of the efficiency. Therefore, a second test is performed using a two-dimensional dynamical model to investigate the performance of the methods with a higher dimensional dynamical model, which will be discussed in Appendix C.

Appendix C

Two-Dimensional Test Case

This chapter explains simulations performed using a two-dimensional test case to test the PDF propagation methods, discussed in Chapter 3.

C-1 Research Setup

The goal of this research is to test several important aspects that are fundamental to multi-dimensional problems. One of these important aspects is correlation, which needs to be accurately modeled. Copulae (Section A-4) are used to model correlation in a multi-dimensional PDF and Cholesky decomposition (Section 3-1-2) is used to obtain correlated samples.

The equations of motion contain multiple sine and cosine functions, so these are included in the dynamical model to investigate the influence of these functions on the evolution of the initial PDF.

An MC simulator and a DPP simulator were developed to perform the simulations. The MC simulator uses the methods discussed in Section 3-1-1 to generate random samples of the initial state and propagates this state so that the distribution of the state at a later time can be investigated. The samples can be generated using a pseudo-random generator or a sobol sampler. The DPP simulator implements the method discussed in Section 3-4 with the option that the state can be propagated forward or backward.

C-2 Dynamical Model

The simulations performed for this test case are performed using a dynamical model described by Equation (C-1). This model is chosen, because it is a non-linear differential equation, which involves sinusoids with a period T. These sinusoids introduce periodic behavior, which is also present in the equations of motion for entry trajectories. Therefore, this test can reveal some problems that may occur when simulating atmospheric entry trajectories.

$$\dot{\boldsymbol{x}} = \begin{pmatrix} \dot{x} \\ \dot{y} \end{pmatrix} = \begin{pmatrix} ay \sin\left(\frac{2\pi x}{T}\right) \\ b \sin\left(\frac{2\pi x}{T}\right) \end{pmatrix} \tag{C-1}$$

As was observed in the first test case, the probability density moves towards stable stationary points. The stationary points for this dynamical model are:

$$\dot{\boldsymbol{x}} = \mathbf{0} \rightarrow x = Tn/2 \quad n \in \aleph \tag{C-2}$$

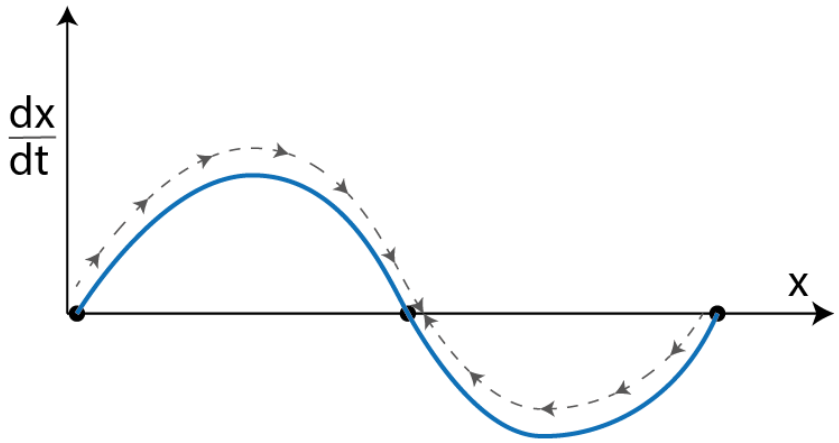

Figure C-1: State derivative vs state plot to illustrate the behaviour of the state over time.

These stationary points are basically stationary lines, because y can have any value. The stable stationary lines are the lines for which the gradient is directed towards these lines, so these lines attract probability. From Figure C-1 it can be derived that the state derivative cause the state to move towards the middle root, so this is a stable stationary point. The other stationary point is unstable, because the state derivative cause the state to move away from this point. The stable stationary points are described as

$$x_{stable} = \begin{cases} Tn + T/2 & y > 0 \\ Tn & \text{otherwise} \end{cases} \tag{C-3}$$

where n is any integer value. Note that the sign of y has an influence on the stable stationary lines, because it mirrors the sinusoid in the dynamical model. It can also be observed that an infinite number of stable stationary lines can be found, so it is expected that the PDF will be multimodal, which means that the PDF contains multiple peaks.

Propagating the initial PDF in time requires that an extra state Ω also needs to be propagated in time. Using the dynamical model and Equations (3-23b) and (3-28), the following equation was derived:

$$\dot{\Omega} = \frac{2\pi ay}{T} \cos\left(\frac{2\pi x}{T}\right) \tag{C-4}$$

No analytical solution for the PDF (Equation (3-27)) can be obtained for this dynamical model, so the solution will be obtained numerically.

C-3 Verification and Results

Several simulations are performed to verify the simulators and to compare the performance of the methods. The results of two cases are presented in this section.

Case A

The first case is performed using a uniform distribution where the random variables are uncorrelated. The following dynamical model was used for the simulations:

$$\begin{pmatrix} \dot{x} \\ \dot{y} \end{pmatrix} = \begin{pmatrix} 0.25y \sin(\pi x) \\ 0.5 \sin(\pi x) \end{pmatrix} \tag{C-5}$$

The distribution of the initial state is a uniform distribution with the following properties:

$$\boldsymbol{\mu} = \begin{pmatrix} 2.0 \\ 0.0 \end{pmatrix} \quad , \quad \boldsymbol{\Sigma} = \begin{bmatrix} 2.0 & 0.0 \\ 0.0 & 2.0 \end{bmatrix}$$

From the covariance matrix it follows that the width of the initial distribution in the x and y direction is equal to $2\sigma\sqrt{3} \approx 4.9$ and there is no correlation between the variables. This means that the PDF can be presented as a flat surface with a constant probability density value.

Figure C-2 displays a solution of the DPP simulator and a solution of the Monte Carlo simulator is shown in Figure C-3. These figures clearly correspond and each feature of the distribution in the samples of the Monte Carlo simulator is observed in the PDF obtained using the DPP simulator, so the simulators provide accurate results.

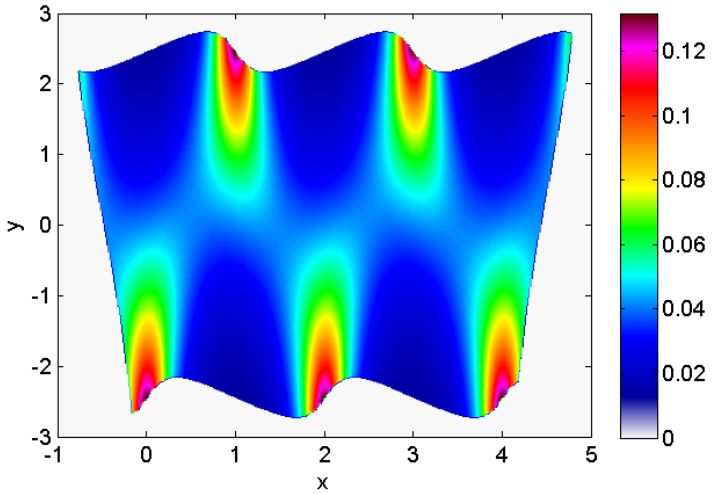

Figure C-2: PDF of the state at $t = 0.6$ obtained usin the DPP method.

The figure shows a periodic behavior in the x direction and the areas with a high probability occur along the stable stationary lines (Section C-2). This confirms the expectation that the

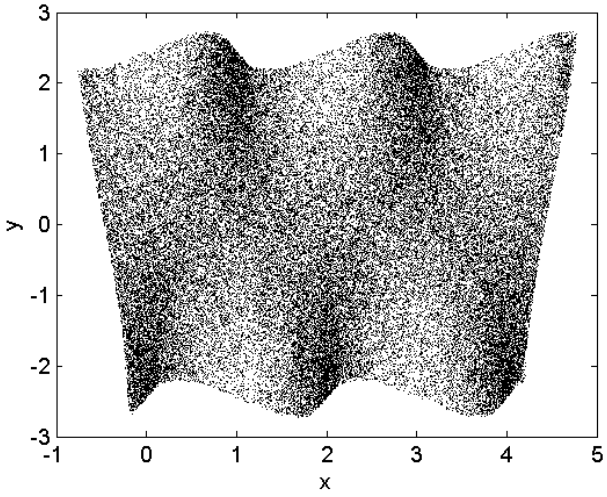

Figure C-3: Monte Carlo solution at $t = 0.6$ for $N = 6 \cdot 10^4$ samples.

probability density flows towards these stationary lines. Furthermore, the shape of the PDF is like a trapezoid, which can be attributed to the location of the stationary lines. For values of $y > 0$, stationary lines are present at $x = -1, 1, 3, 5$ and for values of $y \leq 0$, the stationary lines are located at $x = 0, 2, 4$. These lines correspond to the areas where the probability density is higher in Figure C-2. The waves can be explained by determining the direction in which the state flows, which can be derived from the derivatives:

$$\frac{\dot{y}}{\dot{x}} = \frac{2}{y} \quad \text{if } y \neq 0 \tag{C-6}$$

From this equation it can be observed that the particles starting with $y > 0$ move towards the right and upward, which explains the shape of the waves at the top boundary. Using the same equation, one can derive that the waves are directed in the other direction for values $y < 0$. One can also observe that $\dot{y}/\dot{x}$ becomes large for smaller values of y. Therefore, the particles will move away from $y = 0$ resulting in areas of higher probability density near the upper and lower boundary.

The marginal distributions of X and Y are presented in Figure C-4. These distributions represent the distribution of each variable irrespectively of the value of the other random variable, so without information of the correlation structure. The marginal of X shows a probability density peak at every stable stationary line, so the sine function in the dynamical model results in a multi-modal PDF. These lines are seperated by $T/2 = 1$, because the stable stationary lines alternate depending on the sign of y. The marginal of Y is constant within a large range, which can also be explained using the dynamical model. The derivative of y depends on a sine function of x, so it alternates between positive and negative. Therefore, the number of states that are located in an area with positive $\dot{y}$ is equal to the number of states that are located in an area with negative $\dot{y}$, so the marginal distribution of Y remains constant.

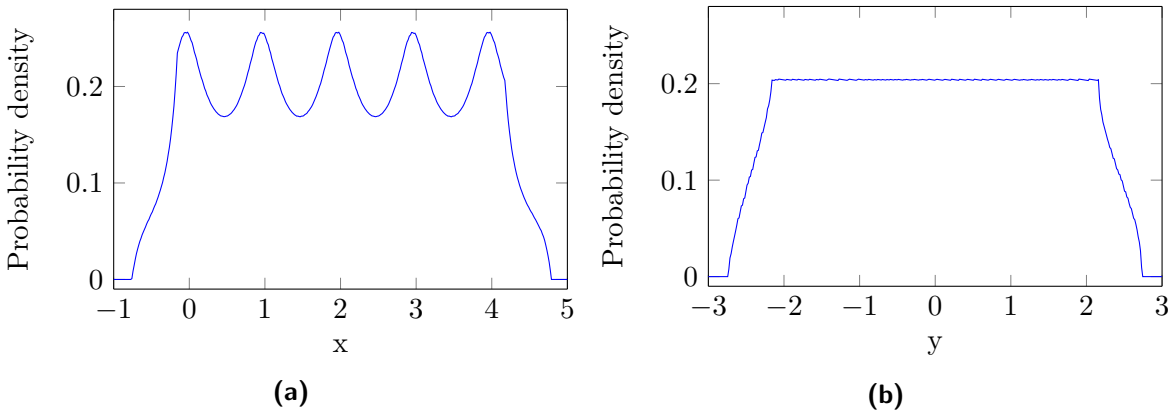

Figure C-4: Marginal distributions of X and Y at $t = 0.6$.

Case B

For the second case an initial distribution is used that contains correlation between the random variables. The following dynamical model was used for the simulations:

$$\begin{pmatrix} \dot{x} \\ \dot{y} \end{pmatrix} = \begin{pmatrix} y \sin(2\pi x) \\ \sin(2\pi x) \end{pmatrix} \tag{C-7}$$

The distribution of the initial state is a joint uniform distribution with the following properties:

$$\boldsymbol{\mu} = \begin{pmatrix} 0.0 \\ 0.0 \end{pmatrix} \quad , \quad \boldsymbol{\Sigma} = \begin{bmatrix} 1.0 & 0.5 \\ 0.5 & 1.0 \end{bmatrix}$$

The covariance matrix $\boldsymbol{\Sigma}$ involves a cross component, so the variables are correlated with a correlation coefficient $\rho = 0.5$. A Gaussian copula (Section A-4) is used to model the joint distribution.

The MC and DPP simulators are used to investigate the evolution of the distribution of the state $[x \quad y]^T$. The initial PDF and samples generated using these simulators are displayed in Figure C-5. The PDF is truncated at a value of 0.3, otherwise the structure in the middle of the PDF is not observable. The figures show that the generated samples match with the initial distribution.

The results of the DPP simulator and the MC simulator are shown in Figure C-6 and Figure C-9 for $t = 0.2$ and $t = 0.8$. Both figures of the PDF are truncated at a maximum PDF value so that the form can be accurately observed. Comparing the figures it can be concluded that all the features that are shown in the PDF are also observed in the samples of the MC simulations.

Similar to the results obtained in case A, the stable stationary lines are also observed in the PDF. In addition, one can observe that the probability density is higher at the upper right and lower left of the figure. This is a consequence of the initial correlation between the variables, because the initial distribution (Figure C-5a) also has this feature.

The marginal distribution of X is shown Figure C-7. This distribution illustrates that the probability density flows towards the stationary lines. The peaks that occur in this distribution do not have the same size, because the variables are correlated. Comparing the marginal

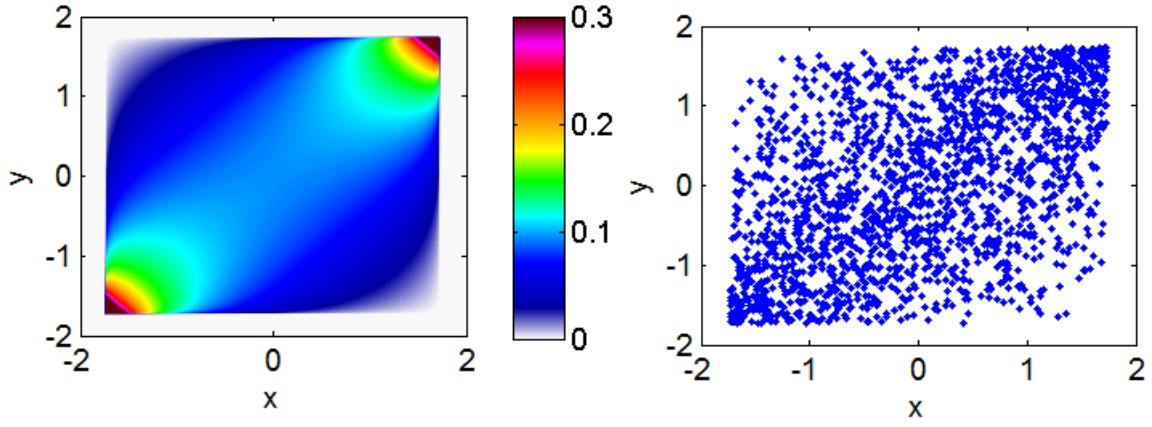

(a) DPP **(b)** MC $2 \cdot 10^3$ samples

Figure C-5: Comparison of samples of the MC simulator and the initial distribution used in the DPP simulator.

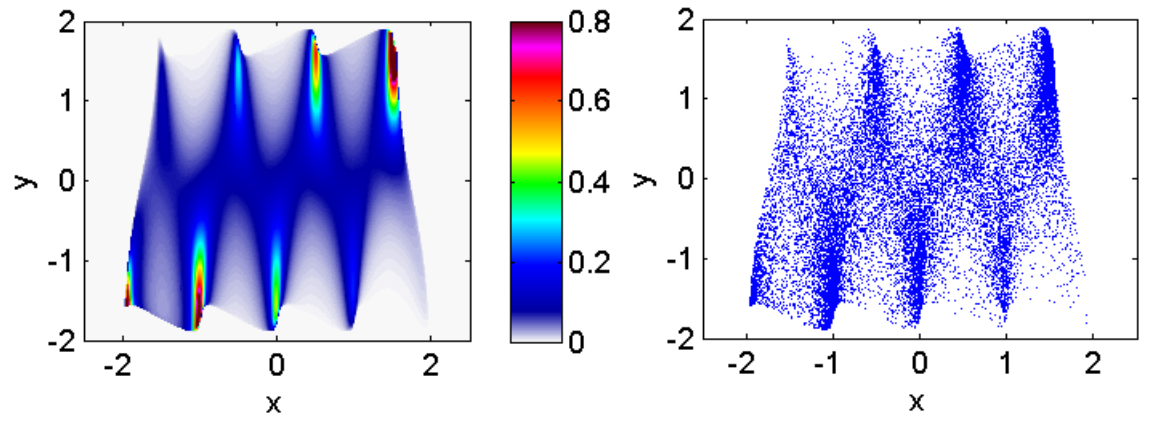

(a) DPP **(b)** 10^4 samples

Figure C-6: Comparison of MC samples and joint PDF obtained using the DPP simulator at $t = 0.2$.

distribution with the joint distribution, one can see that the large peaks in the marginal distributions correspond to the areas of higher probability density.

In addition, two conditional distributions where obtained using the same joint PDF, which are shown in Figure C-8. The first distribution is a distribution of Y with the condition $x = 0$. This condition corresponds to a stationary line for which the stationary line is stable for $y < 0$ and unstable for $y > 0$. The skewness of the distribution is consistent with the fact that the stable stationary line is located at $y < 0$, because this line attracts probability density.

The second conditional distribution (Figure C-8b) is a distribution of X with the condition $y = 1$. The figure shows four peaks that are also observed in the joint PDF along $y = 1$.

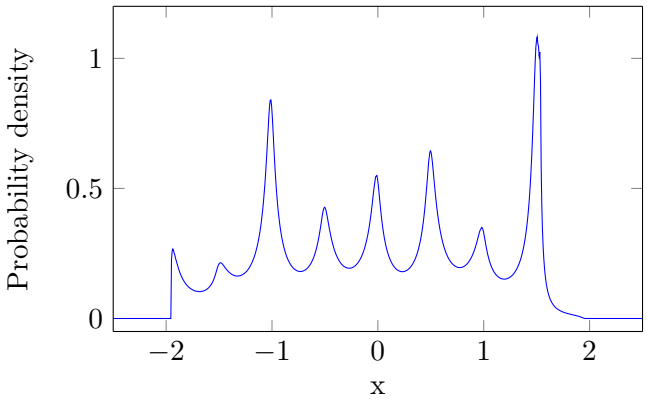

Figure C-7: Marginal distribution of X for $t = 0.2$.

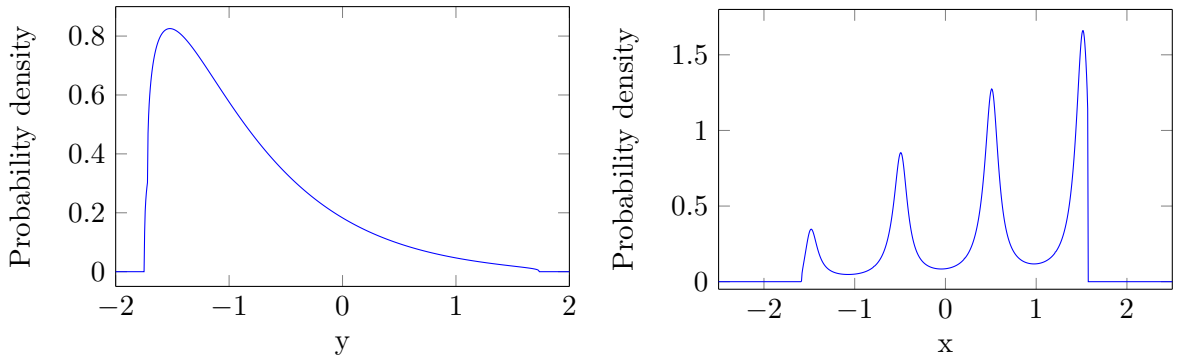

(a) $x = 0$ **(b)** $y = 1$

Figure C-8: Conditional distribution of Y and X at $x = 0$ and $y = 1$ for $t = 0.2$.

The results of the DPP simulator could be obtained using backward or forward propagation of the state as discussed in Section 3-4. The results presented in Figure C-9a are obtained using backward propagation and a rectangularly sampled grid with size of 400x400, so the spacing of the grid is around 0.01. In regions where the probability density changes rapidly, the spacing must be smaller to obtain accurate results. Therefore, the result in Figure C-9a shows inaccuracies around the regions of high probability density, because the spacing is too large.

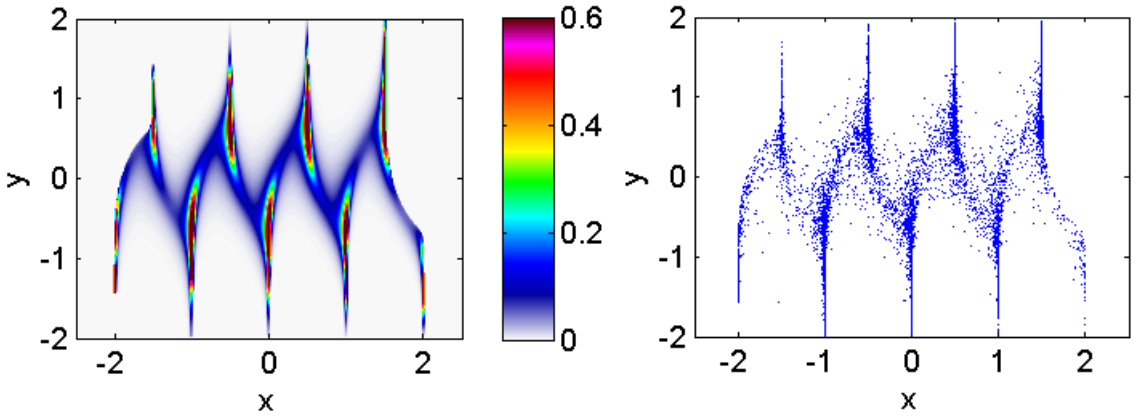

(a) DPP **(b)** 10^4 samples

Figure C-9: Comparison of MC samples and joint PDF obtained using the DPP simulator at $t = 0.8$ (obtained using backward time propagation).

The results of a second simulation using forward state propagation are shown in Figure C-10. The samples that are propagated are mostly concentrated near areas of high probability due to the nature of the differential equations. Therefore, the PDF at regions of high probability is accurately simulated. However, regions of low probability contain a small number of datapoints, so less information of the PDF is obtained for those regions.

The reason that Figure C-10 does not correspond to Figure C-9a is that there are less datapoints in the low probability regions. Because there are no datapoints, Matlab® interpolates the data to plot the figure in those regions. The simulations have shown that the results are more affected by this problem for a large time, because the probability density decreases with time in these regions, so less datapoints are available. This problem is not present if backward propagation is used to determine the distribution, because the location of the datapoints can be pre-determined.

An option of the MC simulator is to use Sobol sampling to generate the samples. Results of the MC simulator using Sobol sampling are shown in Figure C-11. The figures show that the initial samples are more evenly distributed and the obtained samples more clearly match the PDF shown in Figure C-9a. This means that the simulation supports the idea that sobol samples leads to a faster convergence.

C-4 Conclusions

The simulations have shown that sine functions in the dynamical model lead to a multi-modal shape of the PDF. In addition, the second test case has shown that a Gaussian copula can be used to model the initial PDF for uniformly distributed variables that are correlated. Furthermore, the shape of the PDF is largely affected by correlation in the variables, so correlation cannot be neglected. The evolution of the PDF in time also showed that the probability density gets increasingly concentrated even though the marginal distributions do not necessarily show this behavior.

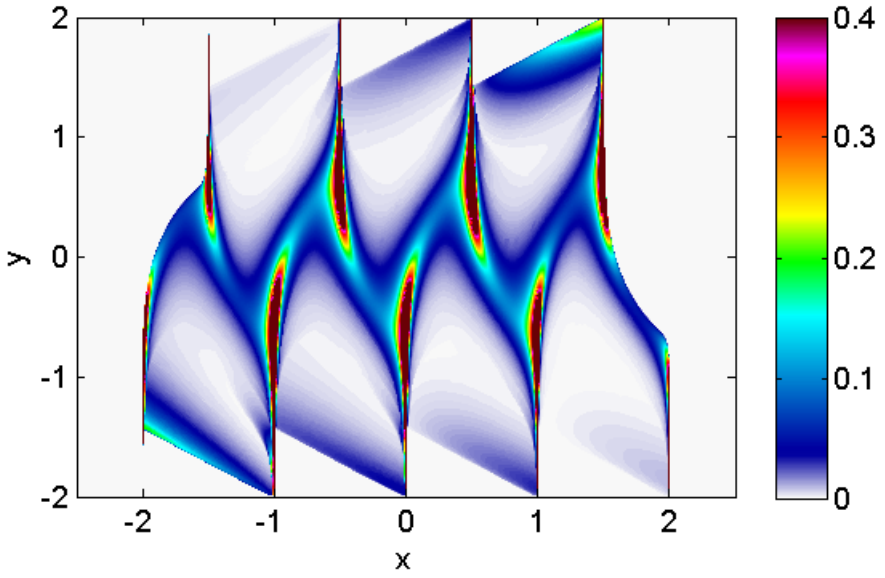

Figure C-10: DPP simulator result for $t = 0.8$ using forward state propagation.

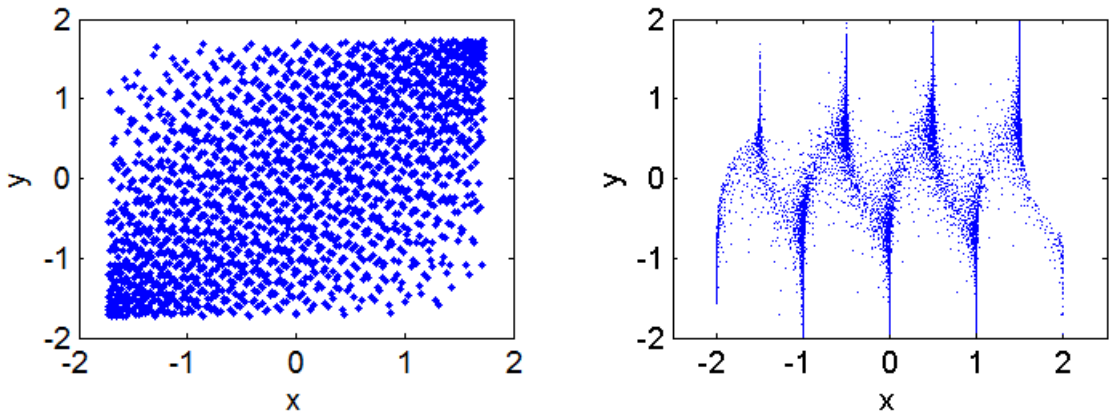

(a) $t = 0$, $N = 2 \cdot 10^3$ **(b)** $t = 0.8$, $N = 10^4$

Figure C-11: Comparison of MC samples using the Sobol sampler at $t = 0$ and $t = 0.8$.

The simulations have shown that backward and forward state propagation both have their advantages and disadvantages. Backward state propagation results in a lower accuracy for regions with rapid changes in probability density. However, the method allows to model the grid in such a way that the most optimal solution of the PDF can be obtained, because the datapoints can be chosen.

Forward state propagation results in datapoints of the final PDF, which the location cannot be chosen, so this can lead to inaccuries for areas where the probability density is low. The results in regions with a high probability density are accurate, because many datapoints are present in these regions.

Appendix D

LSQKD Equations

This chapter describes the equations for the LSQKD method for the one-dimensional case (Section D-1), which is described in Appendix B. In addition, the LSQKD equations are described for a two-dimensional model in Section D-2.

D-1 One-dimensional Test Case

This section describes the LSQKD equations for the one-dimensional case with a Gaussian kernel and a uniform kernel. These equations are implemented in the simulators described in Appendix B. The equations described in this section are derived using a symbolic manipulation software package called Maple®.

D-1-1 Gaussian Kernels

This section describes the LSQKD equations for a one-dimensional case with a Gaussian kernel, given by Equation (D-1):

$$K(x,\mu,\sigma) = \frac{\exp\left(-\frac{(x-\mu)^2}{2\sigma^2}\right)}{\sigma\sqrt{2\pi}} \tag{D-1}$$

The PDF will thus be modeled by a weighted summation of N Gaussian kernels with weights w_i:

$$\varphi(x) = \boldsymbol{w}^T\boldsymbol{P} = \sum_{i=1}^{N} w_i \frac{\exp\left(-\frac{(x-\mu_i)^2}{2\sigma_i^2}\right)}{\sigma_i\sqrt{2\pi}} \tag{D-2a}$$

$$\boldsymbol{P} = \begin{bmatrix} K(x,\mu_1,\sigma_1) & K(x,\mu_2,\sigma_2) & \dots & K(x,\mu_N,\sigma_N) \end{bmatrix}^T \tag{D-2b}$$

$$\boldsymbol{w} = \begin{bmatrix} w_1 & w_2 & \dots & w_N \end{bmatrix}^T \tag{D-2c}$$

The vector with model parameters is thus:

$$\boldsymbol{\beta} = \begin{bmatrix} \mu_1 & \sigma_1 & \mu_2 & \sigma_2 & \dots & \mu_N & \sigma_N \end{bmatrix}^T \tag{D-3}$$

The derivatives of the kernel to the mean μ and standard deviation σ are required to derive the matrices. These derivatives are:

$$\frac{dK}{d\mu} = \frac{(x-\mu)\exp\left(-\frac{(x-\mu)^2}{2\sigma^2}\right)}{\sigma^3\sqrt{2\pi}} \tag{D-4}$$

$$\frac{dK}{d\sigma} = \frac{(x-\mu)^2\exp\left(-\frac{(x-\mu)^2}{2\sigma^2}\right)}{\sigma^4\sqrt{2\pi}} - \frac{\exp\left(-\frac{(x-\mu)^2}{2\sigma^2}\right)}{\sigma^2\sqrt{2\pi}} \tag{D-5}$$

The matrix $\boldsymbol{M}$ can be derived using these derivatives:

$$\boldsymbol{M} = \frac{\partial \boldsymbol{P}}{\partial \boldsymbol{\beta}} = \begin{bmatrix} \frac{\partial K_1}{\partial \mu_1} & \frac{\partial K_1}{\partial \sigma_1} & 0 & 0 & 0 & \dots & 0 \\ 0 & 0 & \frac{\partial K_2}{\partial \mu_2} & \frac{\partial K_2}{\partial \sigma_2} & 0 & \dots & 0 \\ \vdots & \vdots & & & \ddots & \ddots & 0 \\ 0 & 0 & 0 & \dots & 0 & \frac{\partial K_N}{\partial \mu_N} & \frac{\partial K_N}{\partial \sigma_N} \end{bmatrix} \tag{D-6}$$

The matrix $\boldsymbol{A}$ is provided in Equation (D-7):

$$\boldsymbol{A} = \begin{bmatrix} \frac{1}{2\sigma_1\sqrt{\pi}} & \frac{\exp\left(\frac{-(\mu_1^2-2\mu_1\mu_2+\mu_2^2)}{2(\sigma_1^2+\sigma_2^2)}\right)}{\sqrt{2\pi(\sigma_1^2+\sigma_2^2)}} & \dots & \frac{\exp\left(\frac{-(\mu_1^2-2\mu_1\mu_N+\mu_N^2)}{2(\sigma_1^2+\sigma_N^2)}\right)}{\sqrt{2\pi(\sigma_1^2+\sigma_N^2)}} \\ \frac{\exp\left(\frac{-(\mu_2^2-2\mu_2\mu_1+\mu_1^2)}{2(\sigma_2^2+\sigma_1^2)}\right)}{\sqrt{2\pi(\sigma_2^2+\sigma_1^2)}} & \frac{1}{2\sigma_2\sqrt{\pi}} & \vdots & \frac{\exp\left(\frac{-(\mu_2^2-2\mu_2\mu_N+\mu_N^2)}{2(\sigma_2^2+\sigma_N^2)}\right)}{\sqrt{2\pi(\sigma_2^2+\sigma_N^2)}} \\ \vdots & & \ddots & \vdots \\ \frac{\exp\left(\frac{-(\mu_N^2-2\mu_N\mu_1+\mu_1^2)}{2(\sigma_N^2+\sigma_1^2)}\right)}{\sqrt{2\pi(\sigma_N^2+\sigma_1^2)}} & \frac{\exp\left(\frac{-(\mu_N^2-2\mu_N\mu_2+\mu_2^2)}{2(\sigma_N^2+\sigma_2^2)}\right)}{\sqrt{2\pi(\sigma_N^2+\sigma_2^2)}} & \dots & \frac{1}{2\sigma_N\sqrt{\pi}} \end{bmatrix} \tag{D-7}$$

The matrix $\boldsymbol{B}$, given in Equation (D-8) can be divided in several submatrices:

$$\boldsymbol{B} = \begin{bmatrix} B_{11} & B_{12} & \dots & B_{1N} \\ B_{21} & B_{22} & \dots & B_{2N} \\ \vdots & \vdots & \ddots & \vdots \\ B_{N1} & B_{N2} & \dots & B_{NN} \end{bmatrix} \tag{D-8}$$

Two different submatrices occur in the matrix of which the submatrices on the diagonal of the matrix have the form described by Equation (D-9). The matrices that are not placed on the diagonal are given in Equation (D-10). The matrices on the diagonal describe the effect of the parameters of the kernel with itself and the matrices that are not placed on the diagonal describe the effect of the parameters on the parameters of the other kernels.

$$\boldsymbol{B}_{ii} = \begin{bmatrix} \frac{w_i^2}{4\sigma_i^3\sqrt{\pi}} & 0 \\ 0 & \frac{3w_i^2}{8\sigma_i^3\sqrt{\pi}} \end{bmatrix} \tag{D-9}$$

$$\boldsymbol{B}_{ij} = \frac{w_i w_j \exp\left(\frac{-(\mu_i-\mu_j)^2}{2(\sigma_i^2+\sigma_j^2)}\right)}{\sqrt{2\pi}} \begin{bmatrix} \boldsymbol{B}_{ij1} & \boldsymbol{B}_{ij2} \end{bmatrix} \tag{D-10a}$$

$$\boldsymbol{B}_{ij1} = \begin{bmatrix} \frac{\left(-(\mu_i-\mu_j)^2+\sigma_i^2+\sigma_j^2\right)}{(\sigma_i^2+\sigma_j^2)^{5/2}} \\ -\frac{\sigma_i\left(3\sigma_i^2+3\sigma_j^2-(\mu_i-\mu_j)^2\right)(\mu_i-\mu_j)}{(\sigma_i^2+\sigma_j^2)^{7/2}} \end{bmatrix} \tag{D-10b}$$

$$\boldsymbol{B}_{ij2} = \begin{bmatrix} \frac{\sigma_j\left(3\sigma_i^2+3\sigma_j^2-(\mu_i-\mu_j)^2\right)(\mu_i-\mu_j)}{(\sigma_i^2+\sigma_j^2)^{7/2}} \\ \frac{3\sigma_i\sigma_j\left(\frac{1}{3}\mu_i^4-\frac{4}{3}\mu_i^3\mu_j+2\mu_i^2(\mu_j^2-\sigma_i^2-\sigma_j^2)+4\mu_i\mu_j(\sigma_i^2+\sigma_j^2-\frac{1}{3}\mu_j^2)+\frac{1}{3}\mu_j^4-2\mu_j^2(\sigma_i^2+\sigma_j^2)+\left(\sigma_i^2+\sigma_j^2\right)^2\right)}{(\sigma_i^2+\sigma_j^2)^{9/2}} \end{bmatrix} \tag{D-10c}$$

The matrix $\boldsymbol{C}$, given in Equation (D-11) can also be divided in several submatrices:

$$\boldsymbol{C} = \begin{bmatrix} \boldsymbol{C}_1 \\ \boldsymbol{C}_2 \\ \vdots \\ \boldsymbol{C}_N \end{bmatrix} \tag{D-11}$$

These submatrices have the following form:

$$\boldsymbol{C}_i = \begin{bmatrix} C_{i,11} & C_{i,12} & \dots & C_{i,1N} \\ C_{i,21} & C_{i,22} & \dots & C_{i,2N} \end{bmatrix} \tag{D-12}$$

The coefficients of these submatrices can be determined using the following equations:

$$C_{i,1i} = 0 \tag{D-13a}$$

$$C_{i,1j} = \frac{\exp\left(\frac{-(\mu_i-\mu_j)^2}{2(\sigma_i^2+\sigma_j^2)}\right) w_i\sqrt{2}(\mu_i-\mu_j)}{\sqrt{\pi}(\sigma_i^2+\sigma_j^2)^{3/2}} \quad j \neq i \tag{D-13b}$$

$$C_{i,2i} = -\frac{w_i}{2\sqrt{\pi}\sigma_i^2} \tag{D-13c}$$

$$C_{i,2j} = \frac{\sigma_i w_i\sqrt{2}\exp\left(\frac{-(\mu_i-\mu_j)^2}{2(\sigma_i^2+\sigma_j^2)}\right)((\mu_i-\mu_j)^2-\sigma_i^2-\sigma_j^2)}{\sqrt{\pi}(\sigma_i^2+\sigma_j^2)^{5/2}} \quad j \neq i \tag{D-13d}$$

The vectors $\boldsymbol{D}$ and $\boldsymbol{E}$ are derived using the $\boldsymbol{Q}$ vector:

$$\boldsymbol{Q} = \frac{d}{dx}\left(F(x)\boldsymbol{P}\right) = \begin{pmatrix} \frac{dF(x)}{dx}K_1 + \frac{dK_1}{dx}F(x) \\ \vdots \\ \frac{dF(x)}{dx}K_N + \frac{dK_N}{dx}F(x) \end{pmatrix} \tag{D-14a}$$

$$\frac{dK}{dx} = \frac{(x-\mu)\exp\left(-\frac{(x-\mu)^2}{2\sigma^2}\right)}{\sigma^3\sqrt{2\pi}} \tag{D-14b}$$

The vectors $\boldsymbol{D}$ and $\boldsymbol{E}$ are dependent on the dynamical model so they are not provided in this section. However, analytical expressions for these vectors could be obtained using the model presented in Appendix B, but these equations are too long display.

D-1-2 Uniform kernel

The following kernel is used that approaches a uniform distribution for $\alpha \to 0$:

$$K(x,\mu,h,\alpha) = \frac{1}{4h}\left(\frac{x-\mu+h}{\sqrt{\alpha+(x-\mu+h)^2}} - \frac{x-\mu-h}{\sqrt{\alpha+(x-\mu-h)^2}}\right) \tag{D-15}$$

It has been verified that this kernel satisfies the normality condition, so the integral results in 1.

The PDF will thus be modeled by a weighted summation of N Gaussian kernels with weights w_i:

$$\varphi(x) = \boldsymbol{w}^T\boldsymbol{P} = \sum_{i=1}^{N} w_i K_i(x,\mu_i,h_i,\alpha_i) \tag{D-16a}$$

$$\boldsymbol{P} = \begin{bmatrix} K(x,\mu_1,h_1,\alpha_1) & K(x,\mu_2,h_2,\alpha_2) & \dots & K(x,\mu_N,h_N,\alpha_N)\end{bmatrix}^T \tag{D-16b}$$

$$\boldsymbol{w} = \begin{bmatrix} w_1 & w_2 & \dots & w_N\end{bmatrix}^T \tag{D-16c}$$

The vector with model parameters is thus:

$$\boldsymbol{\beta} = \begin{bmatrix}\mu_1 & h_1 & \alpha_1 & \mu_2 & h_2 & \alpha_2 & \dots & \mu_N & h_N & \alpha_N\end{bmatrix}^T \tag{D-17}$$

The derivatives of the kernel to the mean μ and standard deviation σ are required to derive the matrices.

$$\begin{aligned}\frac{dK}{d\mu} = \frac{1}{4h}\Bigg(&\frac{1}{\sqrt{\alpha+(x-\mu-h)^2}} + \frac{(x-\mu-h)(-x+\mu+h)}{(\alpha+(x-\mu-h)^2)^{3/2}} \\ &- \frac{1}{\sqrt{\alpha+(x-\mu+h)^2}} - \frac{(x-\mu+h)(-x+\mu-h)}{(\alpha+(x-\mu+h)^2)^{3/2}}\Bigg)\end{aligned} \tag{D-18}$$

$$\begin{aligned}\frac{dK}{dh} = \frac{1}{4h}\Bigg(&\frac{1}{\sqrt{\alpha+(x-\mu+h)^2}} - \frac{(x-\mu+h)(x-\mu+h)}{(\alpha+(x-\mu+h)^2)^{3/2}} \\ &+ \frac{1}{\sqrt{\alpha+(x-\mu-h)^2}} + \frac{(x-\mu-h)(-x+\mu+h)}{(\alpha+(x-\mu-h)^2)^{3/2}} \\ &- \frac{1}{h}\left(\frac{x-\mu+h}{\sqrt{\alpha+(x-\mu+h)^2}} - \frac{x-\mu-h}{\sqrt{\alpha+(x-\mu-h)^2}}\right)\Bigg)\end{aligned} \tag{D-19}$$

$$\frac{dK}{d\alpha} = \frac{1}{8h}\left(\frac{x-\mu-h}{(\alpha+(x-\mu-h)^2)^{3/2}} - \frac{x-\mu+h}{(\alpha+(x-\mu+h)^2)^{3/2}}\right) \tag{D-20}$$

The matrix $\boldsymbol{M}$ is derived using these derivatives:

$$\boldsymbol{M} = \frac{\partial \boldsymbol{P}}{\partial \boldsymbol{\beta}} = \begin{bmatrix} \frac{\partial K_1}{\partial \mu_1} & \frac{\partial K_1}{\partial h_1} & \frac{\partial K_1}{\partial \alpha_1} & 0 & 0 & 0 & 0 & \dots & 0 \\ 0 & 0 & 0 & \frac{\partial K_2}{\partial \mu_2} & \frac{\partial K_2}{\partial h_2} & \frac{\partial K_2}{\partial \alpha_2} & 0 & \dots & 0 \\ \vdots & \vdots & & & & \ddots & \ddots & \ddots & 0 \\ 0 & 0 & 0 & 0 & \dots & 0 & \frac{\partial K_N}{\partial \mu_N} & \frac{\partial K_N}{\partial h_N} & \frac{\partial K_N}{\partial \alpha_N} \end{bmatrix} \tag{D-21}$$

The vectors $\boldsymbol{D}$ and $\boldsymbol{E}$ are derived using the $\boldsymbol{Q}$ vector:

$$\boldsymbol{Q} = \frac{d}{dx}\left(F(x)\boldsymbol{P}\right) = \begin{pmatrix} \frac{dF(x)}{dx}K_1 + \frac{dK_1}{dx}F(x) \\ \vdots \\ \frac{dF(x)}{dx}K_N + \frac{dK_N}{dx}F(x) \end{pmatrix} \tag{D-22a}$$

$$\begin{aligned} \frac{dK}{dx} = \frac{1}{4h}\Bigg(& \frac{1}{\sqrt{\alpha + (x-\mu+h)^2}} + \frac{(x-\mu-h)(x-\mu-h)}{\left(\alpha + (x-\mu-h)^2\right)^{3/2}} \\ & - \frac{1}{\sqrt{\alpha + (x-\mu-h)^2}} - \frac{(x-\mu+h)(x-\mu+h)}{\left(\alpha + (x-\mu+h)^2\right)^{3/2}} \Bigg) \end{aligned} \tag{D-22b}$$

D-2 Derivation of the LSQKD method with Local State Variables

For a multi-dimensional state derivative model it is possible that for some state variables the evolution in time is highly nonlinear. As a result it is difficult to obtain accurate results with the LSQKD method. An option of the LSQKD method to achieve more accurate results, is to seperate the state variables in local and global state variables. The shape of the PDF of the state is less constraint for the local state variables, so more accurate results can be obtained. An example of such a method is described in the paper of Pantano and Shotorban (2007). This section describes the derivation of the partial differential equations provided in Section 4-A-2 of the paper.

The following dynamical model was used in the paper:

$$\boldsymbol{F}(x,u) = \begin{pmatrix} F_x \\ F_u \end{pmatrix} = \begin{pmatrix} \dot{x} \\ \dot{u} \end{pmatrix} = \begin{pmatrix} u \\ \frac{\phi(x,t)-u}{\tau} \end{pmatrix} \tag{D-23}$$

The PDF is modelled by a single Gaussian kernel:

$$\varphi(u,x,t) = w(x,t)\frac{\exp\left(-\frac{(u-\mu(x,t))^2}{2\sigma(x,t)^2}\right)}{\sigma(x,t)\sqrt{2\pi}} \tag{D-24}$$

This equation shows that the PDF is approximated by a Gaussian distribution in u space and it can take any form in x space, because the parameters are a function of x. The vector $\boldsymbol{P}$ is thus defined as:

$$\boldsymbol{P} = K\left(u, \mu(x,t), \sigma(x,t)\right) = \frac{\exp\left(-\frac{(u-\mu(x,t))^2}{2\sigma(x,t)^2}\right)}{\sigma(x,t)\sqrt{2\pi}} \tag{D-25}$$

The vector $\boldsymbol{Q}$ is found to be:

$$\boldsymbol{Q} = \frac{\partial}{\partial u}\left(F_u K\right) = \frac{\partial F_u}{\partial u}K + \frac{\partial K}{\partial u}F_u \tag{D-26a}$$

$$\boldsymbol{Q} = \frac{-K}{\tau} + \frac{\partial K}{\partial u}F_u \tag{D-26b}$$

The vector $\boldsymbol{V}$ is found to be:

$$\boldsymbol{V} = \frac{\partial}{\partial x}\left[F_x(u)w(x,t)K\left(u,\mu(x,t),\sigma(x,t)\right)\right] \tag{D-27}$$

$$\boldsymbol{V} = u\left[\frac{\partial w}{\partial x}K + \left(\frac{\partial K}{\partial \mu}\frac{\partial \mu}{\partial x} + \frac{\partial K}{\partial \sigma}\frac{\partial \sigma}{\partial x}\right)w\right] \tag{D-28}$$

The vector $\boldsymbol{D}$ is derived:

$$\boldsymbol{D} = 2\int_{-\infty}^{\infty}\left(\boldsymbol{w}^T\boldsymbol{Q} + \boldsymbol{V}\right)\boldsymbol{P}d\boldsymbol{X_G} = \frac{1}{2\sqrt{\pi}\sigma^2\tau}\left(2\frac{\partial w}{\partial x}\mu\sigma\tau - w\left(\sigma - \frac{\partial \mu}{\partial x}\sigma\tau + \frac{\partial \sigma}{\partial x}\mu\tau\right)\right) \tag{D-29}$$

The vector $\boldsymbol{E}$ is derived:

$$\boldsymbol{E} = 2\int_{-\infty}^{\infty}\left(\boldsymbol{w}^T\boldsymbol{Q} + \boldsymbol{V}\right)\boldsymbol{M}^T\boldsymbol{w}d\boldsymbol{X_G} \tag{D-30a}$$

$$\boldsymbol{E} = \frac{w}{4\sqrt{\pi}\sigma^3\tau}\begin{pmatrix} 2\frac{\partial w}{\partial x}\sigma^2\tau + w\left(2\mu + 2\mu\tau\frac{\partial \mu}{\partial x} + \sigma\tau\frac{\partial \sigma}{\partial x}\right) \\ -2\mu\sigma\tau\frac{\partial w}{\partial x} + w\left(3\mu\tau\frac{\partial \sigma}{\partial x} + 3\sigma + \sigma\tau\frac{\partial \mu}{\partial x}\right)\end{pmatrix} \tag{D-30b}$$

Solve system of equations results in:

$$\begin{pmatrix}\dot{w}\\ \dot{\mu}\\ \dot{\sigma}\end{pmatrix} = \begin{pmatrix} -\frac{\partial w}{\partial x}\mu - \frac{\partial \mu}{\partial x}w + \frac{3}{2}\lambda\sqrt{\pi}\sigma \\ -\frac{1}{2}\sigma\left(\frac{2\sigma}{w}\frac{\partial w}{\partial x} + \frac{\partial \sigma}{\partial x}\right) - \mu\left(\frac{\partial \mu}{\partial x} + \frac{1}{\tau}\right) + \frac{\phi}{\tau} \\ -\frac{\partial \mu}{\partial x}\sigma - \mu\frac{\partial \sigma}{\partial x} - \frac{\sigma}{\tau} + \frac{\lambda\sqrt{\pi}\sigma^2}{w}\end{pmatrix} \tag{D-31}$$

This solution can be rewritten to obtain the equations as displayed in the paper using the following equations:

$$\frac{\partial(\ln w)}{\partial x} = \frac{1}{w}\frac{\partial w}{\partial x} \tag{D-32}$$

$$\frac{\partial w\mu}{\partial x} = \frac{\partial w}{\partial x}\mu + \frac{\partial \mu}{\partial x}w \tag{D-33}$$

Rewriting Equations (D-31), results in the following equations:

$$\frac{\partial w}{\partial t} + \frac{\partial w\mu}{\partial x} = 0 \tag{D-34a}$$

$$\frac{\partial \mu}{\partial t} + \sigma^2\frac{\partial \ln w}{\partial x} + \frac{\sigma}{2}\frac{\partial \sigma}{\partial x} + \mu\frac{\partial \mu}{\partial x} = \frac{\phi(x) - \mu}{\tau} \tag{D-34b}$$

$$\frac{\partial \sigma}{\partial t} + \frac{\partial \mu\sigma}{\partial x} = \frac{\sigma}{\tau} \tag{D-34c}$$

These equations match the equations presented in the paper except for the $\sigma^2\frac{\partial \ln w}{\partial x}$ term in the second equation. The equation in the paper does not include the square on σ. These equations have been independently derived and thoroughly verified, so it is concluded that the difference can be atributed to a typing error in the paper.

Appendix E

Impact Time Distributions

The impact time distributions that are discussed in Section 9-2 are displayed in this appendix.

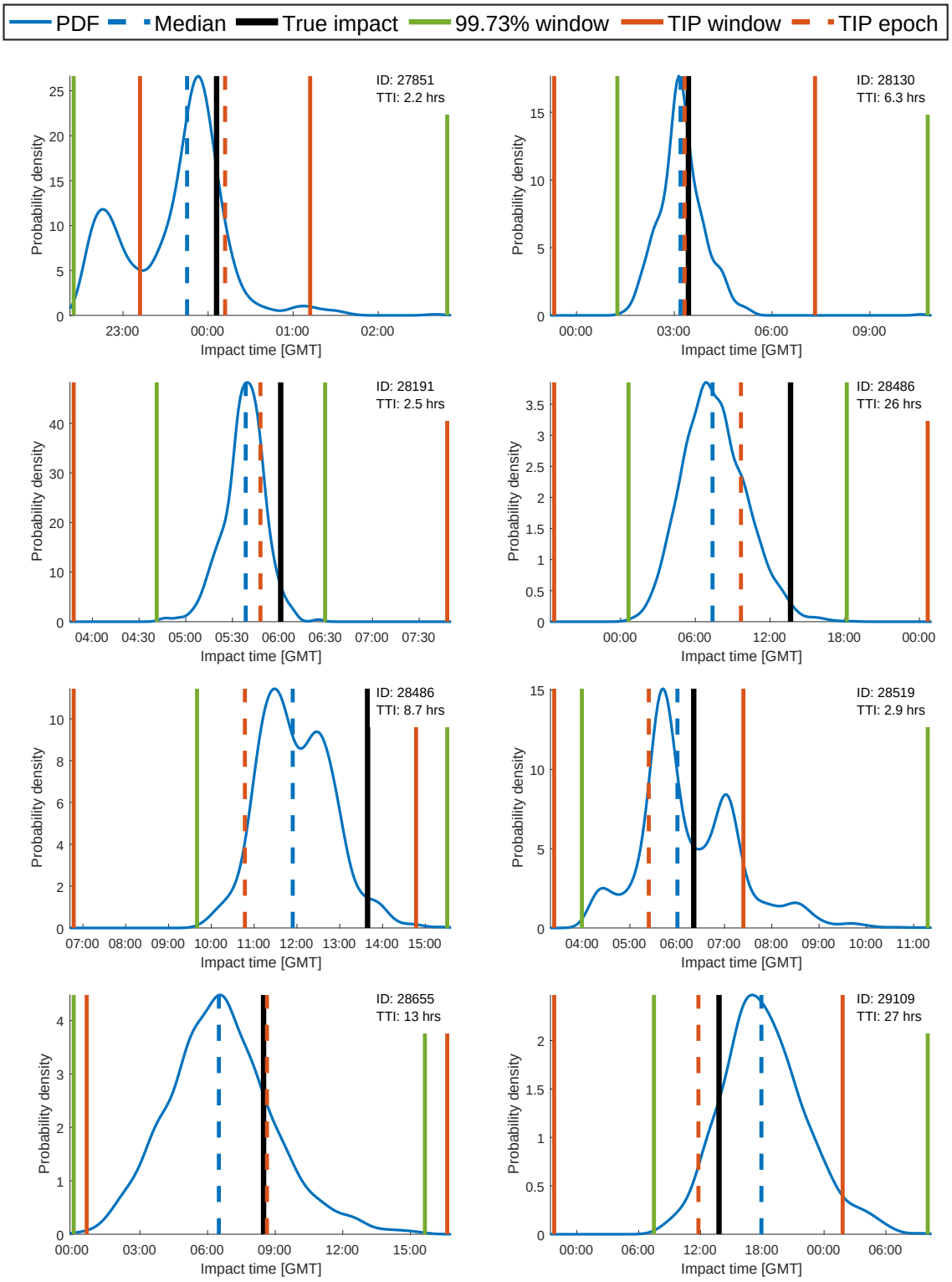

Figure E-1: Impact time distributions derived using the original uncertainty model (1-8).

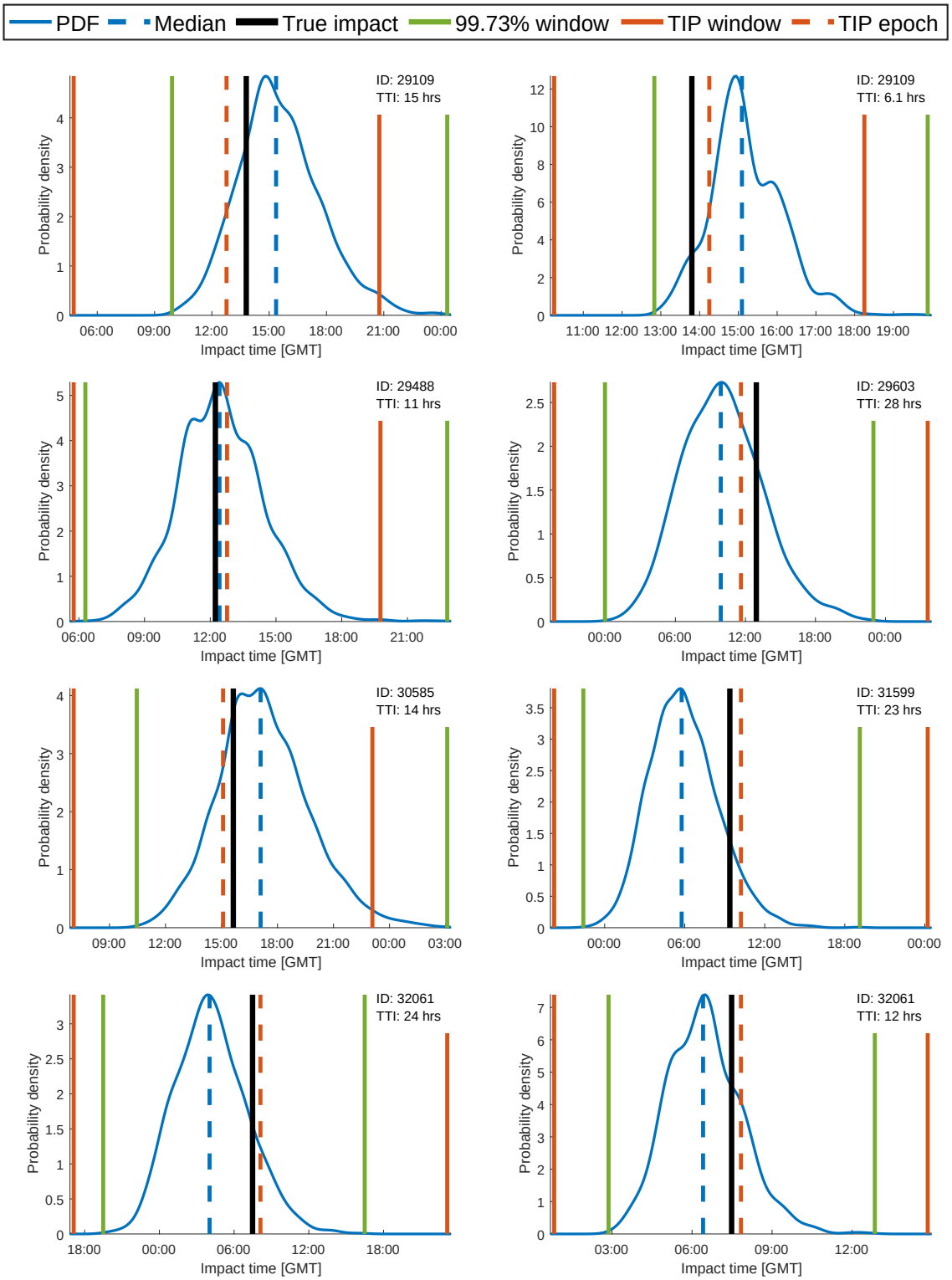

Figure E-2: Impact time distributions derived using the original uncertainty model (9-16).

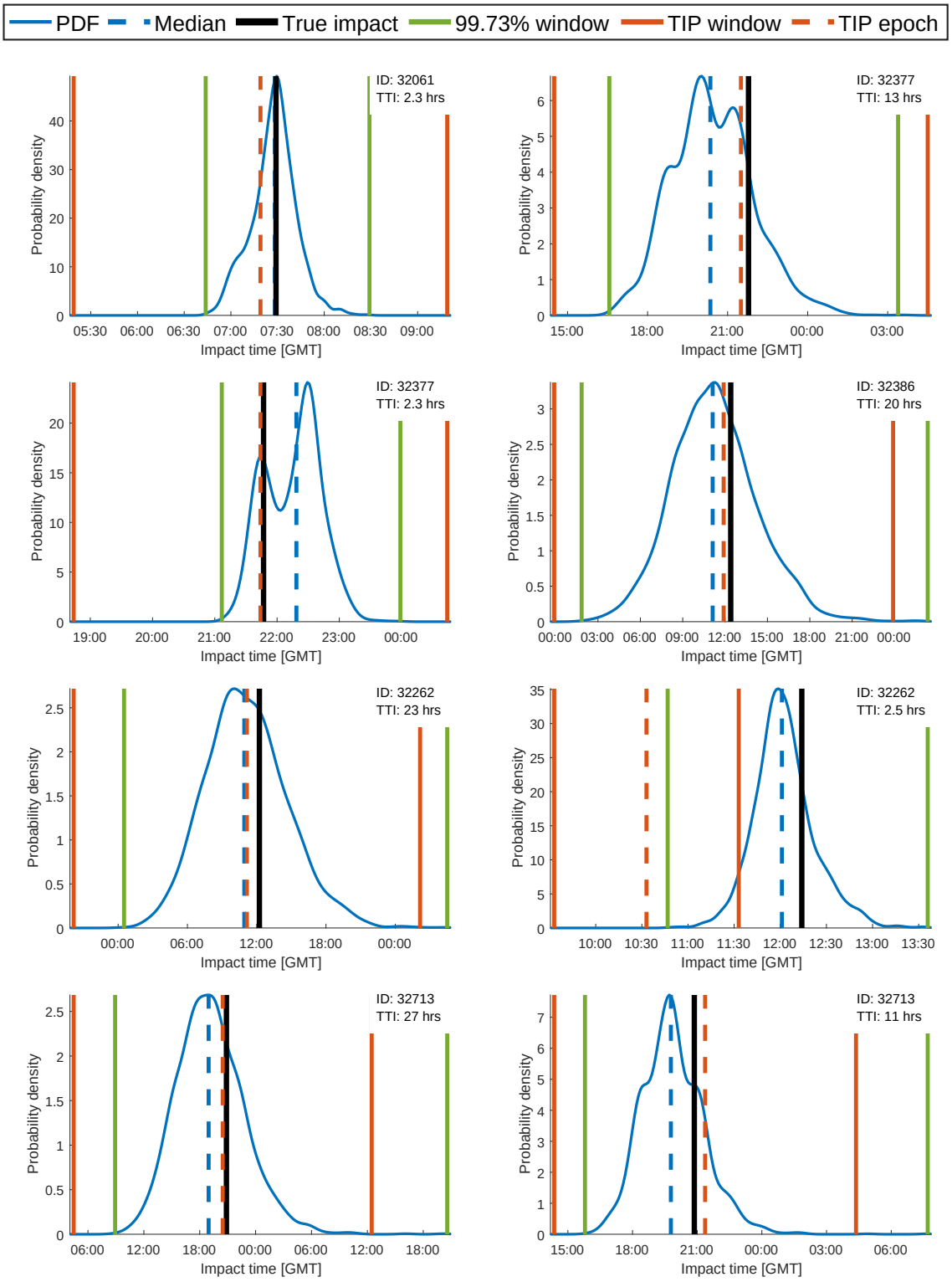

Figure E-3: Impact time distributions derived using the original uncertainty model (17-24).

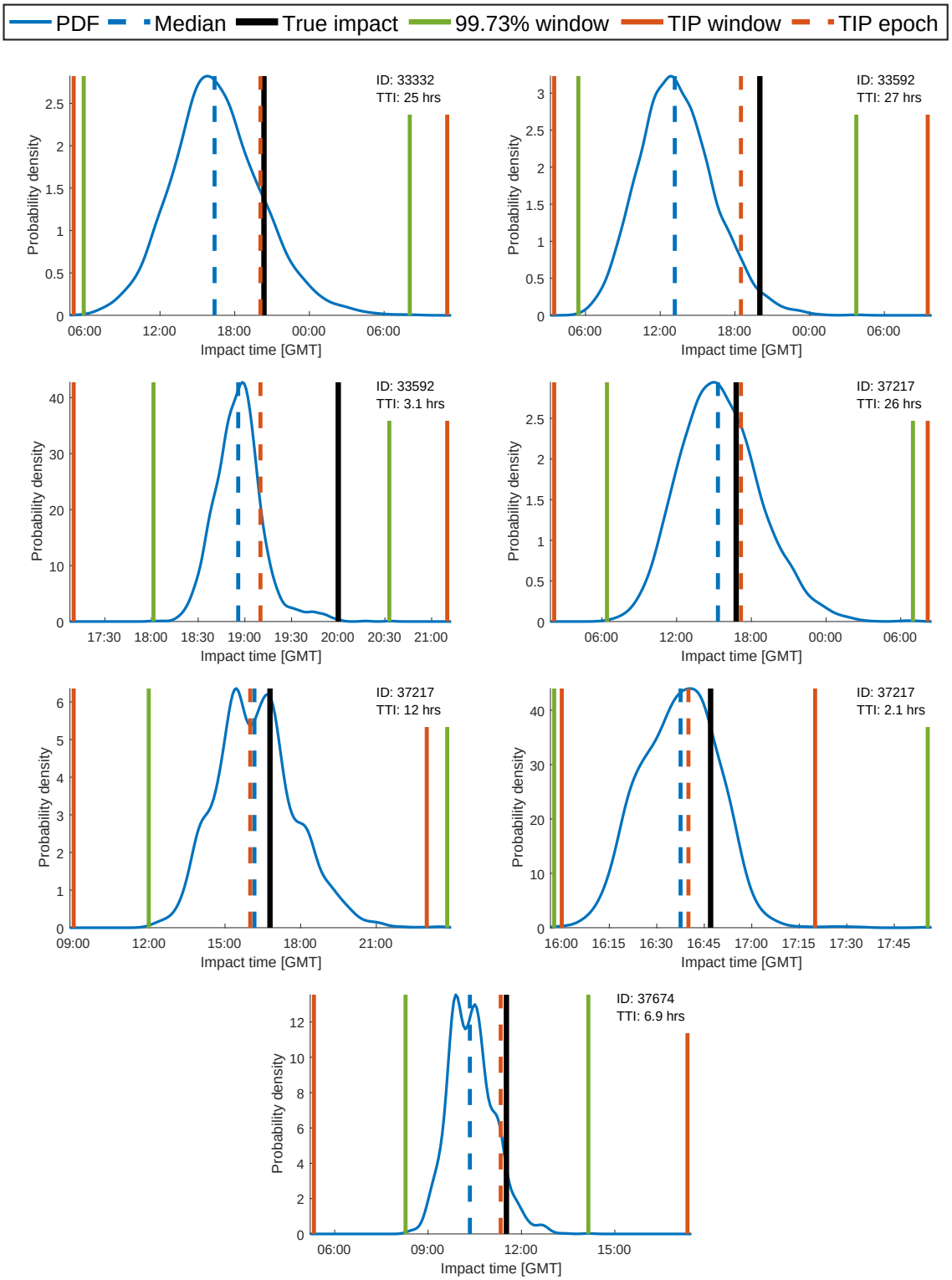

Figure E-4: Impact time distributions derived using the original uncertainty model (25-31).

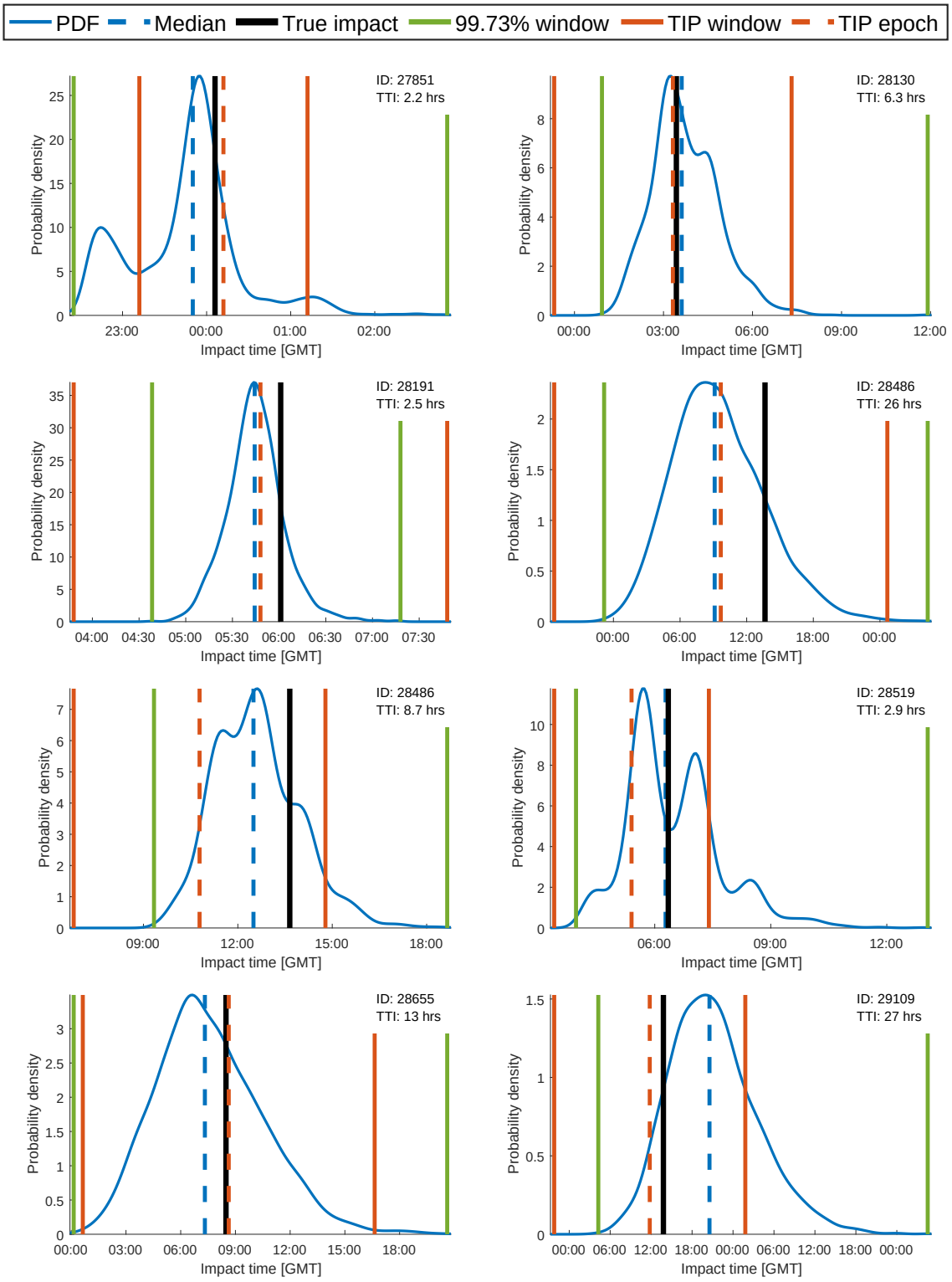

Figure E-5: Impact time distributions derived using the modified uncertainty model (1-8).

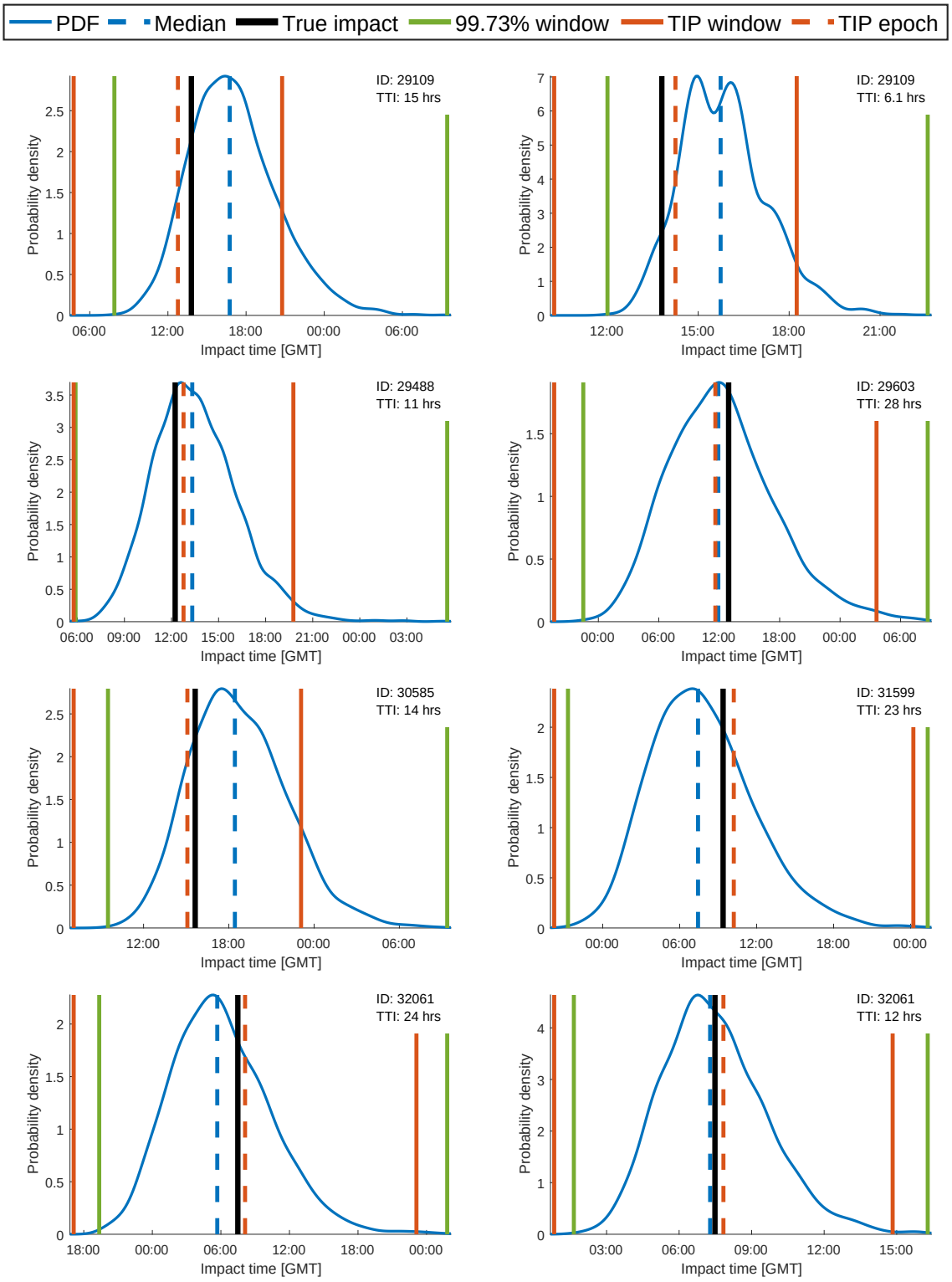

Figure E-6: Impact time distributions derived using the modified uncertainty model (9-16).

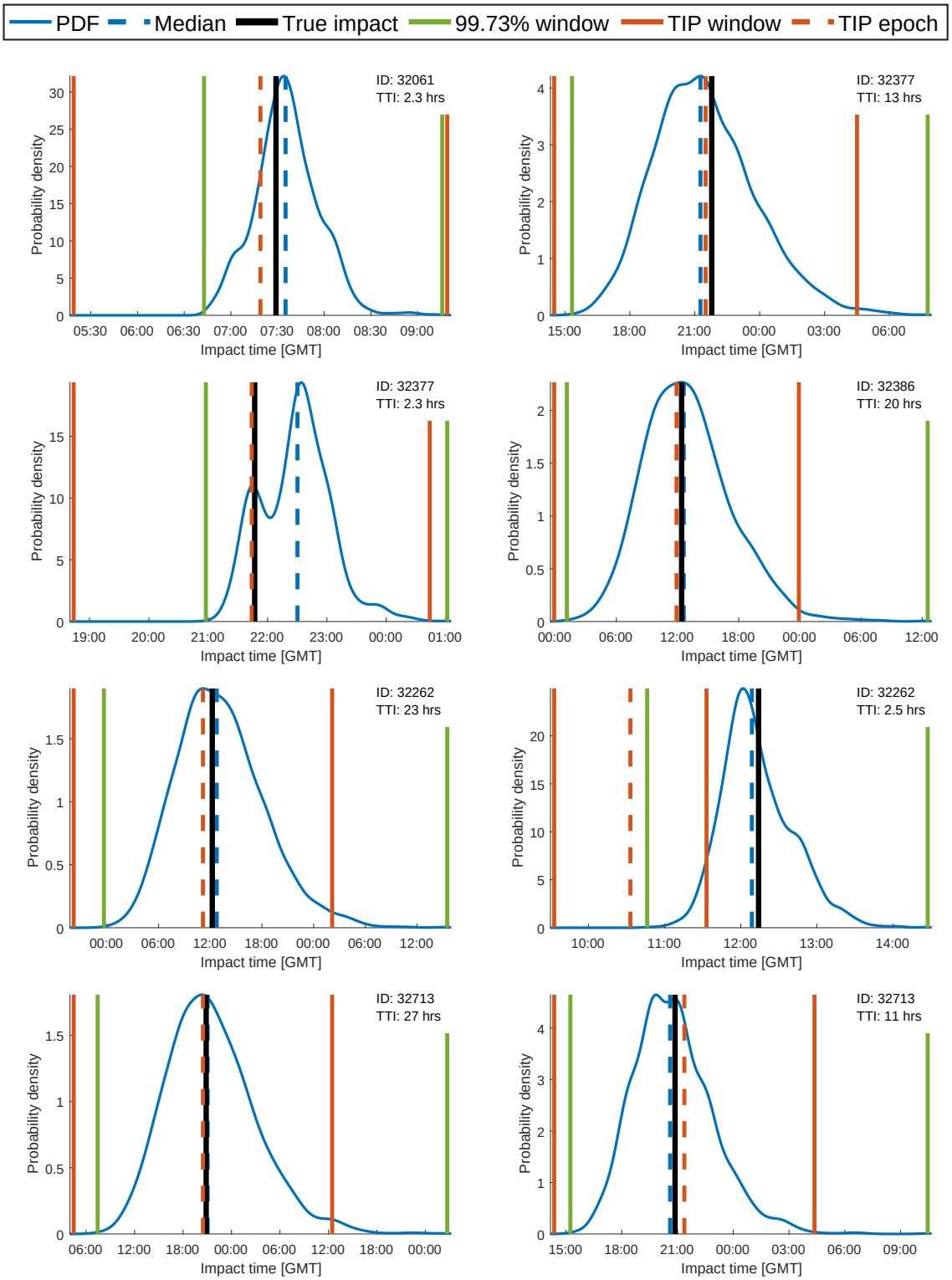

Figure E-7: Impact time distributions derived using the modified uncertainty model (17-24).

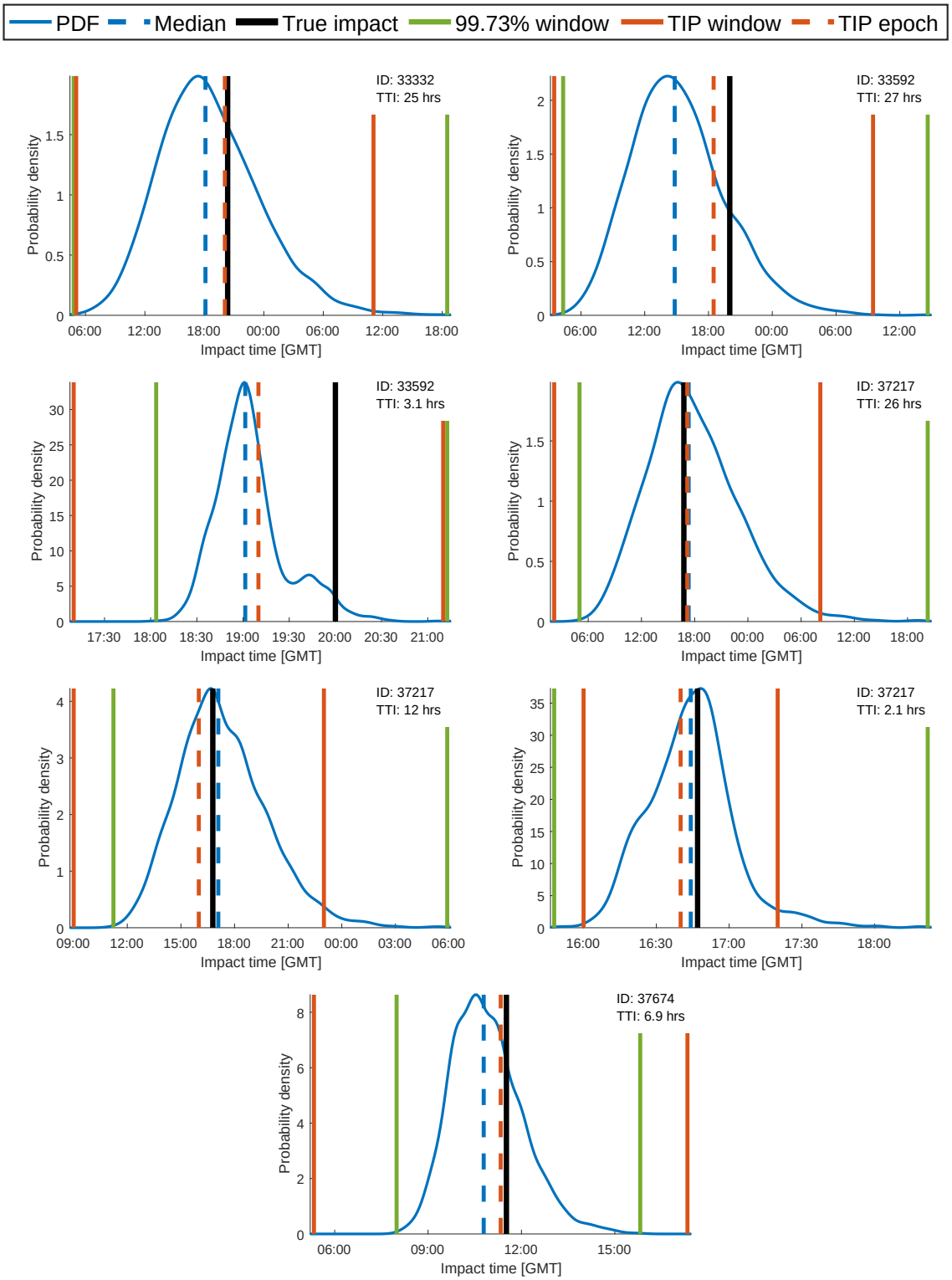

Figure E-8: Impact time distributions derived using the modified uncertainty model (25-31).